JYU DISSERTATIONS 64

Laetitia Canete

High Precision Mass Measurements for Nuclear Astrophysics

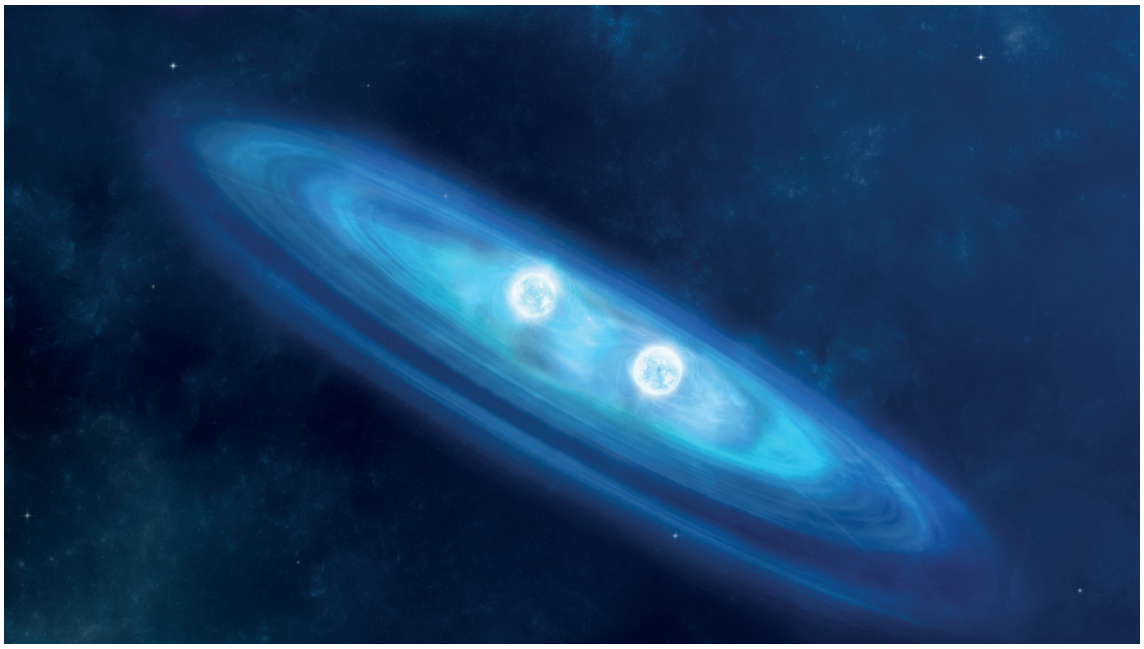

UNIVERSITY OF JYVÄSKYLÄ
FACULTY OF MATHEMATICS
AND SCIENCE

JYU DISSERTATIONS 64

Laetitia Canete

High Precision Mass Measurements for Nuclear Astrophysics

Esitetään Jyväskylän yliopiston matemaattis-luonnontieteellisen tiedekunnan suostumuksella
julkisesti tarkastettavaksi yliopiston Ylistönrinteen salissa FYS1
maaliskuun 8. päivänä 2019 kello 12.

Academic dissertation to be publicly discussed, by permission of
the Faculty of Mathematics and Science of the University of Jyväskylä,
in Ylistönrinne, auditorium FYS1, on March 8, 2019 at 12 o'clock noon.

JYVÄSKYLÄN YLIOPISTO
UNIVERSITY OF JYVÄSKYLÄ

JYVÄSKYLÄ 2019

Editors
Anu Kankainen
Department of Physics, University of Jyväskylä
Ville Korkiakangas
Open Science Centre, University of Jyväskylä

Cover picture: *The fearless twins* by Chloé Cañete.

Permanent link to this publication: http://urn.fi/URN:ISBN:978-951-39-7693-4

ISBN 978-951-39-7693-4 (PDF)
URN:ISBN:978-951-39-7693-4
ISSN 2489-9003

ABSTRACT

Canete, Laetitia
High precision mass measurements for nuclear astrophysics
Jyväskylä: University of Jyväskylä, 2019, 108 p.
(JYU Dissertations
ISSN 2489-9003; 64;)
ISBN 978-951-39-7693-4 (PDF)
Diss.

Masses of neutron-deficient nuclei ^{25}Al, ^{30}P and ^{31}Cl and neutron-rich nuclei ^{67}Fe, ^{69}Co and ^{70}Co have been measured with the JYFLTRAP double Penning trap at the IGISOL-4 facility. The Time-of-Flight Ion Cyclotron Resonance technique has been used to achieve precise mass values whereas the Phase-Imaging Ion Cyclotron Resonance method has been employed for state identification in ^{70}Co. The resonant proton-capture rates for the ^{25}Al$(p,\gamma)^{26}$Si and ^{30}P$(p,\gamma)^{31}$S reactions have been calculated with the Q values determined in this work. The waiting-point conditions for ^{30}S in the rp-process have been studied using the proton separation energy determined for ^{31}Cl. Additionally, the mass-excess value of ^{31}Cl has been used to test the isobaric multiplet mass equation for the T= 3/2 quartet at A=31. The evolution of the mass surface and the N=40 subshell closure below ^{68}Ni has been studied with the new mass values of ^{67}Fe, ^{69}Co and ^{70}Co. The impact on the neutron capture rates ^{67}Fe$(n,\gamma)^{68}$Fe and ^{68}Co$(n,\gamma)^{69}$Co relevant for the weak r-process, and their inverse photodisintegration rates, is discussed.

Keywords: Penning trap, nuclear binding energy, nuclear astrophysics

Author

Laetitia Canete
Department of Physics
University of Jyväskylä
Finland

Supervisor

Dr. Docent Anu Kankainen
Department of Physics
University of Jyväskylä
Finland

Reviewers

Prof. Alan Chen
Department of Physics and Astronomy
Mc Master University
Canada

Dr. Sarah Naimi
RIKEN Nishina Center for Accelerator-Based Science
Japan

Opponent

Prof. Christopher Wrede
Department of Physics and Astronomy
National Superconducting Cyclotron Laboratory
Michigan State University
United States

PREFACE

On a hot day of summer 2014, my path took a lucky bend to the wooden lands of Finland. Along the unique opportunity to improve my mushroom picking skills and to test my own melting point in sauna, my four years and a half of living in Jyväskylä have been filled with friendly and helpful faces.

The realization of this thesis would not have been possible without my supervisor, Anu Kankainen. I warmly thank her for her wise supervision. I have been one of the lucky PhD students who could contact her supervisor at any time and with the feeling of working in a trustful atmosphere. She has been of a great help to me and I am proud to have been her first PhD student.
From my previous academic life, I would like to thank Richard Savage. Without his recommendation letter, I would maybe never have had the opportunity to enter in the IGISOL group.

Working in the IGISOL group has been a very good experience, academically and humanly. The small group became bigger through the years so that we had to consider to push the walls of the meeting room. Huge thanks to all previous and present IGISOL members I had the chance to work with. I would like to thanks the head of the group, Ari Jokinen, who welcomed me at my arrival in Jyväskylä. Among the senior IGISOL members, I particularly thank Tommi Eronen for his valuable advice to tame the Penning beast and Iain Moore for his support and for always making a good atmosphere in the group. Thanks to Dmitry Gorelov for his help at a time he was finishing his PhD in the group meanwhile I was the new lost student, and to Dmitry Nesterenko for his expertise and help on the trap realm. Thanks to the collaborators from GANIL I worked with, in particular Simon Giraud, best of luck for your coming defense! A warm thanks to the administrative staff in particular Marjut Hilska for taking care of all of us at the Department of Physics.

I'll keep very good memories of sharing work and endless parties with fellow IGISOL students and post docs: Sarina, Antoine, Clément, Markus, Ruben, Ilkka, Marjut, Ville, Alexandra and Olga. I wish the best of luck to the nexts in the list: Sarina, Markus, Marjut and Ville. You'll do it great! A warm thanks to Mikael for his kindness during these past months. During the past two years, I had the best housemate I could hope for, thanks Antoine (aka le colloc) for handle my morning mood and my ability to dispatch plants everywhere. It was great to share our Kekkola palace!

A huge thanks to all the people with whom I shared many good memories at Jyväskylä: Hussam, Elise, Alexandre, Akseli, and many more. Kiitos "suomalainen äitini", Anne Hyppä, loputtomasta optimismistasi opettaessasi minulle kaunista ja läpitunkematonta Suomen kieltä.

Music is important to keep the life sweet and smooth between night shifts. I would like to thank the wind orchestra Puhkupillit for the music and the good moments we shared together, and Jimmy for bringing so nice gigs here. Ett varmt tack till Alm för alla natt-långa samtal och de fina minnena vi delade. Du har varit en viktig inspirationskälla för mig under de senaste åren.

Merci à ma famille, en particulier à ma sœur Chloé qui a fait la couverture de cette thèse, à mon frère Guillaume et à mes supers neveux Bastien et Lilian. Finalement, une pensée et un grand merci à Victor, Anne, Marion, Ja (Antoine), Ga (Guillaume) et Ornella de faire partie de ma vie depuis presque le début.

Jyväskylä, February 2019
Laetitia Cañete

LIST OF FIGURES

LIST OF TABLES

CONTENTS

ACKNOWLEDGEMENTS

This work has been supported by the Academy of Finland under the Finnish Centre of Excellence Program (Nuclear and Accelerator Based Physics Research at JYFL 2012-2017). The support from the Academy of Finland (project grants No. 284516 and 312544) are gratefully acknowledged as well as the funding from the European Union's Horizon 2020 research and innovation program under grant agreement No. 771036 (ERC CoG MAIDEN), the bilateral mobility grant from the Institut Français in Finland, the Embassy of France in Finland, the French Ministry of Higher Education and Research and the Finnish Society of Science and Letters and the mobility support from PICS MITICANS (Manipulation of Ions in Traps and Ion sourCes for Atomic and Nuclear Spectroscopy).

LIST OF ARTICLES

This thesis is based on the listed publications. The **Articles I**, **II** and **III** are enclosed at the end of this thesis.

Article I: L. Canete, A. Kankainen, T. Eronen, D. Gorelov, J. Hakala, A. Jokinen, V.S. Kolhinen, J. Koponen, I.D. Moore, J. Reinikainen, and S. Rinta-Antila, *High-precision mass measurements of ^{25}Al and ^{30}P at JYFLTRAP*, European Physical Journal A (2016) 52:124

Article II: A. Kankainen, L. Canete, T. Eronen, J. Hakala, A. Jokinen, J. Koponen, I. D. Moore, D. Nesterenko, J. Reinikainen, S. Rinta-Antila, A. Voss, and J. Äystö, *Mass of astrophysically relevant ^{31}Cl and the breakdown of the isobaric multiplet mass equation*, Physical Review C 93, 041304(R) (2016)

Article III: L. Canete, S. Giraud, A. Kankainen, B. Bastin, F. Nowacki, A. Poves, P. Ascher, T. Eronen, V. Girard Alcindor, A. Jokinen, A. Khanam, I.D. Moore, D. Nesterenko, F. De Oliveira, H. Penttilä, C. Petrone, I. Pohjalainen, A. De Roubin, V. Rubchenya, M. Vilen, and J. Äystö,
Probing the $N = 40$ subshell closure via mass measurements of ^{67}Fe and $^{69,70}Co$, to be submitted.

Article IV: L. Canete, A. Kankainen, T. Eronen, D. Gorelov,J. Hakala, A. Jokinen, V. Kolhinen, J. Koponen, I.D. Moore, J. Reinikainen, S. Rinta-Antila, *High-Precision Proton-Capture Q Values for $^{25}Al(p,\gamma)^{26}Si$ and $^{30}P(p,\gamma)^{31}S$*, JPS Conf. Proc., 020503 (2017). Proceedings of the 14th International Symposium on Nuclei in the Cosmos (NIC2016).

Article V: L. Canete, T. Eronen, A. Jokinen, A. Kankainen, I.D. Moore, D.A. Nesterenko, and Sami Rinta-Antila,
High-precision mass measurements for the rp-process at JYFLTRAP, EPJ Web of Conferences 165, 01008 (2017). Proceedings of the Nuclear Physics in Astrophysics VIII (NPA8).

In addition to the listed papers, the author has actively participated in other experiments at IGISOL, resulting in 10 peer-reviewed publications as a co-author.

1 INTRODUCTION

Nuclear physics is a relatively recent sciences in the human history. The idea of matter organized as atoms was augured by ancient Greek philosophers as Leucippus and Democritus, and also developed later with interesting similarity in ancient Indian philosophy [1].
We know, since the beginning of the twentieth century, that the atoms are not the ultimate constituents of the matter. The atomic nucleus is composed of two kinds of nucleons, protons and neutrons, whose number lead to important properties and features for the nucleus. The total number of nucleons in a nucleus is called the mass number A. Nuclei with the same mass number are called isobars. The proton is a charged particle and it is thus sensitive to the electromagnetic force. Nuclei with the same number of protons are called isotopes. They exhibit similar chemical properties and belong to the same chemical element. Hence, the proton number Z is also known as the atomic number. Chemical elements are arranged according to their atomic number in the famous periodic table developed by Dmitri Ivanovitch Mendeleïev in 1869.
Neutrons do not have an electric charge and are only sensitive to the strong interaction in the nucleus. Neutrons do not live long outside an atomic nucleus. The free neutron half-life, which is the time in which half of the neutrons have decayed is about 10 minutes and 10 seconds. They decay via weak interaction into a proton, electron and antineutrino. The neutron number, N defines the stability of the isotopes. For light elements, the most stable isotopes have about the same number of protons and neutrons. When moving to heavier nuclei, the stability region is progressively moving away from the N=Z line toward the neutron-rich nuclei. Nuclei are commonly mapped in the so-called chart of nuclides where they are arranged according to their proton and neutron numbers (Fig. 1). The chart of nuclides illustrates many nuclear properties. The stable nuclei are found in the so-called valley of stability (in black in Fig. 1). When moving outside the valley of stability, nuclei become radioactive. Except for the heaviest nuclides, nuclei usually β-decay in which a proton is converted to neutron (β^+ decay and electron capture) or a neutron to a proton (β^- decay), moving one step closer to the valley of stability in the isobaric chain. Further from the valley of stability,

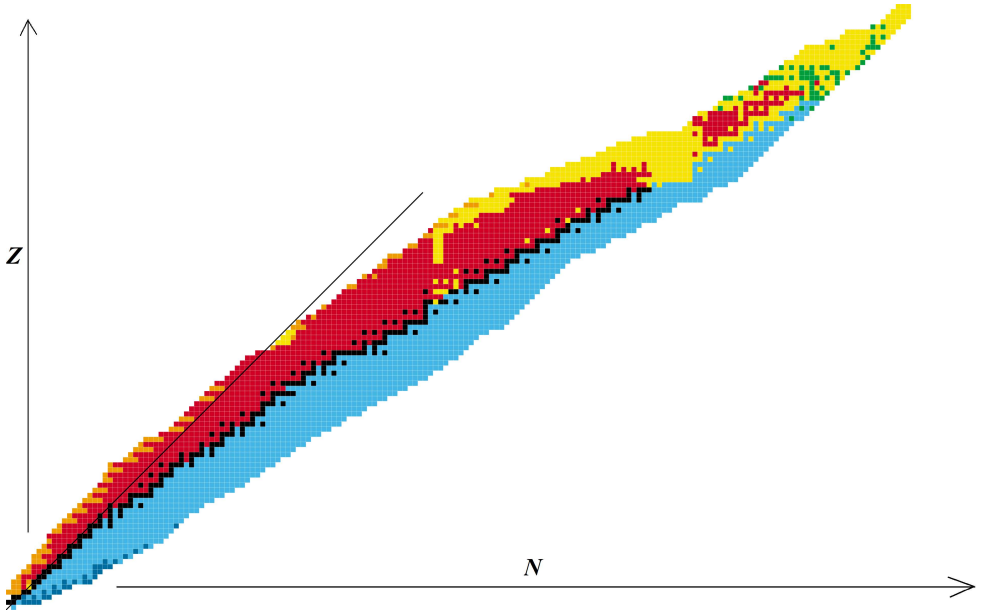

FIGURE 1 Chart of nuclides where the different colours illustrate the decay mode. The stable nuclei are in black, the nuclei that β^--decay are in blue and those that β^+-decay in red. The nuclei that decay by α-emission are represented in yellow, and by spontaneous fission in green. The N=Z line is indicated in black.

the half-lives of nuclei get shorter and hence they have a higher probability to decay. At some point, no more neutrons or protons can be added without inducing a rapid emission of a neutron or proton. This limit on the proton-rich side, the proton drip-line, is well known. The neutron drip-line is unknown above ^{16}O.

The limits of nuclear existence are of particular interest in astrophysics. In stellar environments, very high densities and temperatures can be reached leading to nucleosynthesis of exotic nuclei, close to the neutron and proton drip-lines. The processes in which neutron-rich or neutron-deficient nuclei are produced, such as the rapid neutron-capture process (r-process) and the rapid proton-capture process (rp-process), are an active research area. These are also key processes for understanding heavy element abundancies in the solar system.
It is challenging to study these processes in an accelerator laboratories due to small cross sections and short half-lives. Particle accelerators are needed to produce astrophysically relevant nuclei with small cross sections or study reaction cross sections close to astrophysical energies. The K130 cyclotron in the JYFL Accelerator Laboratory at the University of Jyväskylä can accelerate particles from protons to xenon ions, ideally up to the energy of 130 Q^2/A MeV where Q is the charge of the ion. The facility is used by many reasearch groups. This thesis project has been carried out in the IGISOL group which studies ground state and decay properties of nuclei e.g. via collinear laser spectroscopy or decay spectroscopy, or via high-precision atomic mass measurements using the double Penning trap JYFLTRAP like in this thesis. The masses of nuclei are indeed one of the key inputs for nuclear reactions, leading to the binding energies and Q values needed

for reaction rate calculations.

In the frame of this thesis, both neutron-rich and neutron-deficient nuclei of astrophysical interest have been studied. The masses of ^{25}Al and ^{30}P, relevant for ^{26}Al cosmic gamma rays and nova nucleosynthesis, were measured. For the *rp*-process, the mass of ^{31}Cl has been determined with a high precision. On the neutron-rich side, the mass of ^{67}Fe, the ground and isomeric states of ^{69}Co and the longer-living state of ^{70}Co were measured. ^{67}Fe and ^{69}Co are of particular importance for the weak *r*-process. In addition to astrophysical motivations, nuclei such ^{31}Cl, ^{67}Fe, ^{69}Co and ^{70}Co are relevant for theoretical nuclear physics. The mass of ^{31}Cl can be used to test the isobaric multiplet mass equation for the T=3/2 quartet at A=31. The ^{67}Fe, ^{69}Co and ^{70}Co are close to the N=40 neutron gap and thus interesting for nuclear structure studies far from stability. These results are given and discussed in the chapter 5 of this thesis. The theoretical and astrophysical motivations are given in chapters 2 and 3 followed by a more technical chapter where the experimental method is described.

2 BINDING ENERGY IN NUCLEAR PHYSICS

2.1 Nuclear binding energy

Since the discovery of the atomic nucleus by Ernest Rutherford in 1911 [2], theoretical models have been developed to describe the nucleus and interactions between nucleons. Nowadays, there are several theoretical models to describe the nucleus but they all have some limitations. In many cases the model could be much better if not limited by too demanding and time-consuming computational requirement.
In order to develop better theoretical models, more and accurate experimental data on nuclear properties are needed. Nuclear binding energy is one of the most fundamental properties of a nucleus. It is defined as the energy required to dismantle a nucleus into its constituents, the nucleons. It is commonly expressed as:

$$B(Z,N) = (Zm_p + Nm_n - M(A,Z))c^2 \tag{1}$$

where m_p and m_n are the proton and neutron masses respectively, and $M(A,Z)$ is the total nuclear mass.

The atomic mass m_{atom} takes into account the masses m_e of Z electrons in the electron shell surrounding the nucleus and the sum over the electron binding energies in the atom $B_{e,i}$:

$$m_{atom}(A,Z)c^2 = M(A,Z)c^2 + Zm_ec^2 - \sum_{i=1}^{Z}(B_e)_i \tag{2}$$

By convention, the atomic mass is usually given in atomic mass units u. One atomic mass unit corresponds to the mass of $1/12$ of ^{12}C .
The atomic mass excess Δ is determined as the difference between the atomic mass and the atomic mass number A:

$$\Delta = m_{atom} - A \tag{3}$$

where m_{atom} is given in u. Δ is usually converted in keV (1 u= 931.494$\times 10^3$ keV). Finally, we introduce a very important quantity called the Q-value. It indicates the energy released in or needed for a nuclear reaction. The Q-value is determined as the difference between the initial and final mass values of a reaction:

$$Q = [\sum_i (\Delta_{initial})_i - \sum_j (\Delta_{final})_j] \tag{4}$$

If the Q-value is positive, the reaction releases energy and is called exothermic. Otherwise, the reaction is endothermic.

2.1.1 The liquid drop model

George Gamow suggested an analogy between the surface tension that holds together the molecules in a drop of water and the attractive force that holds the α-particles in a nucleus [3]. This happened already in 1929, at a time when the nature of nucleons was not well known. C.F. von Weizsäcker used this liquid-drop model as a basis to develop a semi-emperical approach for the nuclear binding energy. The model was later slightly simplified by H.A. Bethe and R.F. Bacher [4]. The liquid drop model considers nuclei as incompressible charged fluid droplets. Here the nuclear force acts only on the closest neighbours, and in the same way as the Van der Waals forces in a liquid, the force becomes repulsive at very short ranges. This saturation effect explains how the binding energy per nucleon increases rapidly up to A=12 and stays roughly constant for higher mass numbers [5]:

$$B(N,Z)/A \simeq -8.5[MeV/nucleon] \tag{5}$$

The semi-empirical mass formula of Bethe and Weizsäcker predicts the evolution of the nuclear binding energy as a function of the mass and proton numbers A and Z, respectively, as:

$$B(N,Z) = a_V A - a_S A^{2/3} - a_C \frac{Z^2}{A^{1/3}} - a_l \frac{(N-Z)^2}{A} + \delta(A) \tag{6}$$

where a_V, a_S, a_C, a_l are the coefficients related to volume, surface, Coulomb and asymmetry terms, respectively and $\delta(A)$ is the pairing term.

The volume term $a_V A$ represents the binding energy due to the interaction of each nucleon with its closest neighbours.

The surface term $a_S \mathrm{A}^{2/3}$ takes into account that nucleons located at the surface of the nucleus interact with fewer neighbours than the nucleons inside the nucleus. Considering a nucleus as a sphere with radius R=$r_0 \mathrm{A}^{1/3}$ where r_0=1.2fm and assuming constant density, the surface aera S can be expressed as:

$$S = 4\pi {r_0}^2 A^{2/3} \tag{7}$$

Thus the number of nucleons on the surface of a nucleus is proportional to $A^{2/3}$.

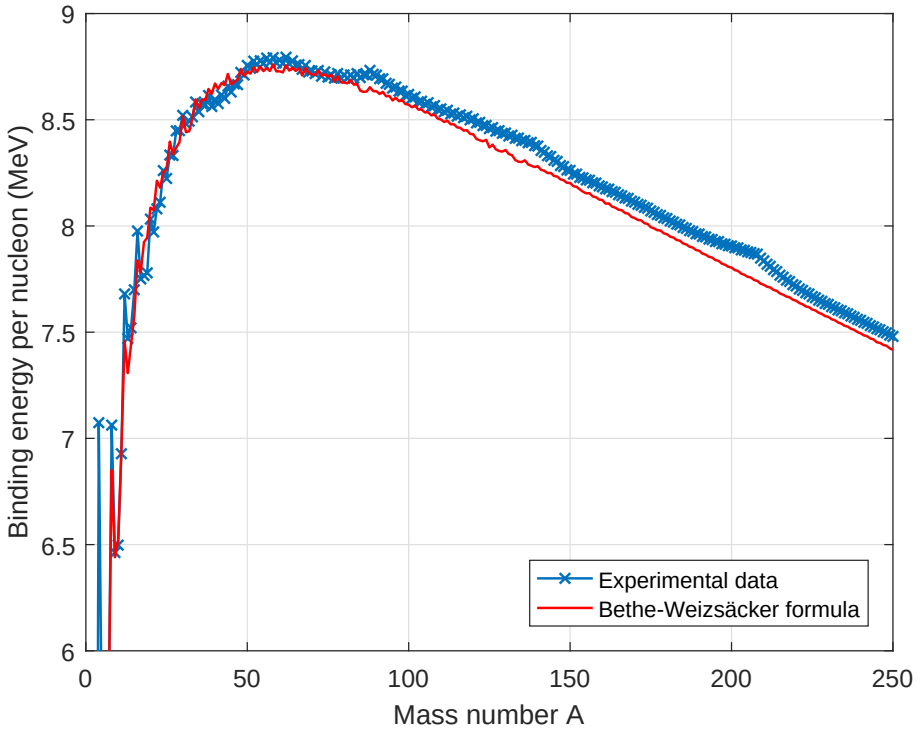

FIGURE 2 Experimental binding energy per nucleon taken from AME2016 [6] and binding energy per nucleon calculated with the semi-empirical mass formula as a function of the mass number A, using the coefficients a_V=15.46 MeV, a_S=17.23 MeV, a_C=0.70 MeV, a_I=23.29 MeV and a_p=12.00 MeV [7].

The Coulomb term $a_C Z^2/A^{1/3}$ takes into account the negative contribution due to the Coulomb repulsion acting between protons. If the charged particles are considered as uniformly distributed in a sphere, the potential energy is given by:

$$E = \frac{3}{5}\frac{1}{4\pi\epsilon_0}\frac{Q^2}{R} \tag{8}$$

where Q is the total charge Ze and ϵ_0 is the vacuum permittivity. The Coulomb term is thus proportional to the number of proton pairs Z^2 and inversely proportional to the radius of the nucleus.

The asymmetry term $a_I(N\text{-}Z)^2/A$ is due to the Pauli exclusion principle stipulating that two identical spin 1/2 particles (fermions) cannot occupy the same quantum state. The lowest energy state of a nucleus is thus reached for an equal number of protons and neutrons. The neutron excess decreases the binding energy proportionally to the difference between the neutron and proton numbers. In heavy nuclei, the number of neutrons must be higher than the number of protons to compensate the Coulomb repulsion due to the protons. The asymmetry term is therefore inversely proportional to the mass of the nucleus.

The last term of the semi-empirical mass formula, $\delta(A)$, is due to the pairing effect. The binding energy is maximum when nucleons form spin-zero pairs. The pairing term will add a positive, zero or negative contribution to the total binding energy depending on neutron and proton numbers:

- $\delta(A) = +\mathrm{a}_p \mathrm{A}^{-1/2}$ for N and Z even (even-even nuclei).

- $\delta(A)$ = -a$_p$A$^{-1/2}$ for N and Z odd (odd-odd nuclei).

- $\delta(A)$ = 0 for all other cases.

The value obtained using the semi-empirical mass formula show discrepancies with the experimental data for some particular number of neutron or proton (see Fig. 2). The liquid drop model is a macroscopic model and ignores the quantum nature of nuclei.

2.1.2 The shell model

A strong motivation to construct an independent-particle nuclear model is the existence of particular configurations of the nuclei for which the energy required to remove a nucleon is specially high. The liquid drop model fails to predict for example why ^{56}Ni (Z=N=28) or ^{132}Sn (Z=50, N=82) are much more bound than their neighboring nuclei. The shell model was developed jointly by E.P. Wigner, M. Goeppert-Mayer and J.H.D. Jensen in 1940s [8]. In this model, nucleons are treated as independent particles in a mean-field created by other nucleons in the nucleus. The nucleons are quantum-mechanical objects and thus, have quantified energies restricted by the Pauli exclusion principle. Nucleons are organized in subshells that are themselves organized in shell. A filled shell results in extra stability for the nuclei. The number of nucleons needed to fill a shell is called a magic number. A nucleus having 2, 8, 20, 28, 50, 82 or 126 protons or neutrons is more tightly bound and is defined as a magic nucleus. The stability is even higher in the special case of a doubly magic nucleus, where both the proton and neutron numbers are equal to a magic number. The average nuclear potential as a function of the distance from the center is known as the Woods-Saxon potential [9]:

$$V(r) = -\frac{V_0}{1 + exp[(r - R)/a]} \tag{9}$$

where V_0 is the depth of the potential well, R is the nuclear radius R=$r_0 A^{1/3}$ and a represents the diffuseness of the nuclear surface. Fig. 3 shows Woods-Saxon potential for typical parameters of V_0=50 MeV and a=0.6 fm.

For protons, the Coulomb interaction has to be added to the potential:

- for r<R:

$$V_{Coulomb}(r) = \frac{1}{4\pi\epsilon_0}\frac{Ze^2}{R}(\frac{3}{2} - \frac{r^2}{2R^2}) \tag{10}$$

- for r>R:

$$V_{Coulomb}(r) = \frac{1}{4\pi\epsilon_0}\frac{Ze^2}{r} \tag{11}$$

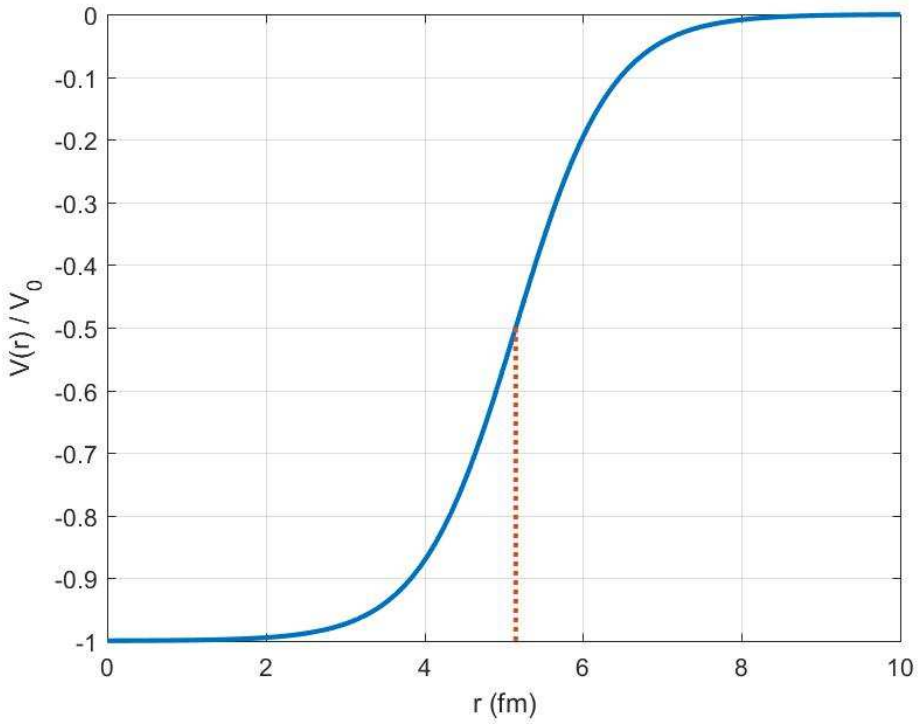

FIGURE 3 Woods-Saxon potential for a nucleus with A=70 as a function of the distance from the nucleus center r. Parameters V_0=50 MeV and a=0.6 fm have been used for the calculation.

As can be seen from Fig. 4, harmonic oscillator, infinite square well or Woods-Saxon potential alone cannot produce the so called magic nucleon numbers, i.e. large shell gaps at correct places. Instead, a spin-orbit coupling must be added to the Woods-Saxon potential. It has the form: $V_{SO}(r)\mathbf{l.s}$ [7]. The operators **l** and **s** represent the orbital and spin angular momenta, respectively. The angular momentum is denoted traditionally using letters s, p, d, f, g, h, i corresponding to l=0, 1, 2, 3, 4,....whereas the spin is either +1/2 or -1/2. According to the Pauli exclusion principle, each l state can contain a maximum of $2(2l+1)$ protons or neutrons. The first l state will be filled for two neutrons or protons, the second for eight protons and neutrons (two in the $1s$ state plus six in the $1p$ state) and so on. For both type of potentials, we can thus reproduce the magic numbers up to 20.

In the case when **l** and **s** are parallel, the energy due to the spin-orbit interaction $j = l + s = l + 1/2$ is positive. If the operators **l** and **s** are anti-parallel, the spin-orbit interaction is negative $j = l + s = l - 1/2$. Thereby, each levels is split into $j = l \pm 1/2$. The function V_{SO} is negative thus the levels $l + 1/2$ are below the levels $l - 1/2$.

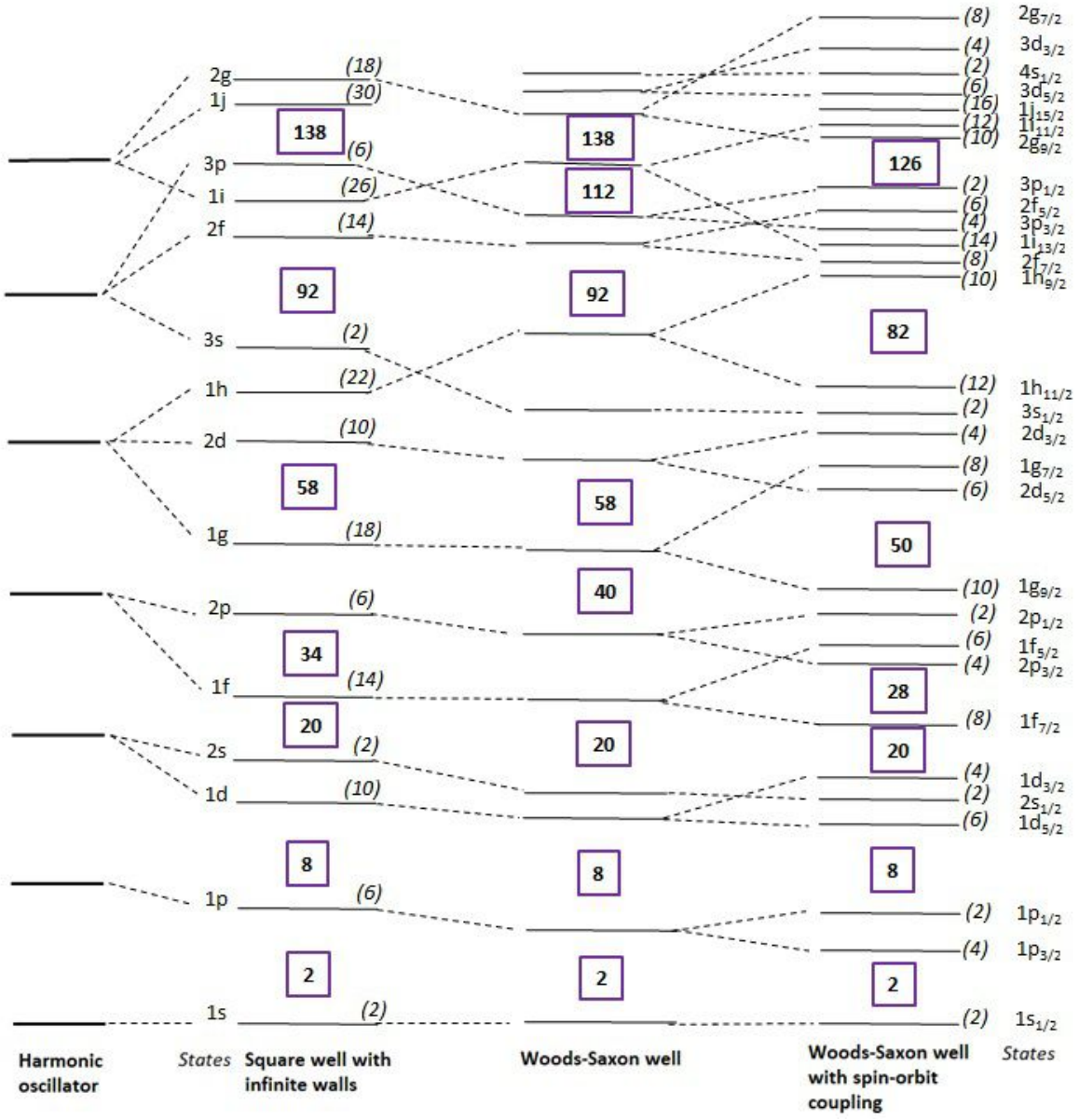

FIGURE 4 Single-particle energy levels calculated with harmonic oscillator, infinite square well and Woods-Saxon well without and with spin-orbit coupling. The maximum number of protons or neutrons allowed in each subshells is given in italic and parenthesis. The purple surrounded numbers indicate the numbers corresponding to the closed shells. The shells are represented from the lowest energy at the bottom to the highest at the top. The nucleons fill the shell from the lowest shell available.

2.1.3 Current theoretical mass models

The liquid drop model and the nuclear shell model are ones of the oldest nuclear models. While the liquid drop model predicts global trends in binding energies, it lacks to explain for example shell closures. In the aim to minimize their internal energy, nuclei can also present deformations of their ground or excited states. The deformations have an impact on the energy gaps between subshells and can even lead to the disappearance of the magic numbers for very deformed nuclei. Deformations can be seen through binding energies via for example discontinuities in the trend of the two neutron separation S_{2n}, defined as:

$$S_{2n}(Z,N) = \Delta(Z,N-2) + 2\Delta(n) - \Delta(Z,N) \tag{12}$$

where $\Delta(n)$ is the neutron mass-excess. A possible consequence of deformations is shape coexistence where two or more shapes coexist within a narrow energy band. Some of the recent theoretical mass models considers the nuclear deformation.
The theoretical mass models described in this section have been developed during the past decades and are used later in the thesis to compare with the experimental data collected in this work.

2.1.3.1 Skyrme models

The nuclear shell model is a phenomenological approach that describe nucleons as independent particles in the mean field created by the other nucleons. Another approach is the so-called Hartree-Fock method [10, 11] which derives the single-particle nuclear potential starting from nucleon-nucleon interactions. It allows to resolve the Schrödinger equation [12] of the system by using a variational principle in which the trial wave functions are Slater determinants:

$$\Psi(\xi_1 ... \xi_A) = |\phi(\xi_1 .... \xi_A)\rangle \tag{13}$$

The components of the Slater determinants are the orthogonal single-particle wave functions of the nucleons. The Hartree-Fock energy defined as $< \phi|\mathrm{H}|\phi >$ where H is the Hamiltonien of the system, must be minimized [5]. These lead to a series of equations, the Hartree-Fock equations, which yield the individual energy levels of the nucleons.

To reproduce the nuclear properties in the best way, the Skyrme force [13] is broadly used in the calculations as a phenomenological effective interaction. The Skyrme interaction has two parts that consists of a two-body interaction and a zero-range three-body interaction [5]:

$$V = \sum_{i<j} V(i,j) + \sum_{i<j<k} V(i,j,k) \tag{14}$$

The two-body part is usually written in the form:

$$V(1,2) = t_0(1 + x_0P^\sigma)\delta(r_1 - r_2) + \frac{1}{2}t_1[\delta(r_1 - r_2)k^2 + k^2\delta(r_1 - r_2)] + t_2k\delta(r_1 - r_2)k + iW_0(\sigma^{(1)} + \sigma^{(2)})k \wedge \delta(r_1 - r_2)k \quad (15)$$

where $k = (1/2i)(\nabla_1 - \nabla_2)$ is the relative momentum operator, P^σ is the spin-exchange operator, σ_i are the Pauli spins matrices and $\delta(r_1 - r_2)$ is the Dirac delta function of the distance between the two nucleons. The three-body force part is:

$$V(1,2,3) = t_3\delta(r_1 - r_2)\delta(r_2 - r_3) \quad (16)$$

In these equations, the parameters t_0, t_1, t_2, t_3, x_0 and W_0 are found by doing a fit to the experimental binding energies. In the Hartree-Fock calculation, the three-body part of the Skyrme force can be simplified to a two-body zero-range interaction. The Hartree-Fock method with Skyrme effective interaction has been used by Vantherin and Brink [14] to find the binding energies, the densities and energies for one superheavy nucleus, considering single particle levels near Fermi level. They extended their calculation to the whole periodic table two years later [15]. Later on, different sets of parameters among these we can mention the SIII [16], SKM [17], SKM* [18] and SLy4 [19] have been developed. The published table of the binding energies using these parameters can be found in [20]. The calculations use in addition to the HF method, the Bardeen, Cooper and Schrieffer (BCS) method [21] for pairing correlations approximation. In UNEDF models, [22], the pairing correlation has been added through a Hartree-Fock-Bogoliubov (HFB) approach to optimize the Skyrme energy density functional. In HFB theory, both HF and BCS theory are combined to obtain the most general wave functions. The UNEDF0 has been improved for large deformation in the so-called UNEDF1 [23] and more recently with UNEDF2 [24].

A model called HFB has been developed by the Bruxelles-Montréal collaboration in the early 2000's [25]. As its name indicates, it is based also on the HFB method and it uses phenomenological corrections to the energy density functional. In this model, the total binding energy is given by:

$$E_{tot} = E_{HFB} + E_W \quad (17)$$

where the HFB energy includes corrections to the spurious rotational energy and to the vibration energy. The second term, called Wigner energy is a phenomenological correction. Many versions have been published. In this model, Skyrme forces utilized are modified for example in HFB-19, HFB-20, and HFB-21 [26] by adding t_4 and t_5 terms to the interaction. The broadly used HFB-24 mass model [27] has been optimized using the data from the 2012 Atomic Mass Evaluation [28].

2.1.3.2 Finite range droplet model

The finite-range droplet model (FRDM) is a macroscopic-microscopic mass model where the nuclear potential energy is split into two terms [29, 30]:

$$E = E_{macr} + E_{micr} \tag{18}$$

The liquid drop model (see 2.1.1) is used as an initial framework for the macroscopic approach. This model has been refined at the end of the 1960's by W.D. Myers and W.J. Swiatecki [31, 32] under the name of droplet model. The idea behind this approach was to use a more realistic nuclear structure description by not considering anymore the nucleon density as homogeneous in a nucleus and with a sharp boundary. In this approach the volume, surface and Coulomb terms of the semi-empirical mass formula (Eq. 6) are developed in Taylor series. It leads to the simplified equation [33] :

$$E = (a_V + a_l\delta^2 - \frac{1}{2}K_{vol}\epsilon^2)A + (a_S + \frac{9a_l^2}{4Q}\delta^2)A^{2/3} + \frac{3e^2}{5r_0}Z^2A^{-1/3} - \frac{9e^4}{400r_0^2Q}Z^4A^{-2} \tag{19}$$

where ϵ is the average deviation of the nucleus bulk density from its nuclear matter value and δ represents the local neutron excess averaged over the nuclear volume. The coefficients Q, K_{vol}, r_0 are the effective surface stiffness, the compressibility and the charge-radius constant, respectively. The addition of a microscopic approach under the form of a folded-Yukawa single-particle potential [34] corrects the droplet model by taking into account the finite range of the nuclear force.
The mass table FRDM1995 [30] includes calculated mass values for 8979 nuclei. This model has been thereafter improved, notably after the publication of the Atomic Mass Evaluation 2003 (AME2003) [35]. By using the updated mass values, the constants of the model were redefined. The enhanced model, so-called FRDM2012 [36], computes also more precisely the mass of axially symmetric nuclei. In total, FRDM2012 includes 339 additional nuclei relevant in astrophysics compared to FRDM1995.

2.1.3.3 Weizsäcker-Skyrme

Two limitations have been pointed out in the FRDM. In its macroscopic- microscopic approach, the parameter value of the shell corrections calculation is different in the microscopic and macroscopic part. The FRDM does not take into account the isospin effects in the calculation of the masses. The Weizsäcker-Skyrme (WS) model has been developed to overcome these limitations [37]. The Skyrme energy density functional in combination with the extended Thomas-Fermi approximation [38] is used in a macroscopic-microscopic approach. The total energy of a nucleus in the WS model is given by the sum of the liquid-drop energy of a spherical nucleus, the Strutinksy shell correction and a residual correction:

$$E(A, Z, \beta) = E_{LD}(A, Z)\prod_{k\geq 2}(1 + b_k\beta_k^2) + \Delta E(A, Z, \beta) + \Delta_{res} \tag{20}$$

The residual correction has been implemented in the WS3 mass model [39]. Further improvement of the WS mass model [40] has been obtained by taking

into account the systematics of the nuclear mass surface by using a radial basis function approach [41] and the Garvey-Kelson relations [42]. In the most recent version of the WS mass model, the WS4 [43], an additional correction for the surface diffuseness in instables nuclei has been added.

2.1.3.4 Duflo-Zuker

The Duflo-Zuker model [44] is a microscopic approach developed in 1995. It uses a Hartree-Fock calculation based on the shell-model where the interaction is defined by two different terms in the Hamiltonian:

$$H = H_m + H_M \tag{21}$$

where H_m is a monopole term and H_M a multipole term. The monopole term is leading the saturation and single-particle properties. It includes terms for spherical and deformed nuclei. The multipole term includes the parameters and corrections. As a starting point, the calculation assumes the existence of a smooth pseudopotential that permits to proceed to Hartree-Fock variation. The model gives a set of 28 parameters that have been initially fitted to the 1751 masses for $N, Z \geq 8$ published in the 1993 Atomic Mass Evaluation table [45]. A revised version of the model has been published since then [46, 47]. Strong deformation and magic numbers are well reproduced by the Duflo-Zuker model but the model does not include rotational energies and spurious center-of-mass [33].

2.2 Isobaric multiplet mass equation

The concept of isospin has been developed by Werner Heisenberg in 1932 [48] to explain the equal intensity of the strong nuclear force between two neutrons and two protons due to the charge symmetry and the very close mass of the two particles. The nuclear force is also mostly charge independent, which means that the nuclear interaction between two identical and two different nucleons is the same [49]. In the isospin model, the neutron and proton are treated as two states of the same particle, the nucleon [50]. Both the neutron and the proton own the same isospin $T = 1/2$ but with a different projection (labeled with notation T_3 or T_z): $T_3 = -1/2$ for proton and $T_3 = +1/2$ for neutron.

For many-nucleon systems, the 3-component represents the total neutron excess of the nucleus [5]:

$$T_3 = \frac{N - Z}{2} \tag{22}$$

The total isospin quantum number T can take the values:

$$|T_3| \leq T \leq \frac{A}{2} \tag{23}$$

For the ground state of a nucleus, T is empirically defined as equal to $|T_3|$. The eigenvalue of the isospin projection, T_3, ranges from -T to T. An isobaric multiplet of states T is formed by isobars owing one of the $(2T+1)$ eigenvalues of T, T_3. The Coulomb interaction is the main reason for the small isospin symmetry breaking [51]. By using first-order perturbation theory on the Coulomb force and Wigner-Eckart theorem [52], the masses of the members in an isobaric multiplet (A,T,T_3) are located on a parabola:

$$M(A,T,T_3) = a(A,T)T_3^2 + b(A,T)T_3 + c(A,T) \tag{24}$$

The so-called isobaric multiplet mass equation (IMME) has been first introduced in by Eugene P. Wigner [53]. The reliability of the equation has been tested for the first time for an isospin $T = 3/2$ quartet at A=9 [54]. In this test, the coefficients of Eq. (24) were determined from the well-known masses of ^{9}Li, ^{9}Be and ^{9}B to calculate the mass of ^{9}C. The calculation showed a very good agreement with the experimental measurement of ^{9}C mass value. Since then, the IMME has been widely used to predict the masses of the exotic members of the isobaric multiplets. The IMME has been also used for isospin quintets since 1973 [55]. However, with the increase of the precision in the mass measurements, the quadratic form of the IMME has been found to breakdown for A=7-8 [56], A=9 [57], A=20-21 [58], A=31 (Article II), A=32 [59], A=35 [60] and A=53 [61]. There have been several explanations for the breakdown of the IMME. For A=32, the isospin-mixing of $T = 2$ with $T = 1$ states has been pointed out, in addition to a charge-dependent effects for A=9 [57]. The breakdown in IMME is still unexplained for the A=53 multiplets [61]. To overcome the failure of the quadratic form, the need of additional polynomial terms in Eq. (24) as cubic or quadratic terms have been suggested [62] and have been calculated by shell-model calculation or fitted on experimental data if available [63, 64].
The mass of multiplet along $N \approx Z$ can be also evaluated via calculation of the mirror and triplet displacement energies (MDEs and TDEs) [65]. The MDEs and TDEs are due to isospin symmetry breaking induced by charge-symmetry and charge-independence breaking [66].

3 ASTROPHYSICAL MOTIVATION

By raising the eyes to a clear sky, we can contemplate the results of powerful nuclear reactions taking place in stars. Here, the time scale touches the extremes: the explosive end of massive stars called supernova is a site of very fast nuclear processes, involving also nuclei that do not live long enough to be synthesized and studied directly in laboratories. At the other end, the lifetime of light stars, smoothly burning their hydrogen in the main sequence, can be as long as several thousands of billions of years. Astronomical observations have provided evidence on the ongoing nucleosynthesis in the Cosmos. One of the earliest observations were the absorption lines of technetium from R Andromedae [67]. Technetium does not have any stable isotopes and the longest lived isotope, ^{98}Tc, has a half-life of around 4.2 million years (My) [68]. Therefore, it must have been produced relatively recently on astronomical timescale. Later on, the observation of 1809 keV γ-rays following the β-decay of ^{26}Al ($T_{1/2} \approx 0.7$ My) done by the $HEAO-3$ spacecraft [69, 70] yielded additional evidence for ongoing nucleosynthesis. Very recently, multimessenger observations from the binary neutron star merger GW170817 [71], including gravitational waves, as well as the whole electromagnetic spectrum (optical, ultraviolet, X-ray, γ-ray, radio, infrared), expanded our understanding of nucleosynthesis in such compact binaries.

3.1 Cosmic gamma rays from ^{26}Al

The 5^+ ground state of ^{26}Al has a long half-life of around 7.17×10^5 years [68]. It decays via electron captures and β^+-decays dominantly to the first excited state of ^{26}Mg which is further de-excited by emitting 1809 keV γ-rays. These γ-rays yield direct information on the ongoing nucleosynthesis in different astrophysical environments.

^{26}Al can be produced via proton-captures on ^{25}Mg in stellar environments provided high enough temperatures and hydrogen densities exist. This produc-

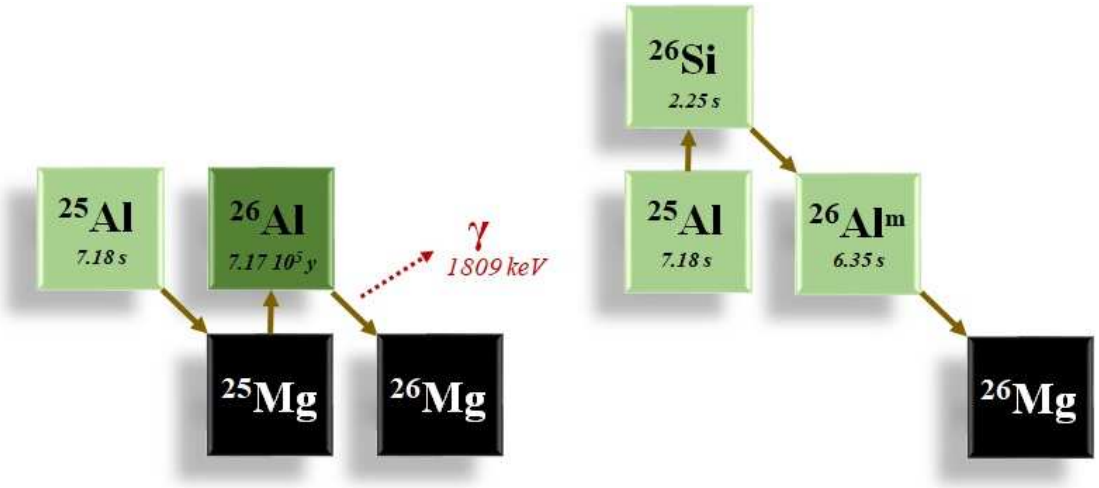

FIGURE 5 Region around ^{26}Al and the sequence leading to the emission of 1809 keV γ-rays following the β-decay of ^{26}Al (left) and the bypass route (right). The half-lives are given in italic in the boxes.

tion route can be bypassed by ^{25}Al$(p,\gamma)^{26}$Si proton captures. The 0^+ ground state of ^{26}Si will β^+-decay to the 0^+ isomeric state at 228 keV in ^{26}Al, which further decays via superallowed Fermi β-decay to the 0^+ ground state of ^{26}Mg. Hence, no 1809-keV γ-rays are produced via this route (Fig. 5).

Several sites are expected to be sources of ^{26}Al: ONe novae, core-collapse supernovae, massive stars as Wolf-Rayet stars, asymptotic giant branch stars and reactions from low-energy heavy cosmic-rays [72]. Based on the $HEAO-3$ observations, novae or a possible supernova remnant encompassing the solar system were proposed as possible sites for the ^{26}Al production [73]. The Compton Gamma Ray Observatory was launched on orbit in 1991. One of its instruments, the Imaging Compton Telescope (COMPTEL) performed an all-sky survey on the 1809-keV γ-rays (see Fig. 6). The distribution gave important information on the possible production sites [72]. The map shows localized and asymmetric concentration of ^{26}Al through the galaxy plane that contradicts the former hypothesis of novae as the main source. Dominant nova or low-mass Asymptotic Giant Branch (AGB) star contribution to the 1809 keV γ-rays would produce a smooth intensity distribution because of their lower individual yields. The distribution given by COMPTEL suggests that massive Wolf-Rayet and AGB stars, and core-collapse supernovae that have a tendency to cluster are the dominant producers of ^{26}Al [74]. This conclusion has been confirmed by more recent observations by the INTEGRAL space telescope and its spectrometer, SPI. From the obtained spectra the total mass of ^{26}Al in the Galaxy has been estimated to be 2.8 $M_\odot$ [75] where the solar mass $M_\odot$= 1.9884×10^{30} kg [76]. The contribution of classical novae to the whole ^{26}Al distribution has been estimated to be less than 0.4 $M\odot$ [77]. Nevertheless, the reaction rates leading to the production of ^{26}Al or its bypass are important to constrain the possible production sites and estimate the amount of ^{26}Al produced.

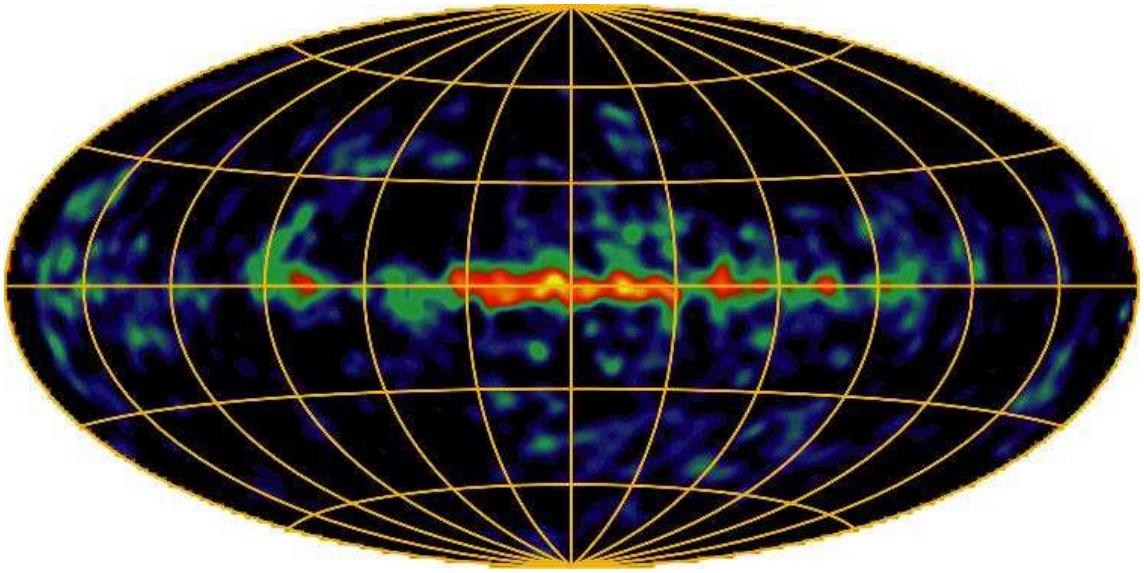

FIGURE 6 COMPTEL all-sky map of ^{26}Al 1.8 MeV γ-rays in the Milky Way. *Credits* : *CGRO/COMPTEL*.

3.2 Nucleosynthesis in novae

Novae are powerful astrophysical events taking place in binary star systems where one of the stars is a white dwarf. It has been estimated that around 35 ± 11 classical novae occur each year in the Galaxy [78]. Most of them are considered as cataclysmic variables but some are also known as symbiotic stars. In the specific case of symbiotic stars, the companion star is a red giant star from which a wind will transfer material that will be partially captured by the white dwarf [79].

In classical novae, hydrogen-rich material from a low-mass star will be transferred around the white dwarf via Roche lobe overflow [80]. A fraction of the material will end up on the surface of the white dwarf. At some point, the accreted material will exceed a critical temperature and lead to a thermonuclear runaway in the electron degenerate conditions on the bottom of the accreted layer. This explosive hydrogen burning together with the heat released from the compression will lead to a powerful and rapid outburst. Novae are recurrent with around 10^4-10^5 years in between the explosions. The nova light curves follow a general trend with a fast increase followed by a slower decrease the rate of which depends on the nova [81]. The infrared and ultraviolet observations from novae yield information on the composition of the ejecta [82, 83]. The produced ejecta will depend on the composition of the white dwarf [84]. A picture of a classical nova, GK Persei, is shown on Fig. 7.

In addition to light curves and luminosity, informations on nucleosynthesis in novae have been also obtained from meteorites. A large carbonaceous chondrite meteorite, the Murchison meteorite, falled in Australia in 1969. The presolar grains on the surface of this meteorite have preserved the initial elemental ratios and have been turned out to be valuable for nuclear astrophysics studies. The grains composed of silicone carbide (SiC) have isotopic ratios similar to the

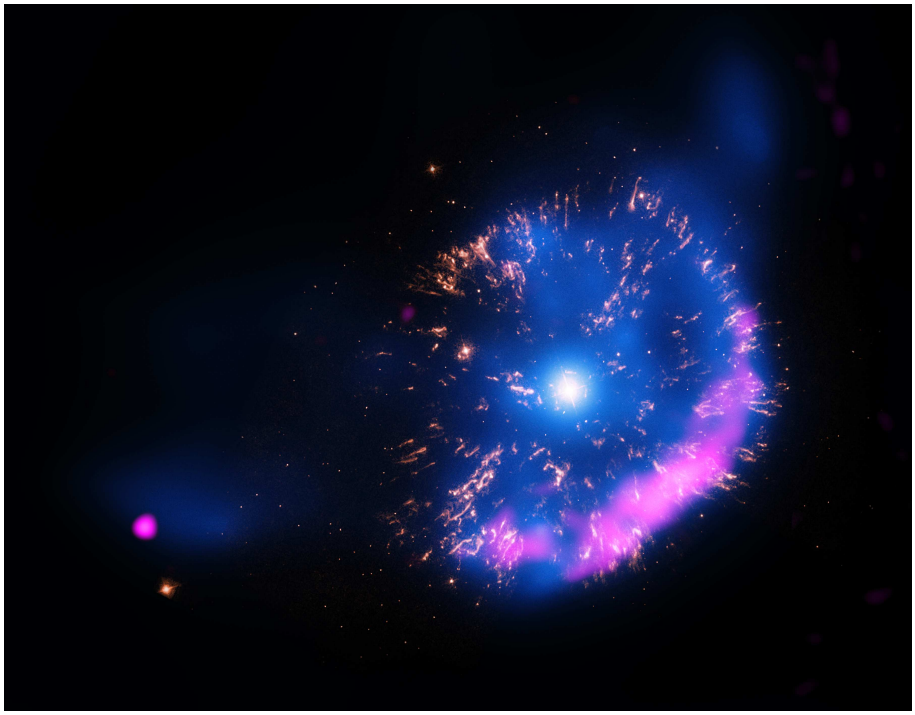

FIGURE 7 Composite picture of the classical nova GK Persei with X-rays from NASA's Chandra X-ray Observatory (blue), optical data from NASA's Hubble Space Telescope (yellow), and radio data from the National Science Foundation's Very Large Array (pink). *Credit: NASA*

ratio expected from simulations and observations of the ejecta of ONe novae [85]. In particular these grains are rich in heavy silicon isotopes (^{29}Si and ^{30}Si), have a low ^{12}C/^{13}C and ^{14}N/^{15}N ratios, and a high ^{26}Al/^{27}Al ratio [86, 85]. In ONe novae, ^{30}Si is produced via the β^+-decay of ^{30}P. This reaction competes with the proton capture reaction ^{30}P$(p,\gamma)^{31}$S (see Fig. 8). The β-decay half-life of ^{30}P is long, 2.5 min, which is comparable to the timescale of nova nucleosynthesis [87]. The alternative route to ^{31}S via β-decay of ^{31}Cl is hindered due to the low proton separation energy of ^{31}Cl. Thus ^{30}P$(p,\gamma)^{31}$S is the key reaction controlling the nucleosynthesis of elements beyond sulfur [88]. The precise knowledge of the proton-capture rate on ^{30}P is therefore required to determine the abundances of heavier elements produced in novae. In addition, it is useful for nova nuclear thermometers O/S, S/Al, O/P, and P/Al [89]. It has been indeed observed that the peak temperature reached during a thermonuclear runaway in a nova is strongly correlated with the white dwarf mass, and consequently, to the elemental abundances in the white dwarf. The composition of the white dwarf is particularly important in the case of ONe novae because the nucleosynthesis toward heavier elements is correlated with the mixing of the accreted material and the white dwarf. The abundance ratio of Si/H from the ejecta is a relevant mixing meter influenced by the ^{30}P$(p,\gamma)^{31}$S reaction rate [90].

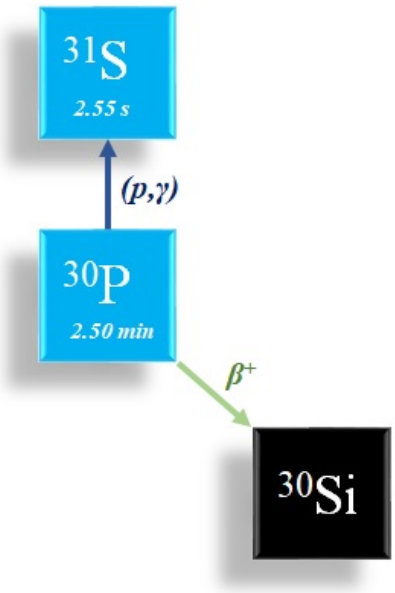

FIGURE 8 Representation of the two competing reactions ^{30}P$(p,\gamma)^{31}$S and the ^{30}P β^+ decay.

3.3 Rapid proton capture (rp) process in type I X-ray bursts

Type I X-ray burst (XRBs) remind classical novae: they also take place in binary star systems but instead of a white dwarf they have a neutron star which accretes material from the companion star. Thus, XRBs are of particular interest for the studies of neutron stars, such as their composition.
Neutron stars are one of the densest objects known in the universe. With a size of few kilometers and mass comparable to the mass of the Sun, a teaspoon of the core of a neutron star would weigh about 5×10^{12}kg. Neutron stars are composed of roughly three regions. The highest densities are reached in the core where the matter is essentially neutron degenerate gas, and where even quark-gluon plasma is plausible [91]. The second region, the inner crust, has a density of $\rho \approx 4.3\times10^{11}$ to 2×10^{14}g/cm^3 [92] and is made of neutron-proton clusters immersed in a sea of free nucleons [93]. The last region, the outer crust, consists of nuclei and free electrons. The matter is considered in nuclear equilibrium and in ground state. The stability of the nuclei in the outer crust increases when going closer to the surface. Close to the inner crust interface, the nuclei are predicted to be neutron rich. The most external part of the crust consists mostly of stable iron and nickel isotopes [93].
In XRBs, if the companion star has a mass well above the neutron star mass ($\geq$10 $M\odot$), it can loose material by stellar winds. Such systems are called High-Mass X-ray Binaries (HMXBs) [94]. In the case of Low-Mass X-ray Binaries (LMXBs), the low mass companion star ($\leq$1.5 $M\odot$) can transfer material to the neutron star by Roche lobe overflow in a similar manner than in classical novae. These binary star systems emit radiation mostly in the range of X-rays. The first X-ray bursts

were observed from the globular cluster NGC6624 in 1976 [95] and from the constellation Norma [96]. These X-ray sources differed from the previously observed X-ray sources by their intensity and their luminosity curve [97]. There are two types of XRBs: the type I XRBs, which will be discussed in this section, and the type II XRBs which are rarer events and most likely due to accretion instabilities [98].

In type I XRBs, the luminosity increases rapidly on a timescale of less than a second to about 10 seconds, followed by a decay lasting from several seconds to a few minutes [98, 99]. The bursts are recurrent with a periodicity of several hours to days. Type I XRBs have a thermonuclear origin. The hydrogen and helium rich matter from the companion star is accreted on a disk around the neutron star falling onto its surface where it is gradually compressed. A part of the energy from the accreting material is rapidly radiated away but the remaining energy feeds thermonuclear reactions and the pressure and temperature become high enough for the electrons to become degenerate [100]. The hydrogen fuses to helium via hot CNO (HCNO) cycles and the material plunge deeper into the star until the falling matter becomes unstable. The burst is initiated by a thermonuclear runaway which is the result of the ignition of helium through triple-α reactions that will cause a series of proton-captures also known as the rapid proton capture process, the rp-process [99, 101]. The rp-process requires a hot and hydrogen-rich environment [102]. It starts with a breakout from the HCNO cycle, and continues then via proton-captures and β^+-decays toward heavier elements, up to SnSbTe region in suitable conditions [103]. In this case, the rp-process ends up in a closed SnSbTe cycle because $^{106-108}$Te are very weakly α-bound and will decay back to Sn isotopes.

On the rp-process path, there are a couple of nuclei with a low or negative proton-capture Q value and a relatively long β-decay half-life. At these so called waiting-points, the process has to wait for the slow β-decay to happen in order to continue its path to heavier elements [101]. The presence of waiting points in the rp-process flow has been used to explain the double peak in the bolometric luminosity of several XRBs observed as 4U/MXB 1636-53 [104], 4U 1608-52 [105], or GX 17+2 [106]. One scenario proposes that the first burst would be a signature of the helium flash shell and the second burst would be due to the rp-process waiting points, such as ^{22}Mg, ^{26}Si, ^{30}S and ^{34}Ar [107]. During the rp-process, most of the flow should proceed through these waiting points.

Of special interest for this thesis is the waiting-point nucleus ^{30}S. It has a long half-life of 1.176(2) s [68], comparable to the time scale of type I XRBs. The route through this point to heavier masses proceeds mostly via proton-captures that are predicted to be non-resonant for low temperatures and resonant on the two lowest excited states in ^{31}Cl for temperatures above T$\approx$0.13 GK (Article II). The ^{30}S waiting point is also affected by the photodisintegration of ^{31}Cl. The reactions around ^{30}S are illustrated in Fig. 9. The unmeasured ^{30}S(α, p)^{33}Cl reaction has to be taken into account for higher temperature range and thus the ^{30}S waiting point conditions are unknown above $\approx$1.0$\pm$0.3 GK [108].

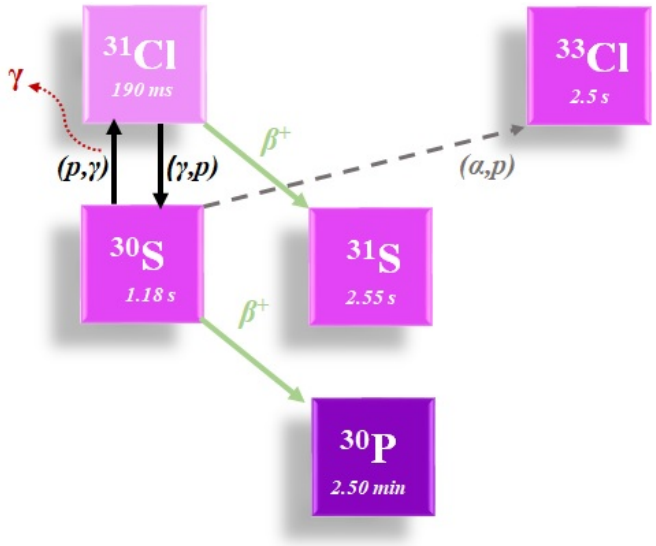

FIGURE 9 Reactions around the ^{30}S waiting point in the *rp*-process.

3.4 Resonant proton-capture rates

Proton-captures on light nuclei, such ^{25}Al, ^{30}P and ^{30}S, are expected to be dominated by resonant proton-captures, and to proceed through a few narrow low-energy resonances in ^{26}Si, ^{31}S and ^{31}Cl, respectively. The total resonant proton capture rate is summed over individual resonances:

$$N_A \langle \sigma v \rangle_{res} = 1.54 \times 10^{11} (\mu T_9)^{-3/2} \sum_i (\omega\gamma)_i \times \exp(-11.605 E_{res,i}/T_9) \text{ cm}^3\text{mol}^{-1}\text{s}^{-1} . \quad (25)$$

where μ is the reduced mass in atomic mass units u, T_9 is the temperature in GK, $(\omega\gamma)_i$ is the resonance strength and $E_{res,i}$ is the resonance energy for a state i, both in MeV. The resonance energy $E_{res,i}$ is given by:

$$E_{res,i} = E_{x,i} - Q_{p,\gamma} \quad (26)$$

where $E_{x,i}$ is the excitation energy for a state i. Thus the resonance states must have an excitation energy above the proton threshold defined by the $Q_{p,\gamma}$ value also known as the proton separation energy S_p. The reaction rate depends also exponentially on the temperature. The resonance strength $\omega\gamma$ for an isolated resonance i can be determined as:

$$\omega\gamma = \frac{2J_i + 1}{2(2J_t + 1)} \frac{\Gamma_p \Gamma_\gamma}{\Gamma_{\text{tot}}} \quad (27)$$

where the spins of the resonance state and the target nucleus are given as J_i and J_t, and the total width of the resonance Γ_{tot}, is:

$$\Gamma_{\text{tot}} = \Gamma_{\text{p}} + \Gamma_\gamma \quad (28)$$

The proton width can be calculated using:

$$\Gamma_{\mathrm{p}} = \frac{2\hbar}{R_n}\sqrt{\frac{2E_{res}}{\mu}}P_l(E_{res}, R_n)C^2S\theta^2_{s.p.} \tag{29}$$

where R_n is the interaction radius, $P_l(E_r, R_n)$ the penetration factor, C^2S the spectroscopic factor and $\theta^2_{s.p.}$ the single-particle reduced width. The proton width Γ_{p} can be scaled from known values using [109]:

$$\Gamma_p \propto \exp\left(-31.29Z_1Z_2\sqrt{\frac{\mu}{E_{res}}}\right) \tag{30}$$

where Z_1 and Z_2 are the atomic numbers of the incoming particles, μ is the reduced mass in u and E_{res} is the center-of-mass resonance energy in keV. At low resonance energies, the proton widths are small compared to the gamma widths, and hence $\Gamma_p\Gamma_g/\Gamma_{tot} \approx \Gamma_p$. The gamma widths can be determined from their lifetimes according to Γ_g=$\hbar/\tau$ where $\hbar$ is the reduced Planck constant and τ is the lifetime.
Most of the proton-captures occur in a narrow energy range corresponding to the width Δ of the Gamow peak E_0 [99]:

$$\begin{aligned} E_0 &= 0.122(Z_1^2Z_2^2\mu T_9^2)^{1/3} \\ \Delta &= 0.2368(Z_1^2Z_2^2\mu T_9^5)^{1/6} \end{aligned} \tag{31}$$

This energy range called Gamow window goes from E_0-$\Delta/2$ to E_0+$\Delta/2$. Such window does not exist if the resonance strength depends only on the γ-ray width i.e. if Γ_p»Γ_γ [99].
For waiting-point nuclei, such as ^{30}S in the rp-process, it is also critical to determine the ratio of the photodisintegration $\lambda_{\gamma,p}$ to the proton-capture rate N_A<σv> [99]:

$$\frac{\lambda_{\gamma,p}}{N_A\langle\sigma v\rangle} = 9.8685\times10^9T_9^{3/2}\frac{g_tg_p}{g_f}\left(\frac{G_tG_p}{G_f}\right)\times\left(\frac{m_tm_p}{m_f}\right)^{3/2}e^{-11.605Q/T_9} \tag{32}$$

where g_t, g_p and g_f are the statistical factors (g=2J+1), G_t, G_p and G_f the normalized partition functions and m_t, m_p and m_f the masses of the target, proton and the final product, respectively [99]. For type I XRBs, the proton capture rate can be determined using:

$$\lambda_{p,\gamma} = N_A\langle\sigma v\rangle\rho\frac{X_i}{m_H} \tag{33}$$

where X_i is the hydrogen mass fraction (X_i=0.73) and ρ is the density (typically ρ=10^6 g/cm^3). It can be estimated that ^{30}S acts as a waiting point when at least 20% of the reaction flow must wait for its β^+-decay [100]. This can be written [108]:

$$\lambda[^{30}S(p,\gamma)^{31}Cl(\beta^+\nu_e)] < 4\lambda[^{30}S(\beta^+\nu_e)] \tag{34}$$

Where under equilibrium conditions [99]:

$$\lambda[^{30}S(p,\gamma)^{31}Cl(\beta^+\nu_e)] = \frac{\lambda_{p,\gamma}}{\lambda_{\gamma,p}}\times\lambda[^{31}Cl(\beta^+\nu_e)] \tag{35}$$

Combining Eq.(34) and (35) leads to the waiting point condition for the ratio of the photodisintegration to proton-capture rate:

$$\frac{\lambda_{\gamma,p}}{\lambda_{p,\gamma}} > \frac{t_{1/2}(^{30}S)}{t_{1/2}(^{31}Cl)} \times \frac{1}{4} \tag{36}$$

With these equations and a precise Q value for the reaction, the waiting-point conditions for ^{30}S can be constrained. The upper temperature limit is constrained by the unmeasured $^{30}\mathrm{S}(\alpha, p)^{33}\mathrm{Cl}$ reaction [110]. The reverse reaction, $^{33}\mathrm{Cl}(p, \alpha)^{30}\mathrm{S}$, has been however measured [111].

3.5 The weak *r*-process

The rapid neutron capture process, the *r*-process [112], produces around half of the elements heavier than iron. The *r*-process is responsible for three abundance peaks at A≈80, 130 and 195. This thesis focuses on the A≈80 peak. The lighter *r*-process elements ($A < 130$) are predicted to be produced in astrophysical environments that offers too low density of free neutrons to induce the production of the heavier *r*-process elements [113]. Also, the abundances of heavy elements in many very metal-poor halo stars reproduce well the solar system *r*-process abundances. It is, however, not true for the lighter *r*-process elements [114, 115]. The production site for the lighter *r*-process elements, produced in the so-called *weak* *r*-process, is thus expected to be different than for the *main* *r*-process responsible for the production of heavier elements [116].

3.5.1 Astrophysical conditions

The *r*-process requires a high flux of neutrons and temperatures high enough to favor neutron captures but not too high to prevent a premature stop of the process due to photodisintegration reactions. The weak *r*-process is expected to be induced by neutrino wind associated with a core-collapse supernova or neutron star mergers [117].
The progenitor of a type II supernova, also called core collapse supernova (CCSN), is a massive star that runs out of its thermonuclear energy sources. A massive star burns hydrogen to helium mainly via CNO cycles during the main sequence which ends up when the hydrogen is exhausted in the core [99]. The formerly created helium will start to fuse and produce carbon. Next step starts when helium is exhausted in the core and several thermonuclear reactions will succeed until the end of the silicon burning stage. The main product of the short-lasting silicon burning will be ^{56}Fe which is one of the most tightly bound nuclei (B/A=8790.354(5) keV [6]). At the end of Si burning, the temperature in the stellar core increases and the matter becomes degenerate. The mass of the star increases with the contribution from the ongoing burning in the overlying shells, and the core will exceed the Chandrasekhar limit at some point. This limit states

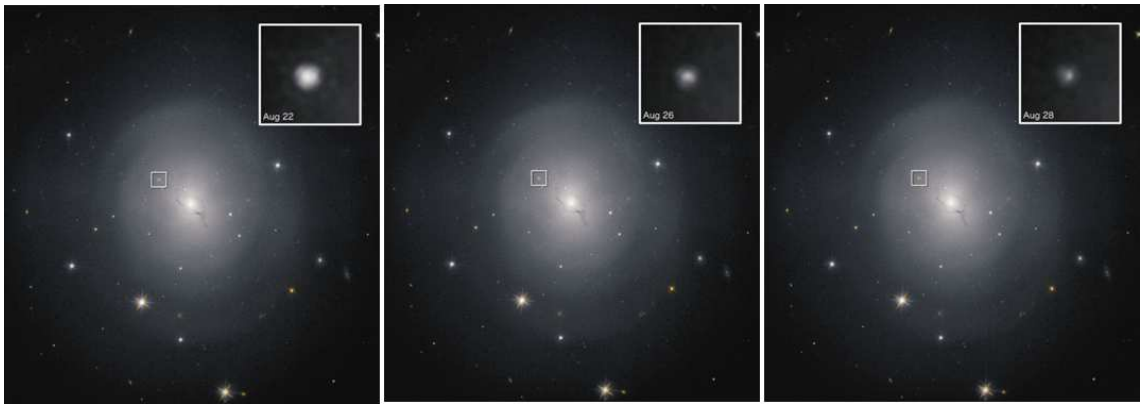

FIGURE 10 The kilonova AT2017gfo following the NS-NS merger detected by LIGO/VIRGO observed by NASA's Hubble Space Telescope during 6 days. *Credits: NASA/ESA*.

that for a mass above around 1.4 $M\odot$, the electron degeneracy pressure cannot counteract gravity anymore, and the core starts to collapse. When the matter in the core reaches a certain density, the falling material will rebound and create a shock wave. At that point the core of the star is described as a proto-neutron star. Simulations show that for an iron core progenitor, the outgoing shockwave is stopped before escaping the collapsing star [112]. It looses most of its energy by neutrino emission and also by fission of heavy nuclei and by electron-capture on free protons. The scenario that explains how the shock wave will be revived to lead to the final explosion is still not fully understood. The huge flux of neutrinos and anti-neutrinos, coming from the still collapsing inner layers of the star and from the proto-neutron core, is a good candidate. The outward moving matter will then very briefly undergo explosive nuclear burning stage, and due to high velocity, it will escape the star and be spread into the interstellar medium.
The production of elements via the *r*-process is suspected to happen through neutrino winds when the core rebounds [113]. The neutrino winds originate from the ablation of the proton-neutron star surface due to the energy deposited by the neutrinos streaming out from the proto-neutron core [112, 118]. The *r*-process depends on the conditions of the wind, such as the wind expansion time scale, the entropy (related to the temperature and density) and on the electron fraction [112, 99]. Recent studies have shown that the wind is not neutron-rich enough (too high electron fraction) to produce heavier *r*-process elements [117].

A core collapse supernova generates a neutron star or a black hole as the remnant of a massive star. Nearby neutron stars can form a pair. The first binary neutron star system, PSR B1913+16, was discovered in the Aquila constellation by the Arecibo Observatory, Puerto Rico in 1975 [119]. This system and those discovered since, have had a great impact on physics as they emit gravitational waves predicted by Albert Einstein's general theory of relativity. Mergers of a neutron star-neutron star system (NS-NS) have been expected from different observations to be the dominant source of the heaviest *r*-process elements [120] and it is in agreement with the predicted rate of the mergers [121].

The first observation of gravitational waves originating from a NS-NS merger

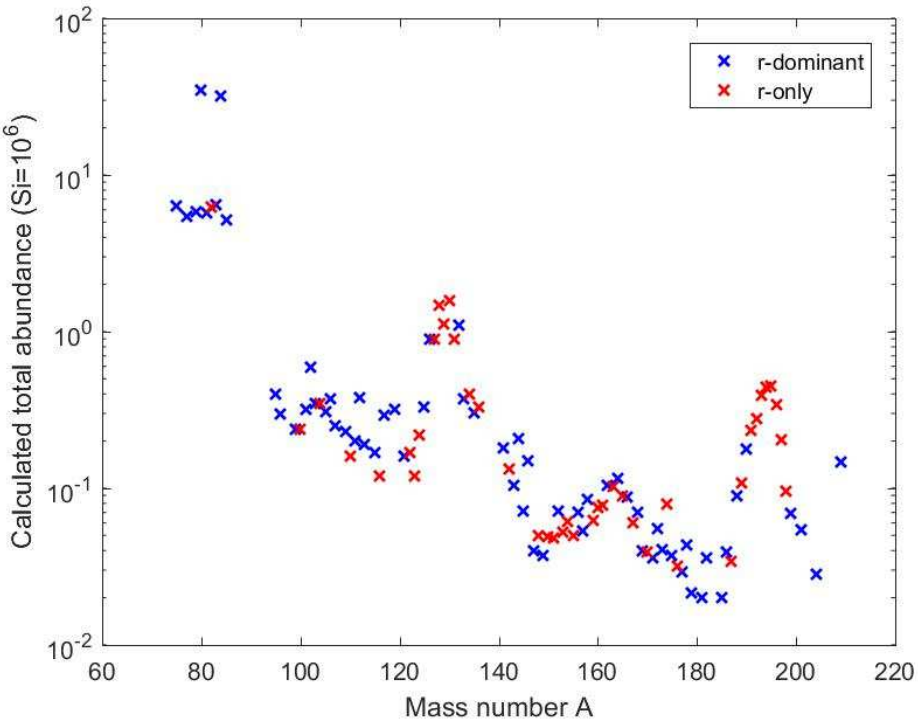

FIGURE 11 Solar system abundances of nuclei created for at least 50% by the *r*-process (*r*-dominant) and at least by 90% (*r*-only).

near the galaxy NGC 4993 was done by LIGO/Virgo detectors [71]. The GW170817 gravitational wave signal was followed by a gamma-ray burst (GRB 170817A) about 1.74 s later [71], confirming the NS-NS mergers as a source of short GRBs. The observed kilonova AT2017gfo following the merger (see Fig. 10) was powered by the radioactive decay of *r*-process products, and therefore gave direct evidence for the *r*-process in mergers, and support the importance of NS-NS mergers in the production of the *r*-process elements[122].

3.5.2 Nucleosynthesis

The abundance distribution of *r*-process nuclei in the solar system is deduced from the known abundance distribution of the slow neutron capture process, the *s*-process [123, 112]. The *r*-dominant and *r*-only nuclei for which more than 90% are produced via *r*-process are represented in Fig. 11. The *r*-process flows far from the valley of stability through neutron-rich radioactive nuclei. As the name says, the process is rapid and takes place on a time scale of the order of $\approx$1 s. The *r*-process starts via neutron-captures on seed nuclei. In classical *r*-process picture where an $(n,\gamma)\leftrightarrow(\gamma,n)$ equilibrium is assumed, the abundances within an isotopic chain are determined by the waiting points, and the elemental abundances by their β-decay half-lives. The waiting points have an even number of neutrons and a significant abundance [99]. Due to the pairing effect, the $Q_{n,\gamma}$ value for even-N isotopes is lower than for odd-N isotopes. A $(n,\gamma)\leftrightarrow(\gamma,n)$ equilibrium is established and the flow continues via β-decay to the next isotopic chain. Thus,

the elemental abundance of an isotopic chain is inversely proportional to the total β-decay constant for the chain. This refers to the steady flow approximation [99] The three *r*-process abundance peaks at A≈80, 130 and 195 are expected to be caused by the magic neutron numbers N=50, 82 and 126. The peak at A≈130 has also been explained by fission cycling [124]. The $Q_{n,\gamma}$ value is particularly small for nuclei with a magic neutron number, and a succession of β-decays and neutron captures along the magic neutron number bring the flow closer to the stability.
A sensitivity study has been performed by Surman *et al*. [116] to determine which neutron capture rates have the highest impact on the abundance distribution in the weak *r*-process. For this purpose, they compared the abundance pattern obtained when varying the neutron-capture rate by a factor of 100, for about ninety astrophysical trajectories. From the fifty-five rates given in the paper, the neutron capture rates on ^{67}Fe and ^{68}Co have been pointed to be among the most influential captures for the final isotopic abundances. The neutron capture-rate sensitivities of ^{67}Fe and ^{68}Co, determined as $F = 100 \sum |X(A) - X_{baseline}(A)|$, where X is the mass fraction, were F=15.8 and 11.6, respectively (Fig. 12). The baseline calculations were done with the NON-SMOKER [125] rates from JINA REACLIB v1.0 [126].

The neutron-capture rate is commonly determined from statistical model calculations [127, 128]. From the capture rate $N_A < \sigma\nu >$, the rate of the reverse reaction, the photodisintegration, is easily calculated:

$$\lambda_{\gamma,n} = \frac{A_i}{A_f^{3/2}} \frac{(2J_i+1)(2J_n+1)}{(2J_f+1)} \frac{G_i}{G_f} T^{3/2} 9.8685 \times 10^9 e^{-Q/kT} N_A < \sigma\nu > \qquad (37)$$

with A being the mass number, J the spins, G the partition function and Q the Q value for the reaction. We see that the Q value and therefore the masses of the involved nuclei have an exponential impact on the photodisintegration rate. At a certain temperature and neutron density, the photodisintegration rate and the neutron capture rate are in equilibrium. From the Saha equation, one can determine the abundance ratio between $A(Z,N)$ and $A+1(Z,N+1)$ [99]:

$$\frac{N_f}{N_i} = N_n \left(\frac{h^2}{2\pi\mu kT}\right)^{3/2} \frac{(2J_f+1)}{(2J_i+1)(2J_n+1)} \frac{G_f}{G_i} e^{Q/kT} \qquad (38)$$

where N_n is the neutron density and μ is the reduced mass μ=$(m_i \times m_n)/(m_i$+$m_n)$. To take into account more parameters and features, the neutron capture rates and their reverse rates are nowadays computed via codes, such as Talys [129] or NON-SMOKER [125], and implemented in nuclear reaction network programs, such as Skynet [130, 131].

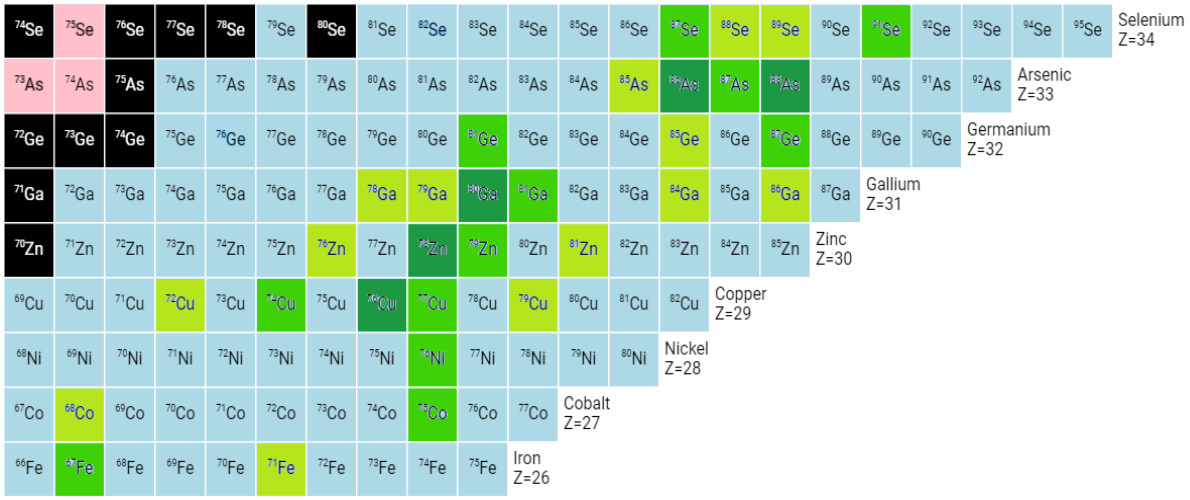

FIGURE 12 Nuclei with high neutron-capture rate sensitivities F in the weak-r process as computed in Surman *et al*. [116]. In light green $10<F<15$, medium green $15<F<20$ and in dark green $F>20$.

4 EXPERIMENTAL METHOD

4.1 Production of radioactive ion beams at IGISOL

There are two main techniques to produce radioactive ion beams: in-flight and isotope separation on-line (ISOL). The in-flight technique is used e.g. at NSCL, GSI and RIBF [132, 133, 134] whereas the ISOL method is used e.g. at ISOLDE, CERN [135] and at the ISAC facility at TRIUMF [136]. The in-flight technique requires high-energy heavy-ion primary beams not available everywhere. On the other hand, the ISOL technique uses typically thick targets and requires a separate ion source to produce the ion beams [137, 138]. To develop a faster and chemically insensitive method, gas-cell based ion-guide method was developed at the University of Jyväskylä in early 1980s [138].

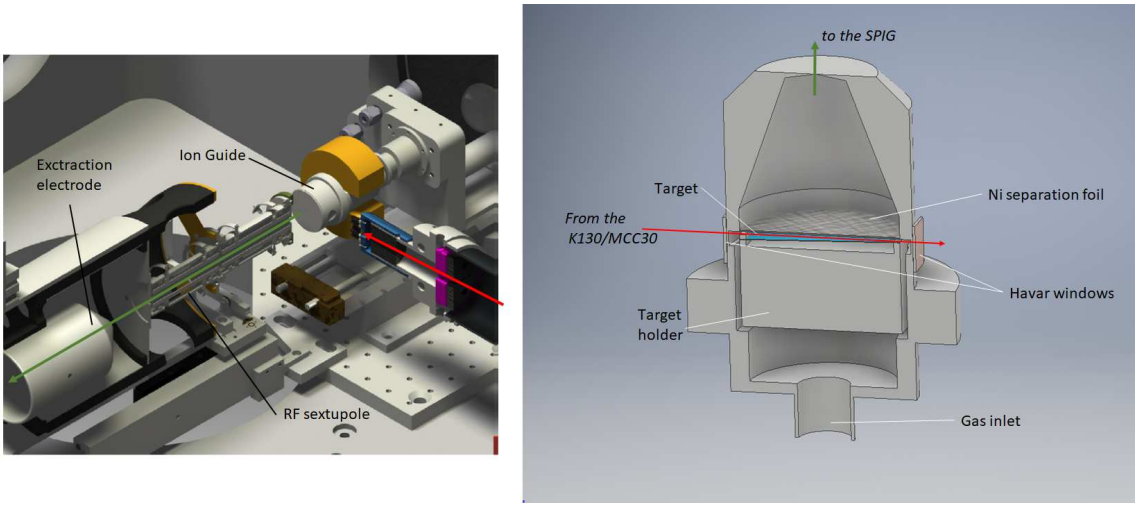

FIGURE 13 The IGISOL target chamber (left) and the fission ion guide (right). The primary beam is represented by a red arrow and the secondary beam by a green arrow. Left figure reproduced with the permission of I.D. Moore.

At the Ion Guide Isotope Separator On Line (IGISOL) facility, radioactive ions are produced via fission or fusion reactions induced by a light or medium-heavy beams on a thin target. The reaction products are stopped in a gas-filled chamber and then extracted using an ion guide and helium gas jet (see Fig. 13). Dedicated ion guides have been developed for different reactions at IGISOL, such as the light-ion ion guide, heavy-ion ion guide and fission ion guide [139]. Nowadays, the ions are extracted out of the gas cell using a sextupole ion guide SPIG [140] and electrostatically accelerated to $30q$ keV. The charge state of the ions q is in most of the cases $+1$. A 55° dipole magnet is used as a mass separator with a resolving power of $M/\Delta M \sim 500$. An example of a dipole magnet mass scan for ion beam intensities measured with a Faraday cup at the electrostatic switchyard is shown in Fig. 14. Typical contaminants highlighted in Fig. 14 are related to air, buffer gas impurities or outgasing to the gas cell walls [141].
The layout of the actual IGISOL facility is represented in Fig. 15. The electrostatic switchyard is used to drive the beam straightforward to the radio-frequency cooler and buncher RFQ [142] or to the spectroscopy line on the right or to the cesium atom trap station [143] on the left. The ions are decelerated before entering into the RFQ where helium buffer gas is used to cool them. In the RFQ, the ions are radially confined by application of a radiofrequency electric field. The ions are released as short bunches, typically 10-15 μs. After the RFQ, the ions can be either transported to the collinear laser spectroscopy line or to the JYFLTRAP double Penning-trap setup.

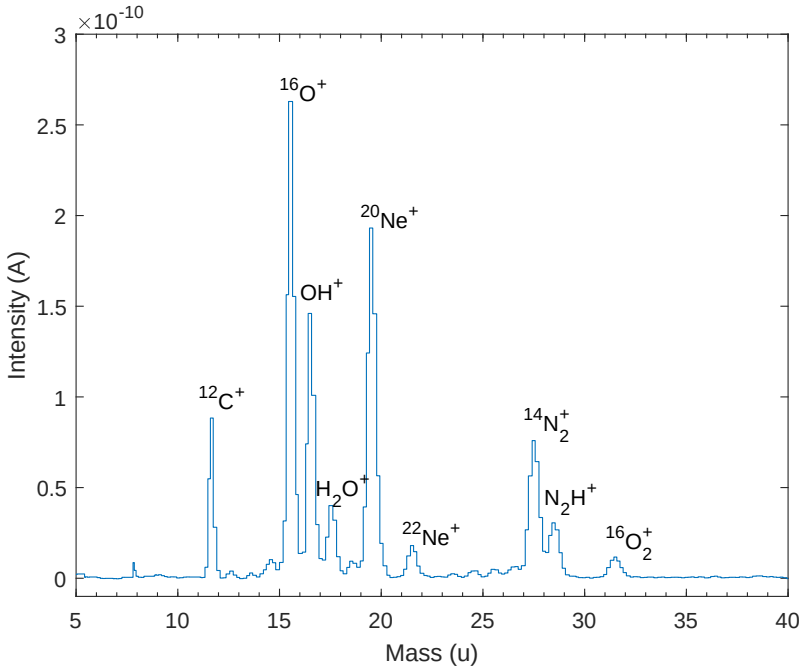

FIGURE 14 A typical mass scan in the lower-mass region performed with the 55° dipole magnet using a Faraday cup at switchyard. The dominant stable ion beams are indicated.

In 2010-2014, the IGISOL facility moved to a new experimental hall, and

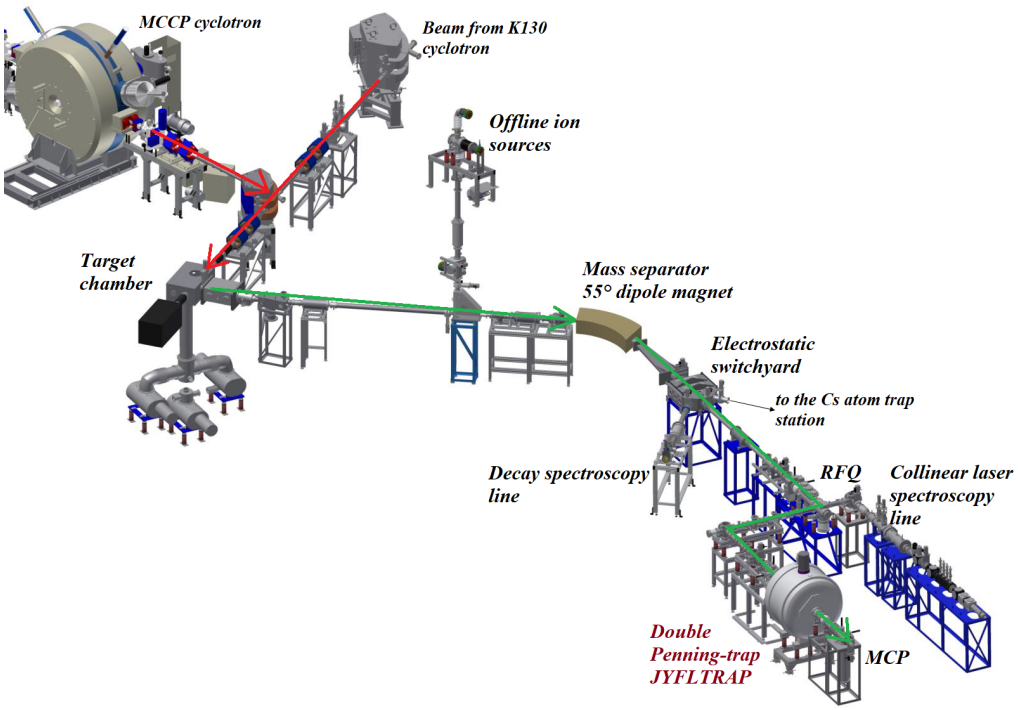

FIGURE 15 Layout of the IGISOL-4 facility. The red arrow represents the primary beam coming from the MCC30 or K130 cyclotron. The green arrows indicate the secondary beam path up to the double Penning-trap JYFLTRAP and the multichannel plate (MCP) detector afterward.

IGISOL-4 was built and commissioned [144]. Several improvements have been made since the development of the first IGISOL [145]. In the early 1990s, the facility, thereafter called IGISOL-2 was moved to the Ylistönrinne campus and connected to the new K130 heavy ion cyclotron which can deliver beams up to energies of 130 Q^2/A MeV. IGISOL was upgraded to IGISOL-3 during 2003 with several technical improvements and an increase of the radiation shielding in the front end. The skimmer that had been used to drive the ions from the ion guide to the mass separator was replaced by a SPIG.

4.2 JYFLTRAP: A double Penning trap mass spectrometer

4.2.1 Ion motion in an ideal Penning trap

A Penning trap is a system to confine charged particles using a homogeneous magnetic field and a quadrupolar electric field [146, 147]. It has been named after the Dutch physicist Frans Michel Penning [148]. The motion of a charged particle in an electromagnetic field is defined by the Lorentz force:

$$\vec{F} = q\vec{E} + q\vec{v} \wedge \vec{B} \tag{39}$$

where q is the charge of the particle, $\vec{E}$ is the electric field, $\vec{v}$ is the particle

velocity and $\overrightarrow{B}$ is the magnetic field. Thus, the first term represents the electric force $\overrightarrow{F_{elec}}$ and the second term the magnetic force $\overrightarrow{F_{mag}}$. The homogeneous magnetic force $\overrightarrow{B}=B_0\overrightarrow{z}$ confines the charged particles radially. In order to confine them axially, an electrostatic force with a quadrupolar form $\overrightarrow{E} = \overrightarrow{\nabla} V$ is applied:

$$V = V_0 \frac{z^2 - \rho^2/2}{2d^2} \tag{40}$$

The potential is obtained with three electrodes: two end electrodes and one ring electrode. V_0 is the difference of potential between two different electrodes, z and ρ are axial and radial coordinates, respectively, and d^2 is related to the trap geometry:

$$d^2 = \frac{z_0^2 + \rho_0^2/2}{2} \tag{41}$$

where z_0 and ρ_0 are the minimum axial and radial distance to the electrodes, respectively. To obtain the eigenmotion of a charged particle in a Penning trap, one has to solve the equations of motion:

$$\begin{aligned} m\overrightarrow{\ddot{\rho}} &= q\frac{V_0}{2d^2}\overrightarrow{\rho} + q\overrightarrow{\dot{\rho}} \wedge \overrightarrow{B} \\ m\ddot{z} &= -q\frac{V_o}{d^2}z \end{aligned} \tag{42}$$

Thus in cartesian coordinates:

$$\begin{aligned} m\ddot{x} &= q\frac{V_0}{2d^2}x + qB_0\dot{y} \\ m\ddot{y} &= q\frac{V_0}{2d^2}y - qB_0\dot{x} \\ m\ddot{z} &= -q\frac{V_0}{d^2}z \end{aligned} \tag{43}$$

For the axial coordinate z, the equation of motion is for the one-dimensional harmonic oscillator, thus:

$$z(t) = R_z cos(\omega_z t + \phi_z) \tag{44}$$

where R_z is the amplitude of the axial displacement, and ω_z is the axial angular frequency:

$$\omega_z = \sqrt{\frac{qV_0}{md^2}} \tag{45}$$

and ϕ_z is the phase at t=0. To solve the radial equations of motion, we set:

$$u = x + iy \tag{46}$$

and

$$m\ddot{u} = -iqB_0\dot{u} + \frac{qV_0}{2d^2}u \tag{47}$$

The solution for this differential equation gives:

$$u(t) = R_+ \exp(-i\omega_+ t + \alpha_+) + R_- \exp(-i\omega_- t + \alpha_-) \tag{48}$$

where

$$\omega_\pm = \frac{1}{2}(\omega_c \pm \sqrt{\omega_c^2 - 2\omega_z^2}) \tag{49}$$

are the reduced cyclotron and the magnetron frequencies, respectively. The parameters R_+ and R_- are the cyclotron and magnetron radii, respectively. The parameter ω_c is the cyclotron frequency:

$$\omega_c = \omega_+ + \omega_- = \frac{qB_0}{m} \tag{50}$$

The radial motion of an ion in an ideal Penning trap is thus:

$$\begin{aligned} x(t) &= R_+(cos\omega_+ t + \phi_+) + R_-(cos\omega_- t + \phi_-) \\ y(t) &= R_+(sin\omega_+ t + \phi_+) + R_-(sin\omega_- t + \phi_-) \end{aligned} \tag{51}$$

In order to have Eq. (49) real, we find out the conditions to confine ions in a Penning trap in an ideal case:

$$\frac{qB_0^2}{m} > \frac{2V_0}{d^2} \tag{52}$$

The eigenmotions of a charged particle in a Penning trap have important features. The motions are represented in Fig. 16. As it can be seen, the relative magnitudes of the eigenfrequencies are:

$$\nu_c > \nu_+ > \nu_z > \nu_- \tag{53}$$

where ν_c=$\omega_c/2\pi$, ν_+=$\omega_+/2\pi$, ν_z=$\omega_z/2\pi$ and ν_-=$\omega_-/2\pi$. Also, the so-called invariance theorem [146] gives:

$$\nu_+ + \nu_- + \nu_z = \nu_c \tag{54}$$

and

$$2\nu_+\nu_- = \nu_z^2 \tag{55}$$

The magnetron angular frequency can be approximated by:

$$\omega_- \approx \frac{V_0}{2d^2B_0} \tag{56}$$

Thus, the magnetron motion is independent of the mass of the ion whereas the reduced cyclotron angular frequency:

$$\omega_+ \approx \omega_c - \frac{V_0}{2d^2B_0} = \frac{qB_0}{m} - \frac{V_0}{2d^2B_0} \tag{57}$$

depends on the stored ion's mass.

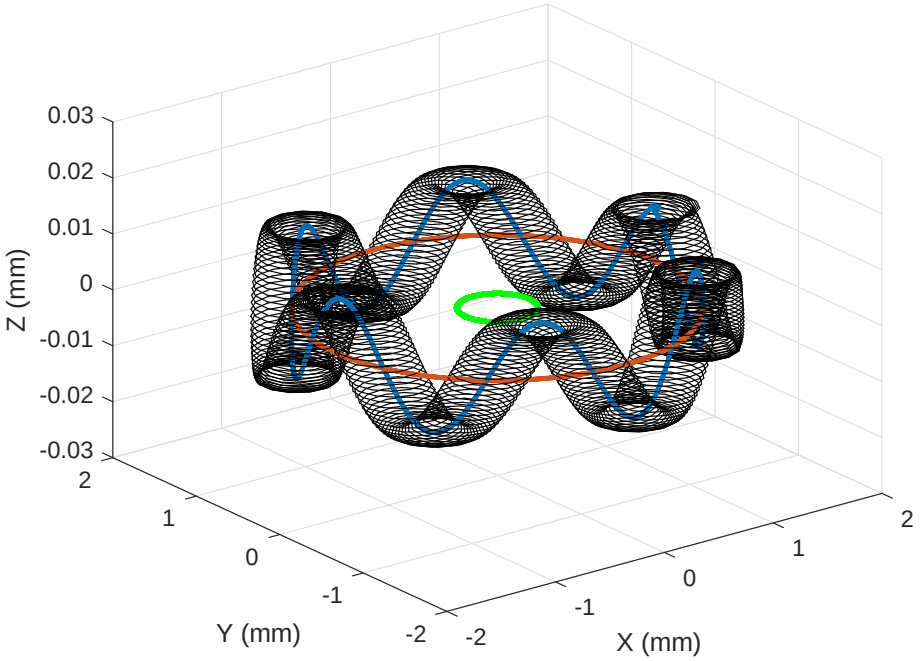

FIGURE 16 Trajectory of a charged particle having only magnetron motion (red), cyclotron motion (green), and with the combination of the three eigenmotions i.e. the actual motion of an ion in a Penning trap (black). The magnetron frequency chosen (ν_-=1.700 kHz) is a typical value at JYFLTRAP, the reduced cyclotron (ν_+=650 kHz) and axial (ν_z=10 kHz) frequencies have been chosen with slightly smaller value than usual ones for the figure clarity.

4.2.2 From an ideal to real Penning trap

The Penning traps have two common geometries: hyperbolic and cylindrical. Each configuration has its own advantages and weaknesses. The hyperbolic geometry is historically the first configuration used for Penning traps [149] because the electric field is easy to make. But to let the ions enter, holes have to be made in the end of the electrodes. The field imperfections created are hard to compensate and the hyperbolical surface needs to be truncated. In a cylindrical configuration as JYFLTRAP, the electric field imperfections are corrected by adding correction electrodes between the ring and the endcap electrodes. The two main advantages of this trap type are that the potentials can be calculated analytically and the electrodes can be manufactured with high precision [150]. The hyperbolic configuration is used for example at ISOLTRAP at CERN [151].

In a real Penning trap like JYFLTRAP (Fig. 17) [152], one has to take into account several factors that reduce the precision of the measurements, such as geometrical imperfections of the trap affecting the electric field, inhomogeneities and fluctuations of the magnetic field, and the presence of possible contaminants i.e. ions with a different mass than the one studied.

In Eq. (40), the potential was given for an ideal case. In reality, the electric field shows always imperfections which add multipoles to the trap potential. In

FIGURE 17 The 7 T superconducting magnet housing the JYFLTRAP Penning trap (top) and the JYFLTRAP with its different electrodes (bottom).

a real trap, the cyclotron frequency is shifted [147]:

$$\Delta\omega_c^{elect} \approx \frac{V_0}{2d^2B}[\frac{3}{2}\frac{C_4}{d^2}(\rho_-^2 - \rho_+^2) + \frac{15}{4}\frac{C_6}{d^4}(\rho_z^2(\rho_-^2 - \rho_+^2) - (\rho_-^4 - \rho_+^4))] \tag{58}$$

Where ρ_-, ρ_+, ρ_z are the amplitudes of the magnetron, reduced cyclotron and axial motion, respectively, and C_4, C_6 are multipoles of the electric field. Correction electrodes placed between the ring and the endcap electrodes permit to compensate the potential in order to reduce or get rid of the unwanted anharmonicities. The magnetic field fluctuations are mostly due to temperature variation and pressure change in the superconducting magnet vessel. They can be characterized experimentally and details of the procedure will be given at the end of this chapter.

4.2.3 Purification of the beam with the purification trap

In order to do precise mass measurements or to perform decay spectroscopy with isotopically or even isomerically pure beams, it is necessary to perform high-resolution beam purification. JYFLTRAP has two Penning traps, the purification trap and the precision trap. The first trap is specifically dedicated to the beam purification while the second trap is used for high precision mass measurements.

When a bunch of ions is released from the RFQ, it enters into the first trap of JYFLTRAP. This trap and the precision trap are both inside the same 7 T superconducting magnet and they consist of a series of gold-plated copper electrodes for a total length of 1046 mm [152] (see Fig. (17)).
When the ions enter in the purification trap, the ions cool down by collisions with the helium buffer gas. The pressure in the first trap is on the order of 10^{-4}

mbar. After some cooling time, a dipolar radiofrequency electric field is applied to the four-fold split ring electrodes. The characteristic of a dipolar excitation is to act only in one eigenmotion of the ions. In this case, the dipolar excitation will increase the radius of the magnetron motion R_-. The magnetron motion has a negative contribution to the overall energy of an ion in a Penning trap:

$$E = \hbar\omega_+(n_+ + 1/2) + \hbar\omega_z(n_z + 1/2) - \hbar\omega_-(n_- + 1/2) \tag{59}$$

and its energy is maximum at the center of the trap. The increase of R_- causes thus a decrease of the overall ion energy. Because the magnetron motion is mass-independent, all ions will move away from the trap center. A quadrupolar radiofrequency electric field is then applied to the ring electrode. The quadrupolar excitation acts on several eigenmotions at the same time. It is applied on the xy-plane with the amplitude:

$$V_{RF} = 2\delta^2 B\frac{\pi}{T_{RF}} \tag{60}$$

where δ is the inner radius of the ring electrode (16 mm) and T_{RF} is the excitation time. With the appropriate amplitude and excitation time, the quadrupolar excitation converts the magnetron motion to cyclotron motion. The helium gas will act on the motion by damping the fast cyclotron motion, and selected ions will finally be centered in the trap [153]. This method enables to get rid of contaminants as the cyclotron motion is mass-dependent and the conversion is thus only acting on the ions of interest with matching resonance frequency. The contaminants will continue to have their magnetron radius increasing by collision with the buffer gas until eventually touching the electrode. The selected ions are centered and can be extracted out through a small diaphragm of 2 mm in diameter [152].

4.2.4 High-precision mass measurements with the precision trap

The precision trap is physically almost identical to the purification trap. The main difference is in the pressure in the trap cavity. No buffer gas is used in the precision trap and the pressure is on the range of $\approx 10^{-8}$-10^{-9} mbar. A 24 mm long diaphragm with a diameter of 4 mm prevents the gas from the purification trap to flow into the precision trap.

4.2.4.1 Time-of-flight Ion Cyclotron Resonance (TOF-ICR) technique

Shortly after the ions have entered in the precision trap, a short dipolar RF excitation at the magnetron frequency ν_- is applied to increase the magnetron radii of the ions. A quadrupolar excitation is then applied to convert the magnetron motion into fast modified cyclotron motion. The magnetron motion of the ion of interest is fully converted to cyclotron motion when ν_{RF}=ν_c for the used excitation amplitude V_{RF} and time T_{RF} which have been determined experimentally for JYFLTRAP [154]:

$$T_{RF}V_{RF} = 11.2mVs \tag{61}$$

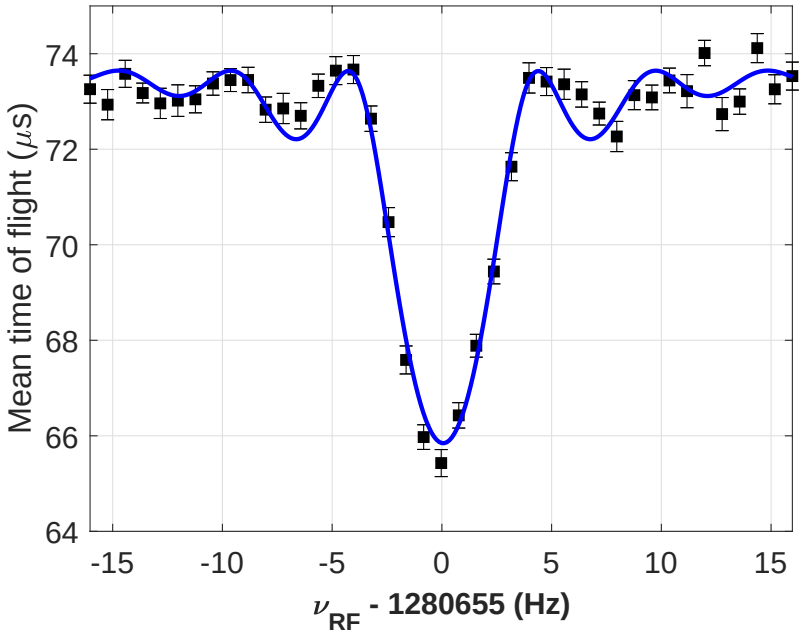

FIGURE 18 A typical TOF-ICR spectrum for $^{84}Kr^{+}$ measured with a 437 ms trap cycle using 200 ms quadrupolar excitation in the measurement trap. The blue line is a fit of the theoretical curve to the experimental data points (in black).

After one full conversion, the ions are extracted from the trap and sent to a microchannel plate detector (MCP). In combination with a trigger placed at the extraction time, the time-of-flight of the ions from the extraction to the MCP is recorded. There is a strong magnetic field gradient from the trap to the MCP, and thus the axial force on the extracted ions is:

$$\vec{F} = -\frac{E_R}{B_0}\frac{\partial B(z)}{\partial z}\hat{z} \tag{62}$$

where E_R is the radial kinetic energy. Therefore, the axial force is maximum for an ion with maximum radial kinetic energy. This is obtained for ions with a full conversion from magnetron to fast cyclotron motion, i.e. for ions for which ν_{RF}=ν_c. A typical time-of-flight spectrum is shown in Fig. 18 for 1441 $^{84}Kr^{+}$ ions.
The resolving power is given by the line width of the resonance [147]:

$$R = \frac{m}{\Delta m} = \frac{\nu_c}{\Delta \nu_c} \tag{63}$$

and is proportional to the excitation time T_{RF}, $R \approx \nu_c T_{RF}$. With the TOF-ICR technique, typical resolving power is about 10^6 for A=100 ions with a typical half-lives of 1 s [147, 152].

4.2.4.2 Time-separated oscillatory fields

Ramsey's method of time-separated oscillatory fields has been broadly utilized for example for measurements of molecular resonances [155], for determination of frequencies for atomic transitions or nuclear magnetic moments [156]. Later on, the method has been extended to Penning trap mass spectrometry to increase the

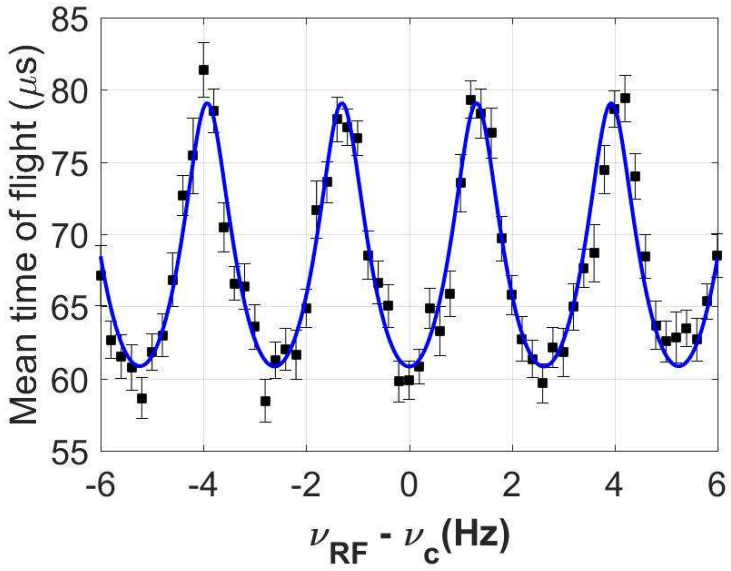

FIGURE 19 Time-of-flight spectrum for $^{30}P^{+}$ ions obtained using the Ramsey's method of time-separated oscillatory fields with an excitation pattern consisting of two 25 ms excitation pulses separated by 350 ms of waiting time. The blue line is a fit of the theoretical curve on the experimental data points (in black).

precision of the measurements [157]. The theoretical foundation of this method is extensively detailed in Ref. [158].

The precision of a cyclotron frequency measurement is directly related to the width of the TOF resonance. In the Ramsey's method, the RF quadrupolar excitation is applied in the second trap as two short pulses separated by a waiting time during which the excitation is off. Theoretically n-excitation pulses could also be used but it has been shown that the reduction of the peak resonance width is more efficient in a two-pulse excitation scheme [159].

In experiments, the width of the resonant peak is reduced by ≈40% when the Ramsey's method is used instead of a one-pulse excitation scheme [159]. The reduced resonance line width increase the resolving power as it was shown in Eq. (63). The precision of the measurement can be reduced by a factor of three. This is mainly due to a thinner resonance but also due to the better resolution of the sidebands [160]. Figure 19 shows a typical Ramsey TOF spectrum measured for $^{30}P^{+}$ ions in this work. A typical Ramsey timing pattern used at JYFLTRAP has two 25 ms excitation pulses separated by 50-750 ms of waiting time. One limitation for the use of the Ramsey's method is the need to have a cleaner bunch of ions than for the normal TOF-ICR (i.e. one excitation pulse pattern) to be able to fit it. It is also not very good for the most exotic isotopes or when there are two isotopes or isomeric states close to each other. The center fringe is checked by doing a normal TOF-ICR measurement before applying Ramsey's method [152].

4.2.4.3 Phase-imaging ion cyclotron resonance method (PI-ICR)

A novel technique, the Phase-Imaging Ion-Cyclotron-Resonance method, has been developed recently at SHIPTRAP at GSI [161]. During 2017, the PI-ICR technique has been commissioned at JYFLTRAP [162]. The method is based on the precise determination of the phase of the radial motion of the ions with a position-sensitive microchannel plate detector with a delay line anode. Two different patterns are used to determine the ion's cyclotron frequency [161, 162]. Firstly, a dipolar excitation is applied at the opposite phase of ion's coherent magnetron motion, reducing the magnetron radius. In a similar way, a dipolar excitation is applied to reduce the inherent axial motion of the ions. A third dipolar excitation at the frequency ν_+ is used to excite the reduced cyclotron motion. A quadrupolar excitation is then applied immediately after this excitation period ends, and the converted magnetron motion is let to accumulate before being extracted and detected by the detector. The total magnetron phase φ_-^{tot} is then:

$$\varphi_-^{tot} = \varphi_- + 2\pi n_- = 2\pi\nu_- t \tag{64}$$

where n_- is the integer number of revolutions after the accumulation time t and φ_- is the phase measured on the detector. To determine the phase φ_-, the trap center is determined beforehand by measuring the phase with a dipolar excitation used only to correct a possible misalignment between the magnetic field and the axis of the trap.
To determine the other radial motion, ν_+, the same procedure is applied except that the quadrupolar excitation is applied after a certain phase accumulation time to convert the fast reduced cyclotron motion to magnetron motion just before the detection. The ions are then immediately extracted and the phase of the reduced cyclotron motion determined:

$$\varphi_+^{tot} = \varphi_+ + 2\pi n_+ = 2\pi\nu_+ t \tag{65}$$

From the measured magnetron and reduced cyclotron phases, the ion's cyclotron frequency ν_c can be computed using:

$$\nu_c = \frac{\alpha_c + 2\pi(n_+ + n_-)}{2\pi t} \tag{66}$$

where α_c is the angle between the positions of the two phase images. An example of a spectrum obtained with the PI-ICR technique is given in Fig. 20. In this example, the reduced cyclotron motion is accumulated for 100 ms, and the ground state (6^-) and the two isomeric states of ^{70}Cu (3^- and 1^+) have been separated. Therefore, the PI-ICR method needs a much shorter time to separate the states compared to the TOF-ICR technique (e.g. 900 ms quadrupolar excitation was used for ^{70}Cu using TOF-ICR method at ISOLTRAP [163]). Faster measurements are very useful for the measurements of exotic nuclei with short half-lives and to separate long-living isomeric state.
The capacity to resolve the phase difference of the cyclotron motions of two ions

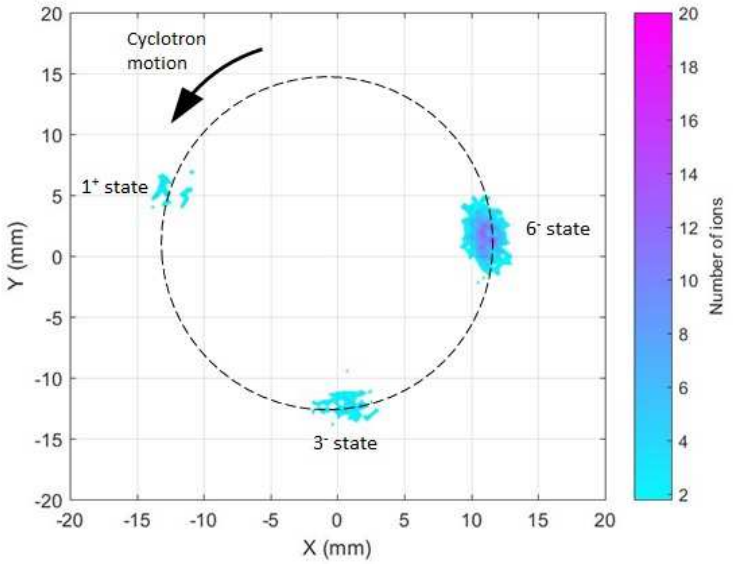

FIGURE 20 A PI-ICR spectrum for $^{70}Cu^{+}$ ions using 100 ms phase accumulation time for the cyclotron motion.

species or states after an accumulated time t defines the resolving power:

$$R = \frac{\nu_c}{\Delta\nu_c} \approx \frac{\nu_+}{\Delta\nu_+} = \frac{2\pi t\nu_+}{\Delta\varphi} \tag{67}$$

Where $\Delta\varphi$ is the resolution of the phase angle between the position before and after the ion motion accumulation. Compared to the Ramsey method, the resolving power is about 40 times higher with the PI-ICR technique resulting to an improvement of the mass value precision by a factor of five [162].

4.3 Analysis of the JYFLTRAP data

4.3.1 Measurement schemes used at JYFLTRAP

For the analysis of the collected JYFLTRAP data, it is useful to first understand how the data are collected. A typical measurement scheme is given in Fig. 21. The first step (the line **I**) is the accumulation of ions in the RFQ. The number of accumulated ions can be adjusted by selecting when the continuous ion beam enters the cooler, i.e. setting when the beamgate is open. The beamgate is controlled with an electrosctatic deflector at switchyard which deflects the beam to the spectroscopy line (instead of the RFQ) when the beamgate is closed. After ions have been accumulated for some time (450 ms in Fig. 21), the extraction electrode of the RFQ is lowered to extract the ions from the RFQ and sent them to the first trap (step **II**). The extraction from the cooler can also be delayed to keep the ions in the RFQ for some time after the beam gate is closed. This is useful for example for estimating half-lives for the ions of interest by measuring the number of ions for different cycle times after the beamgate closure. For a radioactive ion beam,

the ions are produced at rate P_i when the beamgate is open and the number of ions is:

$$N_i(t) = \frac{P_i}{\lambda_i}(1 - e^{-\lambda_i t}) \tag{68}$$

where $\lambda_i = ln(2)/t_{1/2,i}$ is the decay constant of the nuclide of interest. When the beam gate is closed, the ions are not produced anymore and they decay according to the radioactive decay law:

$$N_i(t) = N_i(t = t_{bg})e^{-\lambda_i t} \tag{69}$$

where t_{bg} is the time for which the beamgate is open, i.e. ions are accumulated in the cooler. The total time during which the ions decay according to Eq. (69), t=t_{decay} is from the beam gate closure to the detection on the MCP detector.
The cycle **II a)** in Fig. 21 shows the trap cycle for a TOF-ICR measurement. After a cooling time of some tens of ms in the first trap, a dipolar excitation at magnetron frequency is applied for around 1 to 10 ms and finally the magnetron motion of the ion of interest is converted to cyclotron motion by a quadrupolar excitation. Then the ions are extracted from the purification trap and injected into the precision trap. There a dipolar excitation is immediately followed by a quadrupolar excitation which is typically 50, 100, 200, 400 or 800 ms. When the extraction electrode of the second trap is lowered, the MCP is triggered in order to measure the time-of-flight for the ions. For Ramsey's time-separated oscillatory fields TOF-ICR resonance, preparation of the ions are otherwise the same as for a normal TOF-ICR (**II a**) but instead of a continuous quadrupolar excitation in the second trap, the quadrupolar excitation is applied for a short time (25 ms) followed by a waiting time (typically 150 ms, 350 ms or 750 ms) and another 25 ms excitation in the end (see Fig. 21 **II b**). The total cycle in the trap stays the same as in the normal TOF-ICR shown in **II a)**.

4.3.2 Analysis programmes for JYFLTRAP data

Two programmes developed at JYFLTRAP over the years have been used to analyse normal TOF-ICR or Ramsey-type of TOF-ICR resonances in this work. With the *Lakritsi* programme [154], the TOF spectra can be fitted. For a single peak TOF-ICR, the time-of-flight is given by :

$$T(\omega_{RF}) = \sqrt{\frac{m}{2}} \int_{z_0}^{z_1} \sqrt{\frac{1}{E_0 - qV(z) - E_r(\omega_{RF})B(z)/B_0}} dz \tag{70}$$

where z_0 is the position of trap extraction and z_1 the position of the MCP, E_0 is the total kinetic energy of the ions, $V(z)$ and $B(z)$ are the electric and magnetic field along the ion path, B_0 is the magnetic field at trap extraction, and $E_r(\omega_{RF})$ is the total radial kinetic energy of the ions:

$$E_r(\omega_{RF}) \approx \frac{1}{2} m \rho_+^2(\omega_{RF}) \omega_+^2 \tag{71}$$

where $\rho_+(\omega_{RF})$ is the amplitude of the reduced cyclotron motion. Thus, the fit requires eight parameters that can be fixed or kept free in *Lakritsi*:

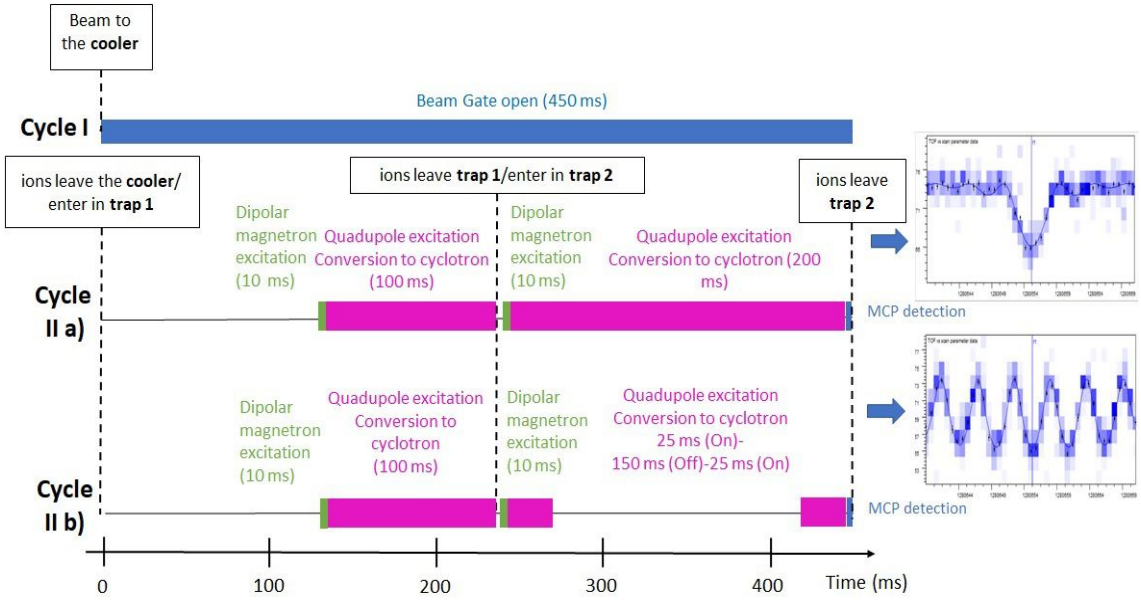

FIGURE 21 Typical measurement schemes at JYFLTRAP. All measurements start with the top cycle **I**. The cycle **II a)** is used for the TOF-ICR measurements and **II b)** is applied for TOF-ICR measurements with the Ramsey's method of time-separated oscillatory fields.

- Cyclotron frequency ν_c (related to the mass m (Eq. 50))
- Pressure in the trap. The value should stay stable ($P \approx 10^{-6}$ mbar) and is related to the amplitude of the motion ρ_+ by acting as a damping parameter.
- Initial axial energy E_{axial} that is linked to the total kinetic energy $E_0 = E_{axial} + E_r$ where E_r is the radial kinetic energy of the ions.
- Initial magnetron radius $\rho_-(t = 0)$ of the ions.
- Initial cyclotron radius $\rho_+(t = 0)$ that is usually equal to zero.
- Phase difference between $\rho_+(0)$ and the driving field, equal to zero also following the last statement.
- Excitation time T_{RF} that is fixed precisely for each measurement.
- Number of full conversions related to the excitation amplitude.

Lakritsi is also used to fit spectra from time-separated oscillatory fields. For two excitation pulses of duration τ_1 separated by a waiting period τ_0 the fitting function is given by [160]:

$$F_2(\delta, \tau_1, \tau_2, g) = \frac{16g^2}{\omega_R^2} sin^2(\frac{\omega_R \tau_1}{2})[cos(\frac{\delta \tau_0}{2})cos(\frac{\omega_R \tau_1}{2}) - \frac{\delta}{\omega_R} sin(\frac{\delta \tau_0}{2})sin(\frac{\omega_R \tau_1}{2})]^2 \quad (72)$$

where g is a coupling constant proportional to the quadrupolar field amplitude, $\omega_R = \sqrt{(2g)^2 + \delta}$ is the analog of the Raby frequency and $\delta = \omega_{RF} - \omega_c$ is the

detuning of the quadrupolar field. For excitations with two fringes, a fit on the TOF-ICR curve requires six parameters in *Lakritsi*:

- Cyclotron frequency ν_c.
- Axial energy E_{axial}.
- Initial magnetron radius $\rho_-(t = 0)$.
- Total time $\tau_{tot} = \tau_0 + \tau_1$.
- Excitation time of one fringe τ_1.
- Quadrupolar field amplitude A_{RF} that is proportional to the coupling constant g.

During mass measurements, several TOF-ICR spectra for the ions of interest are measured, sandwiched by measurements of a reference ion, which has a well known mass. A time-of-flight gate is applied to accept only the ions with a correct time of flight for the mass number in question. The number of ions per bunch can also be selected in the analysis. To take into account shifts due to the presence of possible contaminants, the data can be split according to the number of ions per bunch in the so-called countrate class analysis [164].

Complicated Offline Mass Analyser (*COMA*) program has been used in this work to obtain the frequency ratio r=ν_{ref}/ν_{meas} between the fitted frequencies of the ion of interest and the fitted frequencies of the reference ion. The final frequency ratio is obtained as a weighted mean over all measured frequency ratios. The atomic mass m_{meas} can be determined from the measured frequency ratio r for singly-charged ions:

$$m_{meas} = r(m_{ref} - m_e) + m_e \tag{73}$$

where m_e is the electron mass. The binding energy of the electron is here neglected. If the reference ion is the daughter nucleus in the β-decay of the ion of interest, the β-decay Q value can be very precisely determined as:

$$Q = (m_{meas} - m_{ref})c^2 = (r - 1)(m_{ref} - m_e)c^2 \tag{74}$$

In the *COMA* program, the mass-dependent uncertainty, the error due to the magnetic field fluctuations and the residual systematic uncertainty can be entered and taken into account. The Birge ratio R is also calculated [165] :

$$R = \frac{\sigma_{ext}}{\sigma_{int}} \tag{75}$$

where σ_{ext} is the outer error and σ_{int} the inner error:

$$\sigma_{int}^2 = \frac{1}{\sum_i \sigma_i^{-2}} \tag{76}$$

and

$$\sigma_{ext}^2 = \frac{\sum_i \sigma_i^{-2}(r_i - \bar{r})^2}{(n-1)\sum_i \sigma_i^{-2}} \tag{77}$$

where r_i are the individual frequency ratios. The inner and outer errors give indication about the quality of the measured frequency ratios. The final error of the frequency ratio is the outer error if $R > 1$, otherwise the internal error is adopted. If the Birge ratio is well above 1, the uncertainty of the frequency ratio is not purely statistical may hint that some systematic errors have been omitted.

4.4 Systematic uncertainties of JYFLTRAP

Systematic errors have to be taken into account when measuring atomic masses with a Penning trap. For the special case of a measurement of a doublet ion-of-interest/reference with the same mass number, the uncertainties due to field imperfections cancel out in the frequency ratio. However, the temporal fluctuations of the magnetic field must be included for every measurement. Prior to the relocation of the JYFLTRAP Penning trap to the new IGISOL-4 facility, the magnetic field fluctuation has been studied twice at IGISOL-3 [166, 167]. The 7 T superconducting solenoid magnet of JYFLTRAP was re-energized after the move to IGISOL-4 in 2010. An updated value of the magnetic field fluctuation was thus highly needed.

4.4.1 Time-dependent fluctuations in the magnetic field

The procedure to evaluate the magnetic field fluctuations at JYFLTRAP consisted of a long series of cyclotron frequency measurements for $^{84}Kr^+$ ions. The collected data were temporally divided into smaller subsets. The subsets were further labeled as a measurement or a reference file so that every measurement was sandwiched by two reference files. The cyclotron frequency from the reference files was then interpolated to the middle of the measurement file. This interpolated value was compared to the measured cyclotron frequency of the measurement data file, and the procedure was repeated for different time intervals Δt between the reference files.

At IGISOL-4, the cyclotron frequency for $^{84}Kr^+$ ions was collected for one week in December 2014, using a Ramsey excitation pattern of 25-350-25 ms (On-Off-On) with an amplitude of 224 mV. The data was divided in ≈9.5 min long measurements and thus the shortest time between the references Δt was ≈19 min. Ideally, the interpolated and measured cyclotron frequencies are the same, and the frequency ratio $r = \nu_{interpol}/\nu_{meas} = 1$. To extract uncertainties related to temporal fluctuations in the magnetic field, the deviations:

$$\frac{\Delta B}{B} = \frac{B_{interpol} - B_{meas}}{B_{meas}} = \frac{\nu_{interpol}}{\nu_{meas}} - 1 \tag{78}$$

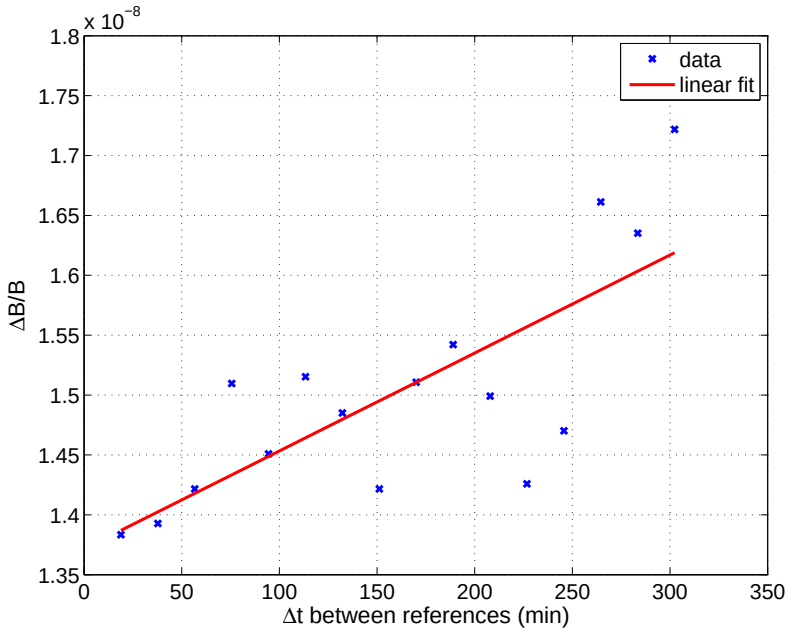

FIGURE 22 Standard deviation of the magnetic field fluctuations obtained for $^{84}Kr^{+}$ ions using different time differences Δt between two reference measurements. The slope of the fit is $8.18(19) \times 10^{-12}$/min.

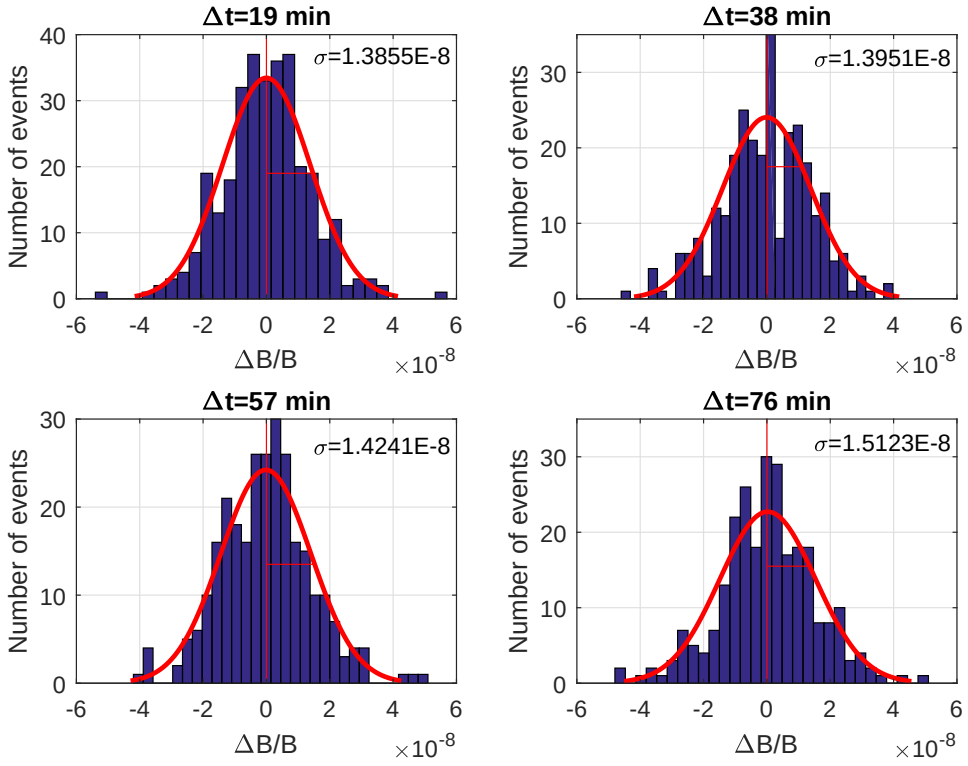

FIGURE 23 Gaussian fits on the histograms of statistical fluctuation for four shortest times between the references (19 , 38 , 57 and 76 min). The standard deviation σ is given for each figure.

are determined for each Δt, and their standard deviations are plotted as a function of Δt (see Fig. 22). The standard deviation for each time Δt was determined by fitting a Gaussian on the histogram of the frequency ratio deviations from the weighted average (Fig. 23). The uncertainties related to temporal fluctuations in the magnetic field have been estimated by fitting a straight line to the data, which yields to $8.18(19)\times10^{-12}/\mathrm{min}\times\Delta t$. The two previous measurements done at IGISOL-3 indicated stronger fluctuations in the magnetic field, $3.22(16)\times10^{-11}/\mathrm{min}\times\Delta t$ [166] and $= 5.7(8)\times10^{-11}/\mathrm{min}\times\Delta t$ [167]. The improvement of the magnetic field stability can be explained by improved conditions at IGISOL-4. There is no longer direct access to outside, and hence the daily temperature fluctuations do not exceed 0.6°C. In addition, the stand of the magnet has been changed to a non-ferromagnetic material, aluminum, and more insulators have been installed for the high voltage cage.

4.4.2 Mass-dependent and residual systematic errors

The mass-dependent effect has to be taken into account in the analysis when the ion of interest has not the same mass number as the reference ion. A systematic study of the mass-dependent uncertainty of JYFLTRAP has been carried out in 2009 using carbon-cluster ions [168]. The study concludes on a value for the mass-dependent uncertainty of $\sigma_m(r)/r$=$(7.5\pm0.4\times10^{-10}/\mathrm{u})\times\Delta m$ for a mass difference not exceeding $\pm$24 u and of $\sigma_m(r)/r$=$(7.8\pm0.3\times10^{-10}/\mathrm{u})\times\Delta m$ otherwise. A residual uncertainty of $\sigma_{res}(r)/r$=7.9×10^{-9} and $\sigma_{res}(r)/r$=1.2×10^{-8} has been computed for the first and second case, respectively.
The mass-dependent and residual systematic errors were restudied at IGISOL-4 after a realignment of the Penning traps in 2017. During one week long offline experiment, a surface ion source made of K-Rb-Cs and a laser-ablation ion source with In and Yb samples were used in front of the RFQ. We measured successively $^{85,87}\mathrm{Rb}^+$, $^{113,115}\mathrm{In}^+$ and $^{171,172,173,174,176}\mathrm{Yb}^+$ ions alternatively with the reference ion $^{133}\mathrm{Cs}^+$ in order to obtain the frequency ratio between the reference ion and the ion of interest. The masses of the studied nuclides are all known with a high precision ($\delta m/m < 2.2\times10^{-6}$). The measured frequency ratio r can then be compared to the calculated ratio based on the literature mass values r_{lit} [6]:

$$\frac{\epsilon(r)}{r} = \frac{r - r_{lit}}{r} \tag{79}$$

where:

$$r_{lit} = \frac{m_{meas} - m_e}{m_{ref} - m_e} \tag{80}$$

where m_{meas} and m_{ref} are the atomic mass values based on the literature [6]. By fitting a straight line on $\epsilon(r)/r$ as a function of $\Delta m = m_{meas} - m_{ref}$, the dependence of the frequency ratio on the mass difference is obtained (see Fig. 24). The resulting mass-dependent uncertainty is $\sigma_m(r)/r$=$(2.2\pm0.6\times10^{-10}/\mathrm{u})\times\Delta m$. The relative difference of the measured frequency ratios corrected by the mass-dependent effect r_{corr} to the calculated ones, r_{calc}, is presented in Fig. 25. The

determined reduced χ^2 for r_{corr}-r_{calc} was less than one (χ^2/N=0.44) and therefore no residual systematic error is needed.

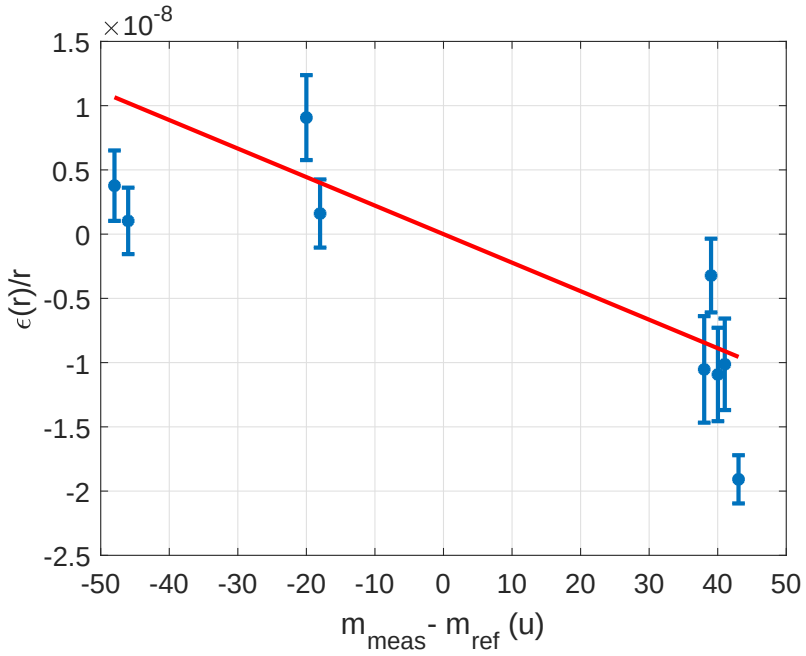

FIGURE 24 Relative differences of the measured frequency ratios to the literature values based on AME2016 [6].

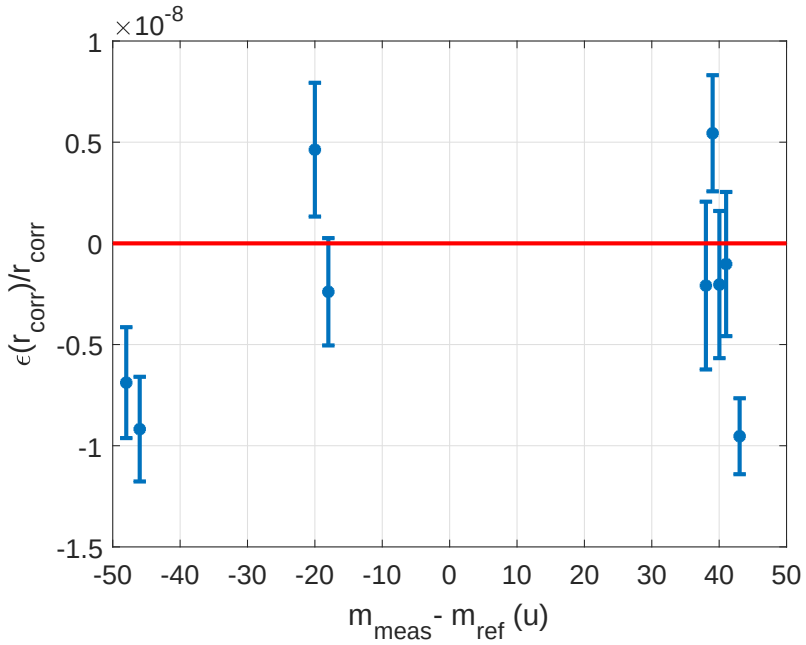

FIGURE 25 Relative differences of the measured frequency ratios corrected by the mass-dependent effect $\sigma_m(r)/r$=(2.2±0.6×10^{-10}/u)×Δm to the literature values based on AME2016 [6].

5 RESULTS AND DISCUSSION

5.1 ^{25}Al

5.1.1 Results

The mass measurement of ^{25}Al was done during one-week experiment in September 2014. It was the first on-line mass measurement at the IGISOL-4 facility. The mass of ^{25}Al had never been measured with a Penning trap prior to this experiment. The mass-excess value in AME2012, $\Delta_{AME2012}$=-8916.2(5) keV [169], is based on Q value measurements for the proton-capture reaction ^{24}Mg$(p,\gamma)^{25}$Al [170, 171, 172]. An independent Penning-trap measurement was thus important. ^{25}Al^{+} ions were produced using 40 MeV protons on a Si target. The JYFLTRAP mass measurement used time-separated oscillatory fields technique with an excitation pattern 25 ms (On) - 150 ms (Off) - 25 ms (On) and ^{25}Mg^{+} ions as reference. The obtained mass-excess value, -8915.962(63) keV, is about 8 times more precise than the AME2012 value, -8916.2(5) keV [169]. Using the new ^{25}Al mass value together with the mass value of ^{26}Si measured previously at JYFLTRAP [173], the proton-capture Q value for ^{25}Al$(p,\gamma)^{26}$Si has been revised to: $Q_{p,\gamma}$=5513.99(13)keV. The electron-capture Q value Q_{EC} for the isosopin T=1/2 mirror nucleus ^{25}Al has also been directly determined: Q_{EC}=4276.805(0.045) keV. The Q_{EC} value is one of the parameters needed to calculate the ft value for this mirror β-decay, and is thus important for testing the Conserved Vector Current hypothesis [174, 175].

5.1.2 Resonant proton-capture rates for ^{25}Al$(p,\gamma)^{26}$Si

The new $Q_{p,\gamma}$ value has been used to compute the resonant proton-capture rates on ^{25}Al. Of the many states observed in ^{26}Si by various spectroscopic studies [176], only a few are relevant for the proton-capture reaction (see Fig. 26). The ground state spin of ^{25}Al is $5/2^{+}$, therefore according to quantum mechanical selection rules l=0 proton-captures will populate states with spins of 2^{+}, 3^{+}, l=1 states with spins of 1^{-}, 2^{-}, 3^{-}, 4^{-}, l=2 states with spins from 0^{+} to 5^{+}, ect... The

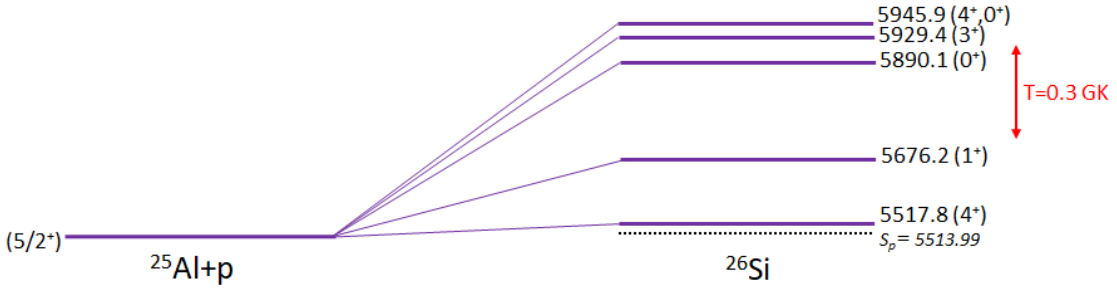

FIGURE 26 States in ^{26}Si populated by resonant proton-captures on ^{25}Al. The excitation energies are given in keV. The arrow indicates the position of the Gamow window for T=0.3 GK.

TABLE 1 Excitation and resonance energies in keV for the main states in ^{26}Si contributing to the resonant proton-capture rate in ^{26}Si. The excitation energies E_x have been taken from NDS [176]. The resonance energies $E_{res,AME12}$ have been calculated with the AME12 mass values [169], and $E_{res,JYFL}$ with the JYFLTRAP mass values determined in this work.

J^π	E_x (keV)	$E_{res,AME12}$ (keV)	$E_{res,JYFL}$ (keV)
1^+	5676.2(3)	162.4(6)	162.2(3)
0^+	5890.1(3)	376.3(6)	376.1(3)
3^+	5929.4(8)	414.9(9)	415.4(8)

dominant states above the proton threshold in ^{26}Si (S_p=5513.99(0.13) keV), are a (4^+) state at 5517.79(23) keV, a 1^+ state at 5676.2(3) keV, a 0^+ state at 5890.1(3) keV, a 3^+ state at 5929.4(8) keV and a state with a tentatively (0^+) spin-parity at 5945.9(4) keV [176]. The total resonant proton-capture rate $N_A < \sigma\nu >$ has been calculated as a sum of the resonant proton-capture rates to these states. However, the level at 5945.9 keV has been ignored due to the lack of information about its spin. The presence of the 5945.9(4) keV has been observed in two separate experiments [177, 178], but only in Matic *et al*. [178] they conclude on a 0^+ spin-parity assignment. However, the possibility of having two 0^+ states, one at 5890.1(3) keV and one at 5945.9(4) keV, instead of having a 4^+ spin for the 5945.9(4) keV state, is still an open question [179]. In addition, the contribution of the 4^+ state to the total resonant-proton capture rate at 5517.79(23) keV can be ignored due to its very low resonance energy (E_{res}=3.8 keV).
The reaction rate N_A<$\sigma\nu$> depends exponentially on the $Q_{p,\gamma}$ value through the resonance energy E_{res}=E_x-$Q_{p,\gamma}$. Thus a precise estimation of the $Q_{p,\gamma}$ value of ^{25}Al$(p,\gamma)^{26}$Si is highly relevant. Based on the new $Q_{p,\gamma}$, the resonance energy E_{res} for the 3^+, 0^+ and 1^+ states in ^{26}Si discussed above have been determined (See Table 1).

The reaction rates N_A<$\sigma\nu$> are tabulated in Table 2 and represented in Fig. 27. Below ≈0.17 GK the 1^+ state (E_{res}=161.9 keV) in ^{26}Si dominates the resonant proton-capture rate. For higher temperatures, the 3^+ state (E_{res}=414.7 keV) be-

TABLE 2 Resonant proton-captures rate $N_A<\sigma\nu>$ for the $^{25}Al(p,\gamma)^{26}Si$ reaction in $cm^3mol^{-1}s^{-1}$ units.

T(GK)	$N_A<\sigma\nu>$	T(GK)	$N_A<\sigma\nu>$
0.10	5.36×10^{-11}	0.32	1.78×10^{-2}
0.12	9.41×10^{-10}	0.34	3.94×10^{-2}
0.14	7.28×10^{-9}	0.36	7.93×10^{-2}
0.16	4.65×10^{-8}	0.38	1.48×10^{-1}
0.18	4.59×10^{-7}	0.40	2.58×10^{-1}
0.20	4.67×10^{-6}	0.42	4.25×10^{-1}
0.22	3.45×10^{-5}	0.44	6.66×10^{-1}
0.24	1.85×10^{-4}	0.46	1.00
0.26	7.61×10^{-4}	0.48	1.45
0.28	2.55×10^{-3}	0.50	2.04
0.30	7.21×10^{-3}		

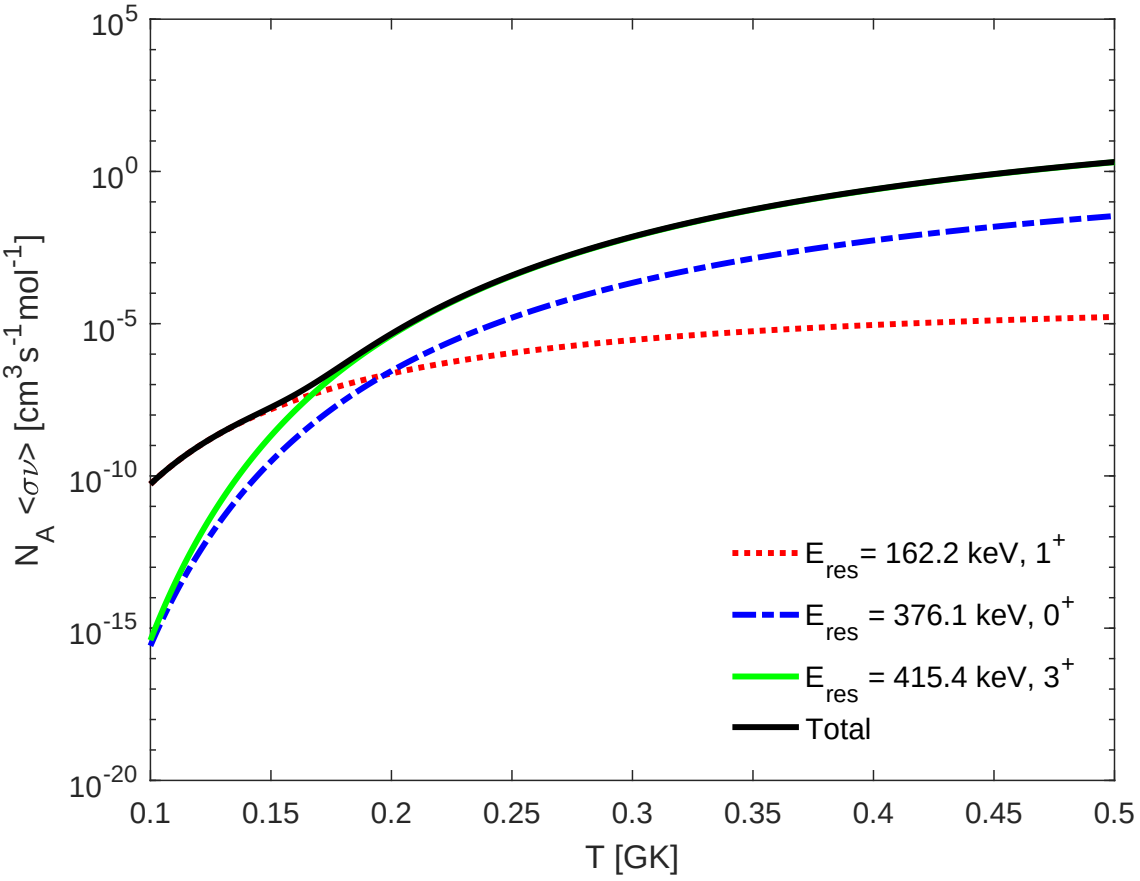

FIGURE 27 The total resonant proton-capture rates $N_A<\sigma\nu>_{res}$ and the individual resonant proton-capture rates $N_A<\sigma\nu>_{i,res}$ for the main states in ^{26}Si calculated with the $Q_{p,\gamma}$ value from this work.

comes dominant.

The reaction rate $N_A<\sigma\nu>$ obtained from our work is a few percent higher than the one computed with the AME2012 value. The uncertainty on $N_A<\sigma\nu>$

related to the Q value has been reduced by around 10–15% compared to the AME2012 value (Article I).

5.2 ^{30}P

5.2.1 Results

^{30}P was produced using 40 MeV protons on a ZnS target at IGISOL-4. It was done during the same week as the ^{25}Al mass measurement. The mass of ^{30}P was measured at JYFLTRAP via time-separated oscillatory fields technique with a 25ms (On) - 350ms (Off) - 25ms (On) excitation pattern and ^{30}Si^{+} ions as reference. The mass of ^{30}P measured at JYFLTRAP, -20200.854(64) keV, is almost five times more precise than the last published atomic mass evaluation value before the experiment, =-20200.6(3) keV [169]. The AME2012 value is based on ^{29}Si$(p,\gamma)^{30}$P [180, 181] and ^{30}Si$(p,n)^{30}$P reactions [182]. This value has been used to calculate the proton-capture Q value for the ^{30}P$(p,\gamma)^{31}$S reaction, $Q_{p,\gamma}$=6130.64(24) keV, where the mass of ^{31}S is from a JYFLTRAP experiment from 2010 [59]. The new $Q_{p,\gamma}$ value is about 1.7 more precise than the $Q_{p,\gamma}$ value from AME2012, $Q_{p,\gamma} = 6130.9(4)$ keV [169].

5.2.2 Resonant proton capture rates for ^{30}P$(p,\gamma)^{31}$S

Resonant proton-captures on ^{30}P play a key role in nova nucleosynthesis toward heavier elements as discussed in Sect. 3.2. The proton-captures on ^{30}P are dominated by resonant captures (Fig. 28). The total resonant proton-capture rate $N_A<\sigma v>_{res}$ is determined as a sum over the resonant states in ^{31}S in the relevant energy region for nova temperatures. So far, a direct measurement of the ^{30}P$(p,\gamma)^{31}$S reaction has not been possible due to too low radioactive ^{30}P beam intensities and reaction cross sections. Therefore, other reactions have been used to explore resonant states in ^{31}S including their spins and excitation energies.
Among these experiments are studies employing ^{31}P(^{3}He,t)^{31}S [183, 110, 184], ^{28}Si(^{4}He,$n\gamma\gamma$)^{31}S [185] and ^{30}P$(d,n)^{31}$S [186] reactions. A thorough evaluation on the excited states has been carried out in 2013 [187] but several studies have been performed after it. Direct information on the excited states, and also on their proton and gamma widths, have been provided via β-decay studies of ^{31}Cl [188, 189, 190]. The number of states between E_x=6390 keV and E_x=6405 keV and the spin assignments for several states have been a subject of debate [87].

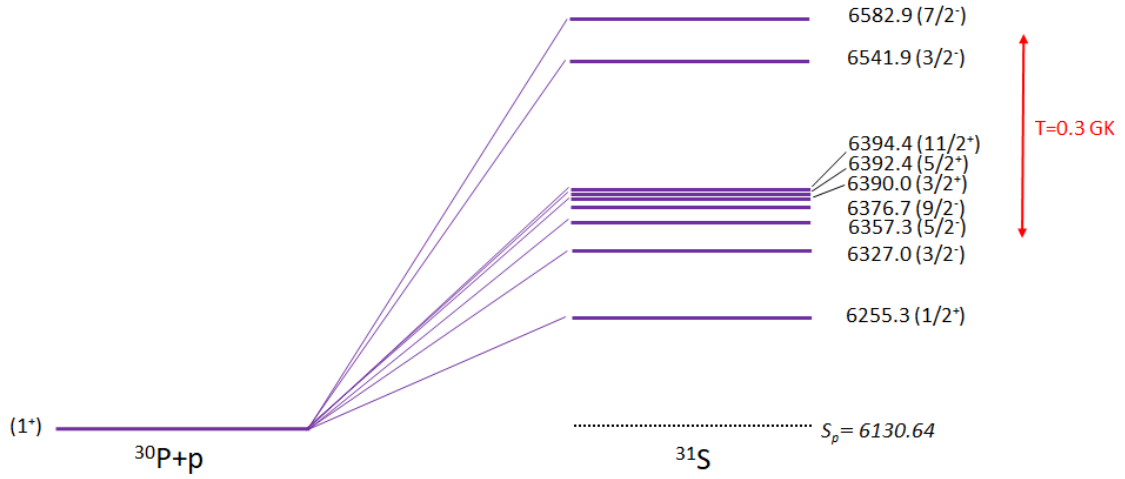

FIGURE 28 States in ^{31}S populated by resonant proton-captures on ^{30}P. The excitation energies are given in keV. The arrow indicates the position of the Gamow window for T=0.3 GK.

TABLE 3 Excitation and resonance energies in keV for the main states on ^{30}P contributing to the resonant proton-capture rate in ^{31}S. The excitation energies E_x have been taken from NDS [187] and Bennett *et al.* [190]. The resonance energies $E_{res,AME12}$ have been calculated with the AME2012 mass values [169], and $E_{res,JYFL}$ with the Q value determined in this work.

J^π	E_x (keV)	$E_{res,AME12}$ (keV)	$E_{res,JYFL}$ (keV)
$1/2^+$	6255.3(5)	124.4(11)	124.7(10)
$3/2^-$	6327.0(5)	196.1(6)	196.4(6)
$5/2^-$	6357.3(2)	226.4(5)	226.7(3)
$9/2^-$	6376.7(3)	245.8(5)	246.1(4)
$3/2^+$	6390.0(6)	259.1(7)	259.4(6)
$5/2^+$	6392.4(2)	261.5(5)	261.8(3)
$11/2^+$	6394.4(2)	263.5(5)	263.7(3)
$3/2^-$	6541.9(4)	411.0(6)	411.3(5)
$7/2^-$	6582.9(2)	452.0(20)	452.3(20)

The total resonant proton-capture rate (see Table 4) has been calculated based on the resonances to the following states in ^{31}S: $1/2^+$ (E_{res}=128.4(10) keV), $3/2^-$ (E_{res}=196.4(6) keV), $5/2^-$ (E_{res}=226.7(4) keV), $9/2^-$ (E_{res}=246.3(5) keV), $5/2^+$ (E_{res} = 261.9(3) keV), $11/2^+$ (E_{res}=263.6(3) keV), $3/2^-$ (E_{res}=411.3(5) keV), $7/2^-$ (E_{res} = 452.5(20) keV) and $9/2^-$ (E_{res}=505.5(7) keV) [187]. Additionally a $3/2^+$ state at E_{res}=259.4(6) keV was taking into account. This state is populated by l=0 proton-captures. The discovery of the $3/2^+$ state has been published by Bennett *et al.* [190] after the publication of Article I. The resonance energies have been calculated using our new value for S_p=6130.64(24) keV (Table 3) and from the excitation energies given in literature [187, 190]. The proton-captures to the $3/2^+$ state with E_R=151.4(20) keV have been ignored in the calculation because they are

H

TABLE 4 Resonant proton-captures rate $N_A<\sigma\nu>_{res}$ for the $^{30}P(p,\gamma)^{31}S$ reaction in $cm^3mol^{-1}s^{-1}$ units.

T(GK)	$N_A < \sigma\nu >$	T(GK)	$N_A < \sigma\nu >$
0.10	3.75×10^{-10}	0.32	1.13×10^{-2}
0.12	1.36×10^{-8}	0.34	2.24×10^{-2}
0.14	2.13×10^{-7}	0.36	4.20×10^{-2}
0.16	1.86×10^{-6}	0.38	7.49×10^{-2}
0.18	1.06×10^{-5}	0.40	1.27×10^{-1}
0.20	4.43×10^{-5}	0.42	2.08×10^{-1}
0.22	1.47×10^{-4}	0.44	3.25×10^{-1}
0.24	4.18×10^{-4}	0.46	4.90×10^{-1}
0.26	1.06×10^{-3}	0.48	7.15×10^{-1}
0.28	2.48×10^{-3}	0.50	1.01
0.30	5.44×10^{-3}		

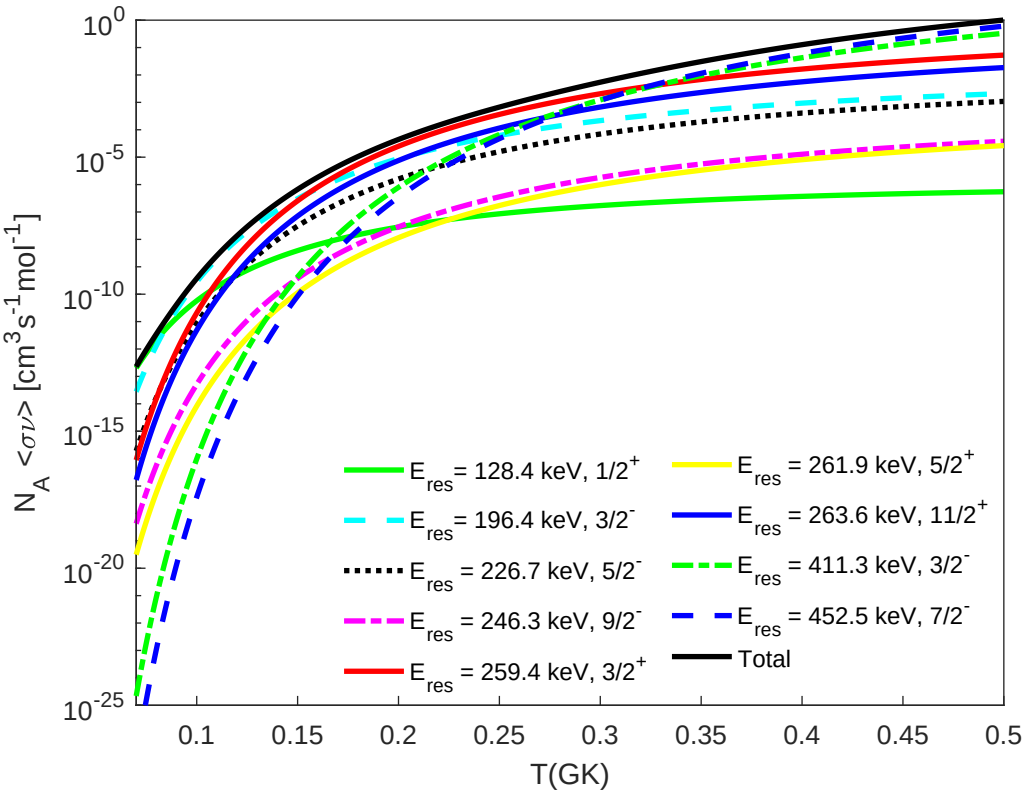

FIGURE 29 The total resonant proton-capture rates $N_A<\sigma\nu>$ and the individual resonant proton-capture rates $N_A<\sigma\nu>_i$ for the main states in ^{31}S calculated with the $Q(p,\gamma)$ value from this work.

isospin-forbidden [185]. The resonance strength parameter $\omega\gamma$ has been computed with the proton width scaled from the literature [183]. For the $3/2^-$ (E_{res}=196.4(6) keV) and $5/2^+$ (E_{res} = 261.9(3) keV) states, the resonance strengths have been taken from Ref.[186]. In this recent publication, the resonance strengths for several resonant states of ^{31}S have been experimentally constrained for the

first time. For the new $3/2^+$ state, the resonance strength is given in Ref.[190]. The individual and total resonant proton-capture rate are represented in Fig. 29. The new $3/2^+$ state dominates the resonant proton-capture for most of the peak nova temperature range (0.16 GK<T<0.32 GK), whereas the $3/2^-$ (E_R=196.4(6) keV) dominates for the lowest temperature and the $3/2^-$ (E_R=411.3(5) keV), $7/2^-$ (E_R=452.5(20) keV) states for the highest temperature.
With JYFLTRAP measurement, the mass-related uncertainty of $N_A<\sigma v>$ has been reduced by around 5–20% compared to the AME2012 value (Article I).

5.3 ^{31}Cl

5.3.1 Results

A 40-MeV proton beam on a 1.8-mg/cm^2 thick ZnS target was used to produce radioactive $^{31}Cl^+$ ions at IGISOL-4 (Article II). The TOF-ICR measurements of ^{31}Cl were done using 50 ms quadrupolar excitation in the second trap. $^{31}P^+$ ions were used as a reference. The mass-excess value in AME2012 [169], Δ=-7070(50) keV, is based on a Q value measurement for the ^{36}Ar(^{3}He,^{8}Li)^{31}Cl reaction done around 40 years ago at Michigan State University [191]. The mass-excess value obtained at JYFLTRAP, Δ=-7034.7(34) keV, is around 35 keV higher and about 15 times more precise than the AME2012 value. The proton separation energy of ^{31}Cl has been determined as S_p=264.6(34) keV using the new mass value of ^{31}Cl. This precise value has been used to test the quadratic form of the isobaric multiplet mass equation (IMME) for the T=3/2 quartet and to study the astrophysical conditions when ^{30}S can act as a waiting point in the rp-process.

5.3.2 Isobaric Multiplet Mass Equation for the T=3/2 quartet at A=31

The nuclei ^{31}Cl, ^{31}S, ^{31}P and ^{31}Si form a T=3/2, $3/2^+$ isospin quartet with the isospin projection T_z equal to -3/2, -1/2, +1/2, +3/2, respectively. The IMME has been computed using the mass values from AME2012 except for ^{31}Cl for which the value from the JYFLTRAP measurement was used. The mass value for ^{31}S in AME2012 is from JYFLTRAP, Δ(^{31}S)=-19042.52(23) keV [59]. The mass of ^{31}P is based on a Penning trap measurement at Florida State University, Δ(^{31}P)=-24440.5411(7) keV [192]. For ^{31}Si, the mass has been determined from a Penning trap measurement of ^{29}Si done at the Massachusetts Institute of Technology [193] and well-known (n,γ) energies [194, 195, 196, 197], resulting a mass-excess value of Δ(^{31}Si)=$-$22949.04(4) keV. The lowest T=3/2, $3/2^+$ state is at E_x=6280.60(16) keV in ^{31}S [187] and at E_x=6380.8(17) keV in ^{31}P [198].

The coefficients of the quadratic IMME fit are a= -15465.4(26), b= -5302.7(32) and c= 209.1(32) as given in Article II. Therefore, the quadratic IMME breaks down at A=31. The reduced chi-square value is χ^2_n=11.6 when it was χ^2_n=0.08 using the AME12 mass value for ^{31}Cl . Also, a cubic fit on the quartet leads to a

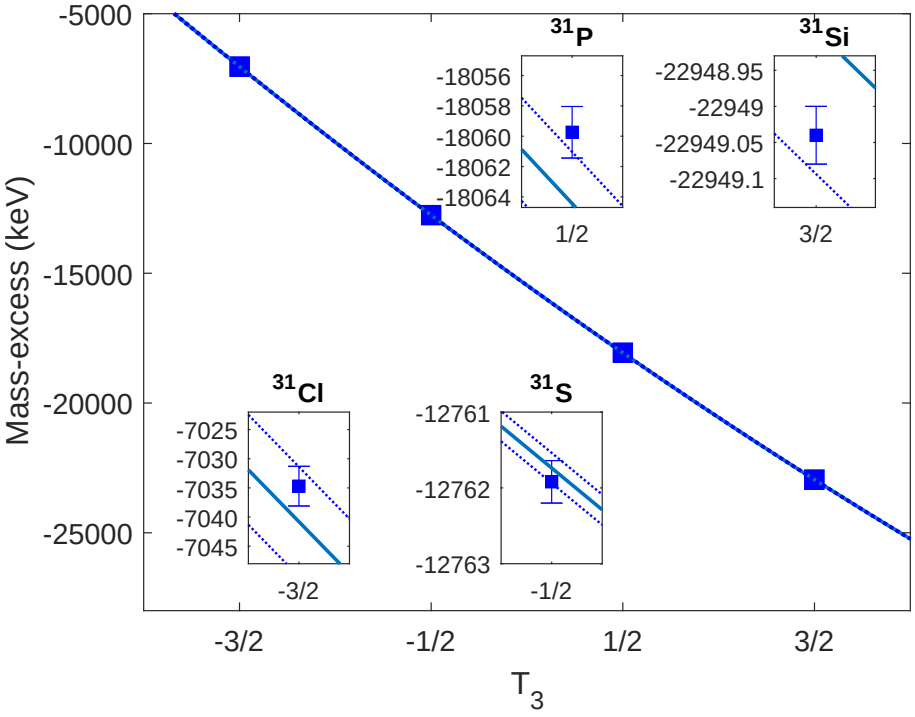

FIGURE 30 Quadratic IMME fit of the T=3/2 isospin quartet at mass A=31 (solid line) and its uncertainty (dashed lines).

non-zero cubic coefficient d=-3.5(11) keV. The quadratic IMME fit on the ^{31}Cl, ^{31}S, ^{31}P and ^{31}Si masses is shown in Fig. 30. The reason for the breakdown is not yet fully understood. One plausible explanation is a possible isospin mixing with the $3/2^+$, T=1/2 state [190].

5.3.3 ^{30}S as a waiting point in type I X-ray bursts

A precise value of the proton separation energy in ^{31}Cl is needed to determine the waiting-point conditions for ^{30}S during the rp-process in type I X-ray bursts. The new value S_p=264.6(34) keV is about 15 times more precise than the AME12 value, S_p=296(50) keV [169]. Using the β-delayed proton data of ^{31}Ar with energies 446(15) and 1415(5) keV in the laboratory frame [199], the excitation energies for the two lowest excited states in ^{31}Cl were determined as 726(16) keV for the $1/2^+$ state and 1728(4) keV for the $5/2^+$ state. These excitation energies have been previously estimated based on mass value for ^{31}Cl determined with the IMME [108]. The estimation was 745(17) keV and 1746(9) keV for the $1/2^+$ and $5/2^+$ states, respectively. The excitation energies have been determined also at GSI via Coulomb breakup of ^{31}Cl using R3B-LAND setup [200] . They obtained 782(32) keV and 1793(26) keV for the $1/2^+$ and $5/2^+$ states, respectively. The results from JYFLTRAP, using the proton energies from [199], are lower but the first excited state is in good agreement with the value given by USDB shell-model calculation (724 keV [200]).

Based on the proton energies from Refs.[199] and [201] and by using the S_p value from this work together with the excitation energy E_x from Ref. [200], the reso-

nance energies E_r=472(14) keV for the $1/2^+$ state and 1464(2) keV for the $5/2^+$ state were obtained as a weighted mean. With the resonant energies, the ratio of the photodisintegration of ^{31}Cl, $\lambda_{\gamma,p}$, to the proton-capture on ^{30}S, $\lambda_{p,\gamma}$, was computed for typical type I XRB conditions. ^{30}S becomes a waiting point for T>0.44(1) GK in type I XRBs (Article II). The unmeasured ^{30}S$(\alpha, p)^{33}$Cl reaction constrains the upper-temperature limit for the ^{30}S waiting point to 1.0(3) GK [110].

5.4 Mass measurements of neutron-rich nuclei close to N=40

Neutron-rich nuclei in the vicinity of ^{78}Ni have been studied in a successful experiment at JYFLTRAP. Altogether masses for 12 nuclides were determined, of which the masses for ^{69}Co^m, ^{70}Co, ^{74,75}Ni were determined for the first time. This PhD thesis focuses on the masses of ^{67}Fe and ^{69,70}Co. The other studied nuclides will be discussed in separate publications.
The neutron-rich isotopes were produced via proton-induced fission on uranium target using 35 MeV protons from K130 cyclotron. For each studied nuclide, ^{84}Kr (Δ_{AME16}=-82439.335(4) keV [6]) was used a reference.
The studied nuclides, ^{67}Fe and ^{69,70}Co have long-living isomeric states. The isomers in ^{69}Co and ^{70}Co have a long enough half-life (see Table. 5) to be detected by a Penning trap. However, only one state has been observed in previous mass measurement studies on these nuclides. ^{67}Fe has two isomeric states but with half-lives too short to be detected by the JYFLTRAP Penning trap. The measured value thus corresponds to the ground state of ^{67}Fe.

TABLE 5 The known states in ^{67}Fe, ^{69}Co and ^{70}Co, their suggested spins and parities, half-lives, and excitation energies based on the NUBASE2016 evaluation [68].

Nuclide	J^π	$t_{1/2}$	E_x (keV)
^{67}Fe	$(1/2^-)$	394(9) ms	
^{67}Fe^m	$(5/2^+,7/2^+)$	64(17) μs	402(9)
^{67}Fe^n	$(9/2^+)$	75(21) μs	450(100)#
^{69}Co	$7/2^-$#	180(20) ms	
^{69}Co^m	$1/2^-$#	750(250) ms	500(200)#
^{70}Co	$(6^-,7^-)$	112(7) ms	
^{70}Co^m	3^+#	470(50) ms	200(200)#

5.4.1 ^{67}Fe

The mass of ^{67}Fe was measured for the first time at the Los Alamos Neutron Science Center (LANSCE) using the Time-of-Flight Isochronous (TOFI) spectrometer [202, 203], Δ_{LANSCE}=-46600(500)keV. A few years later, it was followed by an experiment using isochronous mas spectrometry in the ESR storage ring at GSI [204].

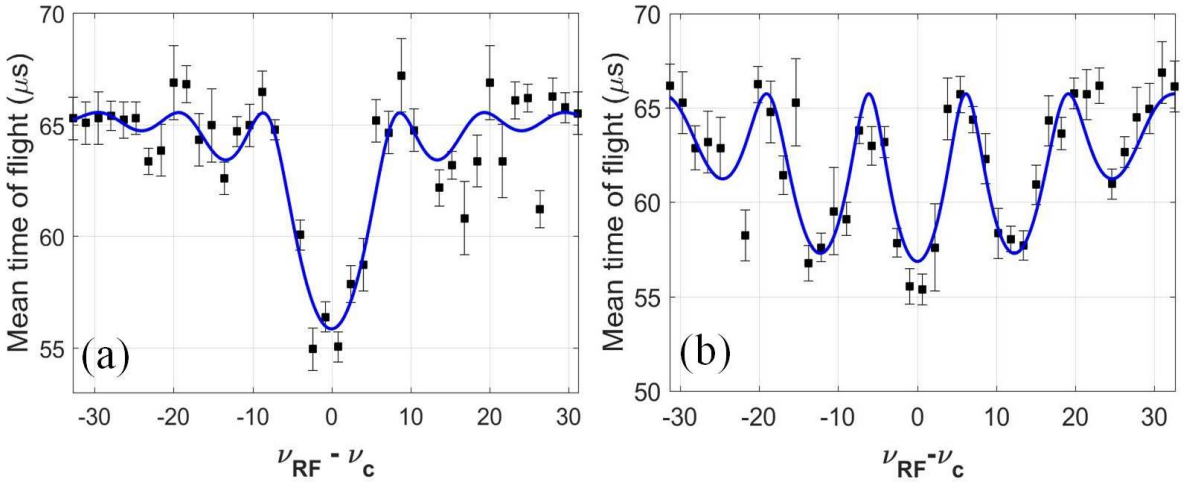

FIGURE 31 TOF-ICR spectra for the $^{67}Fe^{+}$ obtained with 100 ms quadrupolar excitation (a) and with 25 ms-50 ms-25 ms (On-Off-On) Ramsey pattern (b).

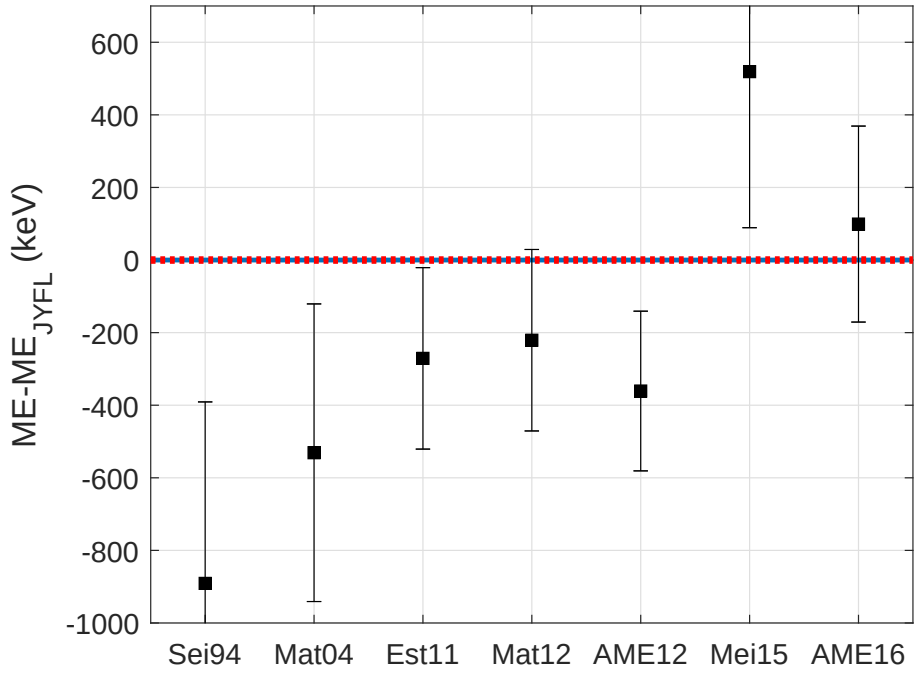

FIGURE 32 Mass-excess values for ^{67}Fe from Seifert *et al*. (Sei94) [202], PhD thesis of Matos (Mat04) [204], Estradé *et al*. (Est11) [205], Matos *et al*. (Mat12) [206], AME2012 [169], PhD thesis of Meisel (Mei15) [207] and AME2016 [6] compared to the mass excess value determined at JYFLTRAP (blue line) with its uncertainty (red dotted line).

More recently, measurements have been performed at the National Superconducting Cyclotron Laboratory (NSCL) at the Michigan State University in USA where fragmentation of ^{86}Kr beam on a Be target has been used to produce neutron-rich isotopes and the masses were determined using the Bρ-TOF technique [205, 206, 207]. The resulting mass-excess value, Δ_{NSCL}=-45980(250) keV,

is more than 600 keV higher than the LANSCE value but both have high uncertainties.
At JYFLTRAP, ^{67}Fe was measured using both normal TOF-ICR with 100 ms quadrupolar excitation and with the Ramsey's method of time-separated oscillatory fields with an excitation pattern 25 ms (On) - 50 ms (Off) - 25 ms (On) (see Fig. 31). The obtained mass-excess value using normal TOF-ICR is Δ=-45709.3(90) keV and with the Ramsey's method Δ=-45709.1(38)keV. It is about 70 times more precise than the value given in AME16 (Δ_{AME16}= -45610(270)keV). A comparison to the literature values is represented in Fig. 32.

5.4.2 ^{69}Co

Similarly to ^{67}Fe, the first mass measurement on ^{69}Co was done at LANSCE [202, 203], followed by a measurement using the Bρ-TOF technique at NSCL [205] and via isochronous mass spectrometry [208]. In AME2016 [6], the ground state mass value for ^{69}Co is $\Delta_{AME2016}$=-50280(140) keV. Recently, a precise measurement of ^{69}Co, produced via fragmentation of ^{76}Ge beam on a Be target, has been performed with the LEBIT Penning trap at NSCL [209]. They assigned the measurement to the shorter-lived $(7/2)^-$ state, expected to be the ground state. However, they could not rule out that the measured state was the longer-living $1/2^-$ isomer [210].

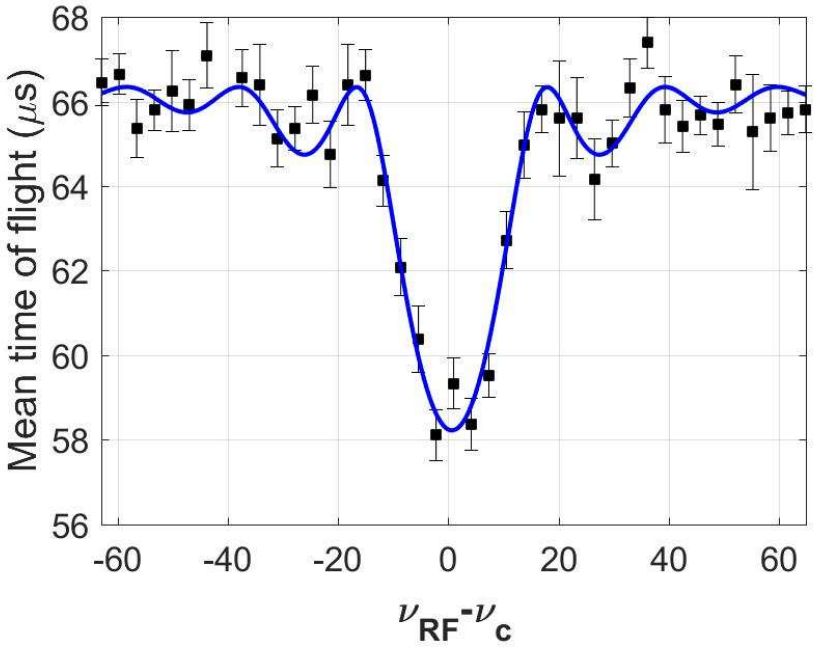

FIGURE 33 TOF-ICR spectrum of ^{69}Co with 50 ms of quadrupolar excitation. The spectrum was collected without additional waiting time in the cooler.

The excitation energy for the isomeric state is estimated to be 500(200)# keV [68]. The proximity of the states did not allow to separate them and fit the two

TABLE 6 Fractions for the ground and isomeric state in ^{69}Co states ratios when the beam gate is closed (t_{bg}), after the shorter trap cycle (t_{short}=226 ms) and after the longer trap cyle (t_{long}=726 ms).

	$f^{gs}(t_{1/2} = 180(20)ms)$	$f^{m}(t_{1/2} = 750(250)ms)$
t_{bg}	67(10)%	33(10)%
t_{short}	51(13)%	49(13)%
t_{long}	19(9)%	81(9)%

states directly on the collected TOF-ICR spectra (see Fig. 33). Since the high-spin ground state has a much shorter half-life , $t_{1/2}$=180(20) ms, compared to the isomer with $t_{1/2}$=750(250) ms [68] , the ratio of the studied states was manipulated by keeping the ions for an additional 500 ms in the cooler after the production of ions was stopped, i.e. after the beamgate was closed. During this time, most of the ions belonging to the shorter-lived state decayed away. Therefore, the measured state had more longer-living state present. In the dataset with a shorter trap measurement cycle, it took only 226 ms for the ions to arrive on the MCP after the production of the ions was stopped (beamgate closed). In the second dataset, the extraction from the RFQ was delayed by 500 ms after the beamgate was closed, and hence the trap cycle after the beamgate closure was 726 ms in total. The yield ratio between the measurements done with short and long trap cycles is:

$$R = \frac{N_{short}}{N_{long}} \tag{81}$$

where N_{short} and N_{long} are the average number of ions detected per one trap cycle, which was 226 ms for N_{short} and 726 ms for N_{long}. The ions were accumulated for the same time, 66 ms, in the cooler in both cases and therefore the differences are due to radioactive decays of the ions. By denoting the number of ions in the ground state and isomeric state at the time the production stops (beamgate is closed) as N_1 and N_2, respectively, we have then:

$$\begin{aligned} N_{short} &= N_1 e^{-\lambda_1 t_{short}} + N_2 e^{-\lambda_2 t_{short}} \\ N_{long} &= N_1 e^{-\lambda_1 t_{long}} + N_2 e^{-\lambda_2 t_{long}} \end{aligned} \tag{82}$$

where λ_1 and λ_2 are the decay constants for the ground state and isomeric state of ^{69}Co, respectively. The fraction of both states when the production stops or in other words when the beam gate was closed is obtained via:

$$\alpha = \frac{N_2}{N_1} = \frac{e^{-\lambda_1 t_{short}} - Re^{-\lambda_1 t_{long}}}{Re^{-\lambda_2 t_{long}} - e^{-\lambda_2 t_{short}}} \tag{83}$$

With the shorter trap cycle, there is about 50%-50% of ground state and isomeric state. With the long cycle, the resonance is dominated by the longer-living isomeric state. The isomer fraction at the time when the beam gate was closed (t_{bg}), and after t_{short} or t_{long} have been calculated and are presented in Table 6.

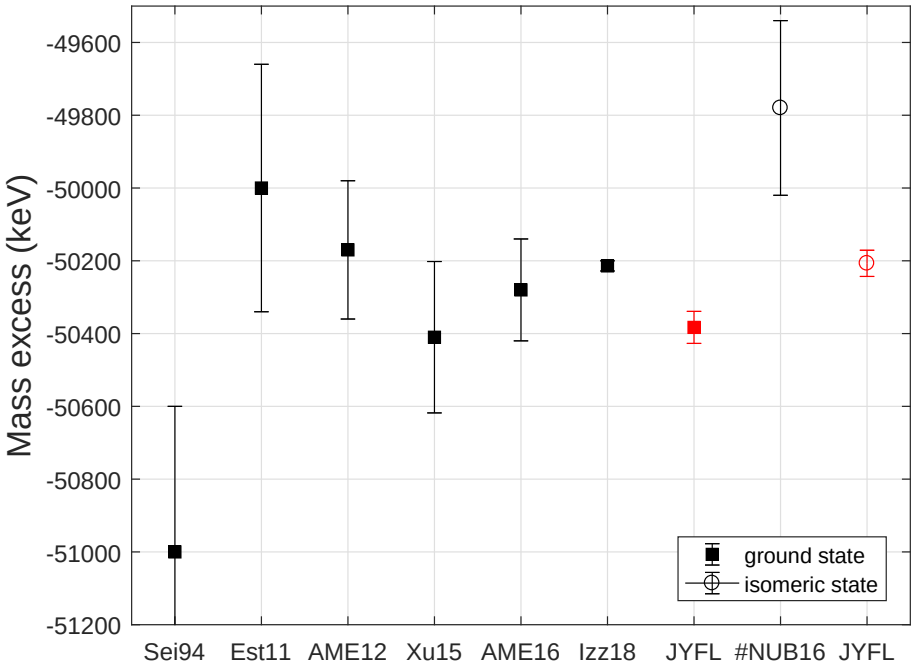

FIGURE 34 Mass excess value of ^{69}Co measured at JYFLTRAP (red points) compared to Seifert *et al*. (Sei94) [202], Estradé *et al*. (Est11) [205], AME 2012 [169], Xu *et al*. (Xu15) [208], Izzo *et al*. (Izz18) [209], AME 2016 [6] and NUBASE 2016 (#NUB16) [68] mass value.

We recovered then the masses for both states knowing that the measured mass-excess values for the short and long trap cycles were Δ_{short}=-50296(15)keV and Δ_{long}=-50238(20)keV respectively, as [28]:

$$\begin{aligned} \Delta_{long} &= f^{gs}_{long}\Delta_{gs} + f^{m}_{long}\Delta_{m} \\ \Delta_{short} &= f^{gs}_{short}\Delta_{gs} + f^{m}_{short}\Delta_{m} \end{aligned} \tag{84}$$

where f^{gs}_{short}, f^{m}_{short}, f^{gs}_{long}, f^{m}_{long} are the ground-state (gs) and isomeric state (m) fractions at the end of the short and long trap cycles, respectively (see Table 6).

To estimate the uncertainties of the mass-excess values, we calculated Δ_{gs} and Δ_{m} using the min-max method: the minimum and maximum of Δ_{long}, Δ_{short}, and the fractions r for the ground state and isomeric state were used to deduce the uncertainties.
The mass-excess values obtained for the ground state and isomeric state using this method were $\Delta(^{69}Co^{gs})$= -50383(44) keV and $\Delta(^{69}Co^{m})$= -50207(36) keV, respectively. For the first time, the mass-excess values for both states were determined. Our values are compared to the literature values in Fig. 34. For the ground state, we are in agreement with Xu *et al*. [208] and AME2016 [6]. Our mass value for the isomeric state is less than the extrapolated value from NUBASE2016 [68] but in very good agreement with the mass value published by Izzo *et al*. [209].

5.4.3 ^{70}Co

The presence of a long-living isomeric state in ^{70}Co was observed already in a β-decay study on ^{70}Co employing laser-ionization isotope-separation on-line method at Louvain-la-Neuve [211]. They assigned a high-spin (6^-,7^-) for the shorter-living state and a low-spin state (3^+) for the longer-living state. The experiment used the same production method as in this work at IGISOL-4, namely proton induced fission on ^{238}U target. At Louvain-la-Neuve, they measured that the yield for the longer-living ($t_{1/2}$= 470(50) ms [68]) low-spin state was double the yield for the shorter-living ($t_{1/2}$= 112(7) ms [68]) high-spin state. Several measurements on ^{70}Co have been performed using fragmentation reaction of ^{86}Kr beam on a Be or Ta target at NSCL [205, 212, 213, 214]. In these studies, usually only the shorter-living high-spin state has been reported. The mass of the ground-state of ^{70}Co is extrapolated in AME2016 [6]. Both the high-spin and low-spin state can be either the ground state or the isomeric state as indicated in the NUBASE2016 evaluation [68]. Estradé *et al*. report a value for the shorter-living state $\Delta(^{70}Co^{h.s.})$= -46820(280) keV but without giving details of how they deduced the measured state [205].

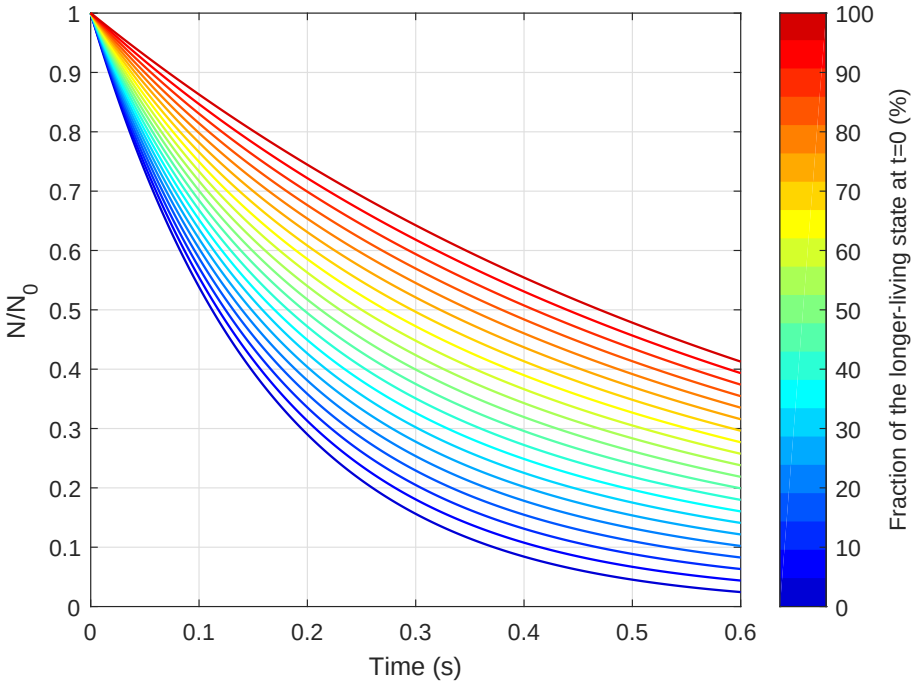

FIGURE 35 Expected evolution of the number of ^{70}Co$^+$ ions N plotted using different values for the fraction of the longer-living state at time t=0 when the beam-gate is closed (see the scale on the right). The total number of ions at t=0 is N_0.

At JYFLTRAP, we measured ^{70}Co with the TOF-ICR technique (see Fig. 36) following the same procedure as for ^{69}Co. In the first set of measurements, there

was no waiting time in the RFQ after the closure of the beam gate. A trap cycle of 282 ms was employed for the first measurement and 232 ms for the following ones without any waiting time in the RFQ after the closure of the beam gate. In the second set of measurements, the ions had to wait 232 ms before being extracted to the trap and therefore the total trap cycle length after the beamgate closure was 513 ms (281+232 ms). No significant difference in the yield was seen between the shorter and longer trap cycles. The primary beam intensity also fluctuated a lot, and was substantially lower for some parts of the shorter-cycle files making the yield measurements somewhat unrealiable. Hence, we did not use the same method as for ^{69}Co to deduce the mass-excess values for ^{70}Co.
In an ideal case, we should obtain a clear decrease of the yield of at least 34(3)% between the short and the long trap cycle if we only observed the longer-living state (Fig. 35). Due to fluctuations in the primary beam intensity, it was difficult to obtain a reliable number for the yield ratio. For some of the shorter-cycle files, the intensity had dropped into half of what it used to be, therefore reducing the number of detected ions and bringing it closer to the values obtained with the longer cycle and higher beam intensity.

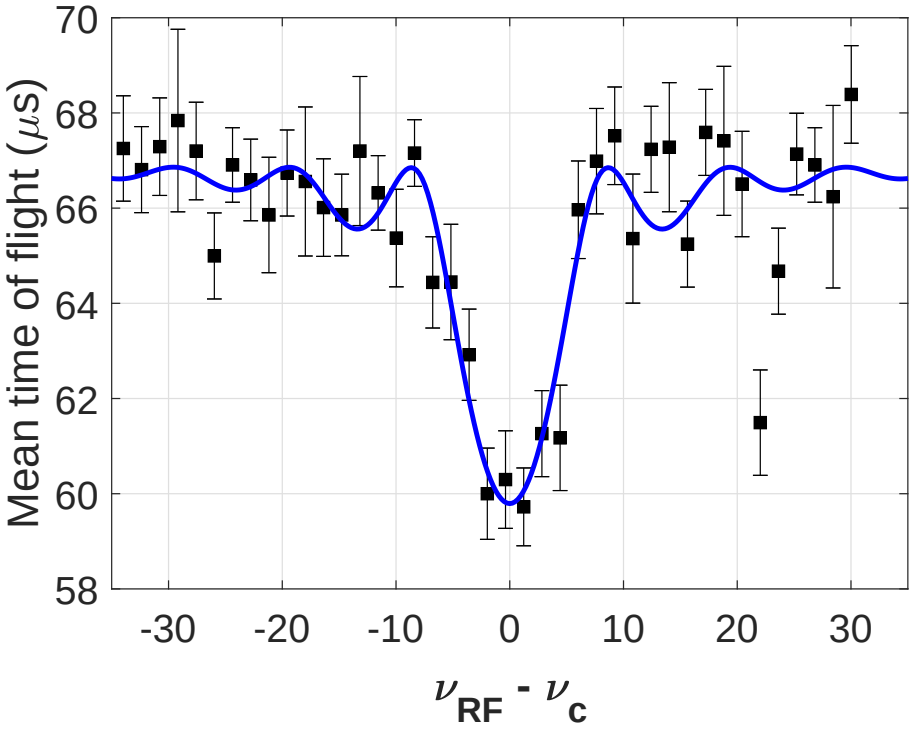

FIGURE 36 A TOF-ICR spectrum for ^{70}Co collected with a 513 ms cycle and using 100 ms quadrupolar excitation in the precision trap. The trap cycle after the beamgate closure lasted 513 ms.

We also made two PI-ICR scans of ^{70}Co with 356.0 ms and 356.3 ms trap cycles after the beamgate closure, both with 50 ms production and without any additional waiting after beamgate closure in the cooler (Fig. 37). Both spectra show the projection of the reduced cyclotron motion converted into magnetron motion via a quadrupolar excitation after 100 ms accumulation time. In the measurement

with 356.3 ms trap cycle, the extraction happened 0.3 ms after the quadrupolar excitation stopped and thus the ions accumulate magnetron motion for 0.3 ms which is approximately half of a typical magnetron period in the trap. In both spectra, a clear blob of ions is visible but there are also some background ions. The statistics is rather low, the total number of ions is 91 for the first spectrum and 87 for the second, with 61 and 56 ions in the dominant ion blob, respectively. Since there is only one state clearly visible, we estimated an upper limit for the possible contribution from the other state. This was done by setting a window at about the same distance from the origin (see Fig. 37). This yielded an upper limit of 7 and 10 ions for the first and the second spectrum, respectively. Considering these values and the durations of the used trap cycles, we can estimate that at least 95% of the measured ions belong to the longer-living state for the TOF-ICR measurements with long trap cycle. For the TOF-ICR measurements with shorter trap cycle, around 83% of the ions should belong to the dominant, longer-living state. Finally the PI-ICR spectra confirm we measured only or dominantly one state. Since the yields did not change with an increase in the trap cycle length, it is most probably the longer-living low-spin state in ^{70}Co. This result is in agreement with the previous proton induced fission experiment where the low spin state was dominating [211, 215].
To be more safe, we used only the TOF-ICR data measured with the long 513 ms cycle where which should be at least 95% of the ions belong to the longer-living state. The obtained mass-excess value is $\Delta(^{70}Co^{l.s.})$= -46525(11) keV.

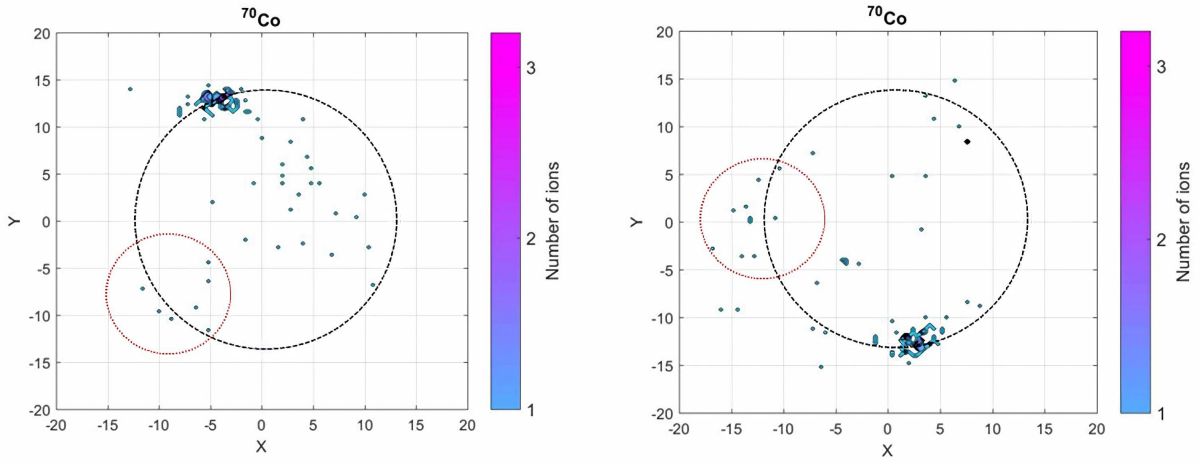

FIGURE 37 PI-ICR spectra of ^{70}Co collected with 356.0 ms and 356.3 ms phase accumulation times, respectively. In the figure on the right, the ions have been extracted 0.3 ms after the conversion (a half of the magnetron phase, i.e. 180°). The dotted black line show the motion orbit and the red dotted line highlight the area on the orbit where the number of ion is maximum beside the main state visible.

The new mass-excess value for ^{70}Co is compared with previously published or extrapolated mass-excess values on Fig. 38. The extrapolated values given in NUBASE2012 [216] and 2016 [68] are expected to be for the isomeric state of ^{70}Co

but the state assignment is uncertain. The mass-excess value for the longer-lived low-spin state of ^{70}Co measured in Jyväskylä is in accordance with the values given in the literature.

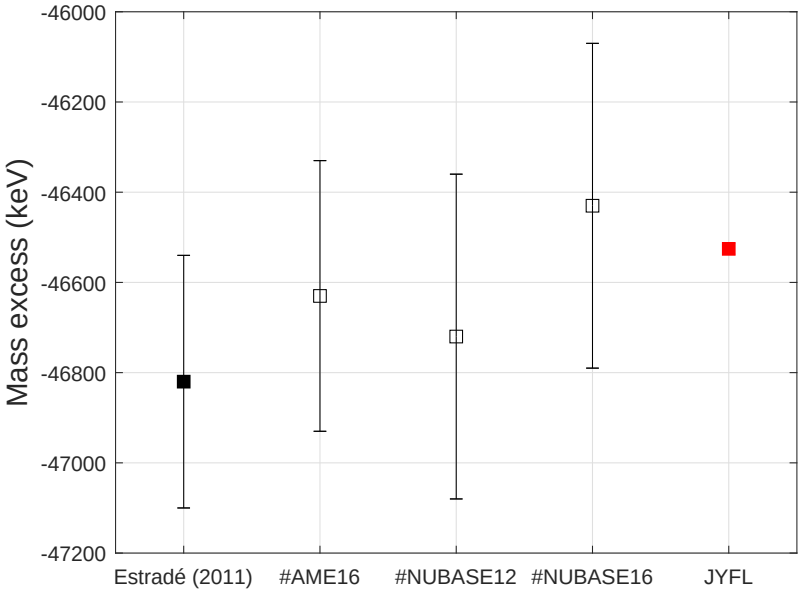

FIGUR 38 Mass excess value of ^{70}Co measured at JYFLTRAP (red square) compared to Estradé *et al.* [205], AME2016 [6], NUBASE 2012 [43] and NUBASE 2016 [68]. The empty symbols indicate extrapolated values.

5.4.4 N=40 subshell gap

The magic nucleon numbers of the shell closures can change for nuclei far from stability. The magicity can disappear as for the $N = 20$ shell closure in ^{32}Mg [217] or magic features can appear, for example for the $N = 40$ subshell closure in ^{68}Ni [218, 219]. For lighter $N = 40$ and therefore more exotic isotones, deformation of the ground state seems to appear quickly [220]. The lack of experimental data in this region make it difficult to conclude on the evolution of the $N = 40$ subshell closure. With 26 protons and 41 neutrons, ^{67}Fe provides information how the binding energies evolve beyond the N=40 subshell closure. A spectroscopic study of the isomeric states in ^{67}Fe has shown that it is a deformed nucleus [221]. The neutron-rich ^{69}Co and ^{70}Co isotopes are important for the evolution of the N=40 neutron subshell gap at Z=27, one proton away from the nickel isotopes. For both nuclei, the order of their ground state and isomeric state is still uncertain. In ^{69}Co, the shorter-living state has been defined as a $7/2^-$ state based on systematics of the other odd-A Co isotopes and on the observed β-decay to a $(5/2^-)$ state in ^{69}Ni [212]. The longer-living state in ^{69}Co was assigned with a spin and parity $1/2^-$ similarly to ^{67}Co and ^{65}Co in which a $1/2^-$ intruder state has been observed [222, 223].

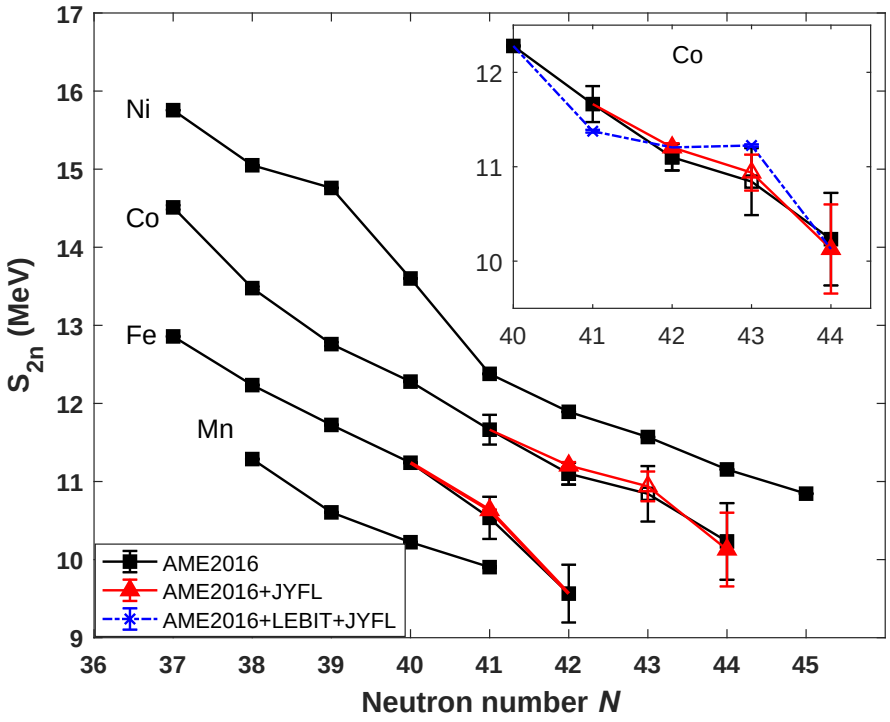

FIGURE 39 Two-neutron separation energies (S_{2n}) as a function of the neutron number N. The values calculated using our results are plotted in red. The recently published mass value of ^{68}Co at LEBIT [209] is used to calculate the S_{2n} represented in blue in the inset. The value taken from AME2016 [6] (in black) are based on experiments except at N=43.

Previously, the ground state of ^{70}Co has been assigned as the shorter-living high-spin (6^-,7^-) state whereas the isomer has been predicted to be the longer-living state with a low-spin (3^+) [211, 221, 224, 225, 213, 214]. The primary single-particle configurations suggested for the high-spin (assumed to be the ground state) is $\pi\ f_{7/2}^{-1}\ \nu\ g_{9/2}^{+3}$ and $\pi\ f_{7/2}^{-1}\ \nu\ p_{1/2}^{-1} g_{9/2}^{+4}$ for the low-spin state, assumed to be the isomer [211]. However, based on recent β-decay study of ^{70}Fe performed at RIKEN in Japan accompanied with Monte Carlo shell-model calculations, the ground state of ^{70}Co has been assigned as the longer-living low spin state with spin and parity (1^+,2^+) [215].
Using our results for ^{67}Fe and ^{69,70}Co, we calculated the two-neutron separation energy, defined in Eq. (12).

If we consider the measured, longer-living state of ^{70}Co as the ground state, the trend in the S_{2n} values is smoother at N=43 (see Fig. 39). We plotted S_{2n} values both with and without the recent mass value of ^{68}Co measured at LEBIT [209]. The result from LEBIT introduces a kink in the slope, suggesting a possible measurement of a dominant isomeric state instead of a pure ground state [210].

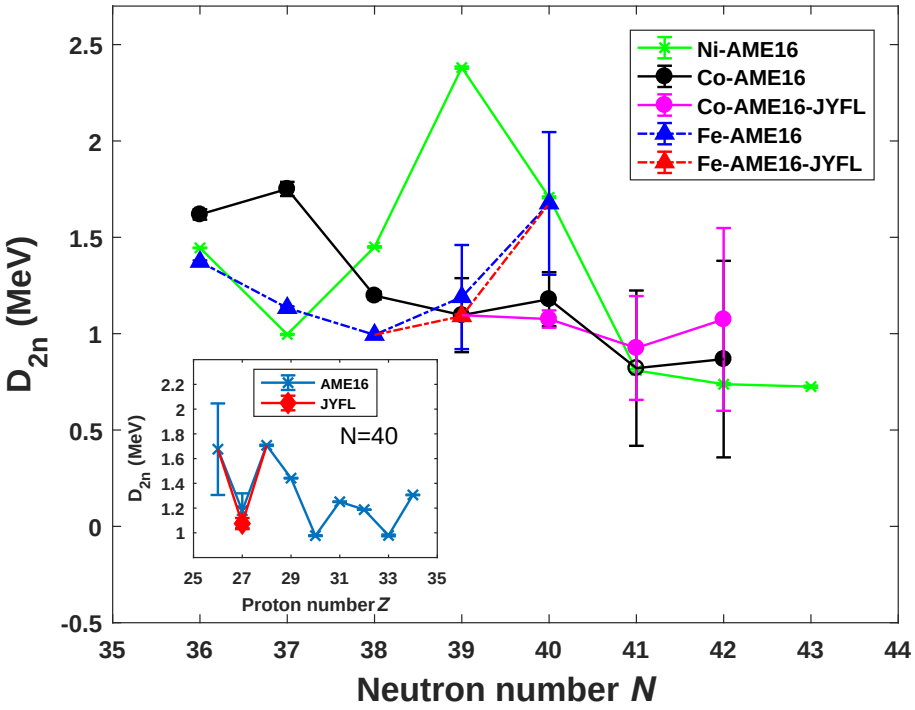

FIGURE 40 Two-neutron shell gap parameter D_{2n} as a function of neutron number N. The values based on our work are plotted in red for Co and in magenta for Fe. The inset gives D_{2n} as a function to the proton number Z for N=40 isotones.

Figure 40 shows the empirical two-neutron shell gap parameter D_{2n} determined as:

$$D_{2n}(N,Z) = S_{2n}(N,Z) - S_{2n}(N+2,Z) \tag{85}$$

Due to the uncertainty in the measured state, the results from LEBIT were excluded. The two-neutron shell gap energy is slightly lower when using our mass value for the ^{69}Co ground state. The D_{2n} values seems to confirm a decrease of the N=40 subshell closure from Z=28 to Z=27. Figure 41 shows the evolution of the N=40 shell gap deduced from various theoretical models (FRDM12 [36], HFB-24 [27], SLy4 [19], UNEDF1 [23], Duflo-Zuker [44], WS4 [43]), experimental data from AME2016 [6] and our mass measurement of ^{69}Co. The theoretical models diverge a lot from each other and from the experimental values. It is thus important to constrain the models with experimental data.
Our result for ^{69}Co seems to confirm the reduction of the N=40 subshell gap at Z=27, below the Z=28 magic number. However, one has to be careful when discussing about shell closure based on mass measurements. Collective effects as shape coexistence can be hidden in two-neutron separation energies trend [226]. The uncertainty at Z=26 comes from the ^{68}Fe mass value from AME2016 Δ=-43490(370) keV [6] that has been experimentally determined [203, 205, 207].

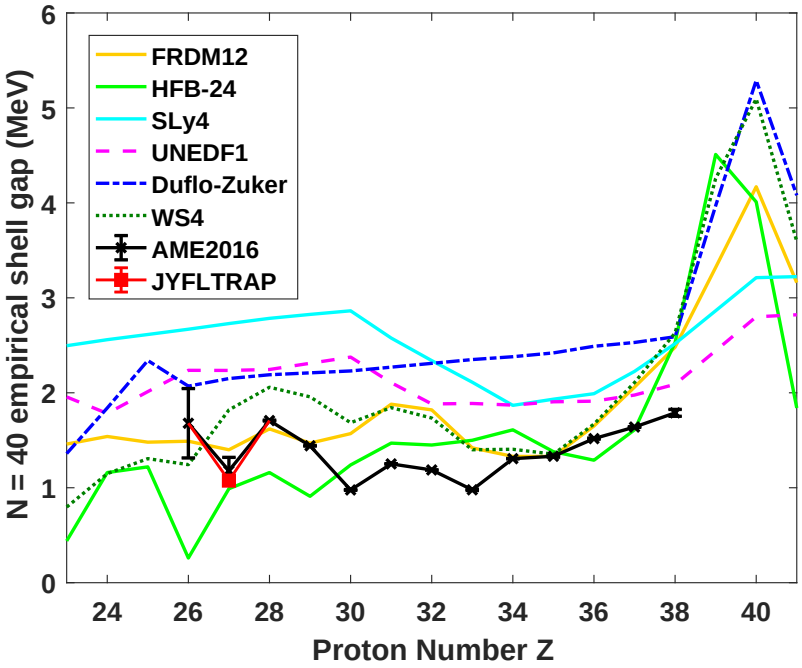

FIGURE 41 Two-neutron shell gap parameter D_{2n} for N=40 subshell closure as a function to the number of proton Z, for experimental data from AME2016 [6] and theoretical models. The mass-excess value of the longer-living state in ^{69}Co obtained in this work has been used to obtain $D_{2n}(N = 40)$ at Z=27 (in red).

5.4.5 Neutron capture rates for the *r*-process

Sensitive studies [116] have shown that the ^{67}Fe$(n,\gamma)^{68}$Fe and ^{68}Co$(n,\gamma)^{69}$Co neutron captures are relevant for the weak *r*-process and its abundance pattern (see Sect. 3.5). The neutron capture rates computed with the Hauser-Feshbach code Talys 1.8 [227, 228] and Q values based on AME2016 and JYFLTRAP mass values are plotted in Figs. 42 and 43. For theoretical neutron capture rate calculations, three parameters are the most sensitive: the neutron-nucleus optical model potential (nOMP), the nuclear level density (NLD) and the γ-ray strength function (γSF) [112]. Two choices are offered in Talys 1.8 for the optical model, six for the NLD and eigth for the electric dipole component ($E1$) of the γSF. For neutron-rich nuclei far away from the valley of stability the microscopic approaches in each parameter are predicted to be the most reliable [112, 229]. Three NLD models (input keywords *ldmodel* 4, 5 and 6) and two γSF models (*strength* 3 and 4) have a microscopic approach. The nOMP seems to be less sensitive than the NLD and the γSF [230]. In this work, the semi-microscopic optical potential of the Jeukenne-Lejeune-Mahaux (*jlmomp y*) was used instead of the phenomenological model. The NLD and γSF have been experimentally constrained and compared to Talys models for neutron capture reaction on ^{68}Ni and ^{69}Ni [231, 230]. In both studies, the microscopic level densities (temperature dependent HFB, Gogny force) from Hilaire's combinatorial tables model (*ldmodel* 6) were excluded due to strong odd-even effects. Within the γSF models, the Brink-Axel single Lorentzian model (*strength* 2) was not considered due to inconsistency with experimental data at

lower γ-ray energies [231].

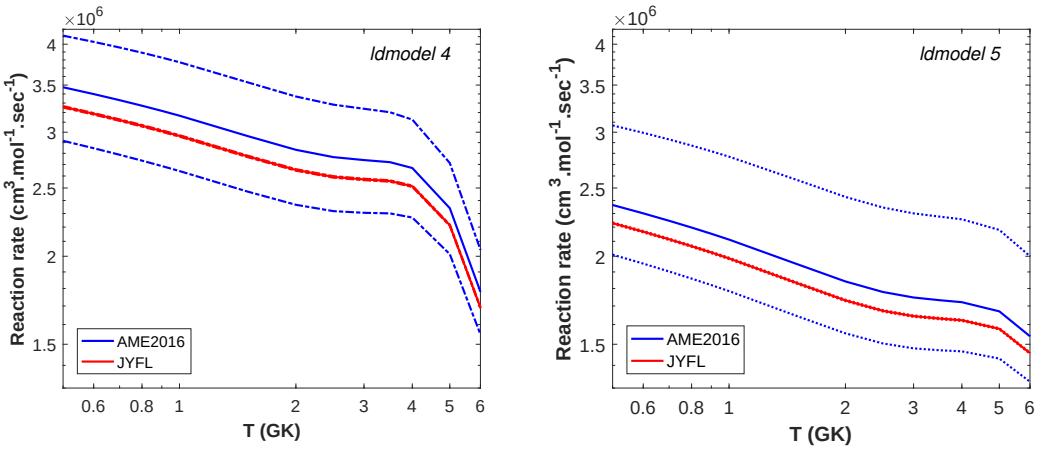

FIGURE 42 Neutron-capture rate on ^{67}Fe calculated with Talys using the ^{67}Fe mass value from AME2016 [6] and from our work. The rate has been computed using *ldmodel* 4 and *ldmodel* 5 as a nuclear level density model.

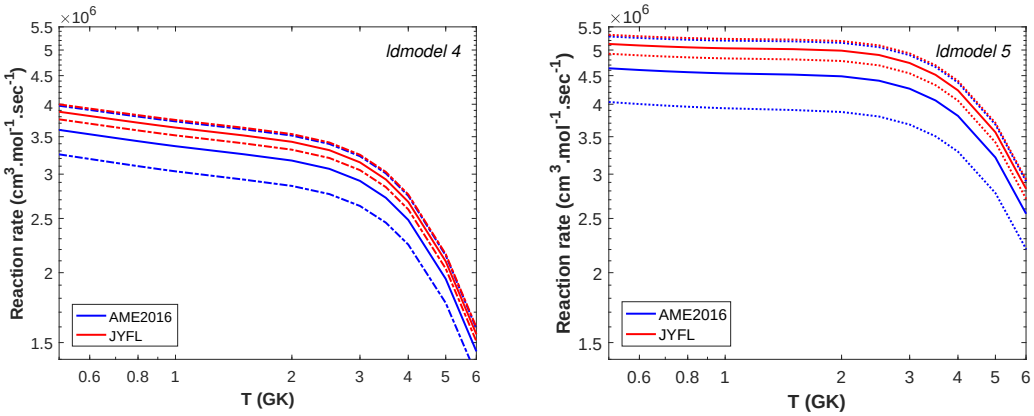

FIGURE 43 Neutron-capture rate on ^{68}Co calculated with Talys using ^{69}Co mass value from AME2016 [6] and from our work. The rate has been computed using *ldmodel* 4 and *ldmodel* 5 as a nuclear level density model.

In Spyrou *et al* study of ^{68}Ni$(n,\gamma)^{69}$Ni reaction [230], the default Talys γSF model, the Kopecky–Uhl generalized Lorentzian (*strength* 1), was found to reproduce very well the shape of the experimental data, and they constrained the γSF by scaling it to match experimental upper and lower limits. This model was also adopted for Figs. 42 and 43. For the NLD, two microscopic level densities (Skyrme force), based on Goriely's tables (*ldmodel* 4) and Hilaire's combinatorial tables (*ldmodel* 5) were used.

The sensitivity studies in Ref.[116] did not employ Talys code for nuclear reaction rate but a different nuclear reaction rate code, NON-SMOKER [232], also based on Hauser-Feshbach statistical model, and the JINA REACLIB v1.0 library [126]. Unfortunately the NON-SMOKER code is not available anymore. Using other models and approaches may lead to a different conclusion on the sensitivity study. Although mass values impact somewhat on the neutron capture rates as show in Figs. 42 and 43, the biggest impact of the reaction Q value is on the photodisintegration rate:

$$\lambda_{\gamma,n} \propto exp(-Q_{n,\gamma}/kT) \tag{86}$$

The REACLIB v.1.0 library, used in the sensitivity study [116] employs experimental mass values from AME1995 [233] by default and FRDM1995 otherwise [30]. The Q values of ^{67}Fe$(n,\gamma)^{68}$Fe and ^{68}Co$(n,\gamma)^{69}$Co neutron capture are tabulated in Table 7 using same masses as in REACLIB v1.0, and with AME2016 masses and ^{67}Fe and ^{69}Co masses from this work (AME2016 for ^{68}Fe and ^{68}Co). For ^{67}Fe$(n,\gamma)^{68}$Fe, the mass of ^{68}Fe has been taken from FRDM1995 for REACLIB v 1.0.
To study the effect of the new mass values on the photodisintegration rates, we calculated the ratio of the photodisintegration rate λ determined with the Q value from this work using JYFLTRAP mass values for ^{67}Fe and ^{69}Co, and AME2016 values for ^{68}Fe and ^{68}Co, to the photodisintegration rate given in REACLIB v1.0 (see Figs. 44 and 45):

$$\frac{\lambda}{\lambda_{REACLIB}} \propto exp((-Q_{n,\gamma} + Q_{n,\gamma}^{REABLIB})/kT) \tag{87}$$

where $Q_{n,\gamma}^{REABLIB}$ is the Q value used in REACLIB v1.0.

The photodisintegration rates calculated with the JYFLTRAP mass value for ^{67}Fe and ^{69}Co are estimated to be around 126000 and 7400 times higher than the REACLIB rates at 1 GK, respectively. The uncertainty due to the Q value in the photodisintegration rate of ^{68}Fe$(\gamma,n)^{67}$Fe at 1 GK has been reduced by a factor of around 190 compared to the REACLIB rate, or by 2600 if we only consider the uncertainty in the ^{67}Fe mass value.

TABLE 7 Q values for the ^{67}Fe$(n,\gamma)^{68}$Fe and ^{68}Co$(n,\gamma)^{69}$Co neutron captures. The uncertainties related to ^{67}Fe and ^{69}Co measured in this work together with the total uncertainties are given.

	$Q_{n,\gamma}^{^{67}Fe}$	$Q_{n,\gamma}^{^{68}Co}$
REACLIB	$6861(470)_{67}(818)_{tot}$	$7291(370)_{69}(496)_{tot}$
AME2016	$5951(270)_{67}(458)_{tot}$	$6421(141)_{69}(236)_{tot}$
JYFLTRAP	$5852(4)_{67}(365)_{tot}$	$6524(44)_{69}(195)_{tot}$

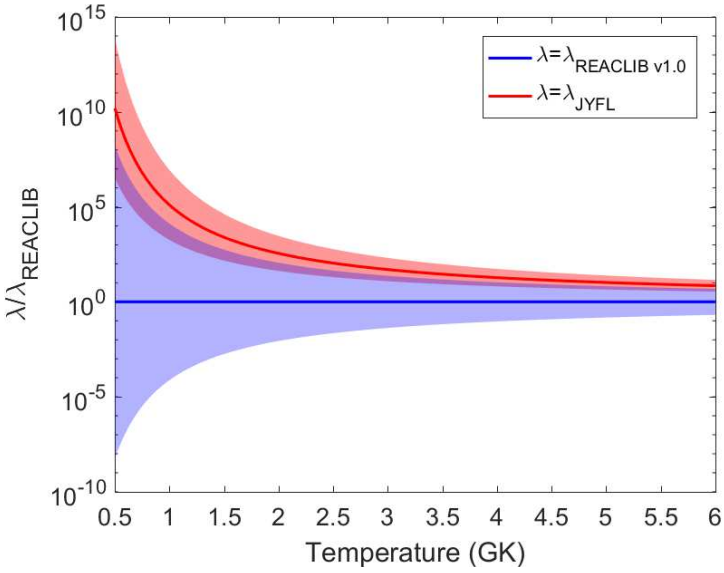

FIGURE 44 Ratio of the photodisintegration rate ^{68}Fe$(\gamma, n)^{67}$Fe calculated with the Q value based on the mass of ^{67}Fe determined in this work together with the AME2016 [6] value for ^{68}Fe, to the REACLIB v1.0 rate, which uses FRDM1995 [30] prediction for ^{68}Fe and AME1995 [233] value for ^{67}Fe. The blue and red areas indicate the Q value related uncertainties for REACLIB v1.0 and JYFLTRAP, respectively.

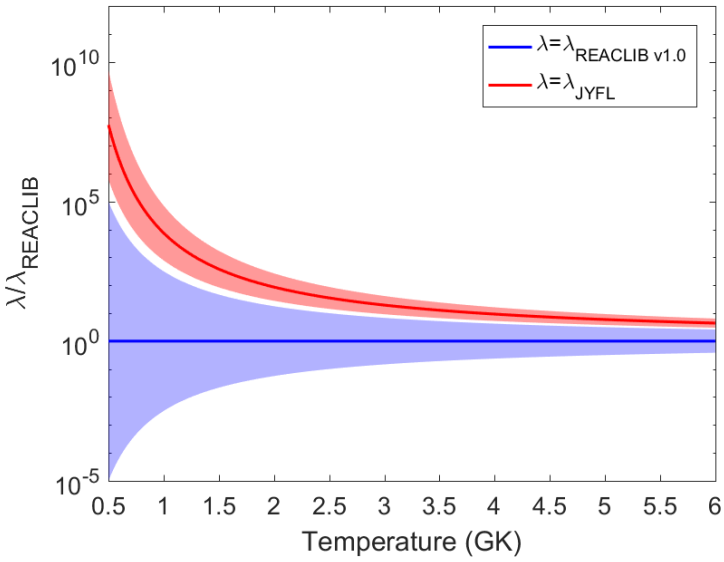

FIGURE 45 Ratio of the photodisintegration rate ^{69}Co$(\gamma, n)^{68}$Co calculated using the Q value based on the mass-excess determined in this work for ^{69}Co together with the AME2016 [6] value for ^{68}Co to the REACLIB v1.0 rate which uses AME1995 [233] value for ^{68}Co and ^{69}Co. The blue and red areas indicate the Q value related uncertainties for REACLIB v1.0 and JYFLTRAP, respectively.

For ^{69}Co$(\gamma, n)^{68}$Co, the uncertainty due to the Q value is decreased by a factor of 33 compared to the REACLIB rate at 1 GK, or around 70 if we only consider the uncertainty in the ^{69}Co mass value.
The ratio of the photodisintegration rate to the neutron capture rate is a relevant quantity for *r*-process studies. This ratio has been plotted in Figs. 46 and 47 using the Talys code with the same parameters for the photodisintegration rate than for the neutron capture rate detailed previously and with *ldmodel* 4. The ratio using *ldmodel* 5 gives very close results and could not be distinguished visually. At 1.5 GK, the JYFLTRAP mass value for ^{67}Fe reduces the uncertainty of the ratio by a factor of ≈70. The photodisintegration dominates for $T \gtrsim 2.9$ GK. The uncertainty of the ratio is reduced by a factor of ≈8 with the JYFLTRAP mass value of ^{69}Co. The photodisintegration dominates for $T \gtrsim 3.2$ GK.
These results illustrate the importance of the temperature condition for the weak *r*-process that is to say astrophysical events that undergo too high temperature would not be able to trigger the process. By giving an estimation of the upper-temperature limit, the astrophysical sites could be refined.

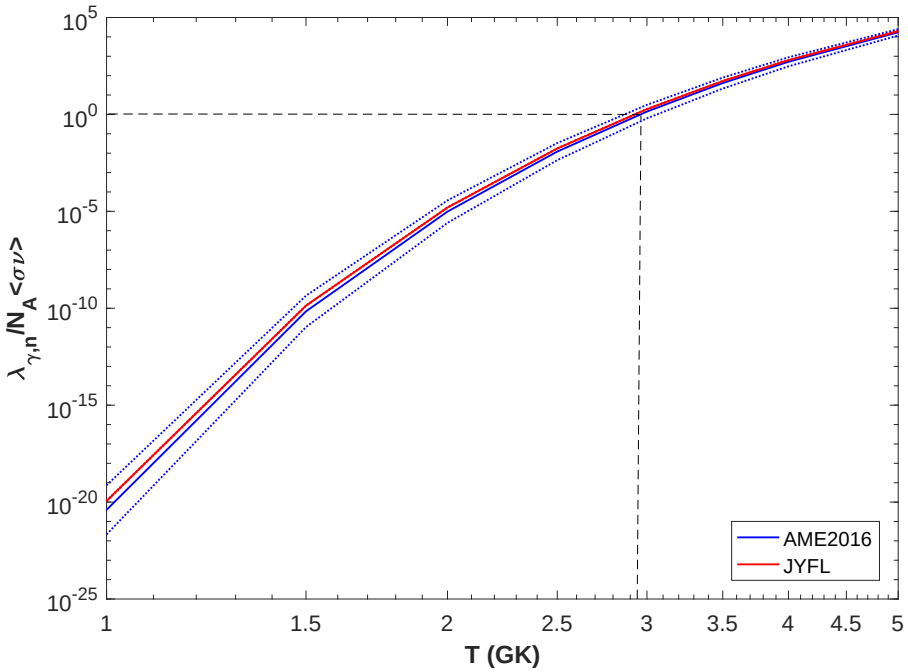

FIGURE 46 Ratio of the photodisintegration rate to the neutron-capture reaction rate on ^{68}Co calculated with Talys using ^{67}Fe mass value from AME2016 [6] and from our work. The black dotted line indicates the temperature for which the rates are equal.

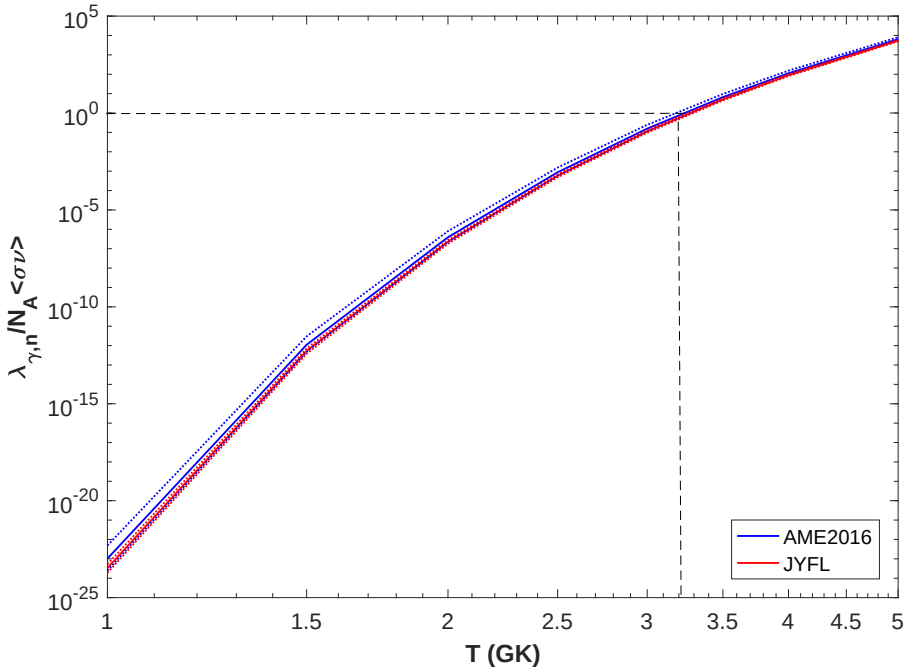

FIGURE 47 Ratio of the photodisintegration rate to the neutron-capture reaction rate on ^{68}Co calculated with Talys using the ^{69}Co mass value from AME2016 [6] and from our work. The black dotted line indicates the temperature for which the rates are equal.

6 SUMMARY AND OUTLOOK

In this thesis work, six nuclides have been studied using the JYFLTRAP double Penning trap at the IGISOL-4 facility: ^{25}Al, ^{30}P, ^{31}Cl, ^{67}Fe, ^{69}Co and ^{70}Co. Of these, the mass of ^{25}Al, $-8915.962(63)$ keV has been used to calculate the $Q_{p,\gamma}$ value of the $^{25}\mathrm{Al}(p,\gamma)^{26}$Si reaction, 5513.99(13) keV. With the revised $Q_{p,\gamma}$ value, the reaction rate $N_A\langle\sigma,\nu\rangle$ was determined. The $^{25}\mathrm{Al}(p,\gamma)^{26}$Si reaction is important for estimating the production of ^{26}Al, responsible for the emission of the 1809 keV cosmic γ-rays. During the same experiment, the mass of ^{30}P was measured as $-20200.854(64)$ keV. $^{30}\mathrm{P}(p,\gamma)^{31}$S is a bottleneck reaction for the nucleosynthesis of the heavier elements in ONe novae. The $Q_{p,\gamma}$ value of this reaction was determined as 6130.64(34) keV and the resonant proton-capture rate $N_A\langle\sigma,\nu\rangle_{res}$ calculated for a temperature range relevant for novae.

The mass-excess of ^{31}Cl, $-7034.7(34)$ keV, determined in this thesis reduces the uncertainty in the mass-excess value by a factor of 15 in comparison to the last published value. ^{30}S is predicted to be a waiting point for the rp-process in type I X-ray bursts. With the new proton separation energy in ^{31}Cl determined in this work, 264.6(34) keV, the lower-temperature limit for the ^{30}S waiting point was found to be $T > 0.44(1)$ GK. The isobaric multiplet mass equation was tested for the T=3/2 quartet at A=31 with the new mass value for ^{31}Cl, and a breakdown of the IMME was concluded.

The neutron-rich nuclei ^{67}Fe, ^{69}Co and ^{70}Co were studied during an experimental campaign on nuclei close to ^{78}Ni at JYFLTRAP. For ^{67}Fe, the determined mass-excess value, $-45709.1(38)$ keV, is about 70 times more precise than the last published value. Masses for the ground and isomeric state in ^{69}Co were determined based on comparisons of normal TOF-ICR spectra collected using different trap cycle times. The mass-excess value obtained for the shorter-living ground state is $-50383(44)$ keV. For the isomeric state, the determined mass-excess value, $-50207(36)$ keV, yields an excitation energy of $E_x = 176(57)$ keV. The mass values for both ^{67}Fe and $^{69}\mathrm{Co}^{gs}$ were used to calculate neutron capture rates relevant for the weak r-process, $^{67}\mathrm{Fe}(n,\gamma)^{67}$Fe and $^{68}\mathrm{Co}(n,\gamma)^{69}$Co, respec-

tively, and their inverse photodisintegration rates.
The PI-ICR method was employed for $^{70}Co^{+}$ ions for the first time. With the PI-ICR measurements and the collected TOF-ICR spectra, we confirm the presence of only one state. The measured mass-excess value, $-46525(11)$ keV belongs to the longer-living state in ^{70}Co expected to be the low-spin state. Two-neutron separation energies and empirical two-neutron shell gap energies for $N = 40$ were studied with our results for ^{67}Fe, ^{69}Co and ^{70}Co. They confirm the reduction of the N=40 subshell closure for Z<28.

In order to provide accurate mass values with a Penning trap, the sources of uncertainties have to be carefully reviewed. During this thesis work, an updated value for time-dependent fluctuations in the magnetic field at JYFLTRAP, $8.18(19)\times10^{-12}/\text{min}\times\Delta t$, was determined. In addition, the mass-dependent uncertainty has been determined to be $2.2\pm0.6\times10^{-10}/\text{u}\times\Delta m$, and no additional residual systematic error is needed for the measured frequency ratios.

Recently, new techniques have been implemented at JYFLTRAP that help to increase the precision of the measurements and also to push further the limits of what can be measured. The PI-ICR method, used to identify states in ^{70}Co in this thesis, should increase the resolving power by a factor of around 40 as compared to the normal TOF-ICR method [162]. Additionally, a multi-reflection time-of-flight mass separator/spectrometer (MR-TOF) is under installation between the RFQ and the JYFLTRAP double Penning trap. The MR-TOF will improve the purification of the beam and thus will allow the access to more exotic nuclei [93]. It can also be used for mass measurements as such.

With these new devices we can extend the mass measurements at JYFLTRAP to regions experimentally unattainable nowadays. Combined with observational data, such as the recent multiwavelength observations of GW170817, it opens a promising future for our understanding of nucleosynthesis, and an opportunity to complete the story of the origin of elements.

REFERENCES

[1] V. Lysenko. Between Materialism and Immaterialism: Atomism in India and Greece. - Materialism and Immaterialism in India and Europe. *Project of History of Indian science and civilization*, 12(5):253–268, 2010.

[2] E. Rutherford. LXXIX. The scattering of α and β particles by matter and the structure of the atom. *The London, Edinburgh, and Dublin Philosophical Magazine and Journal of Science*, 21(125):669–688, 1911.

[3] G. Gamow. Mass defect curve and nuclear constitution. *Proceedings of the Royal Society of London A: Mathematical, Physical and Engineering Sciences*, 126(803):632–644, 1930.

[4] H. A. Bethe and R. F. Bacher. Nuclear Physics A. Stationary States of Nuclei. *Rev. Mod. Phys.*, 8:82–229, Apr 1936.

[5] P. Ring and P. Schuck. *The nuclear many-body problem*. Springer-Verlag, New York, 1980.

[6] M. Wang, G. Audi, F.G. Kondev, W.J. Huang, S. Naimi, and X. Xu. The AME2016 Atomic Mass Evaluation (II). Tables, graphs and references. *Chinese Physics C*, 41(3):030003, 2017.

[7] C.L. Sech and C. Ngô. *Physique nucléaire: Des quarks aux applications*. Physique. Dunod, 2010.

[8] Maria G. Mayer. On closed shells in nuclei. *Phys. Rev.*, 74:235–239, Aug 1948.

[9] R. D. Woods and D. S. Saxon. Diffuse surface optical model for nucleon-nuclei scattering. *Phys. Rev.*, 95:577–578, Jul 1954.

[10] D. R. Hartree. The wave mechanics of an atom with a non-coulomb central field. part I. Theory and Methods. *Mathematical Proceedings of the Cambridge Philosophical Society*, 24(1):89–110, 1928.

[11] V. Fock. Näherungsmethode zur Lösung des quantenmechanischen Mehrkörperproblems. *Zeitschrift für Physik*, 61(1):126–148, Jan 1930.

[12] C. Cohen-Tannoudji, B. Diu, and F. Laloë. *Mécanique quantique*. Hermann, 1986.

[13] T.H.R. Skyrme. The effective nuclear potential. *Nuclear Physics*, 9(4):615 – 634, 1958.

[14] D. Vautherin and D.M. Brink. Hartree-Fock calculations with Skyrme's interaction. *Physics Letters B*, 32(3):149 – 153, 1970.

[15] D. Vautherin and D. M. Brink. Hartree-Fock calculations with Skyrme's interaction. I. Spherical Nuclei. *Phys. Rev. C*, 5:626–647, Mar 1972.

[16] M. Beiner, H. Flocard, Nguyen Van Giai, and P. Quentin. Nuclear ground-state properties and self-consistent calculations with the Skyrme interaction: (I). Spherical description. *Nuclear Physics A*, 238(1):29 – 69, 1975.

[17] H. Krivine, J. Treiner, and O. Bohigas. Derivation of a fluid-dynamical lagrangian and electric giant resonances. *Nuclear Physics A*, 336(2):155 – 184, 1980.

[18] J. Bartel, P. Quentin, M. Brack, C. Guet, and H.-B. Håkansson. Towards a better parametrisation of Skyrme-like effective forces: A critical study of the SkM force. *Nuclear Physics A*, 386(1):79 – 100, 1982.

[19] E. Chabanat, P. Bonche, P. Haensel, J. Meyer, and R. Schaeffer. A Skyrme parametrization from subnuclear to neutron star densities. Part II: Nuclei far from stabilities. *Nuclear Physics A*, 635(1):231 – 256, 1998.

[20] Skyrme mass tables. http://massexplorer.frib.msu.edu/content/DFTMassTables.html.

[21] J. Bardeen, L. N. Cooper, and J. R. Schrieffer. Theory of superconductivity. *Phys. Rev.*, 108:1175–1204, Dec 1957.

[22] M. Kortelainen, T. Lesinski, J. Moré, W. Nazarewicz, J. Sarich, N. Schunck, M. V. Stoitsov, and S. Wild. Nuclear energy density optimization. *Phys. Rev. C*, 82:024313, Aug 2010.

[23] M. Kortelainen, J. McDonnell, W. Nazarewicz, P.-G. Reinhard, J. Sarich, N. Schunck, M. V. Stoitsov, and S. M. Wild. Nuclear energy density optimization: Large deformations. *Phys. Rev. C*, 85:024304, Feb 2012.

[24] M. Kortelainen, J. McDonnell, W. Nazarewicz, E. Olsen, P.-G. Reinhard, J. Sarich, N. Schunck, S. M. Wild, D. Davesne, J. Erler, and A. Pastore. Nuclear energy density optimization: UNEDF2. *Proceedings of the Conference on Advances in Radioactive Isotope Science (ARIS2014)*, 2014.

[25] M. Samyn, S. Goriely, P.-H. Heenen, J.M. Pearson, and F. Tondeur. A Hartree–Fock–Bogoliubov mass formula. *Nuclear Physics A*, 700(1):142 – 156, 2002.

[26] S. Goriely, N. Chamel, and J. M. Pearson. Further explorations of Skyrme-Hartree-Fock-Bogoliubov mass formulas. XII. Stiffness and stability of neutron-star matter. *Phys. Rev. C*, 82:035804, Sep 2010.

[27] S. Goriely, N. Chamel, and J. M. Pearson. Further explorations of Skyrme-Hartree-Fock-Bogoliubov mass formulas. XIII. The 2012 Atomic Mass Evaluation and the symmetry coefficient. *Phys. Rev. C*, 88:024308, Aug 2013.

[28] G. Audi, M. Wang, A.H. Wapstra, F.G. Kondev, M. MacCormick, X. Xu, and B. Pfeiffer. The AME2012 Atomic Mass Evaluation. *Chinese Physics C*, 36(12):1287, 2012.

[29] P. Möller, W.D. Myers, W.J. Swiatecki, and J. Treiner. Nuclear mass formula with a finite-range droplet model and a folded-Yukawa single-particle potential. *Atomic Data and Nuclear Data Tables*, 39(2):225 – 233, 1988.

[30] P. Möller, J.R. Nix, W.D. Myers, and W.J. Swiatecki. Nuclear ground-state masses and deformations. *Atomic Data and Nuclear Data Tables*, 59(2):185 – 381, 1995.

[31] W. D. Myers and W.J. Swiatecki. Average nuclear properties. *Annals of Physics*, 55(3):395 – 505, 1969.

[32] W.D. Myers. *Droplet model of atomic nuclei*. IFI/Plenum, 1977.

[33] D. Lunney, J. M. Pearson, and C. Thibault. Recent trends in the determination of nuclear masses. *Rev. Mod. Phys.*, 75:1021–1082, Aug 2003.

[34] H. J. Krappe, J. R. Nix, and A. J. Sierk. Unified nuclear potential for heavy-ion elastic scattering, fusion, fission, and ground-state masses and deformations. *Phys. Rev. C*, 20:992–1013, Sep 1979.

[35] G. Audi, A.H. Wapstra, and C. Thibault. The AME2003 Atomic Mass Evaluation: (II). Tables, graphs and references. *Nuclear Physics A*, 729(1):337 – 676, 2003.

[36] P. Möller, A.J. Sierk, T. Ichikawa, and H. Sagawa. Nuclear ground-state masses and deformations: FRDM(2012). *Atomic Data and Nuclear Data Tables*, 109-110:1 – 204, 2016.

[37] N. Wang, M. Liu, and X. Wu. Modification of nuclear mass formula by considering isospin effects. *Phys. Rev. C*, 81:044322, Apr 2010.

[38] M. Brack, C. Guet, and H.-B Håkansson. Selfconsistent semiclassical description of average nuclear properties—a link between microscopic and macroscopic models. *Physics Reports*, 123(5):275 – 364, 1985.

[39] M. Liu, N. Wang, Y. Deng, and X. Wu. Further improvements on a global nuclear mass model. *Phys. Rev. C*, 84:014333, Jul 2011.

[40] N. Wang and M. Liu. Nuclear mass predictions with a radial basis function approach. *Phys. Rev. C*, 84:051303, Nov 2011.

[41] R.L. Hardy. Multiquadric equations of topography and other irregular surfaces. *Journal of Geophysical Research*, 76(8):1905–1915.

[42] G. T. Garvey, W. J. Gerace, R. L. Jaffe, I. Talmi, and I. Kelson. Set of nuclear-mass relations and a resultant mass table. *Rev. Mod. Phys.*, 41:S1–S80, Oct 1969.

[43] Ning W., Min L., Xizhen W., and Jie M. Surface diffuseness correction in global mass formula. *Physics Letters B*, 734:215 – 219, 2014.

[44] J. Duflo and A.P. Zuker. Microscopic mass formulas. *Phys. Rev. C*, 52:R23–R27, Jul 1995.

[45] G. Audi and A.H. Wapstra. The 1993 Atomic Mass Evaluation: (I) Atomic mass table. *Nuclear Physics A*, 565(1):1 – 65, 1993.

[46] J. Duflo and A. P. Zuker. The nuclear monopole hamiltonian. *Phys. Rev. C*, 59:R2347–R2350, May 1999.

[47] A. P. Zuker. Three-body monopole corrections to realistic interactions. *Phys. Rev. Lett.*, 90:042502, Jan 2003.

[48] W. Heisenberg. Über den bau der Atomkerne. I. *Zeitschrift für Physik*, 77(1):1–11, Jan 1932.

[49] J.S. Lilley. *Nuclear physics: principles and applications*. Manchester Physics Series. J. Wiley, 2001.

[50] K.S. Krane. *Introductory Nuclear Physics*. Wiley India, 2008.

[51] S. Weinberg and S. B. Treiman. Electromagnetic corrections to isotopic spin conservation. *Phys. Rev.*, 116:465–468, Oct 1959.

[52] N.A. Jelley. *Fundamentals of Nuclear Physics*. Cambridge University Press, 1990.

[53] E. P. Wigner and E. Feenberg. Symmetry properties of nuclear levels. *Reports on Progress in Physics*, 8(1):274, 1941.

[54] J. Cerny, R. H. Pehl, F. S. Goulding, and D. A. Landis. Completion of the Mass-9 Isobaric Quartet via the Three-Neutron Pickup Reaction $C^{12}(He^3, He^6)C^9$. *Phys. Rev. Lett.*, 13:726–728, Dec 1964.

[55] R. G. H. Robertson, S. Martin, W. R. Falk, D. Ingham, and A. Djaloeis. Highly Proton-Rich $T_z = -2$ Nuclides: ^{8}C and ^{20}Mg. *Phys. Rev. Lett.*, 32:1207–1209, May 1974.

[56] R. J. Charity, J. M. Elson, J. Manfredi, R. Shane, L. G. Sobotka, Z. Chajecki, D. Coupland, H. Iwasaki, M. Kilburn, J. Lee, W. G. Lynch, A. Sanetullaev, M. B. Tsang, J. Winkelbauer, M. Youngs, S. T. Marley, D. V. Shetty, A. H. Wuosmaa, T. K. Ghosh, and M. E. Howard. Isobaric Multiplet Mass Equation for A=7 and 8. *Phys. Rev. C*, 84:051308, Nov 2011.

[57] M. Brodeur, T. Brunner, S. Ettenauer, A. Lapierre, R. Ringle, B. A. Brown, D. Lunney, and J. Dilling. Elucidation of the Anomalous A=9 Isospin Quartet Behavior. *Phys. Rev. Lett.*, 108:212501, May 2012.

[58] A. T. Gallant, M. Brodeur, C. Andreoiu, A. Bader, A. Chaudhuri, U. Chowdhury, A. Grossheim, R. Klawitter, A. A. Kwiatkowski, K. G. Leach, A. Lennarz, T. D. Macdonald, B. E. Schultz, J. Lassen, H. Heggen, S. Raeder, A. Teigelhöfer, B. A. Brown, A. Magilligan, J. D. Holt, J. Menéndez, J. Simonis, A. Schwenk, and J. Dilling. Breakdown of the isobaric multiplet mass equation for the $A = 20$ and 21 multiplets. *Phys. Rev. Lett.*, 113:082501, Aug 2014.

[59] A. Kankainen, T. Eronen, D. Gorelov, J. Hakala, A. Jokinen, V. S. Kolhinen, M. Reponen, J. Rissanen, A. Saastamoinen, V. Sonnenschein, and J. Äystö. High-precision mass measurement of ^{31}S with the double Penning trap JYFLTRAP improves the mass value for ^{32}Cl. *Phys. Rev. C*, 82:052501, Nov 2010.

[60] C. Yazidjian, G. Audi, D. Beck, K. Blaum, S. George, C. Guénaut, F. Herfurth, A. Herlert, A. Kellerbauer, H.-J. Kluge, D. Lunney, and L. Schweikhard. Evidence for a breakdown of the isobaric multiplet mass equation: A study of the A=35, T=3/2 isospin quartet. *Phys. Rev. C*, 76:024308, Aug 2007.

[61] Y. H. Zhang, H. S. Xu, Yu. A. Litvinov, X. L. Tu, X. L. Yan, S. Typel, K. Blaum, M. Wang, X. H. Zhou, Y. Sun, B. A. Brown, Y. J. Yuan, J. W. Xia, J. C. Yang, G. Audi, X. C. Chen, G. B. Jia, Z. G. Hu, X. W. Ma, R. S. Mao, B. Mei, P. Shuai, Z. Y. Sun, S. T. Wang, G. Q. Xiao, X. Xu, T. Yamaguchi, Y. Yamaguchi, Y. D. Zang, H. W. Zhao, T. C. Zhao, W. Zhang, and W. L. Zhan. Mass measurements of the neutron-deficient ^{41}Ti, ^{45}Cr, ^{49}Fe, and ^{53}Ni nuclides: First test of the isobaric multiplet mass equation in fp-shell nuclei. *Phys. Rev. Lett.*, 109:102501, Sep 2012.

[62] W. Benenson and E. Kashy. Isobaric quartets in nuclei. *Rev. Mod. Phys.*, 51:527–540, Jul 1979.

[63] M. MacCormick and G. Audi. Evaluated experimental isobaric analogue states from T=1/2 to T=3 and associated IMME coefficients. *Nuclear Physics A*, 925:61 – 95, 2014.

[64] M. MacCormick and G. Audi. Corrigendum to "Evaluated experimental isobaric analogue states from T=1/2 to T=3 and associated IMME coefficients" [nucl. phys. a 925 (2014) 61–95]. *Nuclear Physics A*, 925:296 – 297, 2014.

[65] P. Baczyk, J. Dobaczewski, M. Konieczka, W. Satuła, T. Nakatsukasa, and K. Sato. Isospin-symmetry breaking in masses of N≈Z nuclei. *Physics Letters B*, 778:178 – 183, 2018.

[66] R. Machleidt. High-precision, charge-dependent Bonn nucleon-nucleon potential. *Phys. Rev. C*, 63:024001, Jan 2001.

[67] P. W. Merrill and J. L. Greenstein. Revised list of absorption lines in the spectrum of R Andromedae. *Astrophysical Journal Supplement*, 2:225, January 1956.

[68] G. Audi, F.G. Kondev, M. Wang, W.J. Huang, and S. Naimi. The NUBASE2016 evaluation of nuclear properties. *Chinese Physics C*, 41(3):030001, 2017.

[69] W. A. Mahoney, J. C. Ling, A. S. Jacobson, and R. E. Lingenfelter. Diffuse galactic gamma-ray line emission from nucleosynthetic ^{60}Fe, ^{26}Al, and ^{22}Na - Preliminary limits from HEAO 3. *The Astrophysical Journal*, 262:742, 1982.

[70] W. A. Mahoney, J. C. Ling, W. A. Wheaton, and A. S. Jacobson. HEAO 3 discovery of ^{26}Al in the interstellar medium. *The Astrophysical Journal*, 286:578–585, nov 1984.

[71] B. P. Abbott, R. Abbott, T. D. Abbott, F. Acernese, K. Ackley, C. Adams, T. Adams, P. Addesso, R. X. Adhikari, and V. B. Adya. Gravitational waves and gamma-rays from a binary neutron star merger: GW170817 and GRB 170817a. *The Astrophysical Journal Letters*, 848(2):L13, 2017.

[72] R. Diehl, C. Dupraz, K. Bennett, H. Bloemen, W. Hermsen, J. Knoedlseder, G. Lichti, D. Morris, J. Ryan, V. Schoenfelder, H. Steinle, A. Strong, B. Swanenburg, M. Varendorff, and C. Winkler. Comptel observations of galactic ^{26}Al emission. *Astronomy and Astrophysics*, 298:445, jun 1995.

[73] D. D. Clayton. ^{26}Al in the interstellar medium. *Astrophysical Journal*, 280:144–149, may 1984.

[74] N. Prantzos and R. Diehl. Radioactive ^{26}Al in the galaxy: Observations versus theory. *Physics Report*, 267(1):1–69, 1996.

[75] R. Diehl, H. Halloin, K. Kretschmer, G. G. Lichti, V. Schönfelder, A. W. Strong, A. von Kienlin, W. Wang, P. Jean, J. Knödlseder, J.-P. Roques, G. Weidenspointner, S. Schanne, D. H. Hartmann, C. Winkler, and C. Wunderer. Radioactive ^{26}Al from massive stars in the Galaxy. *Nature*, 439(7072):45–47, 2006.

[76] B. Luzum, N. Capitaine, A. Fienga, W. Folkner, T. Fukushima, J. Hilton, C. Hohenkerk, G. Krasinsky, G. Petit, E. Pitjeva, M. Soffel, and P. Wallace. The IAU 2009 system of astronomical constants: the report of the IAU working group on numerical standards for fundamental astronomy. *Celestial Mechanics and Dynamical Astronomy*, 110(4):293, Jul 2011.

[77] J. José, M. Hernanz, and Al. Coc. New results on ^{26}Al production in classical novae. *Astrophys. J.*, 479:L55–L58, 1997.

[78] A. W. Shafter. On the nova rate in the galaxy. *The Astrophysical Journal*, 20:226–236, 1997.

[79] J. L. Sokoloski. Symbiotic Stars as Laboratories for the Study of Accretion and Jets: A Call for Optical Monitoring. *Image Rochester NY*, 31:14, 2004.

[80] M. F. Bode and Aneurin E. *Classical Novae*. 2008.

[81] C.H.P. Gaposchkin. *The Galactic Novae*. Dover Publications, 1957.

[82] S. N. Shore, S. Starrffield, R. Gonzalez-Riestrat, P. H. Hauschildt, and G. Sonneborn. Dust formation in Nova Cassiopeiae 1993 seen by ultraviolet absorption. *Nature*, 369(6481):539–541, 1994.

[83] R. D. Gehrz, J. W. Truran, R. E. Williams, and S. Starrfield. Nucleosynthesis in Classical Novae and Its Contribution to the Interstellar Medium. *Publications of the Astronomical Society of the Pacific*, 110(743):3–26, 1998.

[84] J. Jose and M. Hernanz. Nucleosynthesis in Classical Novae: CO versus ONe White Dwarfs. *The Astrophysical Journal*, 494(2):680–690, 1998.

[85] S. Amari, X. Gao, L. R. Nittler, E. Zinner, J. José, M. Hernanz, and R. S. Lewis. Presolar Grains from Novae. *The Astrophysical Journal*, 551(2):1065–1072, 2001.

[86] P. Hoppe, S. Amari, E. Zinner, and R. S. Lewis. Isotopic compositions of C, N, O, Mg, and Si, trace element abundances, and morphologies of single circumstellar graphite grains in four density fractions from the Murchison meteorite. *Geochimica et Cosmochimica Acta*, 59(19):4029–4056, 1995.

[87] C. Wrede. The $^{30}\mathrm{P}(p,\gamma)^{31}\mathrm{S}$ reaction in classical novae: Progress and prospects. *AIP Advances*, 4(4):0–17, 2014.

[88] J. Jordi, A. Coc, and M. Hernanz. Synthesis of intermediate-mass elements in classical novae: From Si to Ca. *The Astrophysical Journal*, 560(2):897, 2001.

[89] L. Downen, C. Iliadis, J. José, and S. Starrfield. Nuclear thermometers for classical novae. *Proceedings of Science*, 105, 2012.

[90] K. J. Kelly, C. Iliadis, L. Downen, J. José, and A. Champagne. Nuclear mixing meters for classical novae. *Astrophysical Journal*, 777(2), 2013.

[91] G. Baym, T. Hatsuda, T. Kojo, P. D Powell, Y. Song, and T. Takatsuka. From hadrons to quarks in neutron stars: A review. *Reports on Progress in Physics*, 81(5):056902, 2018.

[92] . B. Rüster, M. Hempel, and J. Schaffner-Bielich. Outer crust of nonaccreting cold neutron stars. *Phys. Rev. C*, 73:035804, Mar 2006.

[93] R. N. Wolf, D. Beck, K. Blaum, Ch Böhm, Ch Borgmann, M. Breitenfeldt, N. Chamel, S. Goriely, F. Herfurth, M. Kowalska, S. Kreim, D. Lunney, V. Manea, E. Minaya Ramirez, S. Naimi, D. Neidherr, M. Rosenbusch, L. Schweikhard, J. Stanja, F. Wienholtz, and K. Zuber. Plumbing neutron

stars to new depths with the binding energy of the exotic nuclide ^{82}Zn. *Physical Review Letters*, 110(4):1–5, 2013.

[94] W. H. G. Lewin and M. van der Klis. *Compact Stellar X-ray Sources*. apr 2006.

[95] J. Grindlay, H. Gursky, H. Schnopper, D. R. Parsignault, J. Heise, A. C. Brinkman, and J. Schrijver. Discovery of intense X-ray bursts from the globular cluster NGC 6624. *The Astrophysical Journal*, 205:L127–L130, may 1976.

[96] R. D. Belian, J. P. Conner, and W. D. Evans. The discovery of X-ray bursts from a region in the constellation Norma. *The Astrophysical Journal*, 206:L135–L138, jun 1976.

[97] J. E. Grindlay. The discovery of bursting X-ray sources. *Comments on Astrophysics*, 6:165–175, 1976.

[98] W. H. G. Lewin, J. van Paradijs, and R. E. Taam. X-ray bursts. *Space Science Reviews*, 62:223–389, sep 1993.

[99] C. Iliadis. *Nuclear Physics of Stars*. Physics textbook. Wiley, 2008.

[100] J. L. Fisker, H. S., and F.-K. Thielemann. Explosive hydrogen burning during type I X-ray bursts. *The Astrophysical Journal Supplement Series*, 174(1):261, 2008.

[101] H. Schatz, A. Aprahamian, J. Göres, M. Wiescher, T. Rauscher, J. F. Rembges, F. K. Thielemann, B. Pfeiffer, P. Möller, K. L. Kratz, H. Herndl, B. A. Brown, and H. Rebel. *Rp*-process nucleosynthesis at extreme temperature and density conditions. *Physics Report*, 294(4):167–263, 1998.

[102] R. K. Wallace and S. E. Woosley. Explosive hydrogen burning. *The Astrophysical Journal Supplement Series*, 45:389–420, feb 1981.

[103] H. Schatz, A. Aprahamian, V. Barnard, L. Bildsten, A. Cumming, M. Ouellette, T. Rauscher, F.-K. Thielemann, and M. Wiescher. End point of the *rp* process on accreting neutron stars. *Phys. Rev. Lett.*, 86:3471–3474, Apr 2001.

[104] M. Sztajno, J. van Paradijs, W. H. G. Lewin, J. Trumper, G. Stollman, W. Pietsch, and M. van der Klis. Unusual X-ray burst profiles from 4U/MXB 1636-53. *The Astrophysical Journal*, 299:487–495, dec 1985.

[105] W. Penninx, E. Damen, J. van Paradijs, J. Tan, and W.H.G. Lewin. EXOSAT observations of the X-ray burst source 4U 1608-52. *Astronomy & Astrophysics*, 208:146–152, 1989.

[106] E. Kuulkers, J. Homan, M. van der Klis, W. H. G. Lewin, and M. Méndez. X-ray bursts at extreme mass accretion rates from GX2. *Astronomy & Astrophysics*, 382(3):947–973, 2002.

[107] J. L. Fisker, F.-K. Thielemann, and M. Wiescher. The nuclear reaction waiting points: ^{22}Mg, ^{26}Si, ^{30}S, and ^{34}Ar and bolometrically double-peaked type I X-ray bursts. *The Astrophysical Journal Letters*, 608(1):L61, 2004.

[108] C. Wrede, J. A. Caggiano, J. A. Clark, C. M. Deibel, A. Parikh, and P. D. Parker. Thermonuclear ^{30}S$(p,\gamma)^{31}$Cl reaction in type I X-ray bursts. *Phys. Rev. C*, 79:045808, Apr 2009.

[109] C.E. Rolfs and W.S. Rodney. *Cauldrons in the Cosmos: Nuclear Astrophysics*. Theoretical Astrophysics. University of Chicago Press, 1988.

[110] C. Wrede, J. A. Caggiano, J. A. Clark, C. M. Deibel, A. Parikh, and P. D. Parker. Measurements of ^{31}S energy levels and reevaluation of the thermonuclear resonant ^{30}P$(p,\gamma)^{31}$S reaction rate. *Phys. Rev. C*, 79:045803, Apr 2009.

[111] C. M. Deibel, K. E. Rehm, J. M. Figueira, J. P. Greene, C. L. Jiang, B. P. Kay, H. Y. Lee, J. C. Lighthall, S. T. Marley, R. C. Pardo, N. Patel, M. Paul, C. Ugalde, A. Woodard, A. H. Wuosmaa, and G. Zinkann. First measurement of the ^{33}Cl$(p,\alpha)^{30}$S reaction. *Phys. Rev. C*, 84:045802, Oct 2011.

[112] M. Arnould, S. Goriely, and K. Takahashi. The *r*-process of stellar nucleosynthesis: Astrophysics and nuclear physics achievements and mysteries. *Physics Reports*, 450(4):97 – 213, 2007.

[113] S. Wanajo and Y. Ishimaru. The weak *r*-process in core-collapse supernovae. In *From Lithium to Uranium: Elemental Tracers of Early Cosmic Evolution*, volume 228 of *IAU Symposium*, pages 435–438, 2005.

[114] J. A. Johnson and M. Bolte. The *r*-process in the early galaxy. *The Astrophysical Journal*, 579(2):616, 2002.

[115] K.-L. Kratz, K. Farouqi, B. Pfeiffer, J. W. Truran, C. Sneden, and J. J. Cowan. Explorations of the *r*-processes: Comparisons between calculations and observations of low-metallicity stars. *The Astrophysical Journal*, 662(1):39, 2007.

[116] R. Surman, M. Mumpower, R. Sinclair, K. L. Jones, W. R. Hix, and G. C. McLaughlin. Sensitivity studies for the weak r process: neutron capture rates. *AIP Advances*, 4(4):041008, 2014.

[117] S. Wanajo. The *r*-process in proto-neutron-star wind revisited. *The Astrophysical Journal Letters*, 770(2):L22, 2013.

[118] A. Arcones and F.-K. Thielemann. Neutrino-driven wind simulations and nucleosynthesis of heavy elements. *Journal of Physics G: Nuclear and Particle Physics*, 40(1):013201, 2013.

[119] R. A. Hulse and J. H. Taylor. Discovery of a pulsar in a binary system. *The Astrophysical Journal Letters*, 195:L51–L53, January 1975.

[120] F.-K. Thielemann, M. Eichler, I. V. Panov, and B. Wehmeyer. Neutron Star Mergers and Nucleosynthesis of Heavy Elements. *Annual Review of Nuclear and Particle Science*, 67:253–274, October 2017.

[121] B. P. Abbott, R. Abbott, T. D. Abbott, M. R. Abernathy, F. Acernese, K. Ackley, C. Adams, T. Adams, P. Addesso, R. X. Adhikari, and et al. Upper Limits on the Rates of Binary Neutron Star and Neutron Star-Black Hole Mergers from Advanced LIGO's First Observing Run. *The Astrophysical Journal Letters*, 832:L21, December 2016.

[122] B. Côté, C. L. Fryer, K. Belczynski, O. Korobkin, M. Chruślińska, N. Vassh, M. R. Mumpower, J. Lippuner, T. M. Sprouse, R. Surman, and R. Wollaeger. The origin of *r*-process Elements in the Milky Way. *The Astrophysical Journal*, 855(2):99, 2018.

[123] H. Palme and H. Beer. *3.4.1 Introduction: Datasheet from Landolt-Börnstein - Group VI Astronomy and Astrophysics · Volume 3A: "Instruments, Methods, Solar System"*. Springer-Verlag Berlin Heidelberg. Copyright 1993 Springer-Verlag Berlin Heidelberg.

[124] J. Beun, G. C. McLaughlin, R. Surman, and W. R. Hix. Fission cycling in a supernova *r* process. *Phys. Rev. C*, 77:035804, Mar 2008.

[125] Non-smoker^{WEB} homepage. https://nucastro.org/websmoker.html.

[126] R. H. Cyburt, A. M. Amthor, R. Ferguson, Z. M., K. S., S. W., A. Heger, R. D. Hoffman, T. Rauscher, A. Sakharuk, H. Schatz, F. K. Thielemann, and M. Wiescher. The JINA REACLIB database: Its recent updates and impact on type-I X-ray bursts. *Astrophys. J. Suppl. Ser.*, 189(1):240, 2010.

[127] J.A. Holmes, S.E. Woosley, William A. Fowler, and B.A. Zimmerman. Tables of thermonuclear-reaction-rate data for neutron-induced reactions on heavy nuclei. *Atomic Data and Nuclear Data Tables*, 18(4):305 – 412, 1976.

[128] T. Rauscher and F.-K. Thielemann. Astrophysical reaction rates from statistical model calculations. *Atomic Data and Nuclear Data Tables*, 75(1):1 – 351, 2000.

[129] Talys homepage. http://www.talys.eu/home/.

[130] J. Lippuner and L. F. Roberts. Skynet: A modular nuclear reaction network library. *The Astrophysical Journal Supplement Series*, 233(2):18, 2017.

[131] Skynet source. https://bitbucket.org/jlippuner/skynet.

[132] A. Gade and B. M. Sherrill. NSCL and FRIB at Michigan State University: Nuclear science at the limits of stability. *Physica Scripta*, 91(5):053003, May 2016.

[133] B. Franzke, H. Geissel, and G. Münzenberg. Mass and lifetime measurements of exotic nuclei in storage rings. *Mass Spectrometry Reviews*, 27(5):428–469, 2008.

[134] H. Sakurai. RI beam factory project at RIKEN. *Nuclear Physics A*, 805(1):526c – 532c, 2008. INPC 2007.

[135] M. J. G. Borge and B. Jonson. Isolde past, present and future. *Journal of Physics G: Nuclear and Particle Physics*, 44(4):044011, 2017.

[136] G. C. Ball, G. Hackman, and R. Krücken. The TRIUMF-ISAC facility: two decades of discovery with rare isotope beams. *Physica Scripta*, 91(9):093002, 2016.

[137] R. Kirchner. Progress in ion source development for on-line separators. *Nuclear Instruments and Methods in Physics Research*, 186(1-2):275–293, 1981.

[138] J. Ärje, J. Äystö, H. Hyvönen, P. Taskinen, V. Koponen, J. Honkanen, K. Valli, A. Hautojärvi, and K. Vierinen. The ion guide isotope separator on-line, IGISOL. *Nuclear Inst. and Methods in Physics Research, A*, 247(3):431–437, 1986.

[139] J. Huikari, P. Dendooven, A. Jokinen, A. Nieminen, H. Penttilä, K. Peräjärvi, A. Popov, S. Rinta-Antila, and J. Äystö. Production of neutron deficient rare isotope beams at IGISOL; on-line and off-line studies. *Nuclear Instruments and Methods in Physics Research Section B: Beam Interactions with Materials and Atoms*, 222(3):632 – 652, 2004.

[140] P. Karvonen, I.D. Moore, T. Sonoda, T. Kessler, H. Penttilä, K. Peräjärvi, P. Ronkanen, and J. Äystö. A sextupole ion beam guide to improve the efficiency and beam quality at IGISOL. *Nuclear Instruments and Methods in Physics Research Section B: Beam Interactions with Materials and Atoms*, 266(21):4794 – 4807, 2008.

[141] I. Pohjalainen. *Gas-phase chemistry , recoil source characterization and in-gas-cell resonance laser ionization of actinides at IGISOL*. PhD thesis, University of Jyväskylä, 2018.

[142] A. Nieminen, J. Huikari, A. Jokinen, J. Äystö, P. Campbell, and E.C.A. Cochrane. Beam cooler for low-energy radioactive ions. *Nuclear Instruments and Methods in Physics Research Section A: Accelerators, Spectrometers, Detectors and Associated Equipment*, 469(2):244 – 253, 2001.

[143] A. Giatzoglou, T. Poomaradee, I. Pohjalainen, S. Rinta-Antila, I. D. Moore, P. M. Walker, L. Marmugi, and F. Renzoni. A facility for production and laser cooling of cesium isotopes and isomers. *Nuclear Instruments and Methods in Physics Research Section A: Accelerators, Spectrometers, Detectors and Associated Equipment*, 908:367 – 375, 2018.

[144] I.D. Moore, T. Eronen, D. Gorelov, J. Hakala, A. Jokinen, A. Kankainen, V.S. Kolhinen, J. Koponen, H. Penttilä, I. Pohjalainen, M. Reponen, J. Rissanen, A. Saastamoinen, S. Rinta-Antila, V. Sonnenschein, and J. Äystö. Towards commissioning the new IGISOL-4 facility. *Nuclear Instruments and Methods in Physics Research Section B: Beam Interactions with Materials and Atoms*, 317:208 – 213, 2013. XVIth International Conference on ElectroMagnetic Isotope Separators and Techniques Related to their Applications, December 2–7, 2012 at Matsue, Japan.

[145] I.D. Moore, P. Dendooven, and J. Ärje. The IGISOL technique-three decades of developments. *Hyperfine Interactions*, 223:17–62, jan 2014.

[146] L. S. Brown and G. Gabrielse. Geonium theeory: Physics of a single electron or ion in a Penning trap. *Reviews of Modern Physics*, 58(1):233–311, 1986.

[147] K. Blaum. High-accuracy mass spectrometry with stored ions. *Physics Reports*, 425(1):1–78, 2006.

[148] F.M. Penning. Die glimmentladung bei niedrigem druck zwischen koaxialen zylindern in einem axialen magnetfeld. *Physica*, 3(9):873 – 894, 1936.

[149] K. Blaum, Yu. N. Novikov, and G. Werth. Penning traps as a versatile tool for precise experiments in fundamental physics. *Contemporary Physics*, 51(2):149–175, 2010.

[150] G. Gabrielse, L. Haarsma, and S.L. Rolston. Open-endcap Penning traps for high precision experiments. *International Journal of Mass Spectrometry and Ion Processes*, 88(2):319 – 332, 1989.

[151] G. Bollen, S. Becker, H.-J. Kluge, M. König, R.B. Moore, T. Otto, H. Raimbault-Hartmann, G. Savard, L. Schweikhard, and H. Stolzenberg. ISOLTRAP: a tandem Penning trap system for accurate on-line mass determination of short-lived isotopes. *Nuclear Instruments and Methods in Physics Research Section A: Accelerators, Spectrometers, Detectors and Associated Equipment*, 368(3):675 – 697, 1996.

[152] T. Eronen, V. S. Kolhinen, V. V. Elomaa, D. Gorelov, U. Hager, J. Hakala, A. Jokinen, A. Kankainen, P. Karvonen, S. Kopecky, I. D. Moore, H. Penttilä, S. Rahaman, S. Rinta-Antila, J. Rissanen, A. Saastamoinen, J. Szerypo, C. Weber, and J. Äystö. JYFLTRAP: a Penning trap for precision mass spectroscopy and isobaric purification. *The European Physical Journal A*, 48(4):46, Apr 2012.

[153] G. Savard, St Becker, G. Bollen, H. J. Kluge, R. B. Moore, T. Otto, L. Schweikhard, H. Stolzenberg, and U. Wiess. A new cooling technique for heavy ions in a Penning trap. *Physics Letters A*, 158(5):247–252, 1991.

[154] Eronen T. *High Precision Q_{EC} Value Measurements Of Superallowed $0^+ \rightarrow 0^+$ Beta Decays With JYFLTRAP*. PhD thesis, University of Jyväskylä, 2008.

[155] N. F. Ramsey. A new molecular beam resonance method. *Phys. Rev.*, 76:996–996, Oct 1949.

[156] N. F. Ramsey. Experiments with separated oscillatory fields and hydrogen masers. *Rev. Mod. Phys.*, 62:541–552, Jul 1990.

[157] G. Bollen, H.-J. Kluge, T. Otto, G. Savard, and H. Stolzenberg. Ramsey technique applied in a Penning trap mass spectrometer. *Nuclear Instruments and Methods in Physics Research Section B: Beam Interactions with Materials and Atoms*, 70(1):490 – 493, 1992.

[158] M. Kretzschmar. The Ramsey method in high-precision mass spectrometry with Penning traps: Theoretical foundations. *International Journal of Mass Spectrometry*, 264(2):122 – 145, 2007.

[159] S. George, K. Blaum, F. Herfurth, A. Herlert, M. Kretzschmar, S. Nagy, S. Schwarz, L. Schweikhard, and C. Yazidjian. The Ramsey method in high-precision mass spectrometry with Penning traps: Experimental results. *International Journal of Mass Spectrometry*, 264(2):110 – 121, 2007.

[160] S. George, S. Baruah, B. Blank, K. Blaum, M. Breitenfeldt, U. Hager, F. Herfurth, A. Herlert, A. Kellerbauer, H.-J. Kluge, M. Kretzschmar, D. Lunney, R. Savreux, S. Schwarz, L. Schweikhard, and C. Yazidjian. Ramsey method of separated oscillatory fields for high-precision Penning trap mass spectrometry. *Phys. Rev. Lett.*, 98:162501, Apr 2007.

[161] S. Eliseev, K. Blaum, M. Block, A. Dörr, C. Droese, T. Eronen, M. Goncharov, M. Höcker, J. Ketter, E. Minaya Ramirez, D. A. Nesterenko, Yu N. Novikov, and L. Schweikhard. A phase-imaging technique for cyclotron-frequency measurements. *Applied Physics B: Lasers and Optics*, 114(1-2):107–128, 2014.

[162] D. A. Nesterenko, T. Eronen, A. Kankainen, L. Canete, A. Jokinen, I. D. Moore, H. Penttilä, S. Rinta-Antila, A. de Roubin, and M. Vilén. Phase-imaging ion-cyclotron-resonance technique at the JYFLTRAP double Penning trap mass spectrometer. *The European Physical Journal A*, 54(9):154, Sep 2018.

[163] C. Guénaut, G. Audi, D. Beck, K. Blaum, G. Bollen, P. Delahaye, F. Herfurth, A. Kellerbauer, H. J. Kluge, J. Libert, D. Lunney, S. Schwarz, L. Schweikhard, and C. Yazidjian. High-precision mass measurements of nickel, copper, and gallium isotopes and the purported shell closure at N=40. *Physical Review C - Nuclear Physics*, 75(4):1–12, 2007.

[164] A. Kellerbauer, K. Blaum, G. Bollen, F. Herfurth, H.-J. Kluge, M. Kuckein, E. Sauvan, C. Scheidenberger, and L. Schweikhard. From direct to absolute mass measurements: A study of the accuracy of ISOLTRAP. *The European Physical Journal D - Atomic, Molecular, Optical and Plasma Physics*, 22(1):53–64, Jan 2003.

[165] R. T. Birge. The calculation of errors by the method of least squares. *Phys. Rev.*, 40:207–227, Apr 1932.

[166] S. Rahaman, J. Hakala, V. V. Elomaa, T. Eronen, U. Hager, A. Jokinen, A. Kankainen, I. D. Moore, H. Penttilä, S. Rinta-Antila, J. Rissanen, A. Saastamoinen, C. Weber, and J. Äystö. Masses of neutron-rich Ni and Cu isotopes and the shell closure at Z = 28 , N = 40. *The European Physical Journal A*, 34(1):5–9, Oct 2007.

[167] J. Hakala, S. Rahaman, V.-V. Elomaa, T. Eronen, U. Hager, A. Jokinen, A. Kankainen, I. D. Moore, H. Penttilä, S. Rinta-Antila, J. Rissanen, A. Saastamoinen, T. Sonoda, C. Weber, and J. Äystö. Evolution of the N=50 shell gap energy towards ^{78}Ni. *Phys. Rev. Lett.*, 101:052502, Jul 2008.

[168] V.-V. Elomaa, T. Eronen, J. Hakala, A. Jokinen, A. Kankainen, I.D. Moore, S. Rahaman, J. Rissanen, C. Weber, and J. Äystö. Systematic studies of the accuracy of the Penning trap mass spectrometer JYFLTRAP. *Nuclear Instruments and Methods in Physics Research Section A: Accelerators, Spectrometers, Detectors and Associated Equipment*, 612(1):97 – 102, 2009.

[169] M. Wang, G. Audi, A.H. Wapstra, F.G. Kondev, M. MacCormick, X. Xu, and B. Pfeiffer. The AME2012 Atomic Mass Evaluation. *Chinese Physics C*, 36(12):1603, 2012.

[170] F. Everling, G. L. Morgan, D. W. Miller, L. W. Seagondollar, and P. W. Tillman Jr. Energies of some ^{25}Al levels from the ^{24}Mg$(p,\gamma)^{25}$Al reaction and the Coulomb-energy differences of analog rotational bands. *Canadian Journal of Physics*, 49(4):402–406, 1971.

[171] M. Piiparinen. Investigation of the gamma decay of excited states in ^{25}Al. *Zeitschrift für Physik A Hadrons and nuclei*, 252(3):206–218, Jun 1972.

[172] M. Uhrmacher, K. Pampus, F.J. Bergmeister, D. Purschke, and K.P. Lieb. Energy calibration of the 500 kV heavy ion implanter ionas. *Nuclear Instruments and Methods in Physics Research Section B: Beam Interactions with Materials and Atoms*, 9(2):234 – 242, 1985.

[173] T. Eronen, V.-V. Elomaa, U. Hager, J. Hakala, A. Jokinen, A. Kankainen, T. Kessler, I. D. Moore, S. Rahaman, J. Rissanen, C. Weber, and J. Äystö. Mass and Q_{EC} value of ^{26}Si. *Phys. Rev. C*, 79:032802, Mar 2009.

[174] N. Severijns, M. Tandecki, T. Phalet, and I. S. Towner. $\mathcal{F}t$ values of the $T = 1/2$ mirror β transitions. *Phys. Rev. C*, 78:055501, Nov 2008.

[175] O. Naviliat-Cuncic and N. Severijns. Test of the conserved vector current hypothesis in $T = 1/2$ mirror transitions and new determination of $|V_{ud}|$. *Phys. Rev. Lett.*, 102:142302, Apr 2009.

[176] M. S. Basunia and A. M. Hurst. Nuclear Data Sheets for A = 26. *Nuclear Data Sheets*, 134:1–148, May 2016.

[177] Y. Parpottas, S. M. Grimes, S. Al-Quraishi, C. R. Brune, T. N. Massey, J. E. Oldendick, A. Salas, and R. T. Wheeler. Astrophysically important ^{26}Si states studied with the $(^3\mathrm{He}, n)$ reaction and the $^{25}\mathrm{Al}(p,\gamma)^{26}\mathrm{Si}$ reaction rates in explosive hydrogen burning environments. *Phys. Rev. C*, 70:065805, Dec 2004.

[178] A. Matic, A. M. van den Berg, M. N. Harakeh, H. J. Wörtche, G. P. A. Berg, M. Couder, J. Görres, P. LeBlanc, S. O'Brien, M. Wiescher, K. Fujita, K. Hatanaka, Y. Sakemi, Y. Shimizu, Y. Tameshige, A. Tamii, M. Yosoi, T. Adachi, Y. Fujita, Y. Shimbara, H. Fujita, T. Wakasa, B. A. Brown, and H. Schatz. High-precision (p,t) reaction to determine $^{25}\mathrm{Al}(p,\gamma)^{26}\mathrm{Si}$ reaction rates. *Phys. Rev. C*, 82:025807, Aug 2010.

[179] K. A. Chipps. Resonances above the proton threshold in ^{26}Si. *Phys. Rev. C*, 93:035801, Mar 2016.

[180] J.P.L. Reinecke, F.B. Waanders, P. Oberholzer, P.J.C.Janse Van Rensburg, J.A. Cilliers, J.J.A. Smit, M.A. Meyer, and P.M. Endt. The energy levels of ^{30}P. *Nuclear Physics A*, 435(2):333 – 351, 1985.

[181] P. M. Wallace, E. G. Bilpuch, C. R. Bybee, G. E. Mitchell, E. F. Moore, J. D. Shriner, J. F. Shriner, G. A. Vavrina, and C. R. Westerfeldt. Spectroscopy of the ^{29}Si(p,γ) reaction for E_p=1.75–2.51 mev. *Phys. Rev. C*, 54:2916–2925, Dec 1996.

[182] J. M. Freeman, R. J. Petty, S. D. Hoath, J. S. Ryder, W. E. Burcham, and G. T. A. Squier. *Some (p,n) and (α,n) Reaction Energies Relevant to Superallowed Beta Decay*, pages 126–132. Springer US, Boston, MA, 1976.

[183] C. Wrede, J. A. Caggiano, J. A. Clark, C. Deibel, A. Parikh, and P. D. Parker. New $^{30}\mathrm{P}(p,\gamma)^{31}\mathrm{S}$ resonances and oxygen-neon nova nucleosynthesis. *Phys. Rev. C*, 76:052802, Nov 2007.

[184] A. Parikh, K. Wimmer, T. Faestermann, R. Hertenberger, J. José, R. Longland, H.-F. Wirth, V. Bildstein, S. Bishop, A. A. Chen, J. A. Clark, C. M. Deibel, C. Herlitzius, R. Krücken, D. Seiler, K. Straub, and C. Wrede. Improving the $^{30}\mathrm{P}(p,\gamma)^{31}\mathrm{S}$ rate in oxygen-neon novae: Constraints on J^π values for proton-threshold states in ^{31}S. *Phys. Rev. C*, 83:045806, Apr 2011.

[185] D. T. Doherty, G. Lotay, P. J. Woods, D. Seweryniak, M. P. Carpenter, C. J. Chiara, H. M. David, R. V. F. Janssens, L. Trache, and S. Zhu. Key resonances in the $^{30}\mathrm{P}(p,\gamma)^{31}\mathrm{S}$ gateway reaction for the production of heavy elements in ONe novae. *Phys. Rev. Lett.*, 108:262502, Jun 2012.

[186] A. Kankainen, P.J. Woods, H. Schatz, T. Poxon-Pearson, D.T. Doherty, V. Bader, T. Baugher, D. Bazin, B.A. Brown, J. Browne, A. Estrade, A. Gade, J. José, A. Kontos, C. Langer, G. Lotay, Z. Meisel, F. Montes, S. Noji, F. Nunes, G. Perdikakis, J. Pereira, F. Recchia, T. Redpath, R. Stroberg,

M. Scott, D. Seweryniak, J. Stevens, D. Weisshaar, K. Wimmer, and R. Zegers. Measurement of key resonance states for the ^{30}P$(p,\gamma)^{31}$S reaction rate, and the production of intermediate-mass elements in nova explosions. *Physics Letters B*, 769:549 – 553, 2017.

[187] C. Ouellet and B. Singh. Nuclear data sheets for A=31. *Nuclear Data Sheets*, 114(2):209 – 396, 2013.

[188] A. Kankainen, T. Eronen, S. P. Fox, H. O. U. Fynbo, U. Hager, J. Hakala, J. Huikari, D. G. Jenkins, A. Jokinen, S. Kopecky, I. Moore, A. Nieminen, H. Penttilä, S. Rinta-Antila, O. Tengblad, Y. Wang, and J. Äystö. Excited states in ^{31}S studied via beta decay of ^{31}Cl. *The European Physical Journal A - Hadrons and Nuclei*, 27(1):67–75, Jan 2006.

[189] A. Saastamoinen. *Studies of T_z=3/2 Nuclei of Astrophysical Interest*. PhD thesis, University of Jyväskylä, 2011.

[190] M. B. Bennett, C. Wrede, B. A. Brown, S. N. Liddick, D. Pérez-Loureiro, D. W. Bardayan, A. A. Chen, K. A. Chipps, C. Fry, B. E. Glassman, C. Langer, N. R. Larson, E. I. McNeice, Z. Meisel, W. Ong, P. D. O'Malley, S. D. Pain, C. J. Prokop, H. Schatz, S. B. Schwartz, S. Suchyta, P. Thompson, M. Walters, and X. Xu. Isospin mixing reveals ^{30}P$(p,\gamma)^{31}$S resonance influencing nova nucleosynthesis. *Phys. Rev. Lett.*, 116:102502, Mar 2016.

[191] W. Benenson, D. Mueller, E. Kashy, H. Nann, and L. W. Robinson. Mass of ^{27}P and ^{31}Cl. *Phys. Rev. C*, 15:1187–1190, Apr 1977.

[192] M. Redshaw, J. McDaniel, W. Shi, and E. G. Myers. Mass ratio of two ions in a Penning trap by alternating between the trap center and a large cyclotron orbit. *International Journal of Mass Spectrometry*, 251(2):125 – 130, 2006.

[193] S. Rainville, J. K. Thompson, E. G. Myers, J. M. Brown, M. S. Dewey, E. G. Kessler Jr, R. D. Deslattes, H. G. Börner, M. Jentschel, P. Mutti, and D. E. Pritchard. A direct test of E=mc^2. *Nature*, 438:1096 EP –, Dec 2005.

[194] M. A. Islam, T. J. Kennett, and W. V. Prestwich. Thermal neutron capture in silicon. *Phys. Rev. C*, 41:1272–1275, Mar 1990.

[195] S. Raman, E. T. Jurney, J. W. Starner, and J. E. Lynn. Thermal-neutron capture by silicon isotopes. *Phys. Rev. C*, 46:972–983, Sep 1992.

[196] S. Röttger, A. Paul, and U. Keyser. Prompt (n,γ)-spectrometry for the isotopic analysis of silicon crystals for the Avogadro project. *IEEE Transactions on Instrumentation and Measurement*, 46(2):560–562, April 1997.

[197] A. Paul, S. Röttger, A. Zimbal, and U. Keyser. Prompt (n,γ) mass measurements for the avogadro project. *Hyperfine Interactions*, 132(1):189–194, Jan 2001.

[198] D. G. Jenkins, A. Meadowcroft, C. J. Lister, M. P. Carpenter, P. Chowdhury, N. J. Hammond, R. V. F. Janssens, T. L. Khoo, T. Lauritsen, D. Seweryniak, T. Davinson, P. J. Woods, A. Jokinen, H. Penttila, G. Martínez-Pinedo, and J. José. Reevaluation of the ^{30}P(p,γ)^{31}S astrophysical reaction rate from a study of the T=1/2 mirror nuclei, ^{31}S and ^{31}P. *Phys. Rev. C*, 73:065802, Jun 2006.

[199] L. Axelsson, J. Äystö, M.J.G. Borge, L.M. Fraile, H.O.U. Fynbo, A. Honkanen, P. Hornshøj, A. Jokinen, B. Jonson, P.O. Lipas, I. Martel, I. Mukha, T. Nilsson, G. Nyman, B. Petersen, K. Riisager, M.H. Smedberg, and O. Tengblad. Beta decay of ^{31}Ar. *Nuclear Physics A*, 634(4):475 – 496, 1998.

[200] C. Langer, O. Lepyoshkina, Y. Aksyutina, T. Aumann, S. Beceiro Novo, J. Benlliure, K. Boretzky, M. Chartier, D. Cortina, U. Datta Pramanik, O. Ershova, H. Geissel, R. Gernhäuser, M. Heil, G. Ickert, H. T. Johansson, B. Jonson, A. Keli ć Heil, A. Klimkiewicz, J. V. Kratz, R. Krücken, R. Kulessa, K. Larsson, T. Le Bleis, R. Lemmon, K. Mahata, J. Marganiec, T. Nilsson, V. Panin, R. Plag, W. Prokopowicz, R. Reifarth, V. Ricciardi, D. M. Rossi, S. Schwertel, H. Simon, K. Sümmerer, B. Streicher, J. Taylor, J. R. Vignote, F. Wamers, C. Wimmer, and P. Z. Wu. Thermonuclear reaction ^{30}S(p,γ)^{31}Cl studied via coulomb breakup of ^{31}Cl. *Phys. Rev. C*, 89:035806, Mar 2014.

[201] H.O.U. Fynbo, M.J.G. Borge, L. Axelsson, J. Äystö, U.C. Bergmann, L.M. Fraile, A. Honkanen, P. Hornshøj, Y. Jading, A. Jokinen, B. Jonson, I. Martel, I. Mukha, T. Nilsson, G. Nyman, M. Oinonen, I. Piqueras, K. Riisager, T. Siiskonen, M.H. Smedberg, O. Tengblad, J. Thaysen, and F. Wenander. The $\beta 2p$ decay mechanism of ^{31}Ar. *Nuclear Physics A*, 677(1):38 – 60, 2000.

[202] H. L. Seifert, J. M. Wouters, D. J. Vieira, H. Wollnik, X. G. Zhou, X. L. Tu, Z. Y. Zhou, and G. W. Butler. Mass measurement of neutron-rich isotopes from^{51}Ca to ^{72}Ni. *Zeitschrift fur Physik A Hadrons and Nuclei*, 349:25–32, March 1994.

[203] Y. Bai, D. J. Vieira, H. L. Seifert, and J. M. Wouters. Mass measurement in the fp-shell using the TOFI spectrometer. In *American Institute of Physics Conference Series*, volume 455 of *American Institute of Physics Conference Series*, pages 90–93, December 1998.

[204] M. Matoš. *Isochronous Mass Measurements of Short-Lived Neutron Rich Nuclides at the FRS-ESR Facilities*. PhD thesis, Justus-Liebig-Universität Giessen, 2004.

[205] A. Estradé, M. Matoš, H. Schatz, A. M. Amthor, D. Bazin, M. Beard, A. Becerril, E. F. Brown, R. Cyburt, T. Elliot, A. Gade, D. Galaviz, S. George, S. S. Gupta, W. R. Hix, R. Lau, G. Lorusso, P. Möller, J. Pereira, M. Portillo, A. M. Rogers, D. Shapira, E. Smith, A. Stolz, M. Wallace, and M. Wiescher. Time-of-flight mass measurements for nuclear processes in neutron star crusts. *Phys. Rev. Lett.*, 107:172503, Oct 2011.

[206] M. Matoš, A. Estradé, H. Schatz, D. Bazin, M. Famiano, A. Gade, S. George, W.G. Lynch, Z. Meisel, M. Portillo, A. Rogers, D. Shapira, A. Stolz, M. Wallace, and J. Yurkon. Time-of-flight mass measurements of exotic nuclei. *Nuclear Instruments and Methods in Physics Research Section A: Accelerators, Spectrometers, Detectors and Associated Equipment*, 696:171 – 179, 2012.

[207] Z.P. Meisel. *Extension of the nuclear mass surface for neutron-rich isotopes of argon through iron*. PhD thesis, Michigan State University, 2015.

[208] Xu X., Wang M., Zhang Y.-H., Xu H.-S., Shuai P., Tu X.-L., Y. A. Litvinov, Zhou X.-H., Sun B.-H., Yuan Y.-J., Xia J.-W., Yang J.-C., K. Blaum, Chen R.-J., Chen X.-C., Fu C.-Y., Ge Z., Hu Z.-G., Huang W.-J., Liu D.-W., Lam Y.-H., Ma X.-W., Mao R.-S., T. Uesaka, Xiao G.-Q., Xing Y.-M., T. Yamaguchi, Y. Yamaguchi, Zeng Q., Yan X.-L., Zhao H.-W., Zhao T.-C., Zhang W., and Zhan W.-L. Direct mass measurements of neutron-rich ^{86}Kr projectile fragments and the persistence of neutron magic number N=32 in Sc isotopes. *Chinese Physics C*, 39(10):104001, 2015.

[209] C. Izzo, G. Bollen, M. Brodeur, M. Eibach, K. Gulyuz, J. D. Holt, J. M. Kelly, M. Redshaw, R. Ringle, R. Sandler, S. Schwarz, S. R. Stroberg, C. S. Sumithrarachchi, A. A. Valverde, and A. C. C. Villari. Precision mass measurements of neutron-rich Co isotopes beyond N=40. *Phys. Rev. C*, 97:014309, Jan 2018.

[210] C. J. Izzo. *Mass measurements of neutron-rich Cobalt isotopes beyond N=40 and the development of a single ion Penning trap mass spectrometer for rare isotopes*. PhD thesis, Michigan State University, 2018.

[211] W. F. Mueller, B. Bruyneel, S. Franchoo, M. Huyse, J. Kurpeta, K. Kruglov, Y. Kudryavtsev, N. V. S. V. Prasad, R. Raabe, I. Reusen, P. Van Duppen, J. Van Roosbroeck, L. Vermeeren, L. Weissman, Z. Janas, M. Karny, T. Kszczot, A. Płochocki, K.-L. Kratz, B. Pfeiffer, H. Grawe, U. Köster, P. Thirolf, and W. B. Walters. β decay of ^{66}Co, ^{68}Co, and ^{70}Co. *Phys. Rev. C*, 61:054308, Apr 2000.

[212] S. N. Liddick, W. B. Walters, C. J. Chiara, R. V. F. Janssens, B. Abromeit, A. Ayres, A. Bey, C. R. Bingham, M. P. Carpenter, L. Cartegni, J. Chen, H. L. Crawford, I. G. Darby, R. Grzywacz, J. Harker, C. R. Hoffman, S. Ilyushkin, F. G. Kondev, N. Larson, M. Madurga, D. Miller, S. Padgett, S. V. Paulauskas, M. M. Rajabali, K. Rykaczewski, D. Seweryniak, S. Suchyta, and S. Zhu. Analogous intruder behavior near Ni, Sn, and Pb isotopes. *Phys. Rev. C*, 92:024319, Aug 2015.

[213] A. Spyrou, S. N. Liddick, F. Naqvi, B. P. Crider, A. C. Dombos, D. L. Bleuel, B. A. Brown, A. Couture, L. Crespo Campo, M. Guttormsen, A. C. Larsen, R. Lewis, P. Möller, S. Mosby, M. R. Mumpower, G. Perdikakis, C. J. Prokop,

T. Renstrøm, S. Siem, S. J. Quinn, and S. Valenta. Strong neutron-γ competition above the neutron threshold in the decay of ^{70}Co. *Phys. Rev. Lett.*, 117:142701, Sep 2016.

[214] A. C. Larsen, J. E. Midtbø, M. Guttormsen, T. Renstrøm, S. N. Liddick, A. Spyrou, S. Karampagia, B. A. Brown, O. Achakovskiy, S. Kamerdzhiev, D. L. Bleuel, A. Couture, L. Crespo Campo, B. P. Crider, A. C. Dombos, R. Lewis, S. Mosby, F. Naqvi, G. Perdikakis, C. J. Prokop, S. J. Quinn, and S. Siem. Enhanced low-energy γ-decay strength of ^{70}Ni and its robustness within the shell model. *Phys. Rev. C*, 97:054329, May 2018.

[215] A.I. Morales, G. Benzoni, H. Watanabe, Y. Tsunoda, T. Otsuka, S. Nishimura, F. Browne, R. Daido, P. Doornenbal, Y. Fang, G. Lorusso, Z. Patel, S. Rice, L. Sinclair, P.-A. Söderström, T. Sumikama, J. Wu, Z.Y. Xu, A. Yagi, R. Yokoyama, H. Baba, R. Avigo, F.L. Bello Garrote, N. Blasi, A. Bracco, F. Camera, S. Ceruti, F.C.L. Crespi, G. de Angelis, M.-C. Delattre, Zs. Dombradi, A. Gottardo, T. Isobe, I. Kojouharov, N. Kurz, I. Kuti, K. Matsui, B. Melon, D. Mengoni, T. Miyazaki, V. Modamio-Hoybjor, S. Momiyama, D.R. Napoli, M. Niikura, R. Orlandi, H. Sakurai, E. Sahin, D. Sohler, H. Schaffner, R. Taniuchi, J. Taprogge, Zs. Vajta, J.J. Valiente-Dobón, O. Wieland, and M. Yalcinkaya. Type II shell evolution in A=70 isobars from the N$\geq$40 island of inversion. *Physics Letters B*, 765:328 – 333, 2017.

[216] M. Wang, G. Audi, F.G. Kondev, B. Pfeiffer, J. Blachot, X. Sun, and M. MacCormick. NUBASE2012 evaluation of nuclear properties. *Nuclear Data Sheets*, 120:6 – 7, 2014.

[217] N. Fukunishi, T. Otsuka, and T. Sebe. Vanishing of the shell gap in N=20 neutron-rich nuclei. *Physics Letters B*, 296(3):279 – 284, 1992.

[218] K. Kaneko, M. Hasegawa, T. Mizusaki, and Y. Sun. Magicity and occurrence of a band with enhanced $B(E2)$ in neutron-rich nuclei ^{68}Ni and ^{90}Zr. *Phys. Rev. C*, 74:024321, Aug 2006.

[219] E.A. McCutchan. Nuclear data sheets for A=68. *Nuclear Data Sheets*, 113(6):1735 – 1870, 2012.

[220] M. Hannawald, T. Kautzsch, A. Wöhr, W. B. Walters, K.-L. Kratz, V. N. Fedoseyev, V. I. Mishin, W. Böhmer, B. Pfeiffer, V. Sebastian, Y. Jading, U. Köster, J. Lettry, H. L. Ravn, and the ISOLDE Collaboration. Decay of neutron-rich Mn nuclides and deformation of heavy Fe isotopes. *Phys. Rev. Lett.*, 82:1391–1394, Feb 1999.

[221] M. Sawicka, R. Grzywacz, I. Matea, H. Grawe, M. Pfützner, J. M. Daugas, M. Lewitowicz, D. L. Balabanski, F. Becker, G. Bélier, C. Bingham, C. Borcea, E. Bouchez, A. Buta, M. La Commara, E. Dragulescu, G. de France,

G. Georgiev, J. Giovinazzo, M. Górska, F. Hammache, M. Hass, M. Hellström, F. Ibrahim, Z. Janas, H. Mach, P. Mayet, V. Méot, F. Negoita, G. Neyens, F. de Oliveira Santos, R. D. Page, O. Perru, Zs. Podolyák, O. Roig, K. P. Rykaczewski, M. G. Saint-Laurent, J. E. Sauvestre, O. Sorlin, M. Stanoiu, I. Stefan, C. Stodel, Ch. Theisen, D. Verney, and J. Żylicz. Low energy levels in ^{72}Ni. *Phys. Rev. C*, 68:044304, Oct 2003.

[222] D. Pauwels, O. Ivanov, N. Bree, J. Büscher, T. E. Cocolios, J. Gentens, M. Huyse, A. Korgul, Yu. Kudryavtsev, R. Raabe, M. Sawicka, I. Stefanescu, J. Van de Walle, P. Van den Bergh, P. Van Duppen, and W. B. Walters. Shape isomerism at $N = 40$: Discovery of a proton intruder state in ^{67}Co. *Phys. Rev. C*, 78:041307, Oct 2008.

[223] D. Pauwels, O. Ivanov, N. Bree, J. Büscher, T. E. Cocolios, M. Huyse, Yu. Kudryavtsev, R. Raabe, M. Sawicka, J. Van de Walle, P. Van Duppen, A. Korgul, I. Stefanescu, A. A. Hecht, N. Hoteling, A. Wöhr, W. B. Walters, R. Broda, B. Fornal, W. Krolas, T. Pawlat, J. Wrzesinski, M. P. Carpenter, R. V. F. Janssens, T. Lauritsen, D. Seweryniak, S. Zhu, J. R. Stone, and X. Wang. Structure of ^{65,67}Co studied through the β decay of ^{65,67}Fe and a deep-inelastic reaction. *Phys. Rev. C*, 79:044309, Apr 2009.

[224] C. J. Prokop, B. P. Crider, S. N. Liddick, A. D. Ayangeakaa, M. P. Carpenter, J. J. Carroll, J. Chen, C. J. Chiara, H. M. David, A. C. Dombos, S. Go, J. Harker, R. V. F. Janssens, N. Larson, T. Lauritsen, R. Lewis, S. J. Quinn, F. Recchia, D. Seweryniak, A. Spyrou, S. Suchyta, W. B. Walters, and S. Zhu. New low-energy 0^+ state and shape coexistence in ^{70}Ni. *Phys. Rev. C*, 92:061302, Dec 2015.

[225] C. J. Chiara, D. Weisshaar, R. V. F. Janssens, Y. Tsunoda, T. Otsuka, J. L. Harker, W. B. Walters, F. Recchia, M. Albers, M. Alcorta, V. M. Bader, T. Baugher, D. Bazin, J. S. Berryman, P. F. Bertone, C. M. Campbell, M. P. Carpenter, J. Chen, H. L. Crawford, H. M. David, D. T. Doherty, A. Gade, C. R. Hoffman, M. Honma, F. G. Kondev, A. Korichi, C. Langer, N. Larson, T. Lauritsen, S. N. Liddick, E. Lunderberg, A. O. Macchiavelli, S. Noji, C. Prokop, A. M. Rogers, D. Seweryniak, N. Shimizu, S. R. Stroberg, S. Suchyta, Y. Utsuno, S. J. Williams, K. Wimmer, and S. Zhu. Identification of deformed intruder states in semi-magic ^{70}Ni. *Phys. Rev. C*, 91:044309, Apr 2015.

[226] S. Naimi. *Onsets of nuclear deformation from measurments with the ISOLTRAP mass spectrometer*. PhD thesis, Université Paris 7 Denis Diderot, 2010.

[227] Modern nuclear data evaluation with the talys code system. *Nuclear Data Sheets*, 113(12):2841 – 2934, 2012. Special Issue on Nuclear Reaction Data.

[228] *TALYS User Manual: A Nuclear Reaction Program*.

[229] I. K. B. Kullmann, E. W. Hafli, A. C. Larsen, and E. Lima. Uncertainties in radiative neutron-capture rates relevant to the A$\sim$80 *r*-process peak. *arXiv e-prints*, page arXiv:1801.07522, January 2018.

[230] A. Spyrou, A. C. Larsen, S. N. Liddick, F. Naqvi, B. P. Crider, A. C. Dombos, M. Guttormsen, D. L. Bleuel, A. Couture, L. Crespo Campo, R. Lewis, S. Mosby, M. R. Mumpower, G. Perdikakis, C. J. Prokop, S. J. Quinn, T. Renstrøm, S. Siem, and R. Surman. Neutron-capture rates for explosive nucleosynthesis: the case of $^{68}Ni(n,\gamma)^{69}$Ni. *Journal of Physics G: Nuclear and Particle Physics*, 44(4):044002, 2017.

[231] S. N. Liddick, A. Spyrou, B. P. Crider, F. Naqvi, A. C. Larsen, M. Guttormsen, M. Mumpower, R. Surman, G. Perdikakis, D. L. Bleuel, A. Couture, L. Crespo Campo, A. C. Dombos, R. Lewis, S. Mosby, S. Nikas, C. J. Prokop, T. Renstrom, B. Rubio, S. Siem, and S. J. Quinn. Experimental neutron capture rate constraint far from stability. *Phys. Rev. Lett.*, 116:242502, Jun 2016.

[232] T. Rauscher and F.-K. Thielemann. Astrophysical reaction rates from statistical model calculations. *Atomic Data and Nuclear Data Tables*, 75(1):1 – 351, 2000.

[233] G. Audi and A.H. Wapstra. The 1995 update to the Atomic Mass Evaluation. *Nuclear Physics A*, 595(4):409 – 480, 1995.

INCLUDED ARTICLES

I

HIGH-PRECISION MASS MEASUREMENTS OF ^{25}Al AND ^{30}P AT JYFLTRAP

by

L. Canete, A. Kankainen, T. Eronen, D. Gorelov, J. Hakala, A. Jokinen, V.S. Kolhinen, J. Koponen, I.D. Moore, J. Reinikainen, and S. Rinta-Antila

European Physical Journal A (2016) 52:124

Eur. Phys. J. A (2016) **52**: 124
DOI 10.1140/epja/i2016-16124-0

THE EUROPEAN PHYSICAL JOURNAL A

Regular Article – Experimental Physics

High-precision mass measurements of ^{25}Al and ^{30}P at JYFLTRAP

L. Canete[a], A. Kankainen, T. Eronen, D. Gorelov, J. Hakala, A. Jokinen, V.S. Kolhinen, J. Koponen, I.D. Moore, J. Reinikainen, and S. Rinta-Antila

University of Jyvaskyla, P.O. Box 35 (YFL), FI-40014 University of Jyvaskyla, Jyvaskyla, Finland

Received: 12 January 2016 / Revised: 7 March 2016
Published online: 11 May 2016 –
Communicated by Alexandra Gade

Abstract. The masses of the astrophysically relevant nuclei ^{25}Al and ^{30}P have been measured with a Penning trap for the first time. The mass-excess values for ^{25}Al ($\Delta = -8915.962(63)$ keV) and ^{30}P ($\Delta = -20200.854(64)$ keV) obtained with the JYFLTRAP double Penning trap mass spectrometer are in good agreement with the Atomic Mass Evaluation 2012 values but $\approx$ 5–10 times more precise. A high precision is required for calculating resonant proton-capture rates of astrophysically important reactions $^{25}\mathrm{Al}(p,\gamma)^{26}\mathrm{Si}$ and $^{30}\mathrm{P}(p,\gamma)^{31}\mathrm{S}$. In this work, $Q_{(p,\gamma)} = 5513.99(13)$ keV and $Q_{(p,\gamma)} = 6130.64(24)$ keV were obtained for ^{25}Al and ^{30}P, respectively. The effect of the more precise values on the resonant proton-capture rates has been studied. In addition to nuclear astrophysics, the measured Q_{EC} value of ^{25}Al, 4276.805(45) keV, is relevant for studies of $T = 1/2$ mirror beta decays which have a potential to be used to test the Conserved Vector Current hypothesis.

1 Introduction

Classical novae are frequent and bright phenomena occurring when a white dwarf accretes hydrogen-rich material from its companion star [1,2]. This leads to a thermonuclear runaway which is observed as a sudden increase in the star's luminosity. Novae reach peak temperatures up to $\approx$ 0.4 GK which limits the nucleosynthesis to nuclei with masses below $A \approx 40$. Detailed reaction network calculations have been carried out for nova nucleosynthesis (see, *e.g.*, refs. [3–5]). As the light nuclei close to the $N = Z$ line have become more and more accessible experimentally, the calculations start to have a solid experimental foundation offering a unique possibility to compare with observations. In this work, we have studied nuclei relevant for nova nucleosynthesis, ^{25}Al and ^{30}P.

Novae have been proposed to contribute to the amount of cosmic, 1809 keV beta-delayed γ-rays of ^{26}Al [6,7] which gave the first evidence for ongoing nucleosynthesis in the interstellar medium [8]. More recent observations with the COMPTEL telescope on CGRO [9] and SPI on INTEGRAL [10] have shown that the ^{26}Al distribution in the Galaxy is irregular with some localized regions extended over the entire plane of the Galaxy, thus pointing towards massive stars and their supernovae as a source for galactic ^{26}Al γ-rays [10–12]. The nova contribution to the galactic ^{26}Al has a smoother distribution and is estimated to be less than 0.4 solar masses [6] compared to 2.8(8) solar masses determined from SPI/INTEGRAL data [10]. However, this contribution has to be taken into account, *e.g.*, when estimating the distribution and frequency of core-collapse supernovae in the Galaxy from the amount of cosmic 1809 keV γ-rays.

The production of the ground state of ^{26}Al can be bypassed in novae and other astrophysical scenarios via a reaction sequence leading to the shorter-lived isomeric state of ^{26}Al: $^{25}\mathrm{Al}(p,\gamma)^{26}\mathrm{Si}(\beta^+)^{26}\mathrm{Al}^m$. The isomeric state $^{26}\mathrm{Al}^m$ decays via superallowed beta decay to the ground state of ^{26}Mg, and thus does not contribute to the amount of galactic 1809 keV γ-rays. The proton-capture rate for $^{25}\mathrm{Al}(p,\gamma)^{26}\mathrm{Si}$ has a direct effect on the production of ^{26}Al: the more likely it is to proceed via proton captures than via the sequence $^{25}\mathrm{Al}(\beta^+)^{25}\mathrm{Mg}(p,\gamma)^{26}\mathrm{Al}$, the fewer 1809 keV γ-rays will be produced. The Q value for the $^{25}\mathrm{Al}(p,\gamma)^{26}\mathrm{Si}$ reaction is essential as the reaction rates for the proton captures as well as for the inverse photodisintegration reactions depend exponentially on it. Since the mass of ^{26}Si has already been determined with a high precision at JYFLTRAP [13], the mass of ^{25}Al remains the limiting factor for the precision of the Q value.

About one third of novae have an underlying white dwarf containing oxygen, neon and magnesium. These ONe novae reach higher peak temperatures and can synthesize heavier elements than classical carbon-oxygen novae [14]. There, the reaction $^{30}\mathrm{P}(p,\gamma)^{31}\mathrm{S}$ acts as a gateaway towards heavier elements since the beta-decay half-life of ^{30}P is long ($\approx$ 2.5 min) compared to typical novae timescales. The alternative route via $^{30}\mathrm{S}(p,\gamma)^{31}\mathrm{Cl}$ is hindered by inverse photodisintegration reactions on ^{31}Cl.

[a] e-mail: lacanete@student.jyu.fi

José *et al.* [15] have shown that changing the ^{30}P$(p,\gamma)^{31}$S rate has a dramatic effect on the abundance of ^{30}Si produced via β^+ decay of ^{30}P. The abundance of ^{30}Si is important for assigning presolar grains as being of nova origin [16,17]. These grains have higher than average ^{30}Si/^{28}Si and close to solar ^{29}Si/^{28}Si abundance ratios. Therefore, a more accurate knowledge on the ^{30}P$(p,\gamma)^{31}$S reaction is needed for calculating abundance ratios for different nova environments, to increase our knowledge of novae and underlying white dwarfs in general. The reaction rate depends exponentially on the proton-capture Q value for which the mass of ^{31}S is already well known [18], thus the mass of ^{30}P is the limiting factor in the precision.

In this paper, we have determined the masses of ^{25}Al and ^{30}P with a Penning trap for the first time. The current mass values in the Atomic Mass Evaluation 2012 (AME12) [19] are mainly based on old (p,γ) experiments on ^{24}Mg and ^{29}Si, respectively. The described experiment was also the first on-line mass measurement of neutron-deficient nuclei at the new Ion Guide Isotope Separator On-Line facility, IGISOL-4, at the University of Jyväskylä [20,21]. The 7 T superconducting solenoid housing the JYFLTRAP double Penning trap spectrometer [22] had to be re-energized at IGISOL-4. Therefore, we have also carried out a new measurement of temporal fluctuations of the magnetic field strength in this work.

2 Experimental method

The IGISOL-4 facility at the Accelerator Laboratory of the University of Jyväskylä was employed in combination with the JYFLTRAP double Penning trap mass spectrometer [22] for the mass measurements of ^{25}Al and ^{30}P. A beam of 40 MeV protons from the K-130 cyclotron impinged into a thin, few mg/cm^2 thick Si or ZnS target at the entrance of the IGISOL gas cell. The fusion-evaporation reaction products were stopped in helium gas and extracted with the help of a sextupole ion guide (SPIG) [23]. The continuous beam was accelerated to 30 keV and the mass number A was selected using a 55° dipole magnet with a mass resolving power $(M/\Delta M)$ of ≈ 500. The mass-separated beam was further sent into a radio frequency quadrupole cooler and buncher (RFQ) [24] which decelerates and cools the ions and releases them into JYFLTRAP as short bunches. JYFLTRAP mass spectrometer consists of two Penning traps, the purification trap, which is used for isobaric purification of the beam via the mass-selective buffer gas cooling-technique [25], and the precision trap, which is used for precision mass measurements.

The time-of-flight ion-cyclotron resonance method (TOF-ICR) [26,27] was utilized for the mass measurements. Once the ions were injected into the precision trap, a short magnetron excitation ν_- was applied followed by a quadrupolar excitation. The frequency of the quadrupolar excitation was scanned around the cyclotron frequency ν_c:

$$\nu_c = \nu_+ + \nu_-, \tag{1}$$

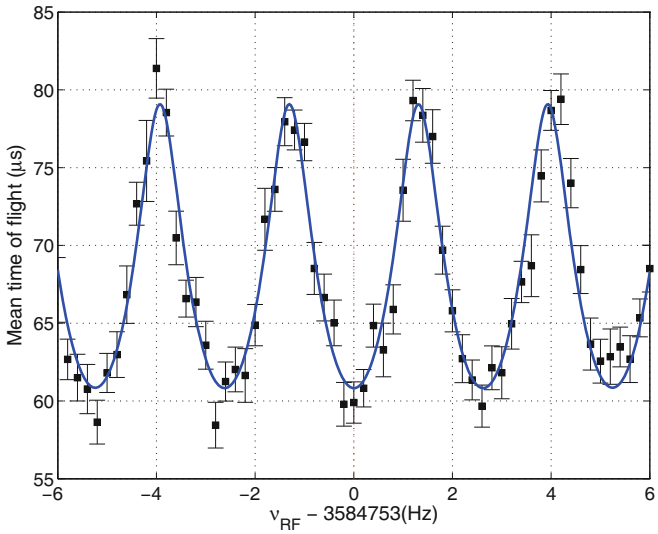

Fig. 1. A Ramsey time-of-flight ion-cyclotron resonance for ^{30}P obtained with an excitation pattern of 25 ms (On) - 350 ms (Off) - 25 ms (On). The number of ions per bunch has been limited to 1-2 ions per bunch and the total number of ions to obtain this spectrum is 1203. The black squares with uncertainties are the average TOF, and the solid (blue) line is the fitted line shape.

where ν_+ is the reduced cyclotron frequency and ν_- the magnetron frequency of the ion. The motion of the ions in the resonance is fully converted from magnetron to cyclotron within the excitation time if the amplitude has been chosen correctly. As a result, the ions in resonance in the strong magnetic field gradient undergo a stronger axial force. Therefore, they have a shorter time of flight from the Penning trap to a micro-channel plate detector (MCP). In this experiment, we used time-separated oscillatory fields for the quadrupolar excitation (Ramsey method) in the precision trap [28–30]. The quadrupolar excitation was applied as two 25 ms fringes separated by 150 ms for ^{25}Al and by 350 ms for ^{30}P. A typical TOF-ICR obtained for ^{30}P is shown in fig. 1.

The mass of the ion m_{ion} depends on the measured cyclotron resonance frequency via eq. (2):

$$\nu_c = \frac{1}{2\pi} \times \frac{qB}{m_{ion}}, \tag{2}$$

where q denotes the charge of the ion and B is the magnetic field strength in the trap. The magnetic field is regularly determined via similar measurements with a reference ion whose atomic mass m_{ref} is already precisely known, and linearly interpolating the cyclotron resonance frequency $\nu_{c,ref}$ to the time of the measurement of the ion of interest. The measured frequencies were corrected for the count-rate effect [31] whenever possible. The atomic mass m for the isotope of interest is then determined via:

$$m = r(m_{ref} - m_e) + m_e, \tag{3}$$

where $r = \nu_{c,ref}/\nu_c$ is the frequency ratio between the reference ion and the ion of interest, and m_e is the electron

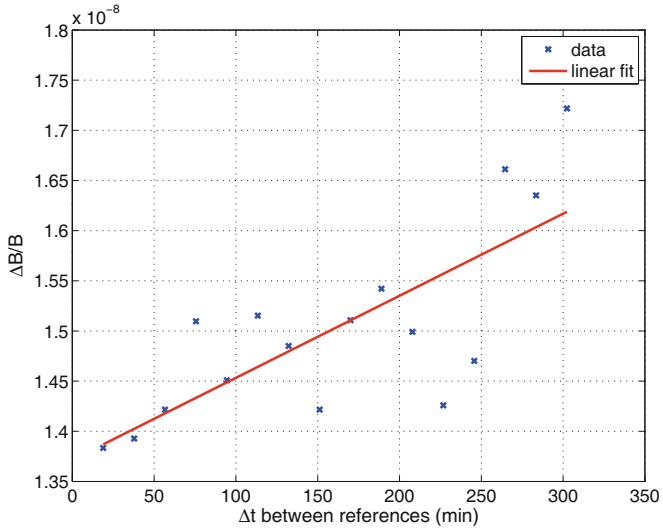

Fig. 2. Standard deviation of the magnetic field obtained for different time differences Δt between two reference measurements taken during one week of frequency measurements using a Ramsey excitation pattern of 25 ms (On) - 350 ms (Off) - 25 ms (On). The slope of the fit is $8.18(19) \times 10^{-12}$/min.

mass. The differences in electron binding energies are sufficiently small to be neglected.

In this work, ^{25}Mg (m = 24.98583698(5) u [32]) and ^{30}Si (m = 29.973770136(23) u [32]) were used as references for ^{25}Al and ^{30}P, respectively. Both reference ions were directly produced from the Si and ZnS targets. The use of ^{25}Mg and ^{30}Si as references had the benefit that systematic effects resulting from field imperfections cancel in the frequency ratio [33]. However, the uncertainty due to temporal fluctuations of the magnetic field strength has to be taken into account for the measured frequency ratios. Since JYFLTRAP was moved to IGISOL-4, the 7 T superconducting solenoid housing it had to be re-energized. To quantify the present magnitude of temporal fluctuations in the magnetic field strength, a separate experiment was carried out in December 2014.

The temporal fluctuations of the magnetic field were studied by measuring the cyclotron frequency of ^{84}Kr$^+$ ions for one week with a Ramsey excitation pattern of 25 ms (On) - 350 ms (Off) - 25 ms (On) with an amplitude of 224 mV. The fluctuation was determined by comparing the cyclotron frequency obtained via interpolating from two reference measurements separated by time Δt to the cyclotron frequency measured in the middle of these two reference measurements. The data were split into ≈ 9.5 min long measurements, thus the shortest time difference between the references was ≈ 19 min. Standard deviations from the weighted average of the frequency ratio were computed for each possible Δt and plotted as a function of Δt (see fig. 2). The obtained magnetic field fluctuation as a function of time is $\sigma_B(\nu_{c,ref})/\nu_{c,ref} = 8.18(19) \times 10^{-12}/\min \times \Delta t$ which is less than previously measured at IGISOL-3, $3.22(16) \times 10^{-11}/\min \times \Delta t$ [34] and $5.7(8) \times 10^{-11}/\min \times \Delta t$ [35]. This is likely to be due to smaller temperature variations at IGISOL-4. Daily fluctuations of temperature were below 0.6 °C in the laboratory. The facility is now located in a separate hall without direct access to outdoors and insulators have been added to the high-voltage cage of JYFLTRAP resulting in more stable conditions. Also, the magnet stand is now made of aluminium and thus does not contain ferromagnetic material anymore.

Table 1. Number of measurements #, frequency ratios r and the mass-excess Δ, Q_{EC} and $Q_{(p,\gamma)}$ values (in keV) determined in this work in comparison with the AME12 values. ^{25}Mg$^+$ ions were used as a reference for ^{25}Al and ^{30}Si$^+$ for ^{30}P.

Ion	^{25}Al	^{30}P
#	42	12
r	1.0001837618(19)	1.0001515804(22)
Δ	−8915.962(63)	−20200.854(64)
Δ_{AME12}	−8916.2(5)	−20200.6(3)
Difference	0.2(5)	−0.2(3)
Q_{EC}	4276.805(45)	4232.106(60)
$Q_{EC,AME12}$	4276.6(5)	4232.4(3)
$Q_{(p,\gamma)}$	5513.99(13)	6130.64(24)
$Q_{(p,\gamma),AME12}$	5513.8(5)	6130.9(4)

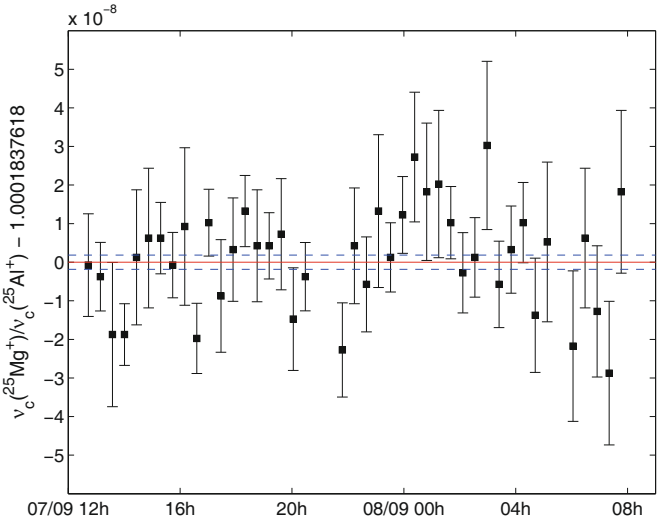

Fig. 3. Measured frequency ratios for ^{25}Al. The red line corresponds to the weighted mean of the frequency ratios and the dashed lines show the 1σ uncertainty limits.

3 Results

3.1 The results for ^{25}Al

The results of this work are summarized in table 1. In total, 42 frequency ratios were measured within 20 hours for ^{25}Al. The weighted mean of the frequency ratios gives r = 1.0001837618(19) (see fig. 3). The Birge ratio was 0.98 [36] which shows that there are no hidden systematic

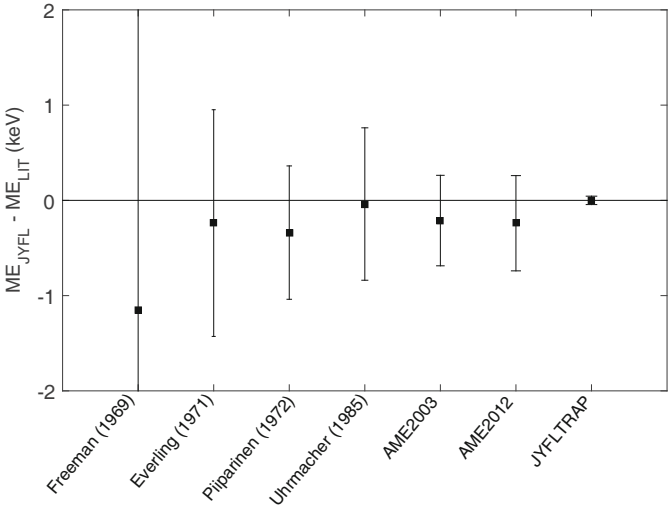

Fig. 4. Mass-excess values of ^{25}Al from previous experiments in comparison with the new JYFLTRAP value. From left to right: Freeman *et al.* ^{25}Mg$(p,n)^{25}$Al [37], Everling *et al.* ^{24}Mg$(p,\gamma)^{25}$Al [38], Piiparinen ^{24}Mg$(p,\gamma)^{25}$Al [39], Uhrmacher *et al.* ^{24}Mg$(p,\gamma)^{25}$Al [40], AME03 [41] and AME12 [32].

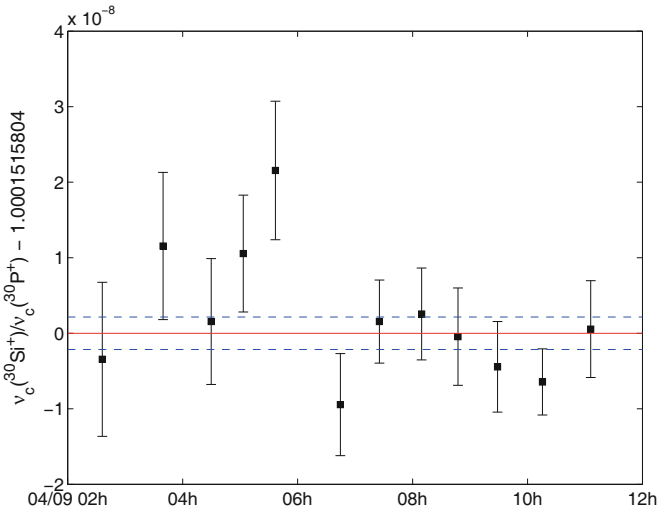

Fig. 5. Measured frequency ratios for ^{30}P. The red line corresponds to the weighted mean of the frequency ratios and the dashed lines show the 1σ uncertainty limits.

errors in our data. Therefore, the inner error was taken as the final uncertainty.

The measured mass-excess value for ^{25}Al, $-8915.962(63)$ keV, is very close to, but about 7 times more precise than the adopted value in the AME12 [32]. The AME12 value is based on ^{25}Mg$(p,n)^{25}$Al [37] and ^{24}Mg$(p,\gamma)^{25}$Al [38–40] experiments (see fig. 4). With our new direct mass measurement of ^{25}Al we can confirm the adopted value and improve the accuracy of the ^{25}Al mass considerably.

We also directly measured the Q_{EC} value of ^{25}Al which is important for fundamental physics as it is an isospin $T = 1/2$ mirror nucleus. Mirror beta-decay Q_{EC} values can be used to extract data for testing the Conserved Vector Current hypothesis provided that the Fermi to Gamow-Teller mixing ratio is already known [42,43]. In this work, we have improved the precision from 500 eV to 45 eV. A more precise Q_{EC} value will result in a more precise ft value for the beta decay which can be used to determine, *e.g.*, the mixing ratio.

Since the mass of ^{26}Si has already been precisely measured with JYFLTRAP [13], a precise proton-capture Q value for ^{25}Al$(p,\gamma)^{26}$Si, $Q_{(p,\gamma)} = 5513.99(13)$ keV, is obtained with the new ^{25}Al mass-excess value. The impact of the new Q value on the astrophysical resonant capture calculations is discussed in sect. 4.

3.2 The results for ^{30}P

Altogether twelve frequency ratios were measured for ^{30}P (see fig. 5). The Birge ratio was 1.13, and thus the outer error was adopted as the final error of the weighted mean $r = 1.0001515804(22)$. The obtained mass-excess value for ^{30}P, -20200.854 (64) keV, is a little lower than in AME12 but almost five times more precise. The adopted mass value of ^{30}P in AME12 has been mainly based on ^{29}Si$(p,\gamma)^{30}$P [44–46] and ^{30}Si$(p,n)^{30}$P [47] measurements (see fig. 6). Our new Penning trap measurement is in a good agreement with the earlier experiments.

The proton-capture Q value for the ^{30}P$(p,\gamma)^{31}$S reaction, $Q_{(p,\gamma)} = 6130.64(24)$ keV, has been determined with an improved precision using the AME12 mass for ^{31}S based on a previous JYFLTRAP measurement [18] and the newly measured ^{30}P mass. The impact of the new proton-capture Q value on resonant proton-capture rates is discussed in sect. 4.

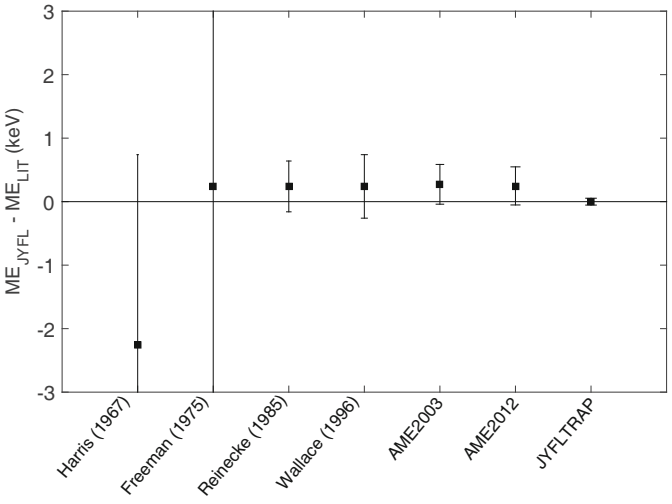

Fig. 6. Mass-excess values of ^{30}P from previous experiments in comparison with the new JYFLTRAP value. From left to right: Harris *et al.* ^{29}Si$(p,\gamma)^{30}$P [44], Freeman *et al.* ^{30}Si$(p,n)^{30}$P [47], Reinecke *et al.* ^{29}Si$(p,\gamma)^{30}$P [45], Wallace *et al.* ^{29}Si$(p,\gamma)^{30}$P [46], AME03 [41] and AME12 [32].

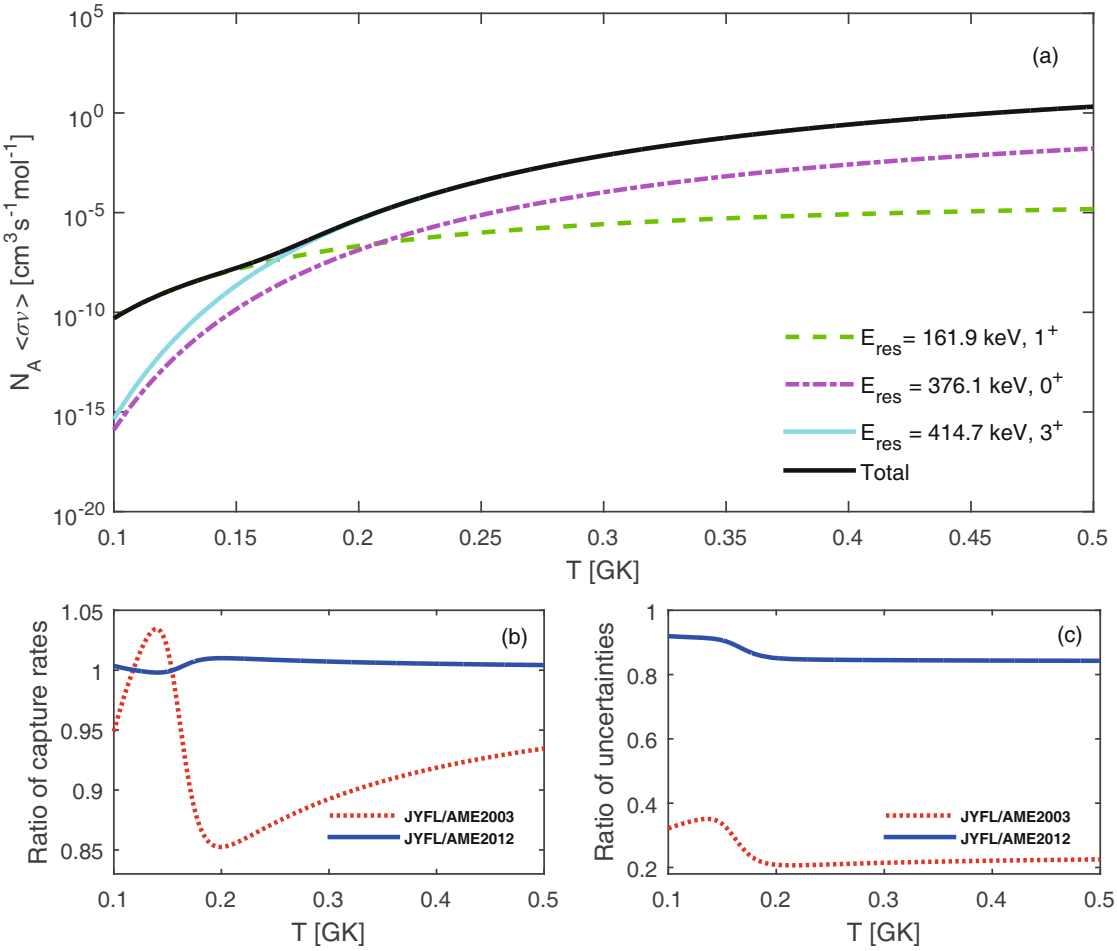

Fig. 7. (a) The resonant proton-capture rates to the 1^+, 0^+ and 3^+ states in ^{26}Si calculated with the $Q_{(p,\gamma)}$ value from this work (JYFL). (b) Ratios of the total resonant proton-capture rate calculated with the JYFLTRAP $Q_{(p,\gamma)}$ value and with the values from AME03 [41] or AME12 [32]. (c) Ratios of the Q-value–related uncertainties in the calculated total resonant proton-capture reaction rates.

4 Discussion

In this section we discuss the impact of the new $Q_{(p,\gamma)}$ values on the resonant proton-capture rates on ^{25}Al and ^{30}P. For both nuclei, the proton captures are dominated by resonant captures to a few states above the proton threshold in ^{26}Si and ^{31}S, respectively. In general, the total resonant proton-capture rate $N_A\langle\sigma v\rangle_{res}$ can be summed over individual resonances to resonance states i located at excitation energies $E_{x,i}$ with resonance energies $E_{r,i} = E_{x,i} - Q_{(p,\gamma)}$:

$$N_A\langle\sigma v\rangle_{res} = 1.54 \times 10^{11}(\mu T_9)^{-3/2} \sum_i (\omega\gamma)_i \times \exp(-11.605 E_{r,i}/T_9)\,\mathrm{cm^3\,mol^{-1}\,s^{-1}}, \quad (4)$$

where the resonance energies are given in MeV, μ is the reduced mass in atomic mass units, T_9 temperature in GK and $\omega\gamma_i$ is the resonance strength. The resonance strength $\omega\gamma_i$ for an isolated resonance in a (p,γ) reaction is given by

$$\omega\gamma = \frac{2J_i+1}{2(2J_t+1)}\frac{\Gamma_p\Gamma_\gamma}{\Gamma_{\mathrm{tot}}}, \quad (5)$$

where J_i and J_t are the spins of the resonance state and the target nucleus ($J_t = 5/2$ for ^{25}Al and $J_t = 1$ for ^{30}P) and the total width Γ_{tot} is the sum of the proton width Γ_p and the gamma width Γ_γ. The proton widths have been scaled from the literature values using the relation [48]:

$$\Gamma_p \propto \exp\left(-31.29 Z_1 Z_2 \sqrt{\frac{\mu}{E_r}}\right), \quad (6)$$

where Z_1 and Z_2 are the proton numbers of the incoming particles, μ is the reduced mass in u and E_r is the center-of-mass resonance energy in keV [48].

The new proton-capture Q value for $^{25}\mathrm{Al}(p,\gamma)^{26}\mathrm{Si}$ is 5513.99(13) keV, which is 0.2 keV higher than in AME12 ($Q_{(p,\gamma)} = 5513.8(5)$ keV [32]) and around 3 keV lower than in AME03 ($Q_{(p,\gamma)} = 5517(3)$ keV [41]). Although the Q value did not change dramatically, the uncertainties related to the proton-capture Q value have been reduced considerably with the high-precision measurements of ^{25}Al (this work) and ^{26}Si [13] at JYFLTRAP: the Q value is now 23 times and 4 times more precise than in AME03 and AME12, respectively.

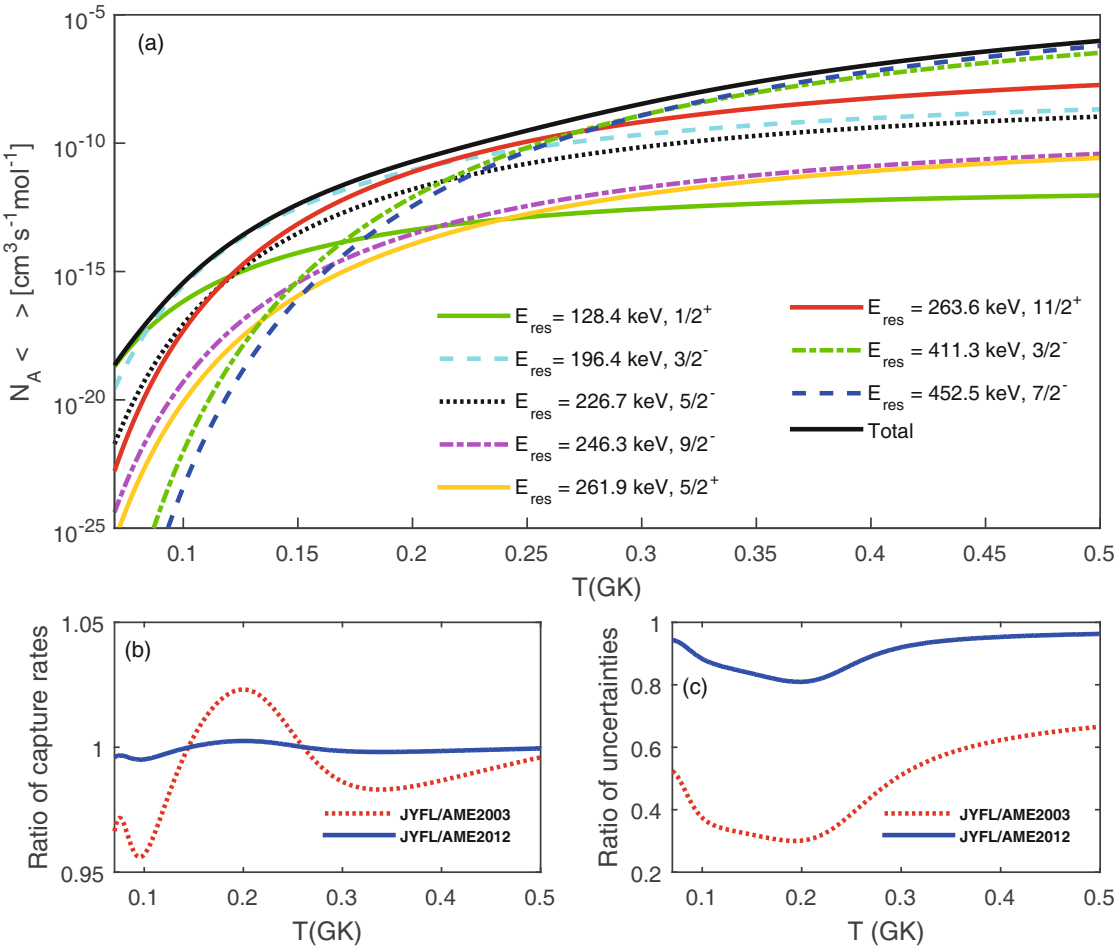

Fig. 8. (a) The resonant proton-capture rates to the $1/2^+$, $3/2^-$, $5/2^-$, $9/2^-$, $5/2^+$, $11/2^+$, $3/2^-$ and $7/2^-$ states in ^{31}S calculated with the $Q_{(p,\gamma)}$ value from this work (JYFL). (b) Ratios of the total resonant proton-capture rate calculated with the JYFLTRAP $Q_{(p,\gamma)}$ value and the values from AME03 [41] or AME12 [32]. (c) Ratios of the Q-value–related uncertainties in the calculated total resonant proton-capture reaction rates.

The resonant proton captures on ^{25}Al are dominated by captures to a few levels with rather low resonance energies. The knowledge of these states has improved considerably thanks to several measurements on the excited levels of ^{26}Si [49–61]. Gamma-decay studies of ^{26}Si performed at Gammasphere [54,60] have shown that there is a 4^+ state at 5517.0 keV, a 1^+ level at 5675.9 keV and a 0^+ state at 5890.1 keV. A 3^+ state at 5928.7 keV has been confirmed via beta-decay studies of ^{26}P [51,58] and it is also supported by [50,53,56]. The spin for the next excited state at 5946 keV is unclear. It has been claimed to be a 0^+ [52] as well as 3^+ [49]. The shell-model calculations [62] suggest it to be 0^+ but interestingly, they do not predict another 0^+ state at around 5890 keV although it has been experimentally observed [57,59,60]. The resonant proton captures to the 1^+ state at 5676 keV dominate the total reaction rate at temperatures below $T \approx 0.15$ GK. At higher temperatures, the captures to the 3^+ state take over (see fig. 7(a)).

To demonstrate the effect of the JYFLTRAP $Q_{(p,\gamma)}$ value for the ^{25}Al$(p,\gamma)^{26}$Si reaction, we have calculated the resonant proton-capture rates in ^{26}Si using the $Q_{(p,\gamma)}$ values from AME03 [41], AME12 [32] and from this work (see fig. 7) to the dominating 1^+, 0^+ and 3^+ states. The level at 5946 keV was not included due to its uncertain spin and parity assignments. The corresponding excitation energies 5675.9(11) keV, 5890.1(6) keV and 5928.7(7) keV were taken from Doherty *et al.* [60] for the 1^+ and 0^+ states, and from Bennett *et al.* [58] for the 3^+ state. We also calculated upper and lower limits for the rates by taking into account the uncertainties in the Q values and compared the widths of these uncertainty bands to each other. For calculating the resonance strengths, proton widths from ref. [62] for the 1^+ state, $\Gamma_p = 6.30 \times 10^{-9}$ eV ($E_{res} = 163$ keV), the 0^+ state $\Gamma_p = 1.6 \times 10^{-2}$ eV ($E_{res} = 434$ keV) and the 3^+ state $\Gamma_p = 3.5$ eV ($E_{res} = 403$ keV) have been scaled using eq. (6). A gamma width of $\Gamma_\gamma = 0.12$ eV was used for the 1^+ and 3^+ states and $\Gamma_\gamma = 8.8 \times 10^{-3}$ eV for the 0^+ state similar to ref. [62]. As can be seen from fig. 7(b), the JYFLTRAP and AME12 rates are very close to each other: the JYFLTRAP Q value gives a few percent higher capture rate than the AME12 value. The Q-value–related uncertainties have been reduced by around 10–15% compared to the AME12 value and 60–80% compared to the AME03 value (see fig. 7(c)).

The proton-capture Q value obtained for $^{30}\mathrm{P}(p,\gamma)^{31}\mathrm{S}$ in this work, 6130.64(24) keV, is ≈ 0.2 keV lower than in AME12 ($Q_{(p,\gamma)} = 6130.9(4)$ keV [32]) and 2.4 keV lower than in AME03 ($Q_{(p,\gamma)} = 6133.0(15)$ keV [41]). The $Q_{(p,\gamma)}$ value is now known with an ≈ 6 times better precision than in AME03 and almost 2 times better than in AME12 due to the JYFLTRAP measurements of ^{30}P (this work) and ^{31}S [18]. The impact of the new Q value on the resonant proton-capture rate on ^{30}P was studied similarly to the $^{25}\mathrm{Al}(p,\gamma)^{26}\mathrm{Si}$ reaction. There are more known resonant states above the proton separation energy in ^{31}S than in ^{26}Si, and they are rather well-known via studies at Gammasphere employing both heavy-ion fusion-evaporation reactions [63,64], and more recently, light-ion fusion-evaporation reactions [65,66]. The resonance states have also been explored, *e.g.*, via $^{31}\mathrm{P}(^3\mathrm{He},t)^{31}\mathrm{S}$ reactions at Yale University's Wright Nuclear Structure Laboratory [67,68] and at Maier-Leibnitz-Laboratorium in Garching [69]. A recent review [70] gives a thorough summary of the previous studies and relevant states in ^{31}S.

Here, we have calculated the resonant proton-capture rates to the $1/2^+$ ($E_{res} = 128.4$ keV), $3/2^-$ ($E_{res} = 196.4$ keV), $5/2^-$ ($E_{res} = 226.7$ keV), $9/2^-$ ($E_{res} = 246.3$ keV), $5/2^+$ ($E_{res} = 261.9$ keV), $11/2^+$ ($E_{res} = 263.6$ keV), $3/2^-$ ($E_{res} = 411.3$ keV) and $7/2^-$ ($E_{res} = 452.5$ keV) states to demonstrate the effect of the new Q value (see fig. 8). The resonant proton captures on ^{30}P are dominated by captures to the $1/2^+$ ($E_{res} = 128.4$ keV) state below $T \approx 0.08$ GK and to the $3/2^-$ ($E_{res} = 196.4$ keV) state at $T \approx 0.08$–0.2 GK. At around $T = 0.2$ GK, captures to the $11/2^+$ ($E_{res} = 263.6$ keV) state become important, and at higher temperatures, the $3/2^-$ ($E_{res} = 411.3$ keV) and $7/2^-$ ($E_{res} = 452.5$ keV) states dominate. The proton widths have been scaled from ref. [67] using eq. (6) and the excitation energies were taken from [65,70]. The state at 6357 keV ($E_{res} = 226.7$ keV) has contradictory spin assignments of $3/2^+$ [69], $5/2^+$ [67,68], and $5/2^-$ [65,66]. Here we have adopted the same assignment as in refs. [67,68] but note that this choice may have an effect on the reaction rate at lower temperatures. The revised total resonant proton-capture rate is very close to the result obtained with the AME12 value (see fig. 8(b)) and the mass-related uncertainties have been reduced by 5–20% compared to the AME12 and 40–70% compared to the AME03 (see fig. 8(c)).

5 Conclusions

We have performed the first Penning-trap mass measurements of ^{25}Al and ^{30}P at JYFLTRAP resulting in unparalleled precisions of 63 eV and 64 eV, respectively. Our results agree with the adopted values in AME12 [32] which are mainly based on (p,γ) reaction studies, and thus confirm that those experiments have not suffered from significant systematic uncertainties. The experiment was also the first on-line mass measurement of neutron-deficient nuclei at IGISOL-4, and therefore an additional study of the stability of the magnetic field inside the JYFLTRAP was carried out using $^{84}\mathrm{Kr}^+$ ions. The temporal fluctuations in the magnetic field were found to be smaller than at the old IGISOL-3 facility, likely to be due to better temperature regulation in the new laboratory hall. The effect of new, more precise mass values on calculated resonant proton-capture rates on ^{25}Al and ^{30}P have been studied. These reactions, $^{25}\mathrm{Al}(p,\gamma)^{26}\mathrm{Si}$ and $^{30}\mathrm{P}(p,\gamma)^{31}\mathrm{S}$, are crucial for estimating the production of ^{26}Al in Galaxy and the abundancies of elements heavier than sulphur synthesized in novae. Although the JYFLTRAP Q values did not change the calculated resonant capture rates considerably, the more accurate Q values reduce the mass-related uncertainties in the reaction rates by $\approx 15\%$ compared to the AME12 values, and confirm that there are no systematic uncertainties related to the adopted Q values.

This work has been supported by the EU 7th framework programme Integrating Activities - Transnational Access, project number: 262010 (ENSAR) and by the Academy of Finland under the Finnish Centre of Excellence Programme 2012-2017 (Nuclear and Accelerator Based Physics Research at JYFL). AK and LC acknowledge the support from the Academy of Finland under project No. 275389.

References

1. J.S. Gallagher, S. Starrfield, Annu. Rev. Astron. Astrophys. **16**, 171 (1978).
2. A. Parikh, J. José, G. Sala, AIP Adv. **4**, 041002 (2014).
3. J. José, M. Hernanz, C. Iliadis, Nucl. Phys. A **777**, 550 (2006) special issue on Nuclear Astrophysics.
4. J. José, M. Hernanz, J. Phys. G: Nucl. Part. Phys. **34**, R431 (2007).
5. J. José, C. Iliadis, Rep. Prog. Phys. **74**, 096901 (2011).
6. J. José, M. Hernanz, A. Coc, Astrophys. J. Lett. **479**, L55 (1997).
7. J. José, A. Coc, M. Hernanz, Astrophys. J. **520**, 347 (1999).
8. W.A. Mahoney, J.C. Ling, A.S. Jacobson, R.E. Lingenfelter, Astrophys. J. **262**, 742 (1982).
9. R. Diehl *et al.*, Astron. Astrophys. **298**, 445 (1995).
10. R. Diehl *et al.*, Nature **439**, 45 (2006).
11. R. Diehl, Astron. Rev. **8**, 030000 (2013).
12. R. Diehl, Rep. Prog. Phys. **76**, 026301 (2013).
13. T. Eronen *et al.*, Phys. Rev. C **79**, 032802 (2009).
14. J. José, M. Hernanz, Astrophys. J. **494**, 680 (1998).
15. J. José, A. Coc, M. Hernanz, Astrophys. J. **560**, 897 (2001).
16. S. Amari *et al.*, Astrophys. J. **551**, 1065 (2001).
17. J. José *et al.*, Astrophys. J. **612**, 414 (2004).
18. A. Kankainen *et al.*, Phys. Rev. C **82**, 052501 (2010).
19. G. Audi *et al.*, Chin. Phys. C **36**, 1287 (2012).
20. I. Moore *et al.*, Nucl. Instrum. Methods Phys. Res. B **317**, 208 (2013).
21. V. Kolhinen *et al.*, Nucl. Instrum. Methods Phys. Res. B **317**, 506 (2013).
22. T. Eronen *et al.*, Eur. Phys. J. A **48**, 46 (2012).
23. P. Karvonen *et al.*, Nucl. Instrum. Methods Phys. Res. B **266**, 4794 (2008).
24. A. Nieminen *et al.*, Nucl. Instrum. Methods Phys. Res. A **469**, 244 (2001).

25. G. Savard *et al.*, Phys. Lett. A **158**, 247 (1991).
26. M. König *et al.*, Int. J. Mass Spectrom. Ion Process. **142**, 95 (1995).
27. G. Gräff, H. Kalinowsky, J. Traut, Z. Phys. A **297**, 35 (1980).
28. S. George *et al.*, Int. J. Mass Spectrom. **264**, 110 (2007).
29. S. George *et al.*, Phys. Rev. Lett. **98**, 162501 (2007).
30. M. Kretzschmar, Int. J. Mass Spectrom. **264**, 122 (2007).
31. A. Kellerbauer *et al.*, Eur. Phys. J. D **22**, 53 (2003).
32. M. Wang *et al.*, Chin. Phys. C **36**, 1603 (2012).
33. C. Roux *et al.*, Eur. Phys. J. D **67**, 146 (2013).
34. S. Rahaman *et al.*, Eur. Phys. J. A **34**, 5 (2007).
35. V.-V. Elomaa *et al.*, Nucl. Instrum. Methods Phys. Res. A **612**, 97 (2009).
36. R.T. Birge, Phys. Rev. **40**, 207 (1932).
37. J.M. Freeman *et al.*, Nucl. Phys. A **132**, 593 (1969).
38. F. Everling *et al.*, Can. J. Phys. **49**, 402 (1971).
39. M. Piiparinen, Z. Phys. **252**, 206 (1972).
40. M. Uhrmacher *et al.*, Nucl. Instrum. Methods Phys. Res. B **9**, 234 (1985).
41. G. Audi, A. Wapstra, C. Thibault, Nucl. Phys. A **729**, 337 (2003).
42. N. Severijns, M. Tandecki, T. Phalet, I.S. Towner, Phys. Rev. C **78**, 055501 (2008).
43. O. Naviliat-Cuncic, N. Severijns, Phys. Rev. Lett. **102**, 142302 (2009).
44. G.I. Harris, A.K. Hyder, Phys. Rev. **157**, 958 (1967).
45. J. Reinecke *et al.*, Nucl. Phys. A **435**, 333 (1985).
46. P.M. Wallace *et al.*, Phys. Rev. C **54**, 2916 (1996).
47. J.M. Freeman *et al.*, *Proceedings of the 5th International Conference on Atomic Masses and Fundamental Constants AMCO-5*, edited by J.H. Sanders, A.H. Wapstra (Plenum Press, London, New York, 1975) p. 126.
48. C.E. Rolfs, W.S. Rodney, *Cauldrons in the Cosmos* (The University Chicago Press, Chicago, 1988).
49. J.A. Caggiano *et al.*, Phys. Rev. C **65**, 055801 (2002).
50. D.W. Bardayan *et al.*, Phys. Rev. C **65**, 032801 (2002).
51. J.-C. Thomas *et al.*, Eur. Phys. J. A **21**, 419 (2004).
52. Y. Parpottas *et al.*, Phys. Rev. C **70**, 065805 (2004).
53. D.W. Bardayan *et al.*, Phys. Rev. C **74**, 045804 (2006).
54. D. Seweryniak *et al.*, Phys. Rev. C **75**, 062801 (2007).
55. P.N. Peplowski *et al.*, Phys. Rev. C **79**, 032801 (2009).
56. K.A. Chipps *et al.*, Phys. Rev. C **82**, 045803 (2010).
57. N. de Séréville *et al.*, PoS **NIC XI**, 212 (2010).
58. M.B. Bennett *et al.*, Phys. Rev. Lett. **111**, 232503 (2013).
59. T. Komatsubara *et al.*, Eur. Phys. J. A **50**, 136 (2014).
60. D.T. Doherty *et al.*, Phys. Rev. C **92**, 035808 (2015).
61. Y. Parpottas *et al.*, Phys. Rev. C **73**, 049907 (2006).
62. W.A. Richter, B.A. Brown, A. Signoracci, M. Wiescher, Phys. Rev. C **83**, 065803 (2011).
63. D.G. Jenkins *et al.*, Phys. Rev. C **72**, 031303 (2005).
64. D.G. Jenkins *et al.*, Phys. Rev. C **73**, 065802 (2006).
65. D.T. Doherty *et al.*, Phys. Rev. Lett. **108**, 262502 (2012).
66. D.T. Doherty *et al.*, Phys. Rev. C **89**, 045804 (2014).
67. C. Wrede *et al.*, Phys. Rev. C **76**, 052802 (2007).
68. C. Wrede *et al.*, Phys. Rev. C **79**, 045803 (2009).
69. A. Parikh *et al.*, Phys. Rev. C **83**, 045806 (2011).
70. C. Wrede, AIP Adv. **4**, 041004 (2014).

Eur. Phys. J. A (2016) **52**: 302
DOI 10.1140/epja/i2016-16302-0

THE EUROPEAN PHYSICAL JOURNAL A

Erratum

Erratum to: High-precision mass measurements of ^{25}Al and ^{30}P at JYFLTRAP

L. Canete[a], A. Kankainen, T. Eronen, D. Gorelov, J. Hakala, A. Jokinen, V.S. Kolhinen, J. Koponen, I.D. Moore, J. Reinikainen, and S. Rinta-Antila

University of Jyvaskyla, P.O. Box 35 (YFL), FI-40014 University of Jyvaskyla, Jyvaskyla, Finland

Original article: Eur. Phys. J. A (2016) **52**: 124, DOI: 10.1140/epja/i2016-16124-0

Received: 11 August 2016
Published online: 30 September 2016 –

The scaling values on the y-axis of fig. 8(a) were not properly indicated. The correct fig. 8 is given below. This does not affect the results of the publication and the overall shape of the plot.

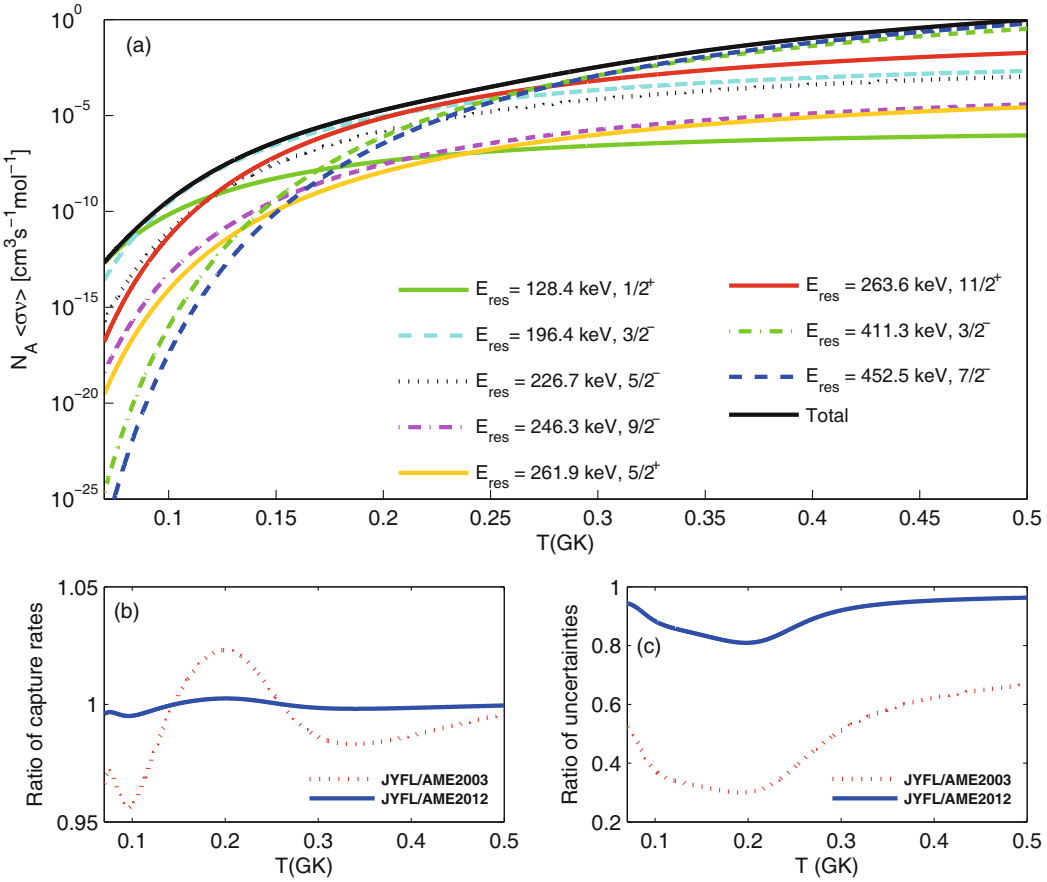

Fig. 8. (a) The resonant proton-capture rates to the $1/2^+$, $3/2^-$, $5/2^-$, $9/2^-$, $5/2^+$, $11/2^+$, $3/2^-$ and $7/2^-$ states in ^{31}S calculated with the $Q_{(p,\gamma)}$ value from this work (JYFL). (b) Ratios of the total resonant proton-capture rate calculated with the JYFLTRAP $Q_{(p,\gamma)}$ value and the values from AME03 [41] or AME12 [32]. (c) Ratios of the Q-value–related uncertainties in the calculated total resonant proton-capture reaction rates.

[a] e-mail: lacanete@student.jyu.fi

II

MASS OF ASTROPHYSICALLY RELEVANT ^{31}Cl AND THE BREAKDOWN OF THE ISOBARIC MULTIPLET MASS EQUATION

by

A. Kankainen, L. Canete, T. Eronen, J. Hakala, A. Jokinen, J. Koponen, I. D. Moore, D. Nesterenko, J. Reinikainen, S. Rinta-Antila, A. Voss, and J. Äystö

Physical Review C 93, 041304(R) (2016)

PHYSICAL REVIEW C **93**, 041304(R) (2016)

Mass of astrophysically relevant ^{31}Cl and the breakdown of the isobaric multiplet mass equation

A. Kankainen,[1,*] L. Canete,[1] T. Eronen,[1] J. Hakala,[1] A. Jokinen,[1] J. Koponen,[1] I. D. Moore,[1] D. Nesterenko,[1] J. Reinikainen,[1] S. Rinta-Antila,[1] A. Voss,[1] and J. Äystö[2]

[1]*University of Jyvaskyla, P.O. Box 35, FI-40014 University of Jyvaskyla, Finland*

[2]*Helsinki Institute of Physics, P.O. Box 64, FI-00014 University of Helsinki, Finland*

(Received 25 November 2015; revised manuscript received 16 March 2016; published 22 April 2016)

The mass of ^{31}Cl has been measured with the JYFLTRAP double-Penning-trap mass spectrometer at the Ion Guide Isotope Separator On-Line (IGISOL) facility. The determined mass-excess value, −7034.7(34) keV, is 15 times more precise than in the Atomic Mass Evaluation 2012. The quadratic form of the isobaric multiplet mass equation for the $T = 3/2$ quartet at $A = 31$ fails ($\chi_n^2 = 11.6$) and a nonzero cubic term, $d = -3.5(11)$ keV, is obtained when the new mass value is adopted. ^{31}Cl has been found to be less proton-bound, with a proton separation energy of $S_p = 264.6(34)$ keV. Energies for the excited states in ^{31}Cl and the photodisintegration rate on ^{31}Cl have been determined with significantly improved precision by using the new S_p value. The improved photodisintegration rate helps to constrain astrophysical conditions where ^{30}S can act as a waiting point in the rapid proton capture process in type-I x-ray bursts.

DOI: 10.1103/PhysRevC.93.041304

^{31}Cl is a short-lived [$T_{1/2} = 190(1)$ ms [1]] sd-shell nucleus and a well-known beta-delayed proton emitter [1–5]. However, its mass-excess value ($\Delta = -7066(50)$ keV [6]) is still based on a single Q-value measurement of the ^{36}Ar(^{3}He,^{8}Li)^{31}Cl reaction performed at Michigan State University in the 1970s [7]. The mass of ^{31}Cl is relevant for testing the isobaric multiplet mass equation (IMME) [8,9] because it is a member of the $T = 3/2$ isobaric quartet with isospin projection $T_Z = (N - Z)/2 = -3/2$. According to the IMME, the masses of the isobaric analog states (IASs) in a mass multiplet should show purely quadratic behavior: $M(A,T,T_Z) = a(A,T) + b(A,T)T_Z + c(A,T)T_Z^2$ after treating the Coulomb interaction by using first-order perturbation theory. Previous IMME evaluations have shown that the quadratic form works well for the $T = 3/2$ quartet at $A = 31$ [10–14] but the test has not been very stringent, mainly due to the uncertainty in the ^{31}Cl mass. Overall, the quadratic form of the IMME has failed only in a few cases, such as at $A = 8$ [15], $A = 9$ [16], $A = 21$ [17], $A = 32$ [18,19], $A = 35$ [20], and $A = 53$ [21]. The breakdown of the IMME has been explained, e.g., by isospin mixing of the states and charge-dependent effects [16,22]. However, for some cases, such as for the $A = 53$ quartet [21], even detailed shell-model calculations have not been able to describe the breakdown.

The mass of ^{31}Cl is also relevant for the rapid proton capture (rp) process occurring in type-I x-ray bursts (XRBs) [23,24]. There, most of the nucleosynthetic flow proceeds through ^{30}S, which can act as a waiting point due to its half-life [1.178(5) s [25]] and low proton-capture Q value establishing a $(p,\gamma) - (\gamma,p)$ equilibrium towards ^{30}S at high temperatures. The route via the ^{30}S$(\alpha,p)^{33}$Cl reaction is hindered by the Coulomb barrier at typical XRB temperatures of around 1 GK. Waiting points, such as ^{30}S, have been proposed to be responsible for the double-peaked structure observed in XRB luminosity curves [23].

Nonresonant proton captures contribute to the total proton-capture rate of ^{30}S at lower temperatures, whereas above $T \approx 0.13$ GK, the rate is dominated by resonant proton captures to the two lowest excited states in ^{31}Cl. These have been studied via beta-delayed proton decay of ^{31}Ar [26–29] with observed laboratory energies of 446(15) and 1415(5) keV [26] and 1416(2) keV [28]. Recently, ^{31}Cl has been studied via Coulomb breakup of ^{31}Cl at high energy in inverse kinematics by using the R^{3}B-LAND setup at GSI [30]. The two lowest-lying levels, $1/2^+$ at 782(32) keV and $5/2^+$ at 1793(26) keV [30], were found to be in a reasonable agreement with the estimates, 745(17) and 1746(9) keV [31], based on the IMME and beta-delayed proton data. A similar Coulomb dissociation study of ^{31}Cl performed at RIKEN resulted in resonance energies around 0.45 and 1.3 MeV [32]. In order to compare the results from R^{3}B-LAND with the beta-delayed proton data and to verify the excitation energies of the lowest resonance states in ^{31}Cl, the proton separation energy of ^{31}Cl, i.e., its mass, has to be known more precisely.

To estimate the waiting-point conditions for ^{30}S, also the rate for photodisintegration reactions on ^{31}Cl ($\lambda_{\gamma,p}$) has to be taken into account. The ratio of $\lambda_{\gamma,p}$ to the proton-capture reaction rate $N_A\langle\sigma v\rangle$ depends exponentially on the proton-capture Q value on ^{30}S (i.e., the proton separation energy S_p of ^{31}Cl) [33]:

$$\frac{\lambda_{\gamma,p}}{N_A\langle\sigma v\rangle} = 9.8685\times10^9 T_9^{3/2}\frac{g_S g_p}{g_{Cl}}\left(\frac{G_S G_p}{G_{Cl}}\right)\times\left(\frac{m_S m_p}{m_{Cl}}\right)^{3/2} e^{-11.605Q/T_9}, \quad (1)$$

where m_i are the masses in atomic mass units, g_i are the statistical factors $g_i = 2J_i + 1$, and G_i are normalized partition functions for ^{30}S, p, and ^{31}Cl. The normalized partition functions [34] are close to one in the relevant energy region. The uncertainty in the present Q value has been shown to significantly affect XRB nucleosynthesis calculations in a high-temperature ($T_{\rm peak} = 2.50$ GK) scenario with normal

*anu.kankainen@jyu.fi

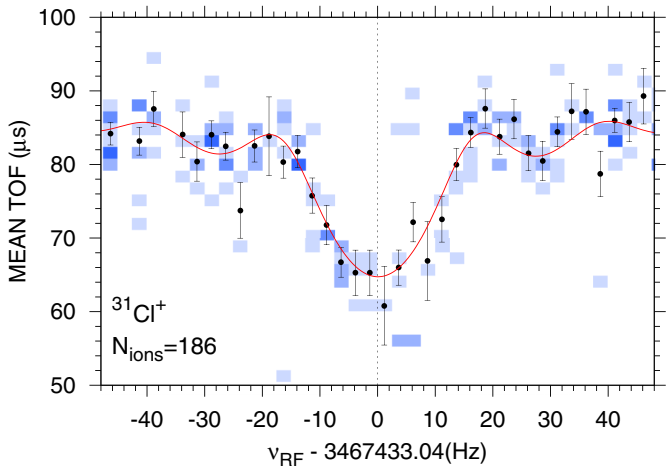

FIG. 1. TOF-ICR spectrum of $^{31}Cl^+$ with a quadrupolar radiofrequency excitation of 50 ms. The spectrum represents a typical resonance of ^{31}Cl obtained in 140 minutes. The blue squares indicate the number of ions in each time-of-flight bin: the darker the color, the greater the number of ions.

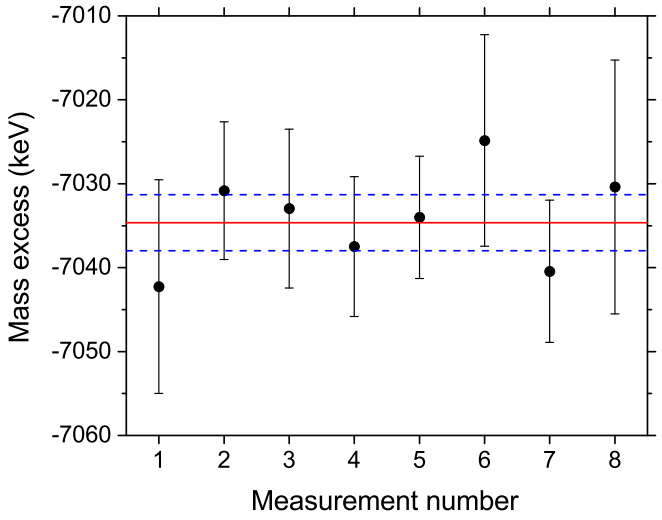

FIG. 2. Mass-excess values determined in this work. The red line shows the weighted mean of the results and the dashed blue lines 1σ error bands.

burst duration (≈100s) as well as in a short-burst (≈10 s) scenario with $T_{peak} = 1.36$ GK [35].

$^{31}Cl^+$ ions were produced via $^{32}S(p,2n)^{31}Cl$ reactions by using a 40 MeV proton beam impinging on a 1.8-mg/cm^2-thick ZnS target at the IGISOL facility [36]. The reaction products were stopped in helium gas and extracted with a sextupole ion guide [37] and accelerated to 30 keV before mass separation with a 55° dipole magnet. A radio-frequency quadrupole cooler and buncher [38] was implemented to convert the continuous $A = 31$ beam into short ion bunches which are released into the JYFLTRAP double-Penning-trap mass spectrometer [39]. Simultaneous magnetron and cyclotron excitations were applied for the ions in the purification trap for 40 ms to select the $^{31}Cl^+$ ions by using the mass-selective buffer gas cooling method [40]. In the precision trap, a 10-ms magnetron excitation was followed by a short, 50 ms cyclotron excitation to minimize the decay losses of ^{31}Cl. The ion's cyclotron resonance frequency $\nu_c = qB/(2\pi m)$, where q and m are the charge and mass of the ion, respectively, was determined by using the time-of-flight ion cyclotron resonance (TOF-ICR) technique [41] (see Fig. 1). The magnetic field strength B was calibrated by using $^{31}P^+$ ions as a reference [$m(^{31}P) = 30.9737619984(7)$ u [6]]. Thus, the atomic mass of ^{31}Cl was determined using $m(^{31}Cl) = r(m_{ref} - m_e) + m_e$, where $r = \frac{\nu_{c,ref}}{\nu_c}$ is the cyclotron frequency ratio of $^{31}P^+$ and $^{31}Cl^+$, m_{ref}, and m_e are the ^{31}P and electron masses, respectively. The weighted mean of the measured frequency ratios was $r = 1.00060330(12)$ resulting in a mass-excess value $\Delta = -7034.7(34)$ keV (see Fig. 2), which is 31 keV higher than the value in the Atomic Mass Evaluation 2012 (AME12) [6]. The uncertainty is dominated by the statistical error of the frequency fit. The systematic uncertainties, as described in Ref. [42], have a negligible contribution to the final result.

The IMME was studied at $A = 31$ by using the new mass value for ^{31}Cl. The ground-state masses for the other members of the multiplet have been taken from AME12 [6] (see Table I). The mass values of ^{31}S and ^{31}P are based on Penning-trap measurements at JYFLTRAP [18] and the Florida State University trap [43], respectively. The mass of ^{31}Si is linked via (n,γ) measurements (see, e.g., Refs. [44–47]) to ^{29}Si, which has been precisely measured with a Penning trap at the Massachusetts Institute of Technology [48]. The excitation energy for the $T = 3/2$ IAS in ^{31}S is based on data from beta-delayed γ rays of ^{31}Cl [1,5] as well as from $^{31}P(^3He,t)$ [49] and $^{33}S(p,t)$ reactions [50]. The energy for the IAS in ^{31}P has been determined with high precision by using the Gammasphere detector array [51]. A similar excitation energy, $E_x = 6380.0(20)$ keV, has also been obtained via $^{30}Si(p,\gamma)$ measurements [52–54]. Thus, the data for the IMME are based on various independent measurements which do not show any significant discrepancies.

Table II summarizes the IMME fit results. With the new ^{31}Cl mass value, the quadratic IMME fails ($\chi^2_n = 11.6$) and a significant nonzero cubic coefficient $d = -3.5(11)$ keV is obtained. The more precise mass for ^{31}Cl reveals the breakdown of the IMME: with the AME12 mass value for ^{31}Cl the quadratic IMME fits perfectly well ($\chi^2_n = 0.08$). So far, only $A = 9$ [16], $A = 35$ [20], $A = 53$ [21], and recently $A = 21$ [17], of the known $T = 3/2$ quartets have shown significant nonzero

TABLE I. Mass-excess values Δ and excitation energies E_x for the $J^\pi = 3/2^+, T = 3/2$ isobaric analog states at $A = 31$. The mass-excess value of ^{31}Cl is from this work, the others are from the AME12 [6].

Nucleus	T_Z	Δ (keV)	E_x (keV)
^{31}Cl	−3/2	− 7034.7(34)	0
^{31}S	−1/2	− 19042.52(23)	6280.60(16) [60]
^{31}P	+1/2	− 24440.5411(7)	6380.8(17) [51]
^{31}Si	+3/2	− 22949.04(4)	0

TABLE II. Coefficients for the quadratic and cubic IMME fits (in keV) for the $T = 3/2$ quartet at $A = 31$.

	Quadratic	Cubic
a	$-15465.4(26)$[a]	$-15463.2(10)$
b	$-5302.7(32)$[a]	$-5296.9(20)$
c	209.1(32)[a]	209.5(10)
d		$-3.5(11)$[b]
χ^2_n	11.6	

[a]The parameter uncertainty has been scaled with $\sqrt{\chi^2_n}$.
[b]During the review process, $E_x = 6279.0(6)$ keV [59] for the IAS in ^{31}S was published. The new value, which differs 2.6σ from Ref. [60], yields $\chi^2/n = 16.2$ for the quadratic IMME and a cubic coefficient of $d = -4.3(11)$ keV.

cubic coefficients (see Fig. 3). New precision measurements pave the way toward a more fundamental understanding of the reasons behind the breakdown. Isospin mixing has successfully explained the breakdown of the IMME at $A = 9$ [16] and $A = 32$ [22] but failed at $A = 21$ [17], albeit detailed shell-model calculations were carried out.

The role of isospin mixing in the IMME is not straightforward. The quadratic IMME works well for the $A = 33$, $J^\pi = 1/2^+$, $T = 3/2$ quartet ($\chi^2_n = 0.06$ [13]), although isospin-forbidden beta-delayed protons observed from the IAS at 5548 keV in ^{33}Cl (see, e.g., Refs. [55,56]) imply that there must be isospin mixing in the IAS. Interestingly, the cubic coefficients for the $A = 31$ [$d = -3.5(11)$ keV] and $A = 35$ [$d = -3.37(38)$ keV [13]] $J^\pi = 3/2^+$, $T = 3/2$ quartets are very similar, which motivates further theoretical studies of these neighboring members of the $A = 4n + 3$ series of the $T = 3/2$ quartets. Isospin mixing has been discussed for $A = 35$ [20,57] but no clear explanation for the breakdown has been given so far. Isospin mixing is plausible also for the $A = 31$ quartet because there are candidates for the $T = 1/2,3/2^+$ states [58,59] close to the $T = 3/2$ IAS.

The breakdown of the IMME at $A = 31$ is a crucial finding since the proton separation energy $S_p = 282.8(44)$ keV based on the quadratic IMME prediction from Ref. [1] has been used in Ref. [60] to determine the adopted level energies in ^{31}Cl from the beta-delayed proton data of ^{31}Ar [26–29]. The new mass value of ^{31}Cl shows it is less bound than previously expected. The proton separation energy $S_p = 264.6(34)$ keV is 31 keV lower and ≈15 times more precise than the AME12 value [$S_p = 296(50)$ keV [6]]. The new mass measurement shifts all levels based on beta-delayed proton data [26–29] 18 keV lower in energy and reduces the inherent systematic uncertainties from 50 keV to 3.4 keV. The revised energy for the $J^\pi = 5/2^+, T = 5/2$ IAS in ^{31}Cl, the member of the $T = 5/2$ sextet at $A = 31$, is 12292.2(23) keV based on Refs. [26,28] and the S_p and S_{2p} values from this work.

The two lowest excited states in ^{31}Cl are relevant for the radiative resonant proton captures in the rp process. By combining the new S_p value with the beta-delayed proton data of Refs. [26,28], excitation energies of 726(16) and 1728(4) keV are obtained for the $1/2^+$ and $5/2^+$ states, respectively. The excitation energy for the first-excited state agrees well with the USDB shell-model value of 724 keV [30]. However, the excitation energies are lower than the presently recommended values [740(50) and 1746(5) keV [60]] and the recent results from R^{3}B [782(32) and 1793(26) keV [30]]. The weighted mean for the resonance energies was calculated from Refs. [26,28,30] by using the S_p value from this work for Ref. [30]. The resulting resonance energies, $E_r = 472(14)$ keV and 1464(2) keV, are very close to the beta-delayed proton data [26,28] [$E_r = 461(16)$ keV and 1464(2) keV]. The resonant proton capture rate to the first-excited state is slightly lower with the new resonance energy but, because the

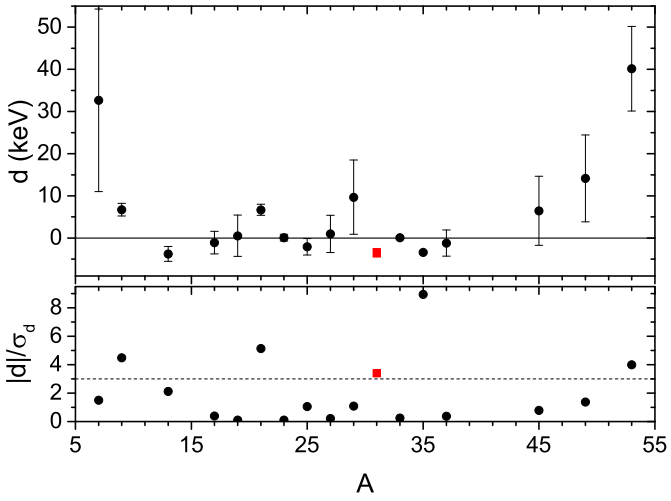

FIG. 3. Cubic coefficients for the known (lowest) $T = 3/2$ isobaric quartets. The value for $A = 31$ (red square) is from this work, for $A = 21$ from Ref. [17], and the rest have been adopted from Ref. [13]. The lower panel shows the significance of the deviation from zero.

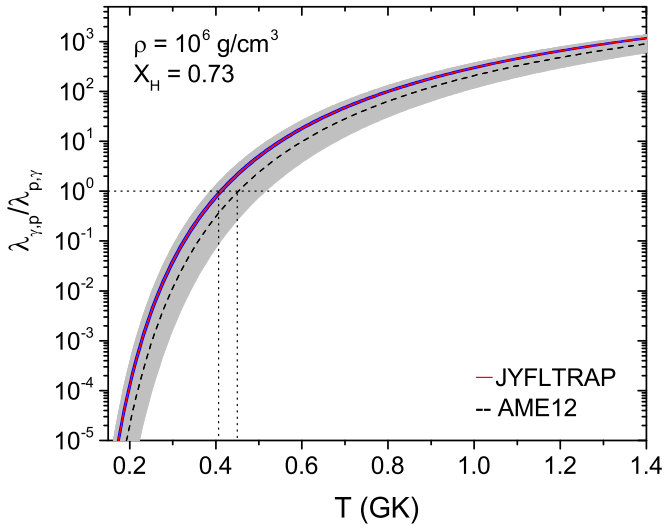

FIG. 4. The ratio of (γ,p) to (p,γ) rates for typical XRB conditions. The uncertainties related to the JYFLTRAP Q value are shown by the blue lines and to the AME12 value by the gray-shaded area. The dashed lines indicate the temperatures where $\lambda_{\gamma,p}$ is equal to $\lambda_{p,\gamma}$.

resonance energies agree within the error bars, the calculated proton-capture rates do not change significantly from Ref. [31].

The new S_p value was used to compute the ratio of photodisintegration rate on ^{31}Cl to the proton capture rate on ^{30}S according to Eq. (1) and using $\lambda_{p,\gamma} = N_A\langle\sigma v\rangle_r \rho \frac{X_i}{m_H}$ for typical XRB conditions with density $\rho = 10^6$ g/cm^3 and hydrogen mass fraction of $X_H = 0.73$. The uncertainty related to the Q value has been significantly reduced and the photodisintegration rate takes over at lower temperatures compared to the ratio calculated with the AME12 Q value (see Fig. 4). Above 0.44(1) GK, at least 20% of the reaction and decay flow has to wait for β^+ decay of ^{30}S and it becomes a waiting point. The upper-temperature limit for the ^{30}S waiting point, 1.0(3) GK, comes from the rate of the unmeasured ^{30}S$(\alpha, p)^{33}$Cl reaction [31].

The JYFLTRAP Penning-trap mass measurement of ^{31}Cl has shown that the quadratic IMME fails at $A = 31$ and the cubic term is nonzero. Theoretical calculations are anticipated to explain the deviation from the quadratic form and to explore possible underlying reasons for similarities in the cubic coefficients for $A = 31$ and $A = 35$. Isospin mixing between $T = 1/2$ and $T = 3/2$ states is plausible because there are candidates for $3/2^+$ states lying nearby the IAS. The improved precision in the proton separation energy of ^{31}Cl has reduced the uncertainties related to excitation energies in ^{31}Cl and the photodisintegration rate of ^{31}Cl. Photodisintegration starts to dominate at lower temperatures than previously thought. The improved rate will be useful for future XRB model calculations helping to interpret the observed double-peaked structure in the luminosity curves.

This work has been supported by the Academy of Finland under the Finnish Centre of Excellence Programme 2012–2017 (Nuclear and Accelerator Based Physics Research at JYFL). A.K., D.N., and L.C. acknowledge support from the Academy of Finland under project No. 275389.

[1] A. Saastamoinen, Ph.D. thesis University of Jyväskylä, Jyväskylä, Finland, 2011.
[2] J. Äystö, J. Honkanen, K. Vierinen, A. Hautojärvi, K. Eskola, and S. Messelt, Phys. Lett. B **110**, 437 (1982).
[3] J. Äystö, P. Taskinen, K. Eskola, K. Vierinen, and S. Messelt, Phys. Scr. **1983**, 193 (1983).
[4] T. J. Ognibene, J. Powell, D. M. Moltz, M. W. Rowe, and J. Cerny, Phys. Rev. C **54**, 1098 (1996).
[5] A. Kankainen, T. Eronen, S. Fox, H. Fynbo, U. Hager, J. Hakala, J. Huikari, D. Jenkins, A. Jokinen, S. Kopecky, I. Moore, A. Nieminen, H. Penttilä, S. Rinta-Antila, O. Tengblad, Y. Wang, and J. Äystö, Eur. Phys. J. A **27**, 67 (2006).
[6] M. Wang, G. Audi, A. Wapstra, F. Kondev, M. MacCormick, X. Xu, and B. Pfeiffer, Chin. Phys. C **36**, 1603 (2012).
[7] W. Benenson, D. Mueller, E. Kashy, H. Nann, and L. W. Robinson, Phys. Rev. C **15**, 1187 (1977).
[8] E. Wigner, *Conf. on Chem. Res., Houston*, edited by W. O. Millikan (Robert A. Welch Foundation, Houston, 1957), Vol. 1.
[9] S. Weinberg and S. B. Treiman, Phys. Rev. **116**, 465 (1959).
[10] W. Benenson and E. Kashy, Rev. Mod. Phys. **51**, 527 (1979).
[11] J. Britz, A. Pape, and M. Antony, At. Data Nucl. Data Tables **69**, 125 (1998).
[12] Y. H. Lam, B. Blank, N. A. Smirnova, J. B. Bueb, and M. S. Antony, At. Data Nucl. Data Tables **99**, 680 (2013).
[13] M. MacCormick and G. Audi, Nucl. Phys. A **925**, 61 (2014).
[14] M. MacCormick and G. Audi, Nucl. Phys. A **925**, 296 (2014).
[15] R. J. Charity, J. M. Elson, J. Manfredi, R. Shane, L. G. Sobotka, Z. Chajecki, D. Coupland, H. Iwasaki, M. Kilburn, J. Lee, W. G. Lynch, A. Sanetullaev, M. B. Tsang, J. Winkelbauer, M. Youngs, S. T. Marley, D. V. Shetty, A. H. Wuosmaa, T. K. Ghosh, and M. E. Howard, Phys. Rev. C **84**, 051308 (2011).
[16] M. Brodeur, T. Brunner, S. Ettenauer, A. Lapierre, R. Ringle, B. A. Brown, D. Lunney, and J. Dilling, Phys. Rev. Lett. **108**, 212501 (2012).
[17] A. T. Gallant, M. Brodeur, C. Andreoiu, A. Bader, A. Chaudhuri, U. Chowdhury, A. Grossheim, R. Klawitter, A. A. Kwiatkowski, K. G. Leach, A. Lennarz, T. D. Macdonald, B. E. Schultz, J. Lassen, H. Heggen, S. Raeder, A. Teigelhöfer, B. A. Brown, A. Magilligan, J. D. Holt, J. Menéndez, J. Simonis, A. Schwenk, and J. Dilling, Phys. Rev. Lett. **113**, 082501 (2014).
[18] A. Kankainen, T. Eronen, D. Gorelov, J. Hakala, A. Jokinen, V. S. Kolhinen, M. Reponen, J. Rissanen, A. Saastamoinen, V. Sonnenschein, and J. Äystö, Phys. Rev. C **82**, 052501 (2010).
[19] A. A. Kwiatkowski, B. R. Barquest, G. Bollen, C. M. Campbell, D. L. Lincoln, D. J. Morrissey, G. K. Pang, A. M. Prinke, J. Savory, S. Schwarz, C. M. Folden, D. Melconian, S. K. L. Sjue, and M. Block, Phys. Rev. C **80**, 051302 (2009).
[20] C. Yazidjian, G. Audi, D. Beck, K. Blaum, S. George, C. Guénaut, F. Herfurth, A. Herlert, A. Kellerbauer, H.-J. Kluge, D. Lunney, and L. Schweikhard, Phys. Rev. C **76**, 024308 (2007).
[21] Y. H. Zhang, H. S. Xu, Y. A. Litvinov, X. L. Tu, X. L. Yan, S. Typel, K. Blaum, M. Wang, X. H. Zhou, Y. Sun, B. A. Brown, Y. J. Yuan, J. W. Xia, J. C. Yang, G. Audi, X. C. Chen, G. B. Jia, Z. G. Hu, X. W. Ma, R. S. Mao, B. Mei, P. Shuai, Z. Y. Sun, S. T. Wang, G. Q. Xiao, X. Xu, T. Yamaguchi, Y. Yamaguchi, Y. D. Zang, H. W. Zhao, T. C. Zhao, W. Zhang, and W. L. Zhan, Phys. Rev. Lett. **109**, 102501 (2012).
[22] A. Signoracci and B. A. Brown, Phys. Rev. C **84**, 031301 (2011).
[23] J. L. Fisker, F.-K. Thielemann, and M. Wiescher, Astrophys. J. **608**, L61 (2004).
[24] J. L. Fisker, H. Schatz, and F.-K. Thielemann, Astrophys. J., Suppl. Ser. **174**, 261 (2008).
[25] H. S. Wilson, R. W. Kavanagh, and F. M. Mann, Phys. Rev. C **22**, 1696 (1980).
[26] L. Axelsson, J. Äystö, M. Borge, L. Fraile, H. Fynbo, A. Honkanen, P. Hornshj, A. Jokinen, B. Jonson, P. Lipas, I. Martel, I. Mukha, T. Nilsson, G. Nyman, B. Petersen, K. Riisager, M. Smedberg, and O. Tengblad, Nucl. Phys. A **634**, 475 (1998).
[27] L. Axelsson, J. Äystö, M. Borge, L. Fraile, H. Fynbo, A. Honkanen, P. Hornshj, A. Jokinen, B. Jonson, P. Lipas, I. Martel, I. Mukha, T. Nilsson, G. Nyman, B. Petersen, K. Riisager, M. Smedberg, and O. Tengblad, Nucl. Phys. A **641**, 529 (1998).
[28] H. Fynbo, M. Borge, L. Axelsson, J. Äystö, U. Bergmann, L. Fraile, A. Honkanen, P. Hornshj, Y. Jading, A. Jokinen,

B. Jonson, I. Martel, I. Mukha, T. Nilsson, G. Nyman, M. Oinonen, I. Piqueras, K. Riisager, T. Siiskonen, M. Smedberg, O. Tengblad, J. Thaysen, and F. Wenander, Nucl. Phys. A **677**, 38 (2000).

[29] G. T. Koldste, B. Blank, M. J. G. Borge, J. A. Briz, M. Carmona-Gallardo, L. M. Fraile, H. O. U. Fynbo, J. Giovinazzo, B. D. Grann, J. G. Johansen, A. Jokinen, B. Jonson, T. Kurturkian-Nieto, J. H. Kusk, T. Nilsson, A. Perea, V. Pesudo, E. Picado, K. Riisager, A. Saastamoinen, O. Tengblad, J.-C. Thomas, and J. Van de Walle, Phys. Rev. C **89**, 064315 (2014).

[30] C. Langer, O. Lepyoshkina, Y. Aksyutina, T. Aumann, S. Beceiro Novo, J. Benlliure, K. Boretzky, M. Chartier, D. Cortina, U. Datta Pramanik, O. Ershova, H. Geissel, R. Gernhäuser, M. Heil, G. Ickert, H. T. Johansson, B. Jonson, A. Kelić-Heil, A. Klimkiewicz, J. V. Kratz, R. Krücken, R. Kulessa, K. Larsson, T. Le Bleis, R. Lemmon, K. Mahata, J. Marganiec, T. Nilsson, V. Panin, R. Plag, W. Prokopowicz, R. Reifarth, V. Ricciardi, D. M. Rossi, S. Schwertel, H. Simon, K. Sümmerer, B. Streicher, J. Taylor, J. R. Vignote, F. Wamers, C. Wimmer, and P. Z. Wu, Phys. Rev. C **89**, 035806 (2014).

[31] C. Wrede, J. A. Caggiano, J. A. Clark, C. M. Deibel, A. Parikh, and P. D. Parker, Phys. Rev. C **79**, 045808 (2009).

[32] Y. Togano, T. Motobayashi, N. Aoi, H. Baba, S. Bishop, X. Cai, P. Doornenbal, D. Fang, T. Furukawa, K. Ieki, N. Iwasa, T. Kawabata, S. Kanno, N. Kobayashi, Y. Kondo, T. Kuboki, N. Kume, K. Kurita, M. Kurokawa, Y. G. Ma, Y. Matsuo, H. Murakami, M. Matsushita, T. Nakamura, K. Okada, S. Ota, Y. Satou, S. Shimoura, R. Shioda, K. N. Tanaka, S. Takeuchi, W. Tian, H. Wang, J. Wang, K. Yamada, Y. Yamada, and K. Yoneda, J. Phys.: Conf. Ser. **312**, 042025 (2011).

[33] C. Iliadis, *Nuclear Physics of Stars* (Wiley, Weinheim, 2007).

[34] T. Rauscher and F.-K. Thielemann, At. Data Nucl. Data Tables **75**, 1 (2000).

[35] A. Parikh, J. José, C. Iliadis, F. Moreno, and T. Rauscher, Phys. Rev. C **79**, 045802 (2009).

[36] I. Moore, T. Eronen, D. Gorelov, J. Hakala, A. Jokinen, A. Kankainen, V. Kolhinen, J. Koponen, H. Penttilä, I. Pohjalainen, M. Reponen, J. Rissanen, A. Saastamoinen, S. Rinta-Antila, V. Sonnenschein, and J. Äystö, Nucl. Instrum. Methods Phys. Res., Sect. B **317**, 208 (2013).

[37] P. Karvonen, I. Moore, T. Sonoda, T. Kessler, H. Penttilä, K. Peräjärvi, P. Ronkanen, and J. Äystö, Nucl. Instrum. Methods Phys. Res., Sect. B **266**, 4794 (2008).

[38] A. Nieminen, J. Huikari, A. Jokinen, J. Äystö, P. Campbell, and E. C. A. Cochrane, Nucl. Instrum. Methods Phys. Res., Sect. A **469**, 244 (2001).

[39] T. Eronen, V. Kolhinen, V.-V. Elomaa, D. Gorelov, U. Hager, J. Hakala, A. Jokinen, A. Kankainen, P. Karvonen, S. Kopecky, I. Moore, H. Penttilä, S. Rahaman, S. Rinta-Antila, J. Rissanen, A. Saastamoinen, J. Szerypo, C. Weber, and J. Äystö, Eur. Phys. J. A **48**, 46 (2012).

[40] G. Savard, S. Becker, G. Bollen, H. J. Kluge, R. B. Moore, T. Otto, L. Schweikhard, H. Stolzenberg, and U. Wiess, Phys. Lett. A **158**, 247 (1991).

[41] M. König, G. Bollen, H. J. Kluge, T. Otto, and J. Szerypo, Int. J. Mass Spectrom. Ion Processes **142**, 95 (1995).

[42] V.-V. Elomaa, T. Eronen, J. Hakala, A. Jokinen, A. Kankainen, I. D. Moore, S. Rahaman, J. Rissanen, C. Weber, and J. Äystö, Nucl. Instrum. Methods Phys. Res., Sect. A **612**, 97 (2009).

[43] M. Redshaw, J. McDaniel, and E. G. Myers, Phys. Rev. Lett. **100**, 093002 (2008).

[44] M. A. Islam, T. J. Kennett, and W. V. Prestwich, Phys. Rev. C **41**, 1272 (1990).

[45] S. Raman, E. T. Jurney, J. W. Starner, and J. E. Lynn, Phys. Rev. C **46**, 972 (1992).

[46] S. Röttger, A. Paul, and U. Keyser, IEEE Trans. Instrum. Meas. **46**, 560 (1997).

[47] A. Paul, S. Röttger, A. Zimbal, and U. Keyser, Hyperfine Interact. **132**, 189 (2001).

[48] S. Rainville, J. K. Thompson, E. G. Myers, J. M. Brown, M. S. Dewey, E. G. Kessler, R. D. Deslattes, H. G. Borner, M. Jentschel, P. Mutti, and D. E. Pritchard, Nature (London) **438**, 1096 (2005).

[49] C. Wrede, J. A. Caggiano, J. A. Clark, C. M. Deibel, A. Parikh, and P. D. Parker, Phys. Rev. C **79**, 045803 (2009).

[50] H. Nann and B. H. Wildenthal, Phys. Rev. C **19**, 2146 (1979).

[51] D. G. Jenkins, A. Meadowcroft, C. J. Lister, M. P. Carpenter, P. Chowdhury, N. J. Hammond, R. V. F. Janssens, T. L. Khoo, T. Lauritsen, D. Seweryniak, T. Davinson, P. J. Woods, A. Jokinen, H. Penttilä, G. Martínez-Pinedo, and J. José, Phys. Rev. C **73**, 065802 (2006).

[52] H. Willmes and G. I. Harris, Phys. Rev. **162**, 1027 (1967).

[53] A. Wolff, M. Meyer, and P. Endt, Nucl. Phys. A **107**, 332 (1968).

[54] E. de Neijs, G. Haasbroek, M. Meyer, R. Rossouw, and D. Reitmann, Nucl. Phys. A **254**, 45 (1975).

[55] A. Honkanen, L. Axelsson, J. Äystö, M. Borge, B. Jonson, A. Jokinen, I. Martel, G. Martínez-Pinedo, I. Mukha, T. Nilsson, G. Nyman, B. Petersen, A. Poves, M. Smedberg, A. Teijeiro, and O. Tengblad, Nucl. Phys. A **611**, 47 (1996).

[56] N. Adimi, R. Domínguez-Reyes, M. Alcorta, A. Bey, B. Blank, M. J. G. Borge, F. de Oliveira Santos, C. Dossat, H. O. U. Fynbo, J. Giovinazzo, H. H. Knudsen, M. Madurga, I. Matea, A. Perea, K. Sümmerer, O. Tengblad, and J. C. Thomas, Phys. Rev. C **81**, 024311 (2010).

[57] J. Ekman, D. Rudolph, C. Fahlander, A. P. Zuker, M. A. Bentley, S. M. Lenzi, C. Andreoiu, M. Axiotis, G. de Angelis, E. Farnea, A. Gadea, T. Kröll, N. Mărginean, T. Martinez, M. N. Mineva, C. Rossi-Alvarez, and C. A. Ur, Phys. Rev. Lett. **92**, 132502 (2004).

[58] D. T. Doherty, P. J. Woods, G. Lotay, D. Seweryniak, M. P. Carpenter, C. J. Chiara, H. M. David, R. V. F. Janssens, L. Trache, and S. Zhu, Phys. Rev. C **89**, 045804 (2014).

[59] M. B. Bennett, C. Wrede, B. A. Brown, S. N. Liddick, D. Pérez-Loureiro, D. W. Bardayan, A. A. Chen, K. A. Chipps, C. Fry, B. E. Glassman, C. Langer, N. R. Larson, E. I. McNeice, Z. Meisel, W. Ong, P. D. O'Malley, S. D. Pain, C. J. Prokop, H. Schatz, S. B. Schwartz, S. Suchyta, P. Thompson, M. Walters, and X. Xu, Phys. Rev. Lett. **116**, 102502 (2016).

[60] C. Ouellet and B. Singh, Nucl. Data Sheets **114**, 209 (2013).

III

PROBING THE N = 40 SUBSHELL CLOSURE VIA MASS MEASUREMENTS OF ^{67}Fe AND ^{69,70}Co

by

L. Canete, S. Giraud, A. Kankainen, B. Bastin, F. Nowacki, A. Poves, P. Ascher, T. Eronen, V. Girard Alcindor, A. Jokinen, A. Khanam, I.D. Moore, D. Nesterenko, F. De Oliveira, H. Penttilä, C. Petrone, I. Pohjalainen, A. De Roubin, V. Rubchenya, M. Vilen, and J. Äystö

To be submitted.

=

Probing the $N = 40$ subshell closure via mass measurements of ^{67}Fe and ^{69,70}Co

L. Canete,[1,*] S. Giraud,[2,†] A. Kankainen,[1] B. Bastin,[2] F. Nowacki,[3] A. Poves,[4] P. Ascher,[5] T. Eronen,[1] V. Girard Alcindor,[2] A. Jokinen,[1] A. Khanam,[1] I.D. Moore,[1] D. Nesterenko,[1] F. De Oliveira Santos,[2] H. Penttilä,[1] C. Petrone,[6] I. Pohjalainen,[1] A. De Roubin,[1] V.A. Rubchenya,[1] M. Vilen,[1] and J. Äystö[1]

[1] *University of Jyvaskyla, P.O. Box 35, FI-40014 University of Jyvaskyla, Finland*
[2] *GANIL, Bd Henri Becquerel, BP 55027, F-14076 Caen Cedex 5, France*
[3] *Université de Strasbourg, IPHC, 23 rue du Loess 67037 Strasbourg, France*
[4] *Departamento de Física Teórica e IFT-UAM/CSIC, Universidad Autónoma de Madrid, E-28049 Madrid, Spain*
[5] *CENBG, CNRS/IN2P3Université Bordeaux 1, 33175 Gradignan Cedex, France*
[6] *IFIN-HH, P.O. Box MG-6, 077125 Bucharest-Magurele, Romania*

(Dated: February 25, 2019)

Masses of neutron-rich iron and cobalt isotopes ^{67}Fe and ^{69,70}Co have been determined with the JYFLTRAP double Penning trap mass spectrometer. The measurements yield a smoother trend on the mass surface and extend it beyond $N = 40$. The moderate $N = 40$ subshell gap has been found to weaken below ^{68}Ni, region known for deformation and shape coexistence. The excitation energy for the $1/2^-$ intruder state in ^{69}Co has been determined for the first time and is compared to large-scale shell-model calculations which predict a reversed order for the $7/2^-$ and $1/2^-$ states. The new mass values also reduce mass-related uncertainties for the astrophysical rapid neutron capture process.

Nuclear mass is an intrinsic property of atomic nuclei. It provides a way to determine nuclear binding energy, which holds the nucleons together and reflects subtle changes in the inner structure of nuclei (see e.g. [1]). Binding energies yield information, for example, on the evolution and magnitude of shell closures at magic neutron (N) and/or proton (Z) numbers (see e.g. [2–5]). They are one of the main nuclear inputs for the rapid neutron capture process (r-process) [6–8] producing around half of the elements heavier than iron. Nuclear masses have a strong effect on the calculated final r-process abundances [9–11]. Whereas heavier r-process elements have recently been confirmed to be synthesized in binary neutron star mergers [12], several astrophysical sites are likely to contribute to the production of lighter r-process elements [13–18]. Sensitivity studies [19] have shown that the neutron capture rates $^{67}\mathrm{Fe}(n,\gamma)^{68}\mathrm{Fe}$ and $^{68}\mathrm{Co}(n,\gamma)^{69}\mathrm{Co}$ have a particularly strong impact on the calculated abundances in the weak r-process. These rates, and in particular their inverse photodissociation rates, depend sensitively on the reaction Q-value, i.e on nuclear masses. In addition, long-living excited states known as isomers can play a role in stellar environments where nuclei are thermally excited [7]. Isomers can be studied by mass measurements and by decays spectroscopy. They provide data on nuclear structure with respect to nucleon degrees of freedom, such as differences in angular momentum, its orientation and shape coexistence [20, 21].

In this Letter, neutron-rich iron ($Z = 26$) and cobalt ($Z = 27$) isotopes beyond the $N = 40$ subshell closure are investigated. The studied nuclei lie below ^{68}Ni ($Z = 28$, $N = 40$), which exhibits some typical doubly-magic characteristics: a high excitation energy of the first 2^+ state at 2033 keV [22] and a low reduced transition probability of $B(E2) = 260(50)\ e^2fm^4$ [23, 24] to the first excited 2_1^+ state. The observed values, however, have not been interpreted as evidence for a strong $N = 40$ closure. Detailed theoretical calculations [25] have shown that most of the $B(E2)$ strength is located above 4 MeV, leaving only a small fraction to the first excited state which is dominated by neutron excitations. Furthermore, one particle - one hole (1p-1h) excitations from the negative-parity νfp orbitals are no longer allowed and only a pair of neutrons can be promoted to the positive-parity $\nu g_{9/2}$ orbital to make a 2^+ state [26], increasing the excitation energy. So far, precision mass measurements on nickel, copper and gallium isotopes have indicated only a localized weak subshell closure at ^{68}Ni [27, 28] but have not provided sufficient data on the $N = 40$ subshell closure below nickel. While cobalt and iron isotopes up to ^{69}Co [29, 30] and ^{66}Fe [29, 31] have been studied at the LEBIT Penning trap, the overall trend after $N = 40$ has remained unclear, partly due to long-living isomers. Here we extend these studies to ^{67}Fe and ^{69,70}Co.

The $N = 40$ region is known for shape coexistence [32]. Low-lying 0^+ states have been observed in ^{68}Ni [33–37] as well as in ^{70}Ni [37–39]. In ^{68}Ni, the 0_1^+ ground state is spherical but the 0_2^+ state at 1604 keV and 0_3^+ at 2511 keV are expected to be weakly oblate and strongly prolate, respectively, based on large-scale shell-model calculations [35, 36, 40, 41]. The 0_2^+ state has been interpreted to originate from 2p-2h excitations across $N = 40$ whereas the 0_3^+ state is dominated by proton excitations

across $Z = 28$. The presence of neutrons in the $g_{9/2}$ orbital makes these proton excitations more likely due to attractive interaction between the $f_{7/2}$ and $f_{5/2}$ proton orbitals, triggered by the tensor force [40, 42, 43].

Beta-delayed [44, 45] and prompt γ-rays [46] observed from ^{67}Co suggest shape coexistence also in ^{67}Co, which has one proton less than ^{68}Ni. The $(7/2^-)$ ground state in ^{67}Co is described by shell-model calculations as a proton hole coupled to the spherical ^{68}Ni ground state. On the other hand, the $(1/2^-)$ isomeric state at 491.6(10) keV with a half-life of 496(33) ms [44] has been interpreted as a prolate $[321]1/2^-$ proton intruder state where one proton from the $f_{7/2}$ shell has been excited across $Z = 28$ [44]. The role of 4p-4h excitations across $N = 40$ reducing the effective proton gap for the $1/2^-$ state has also been discussed in [46]. Strong quadrupole correlations drive these intruder states lower in energy, and an island of inversion can occur in the $N = 40$ region [47].

The energy of the deformed $1/2^-$ state in ^{69}Co has remained unknown although two long-living states have been observed [48]. The shorter-living $(7/2^-)$ state ($T_{1/2}$ = 180(29) ms [48]), feeds strongly $(5/2^-)$ states in ^{69}Ni, and has been observed in several studies [48–52] whereas only Ref. [48] reports on a longer-living 750(250) ms state, based on a fit on the total decay curve of ^{69}Fe. Further evidence for the existence of two long-living states are the γ-transitions at 1128, 1319, 1343, 1545, and 1642 keV, which were unplaced in Ref. [50] but found to be much more populated via beta decay of ^{69}Fe $(1/2^-)$ than via prompt ^{69}Co production in [48]. Therefore, the longer-living state is likely $1/2^-$, similarly to the proton intruder states at 491.6(10) keV in ^{67}Co [44] and at 1095.0 keV in ^{65}Co [45]. The order of the two states is not yet certain, however, the excitation energy for the intruder state has been estimated to be less than 467 keV based on the unobserved $1/2^- \rightarrow 7/2^-$ $M3$ transitions [48]. In this Letter, we employ Penning trap mass spectrometry to determine the location of the $(1/2^-)$ state beyond the $N = 40$ subshell closure.

The evolution of the states in even-A Co isotopes is more complicated. In ^{70}Co, the ground state has been predicted to be the shorter-living high-spin state with $(6^-,7^-)$ and $T_{1/2}$ = 112(7) ms, and the isomer the longer-living state with $T_{1/2} = 470(50)$ ms and a spin 3^+ based on systematics [53]. Previous decay studies of ^{70}Co [38, 54–56], have mainly employed fragmentation of ^{76}Ge or ^{84}Kr, which seems to favor the shorter-living high-spin state, whereas the only experiment employing the same production method as in this work, proton-induced fission on uranium, favoured the longer-living low-spin state [57]. A recent beta-decay study of ^{70}Fe [58] and Monte Carlo shell-model calculations based on the A3DA Hamiltonian [59], suggest that the ground state of ^{70}Co is a $(1^+, 2^+)$ state with $T_{1/2}$=508(7) ms. The long half-life is explained by the stabilizing effect of the type II shell evolution [40]. The minimum of the potential energy surface of ^{70}Co has been predicted to correspond deformed single-particle orbitals analogous to Nilsson $\pi[321]1/2^-$ and $\nu[301]1/2^-$ orbitals [58]. The $1/2^-$ isomer in ^{67}Fe has also been interpreted as $\nu[301]1/2^-$, however, the isomers in ^{67}Fe [60, 61] are too short-living for Penning-trap mass spectrometry.

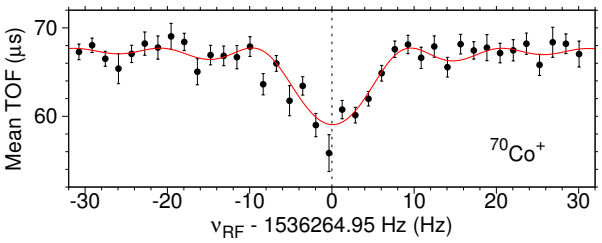

FIG. 1. Time-of-flight spectrum for ^{70}Co collected with 100 ms quadrupolar excitation for the longer, 513 ms measurement cycle. The solid red line is a fit of the data (black points) to the theoretical line shape [62].

The neutron-rich iron and cobalt isotopes were produced by 35-MeV protons impinging on a 15 mg/cm^2-thick ^{nat}U target at the IGISOL facility [63]. The reaction products were thermalized in helium gas, extracted out from the gas cell using a sextupole ion guide SPIG [64] and accelerated to 30 keV before mass-separation with a dipole magnet. A radiofrequency cooler and buncher (RFQ) [65] released the ions as short bunches into the double Penning trap mass spectrometer JYFLTRAP [66]. There the ions were first purified via buffer gas cooling technique [67] before transfer to the precision trap for high-precision mass measurements. The ion's cyclotron resonance frequency $\nu_c = \frac{1}{2\pi}\frac{q}{m}B$, where q and m are the charge and mass of the ion, respectively, was measured using the time-of-flight ion cyclotron resonance (TOF-ICR) technique [62, 68] (see Fig. 1). The magnetic field strength B was determined with ^{84}Kr$^+$ ions as a reference. For ^{69,70}Co, quadrupolar excitation times of 50 ms and 100 ms were employed. The ^{67}Fe data were collected using Ramsey's method of time-separated oscillatory fields [69–71] with an excitation pattern of 25-50-25 ms (On-Off-On). Systematic errors due to temporal fluctuations in the magnetic field, $\sigma_B(\nu_{c,ref})/\nu_{c,ref}$=(8.18(19)$\times 10^{-12}$/min)$\times\Delta t$ [72], and the mass-dependent uncertainty $\sigma_m(r)/r$=(2.2(6) $\times$ $10^{-10}/u$)$\times\Delta m$ [73], were quadratically added to the statistical uncertainties.

The results are summarized in Table I. The mass of ^{67}Fe is about 70 times more precise and around 100 keV lower than the previously recommended value [74] based on less precise methods, such as the time-of-flight isochronous (TOFI) spectrometer at Los Alamos [75, 76], $B\rho$-TOF method at NSCL [77–79] and isochronous mass spectrometry at the ESR storage ring [80].

For ^{69}Co, it was not possible to separate the two long-living states from each other using the TOF-ICR tech-

TABLE I. The half-lives, spins and parities for the ions of interest based on [53], measured frequency ratios $r = \nu_{ref}/\nu$, and mass-excess values Δ in comparison with the literature values from [53, 74]. '#' denotes a value based on extrapolations or systematics. Singly-charged ions of ^{84}Kr ($m = 83.911497729(4)$ u [74]) were used as a reference for all studied cases.

Nuclide	$T_{1/2}$	I^π	r	Δ_{JYFL} (keV)	Δ_{lit} (keV)	Diff. (keV)
^{67}Fe	394(9) ms	$(1/2^-)$	0.797874190(8)	-45709.1(3.8)	-45610(270)	-99.1(270)
^{69}Co	180(29) ms	$(7/2^-)$#	0.821649141(428)[a]	-50383(44)	-50280(140)	-103(147)
^{69}Co^m	750(250) ms	$1/2^-$#	0.821651504(291)[a]	-50207(36)	-49780(240)#	-430(240)#
^{70}Co[b]	508(7) ms [58]	$1^+, 2^+$[58]	0.833615937(21)	-46525(11)	-46430(360)#	105(300)

[a] Calculated based on the isomeric fractions f_l for the longer-living state and the frequency ratios determined from the files using the 226-ms cycle ($f_l = 49(13)$ %, $r = 0.821650299(36)$) and the 726-ms cycle ($f_l = 81(9)$ %, $r = 0.821651055(92)$), see text for details.
[b] Assigned as the ground state in [58]. Considered as an isomer 200(200)# keV above a $(6^-, 7^-)$, $T_{1/2}$=112(7) ms state in [53].

nique. Since the half-lives of the two states are significantly different (see Table I), the composition of the ion bunches was manipulated by changing the waiting time, t_{wait}, from the moment the ion beam accumulation in the cooler was stopped to the extraction toward JYFLTRAP. The two measurement sets for ^{69}Co had otherwise identical measurement schemes, except for $t_{wait} = 500$ ms in the long cycle, which lasted in total 726 ms after the ion beam production had stopped. There was no waiting time in the short, 226 ms cycle. Due to the much longer half-life of the $(1/2^-)$ state, it is likely to dominate the measurements using the long cycle. Based on the ratio of the average number of ions in the short- and long-cycle measurements, $R = N_{short}/N_{long} = 2.6(4)$, the fraction of the longer-living state in the beam (f_l) was determined at the moment the production stopped ($f_l = 33(10)\%$), as well as 226 ms ($f_l = 49(13)\%$) and 726 ms ($f_l = 81(9)\%$) after it, assuming the short-living state makes $f_s = 1 - f_l$ of the beam. The mass-excess values for the longer and shorter-living states ($\Delta_{l,s}$), were determined from the measured mass-excess values, which were $-50296(15)$ keV and $-50238(20)$ keV for the 226 ms and 726 ms cycles, respectively, obtained using $\Delta_{meas}(t) = [1 - f_l(t)]\Delta_s + f_l(t)\Delta_l$.

The determined mass excess for ^{69}Co, $-50383(44)$ keV, is in good agreement with the most recent Atomic Mass Evaluation (AME16) [74] value based on measurements using the TOFI spectrometer [75, 76], $B\rho$-TOF method [77, 78] and isochronous mass spectrometry [81]. The determined mass excess for the isomer ^{69}Co^m, $-50207(36)$ keV, is in perfect agreement with the ground-state value, $-50214(14)$ keV [30], reported recently from the LEBIT Penning trap, suggesting they have actually measured the isomer.

The excitation energy $E_x = 176(57)$ keV for the deformed $1/2^-$ state in ^{69}Co has been determined for the first time. While the energy differences between the $1/2^-$ and $7/2^-$ states for ^{67,69}Co match well with the shell-model calculations employing Lenzi-Nowacki-Poves-Sieja (LNPS) interaction in the *pf-sdg* valence space [82] (see Fig. 2), predicting a minimum for the $1/2^-$ states at ^{69}Co, the experimental $1/2^-$ state remains above the

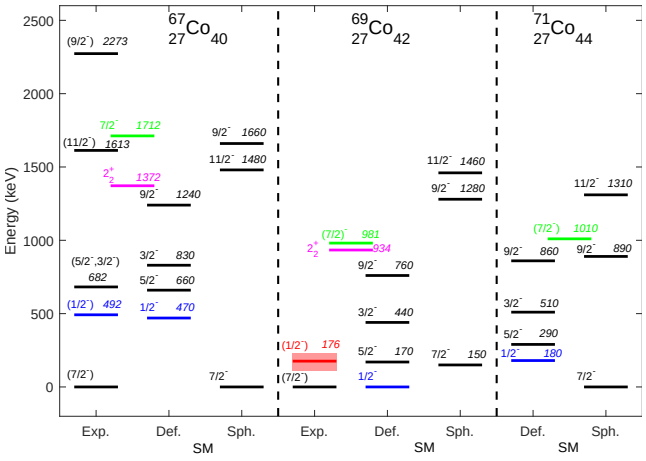

FIG. 2. Experimental level schemes for ^{67}Co [44, 46] and ^{69}Co (based on this work, in red) in comparison with the shell-model calculations for the deformed $K = 1/2^-$ and spherical bands. The 2_2^+ states [36, 38, 39] for Ni (in magenta) and $7/2^-$ states [83] for Cu isotones (in green), stemming from proton excitations across $Z = 28$, follow a similar trend as the $1/2^-$ states in Co (in blue). The 2_2^+ energies have been divided by two.

$7/2^-$ level in ^{69}Co, contrary to the predictions.

For ^{70}Co, the new phase-imaging ion-cyclotron-resonance technique (PI-ICR) [84, 85] was used to identify the composition of the beam. Unfortunately, there was no sign of another long-lived state at a statistically significant level. The production rates and determined mass-excess values for ^{70}Co changed only moderately when the measurement cycle was increased from 232 ms to 513 ms, supporting that it was the 508(7) ms, $(1^+, 2^+)$ state [58]. Using the PI-ICR data, we could set an upper limit for the $(6^-, 7^-)$ state contribution in the beam, which was $\leq 17\%$ and $\leq 5\%$ for the short and long cycles, respectively. For the final result, the value determined with the long cycle was adopted.

Our mass-excess value for ^{70}Co agrees with the extrapolation given in AME16 [74], and is 295(280) keV above the only previous experimental value [77] which was rejected in AME16 as an anomalous point, e.g. it intro-

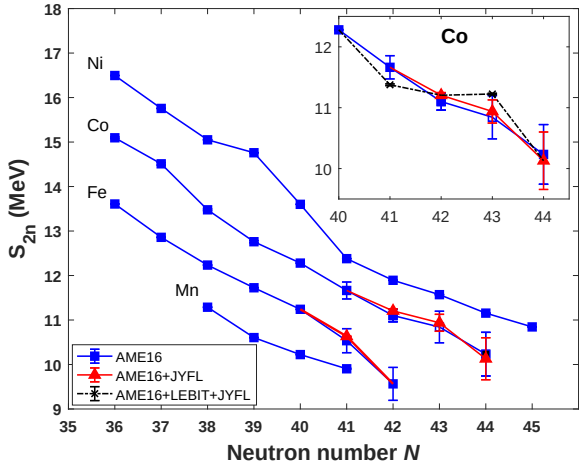

FIG. 3. Two-neutron separation energies based on experimental values from AME16 [74] (in blue) and including the results from this work (in red). In the inset, the black dashed line is plotted with the recent value for ^{68}Co [30] which is likely to belong to the isomer. For ^{70}Co, AME16 is based on extrapolations and our value is for the $(1^+, 2^+)$ state.

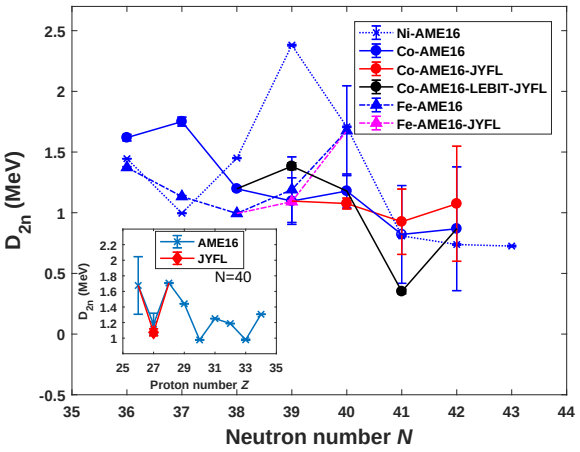

FIG. 4. Two-neutron shell gap parameter $D_{2n}(Z,N) = S_{2n}(Z,N) - S_{2n}(Z,N+2)$ based on AME16 [74] (in blue) and this work (red/magenta). The inset shows D_{2n} for $N = 40$. Including ^{68}Co from LEBIT [30] (in black) results in a kink at $N = 40$, pointing toward an isomeric state measurement.

duces a kink on the S_{2n} values. A much smoother trend is obtained with our new value as shown in Fig. 3 giving further support that the $(1^+, 2^+)$ is the ground state as suggested in Ref. [58]. If we measured the isomer, then the S_{2n} value for ^{70}Co would be larger, introducing a prominent kink at $N = 43$. We also noticed that using the value from [30] for ^{68}Co introduces an anomaly from $N = 41$ to 43 suggesting that the longer-living isomeric state was measured both for ^{68}Co and ^{69}Co in Ref. [30]. This is further supported by a measurement done at the ESR storage ring for an unknown mixture of ^{68}Co [86] which falls 195(96) keV below the value reported for the ground state in Ref. [30].

The present data confirm that the $N = 40$ subshell closure gets weaker below nickel. Two-neutron separation energies in the studied iron and cobalt isotopic chains do not drop significantly after $N = 40$, and the empirical two-neutron shell-gap energy for $N = 40$ at ^{67}Co is almost 0.7 MeV lower than at ^{68}Ni (see Figs. 3-4). This supports the earlier spectroscopic studies [87–90] indicating increased collectivity below nickel.

Mass surface close to $N = 40$ is also relevant for astrophysics. ^{67}Fe$(n,\gamma)^{68}$Fe has been highlighted as one of the most influential neutron-capture rates $N_A\langle\sigma v\rangle$ for the weak r-process with an impact factor $F = 15.8$ on the abundances when the rate is varied by a factor of 100 [19]. More importantly, its inverse photodissociation rate $\lambda_{\gamma,n}$, also affecting the abundances, depends exponentially on the reaction Q-value: $\lambda_{\gamma,n} \propto N_A\langle\sigma v\rangle exp[-Q/(kT)]$ for temperature T. Figure 5 shows a comparison of photodissociation rates and mass-related uncertainties for ^{68}Fe$(\gamma,n)^{67}$ Fe from this work and from REACLIB v1.0 [91] used for the sensitivity study in Ref. [19]. The photodissociation rate calculated with ^{67}Fe from this work and ^{68}Fe from AME16 [74], $Q = 5.85(37)$ MeV, is significantly higher than obtained with REACLIB v1.0, which relies on NON-SMOKER [92, 93] neutron-capture rates with $Q = 6.86(82)$ MeV, based on experimental AME95 [94] and theoretical FRDM1995 [95] values for ^{67}Fe and ^{68}Fe, respectively. At 1.5 GK, the new rate is around 2500 times higher and mass-related uncertainties have been reduced by a factor of ≈30.

In conclusion, we reported on the first precision mass measurements of ^{67}Fe and ^{70}Co. The position of the deformed $1/2^-$ state in ^{69}Co was determined for the first time. The trend of the $K = 1/2^-$ band-heads in neutron-rich ^{65,67,69}Co isotopes follows a parabolic pattern, a typical shape coexistence characteristics observed across the

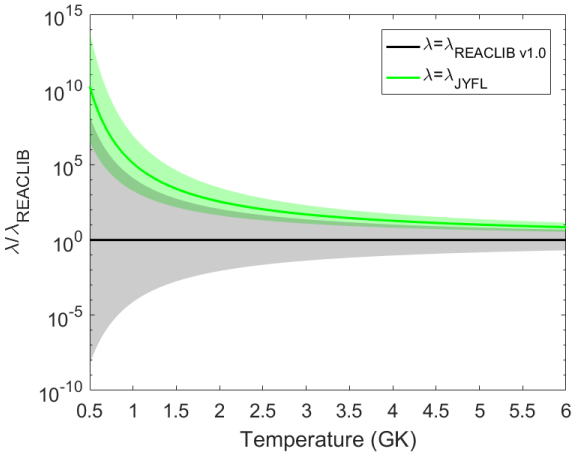

FIG. 5. Rates and mass-related uncertainties for ^{68}Fe$(\gamma,n)^{67}$Fe based on this work (JYFL) and REACLIB [91].

chart of nuclides. The results are in agreement with the large-scale shell-model calculations but the order of the $(7/2)^-$ and $(1/2^-)$ states is reversed at ^{69}Co. No strong subshell closure is observed below nickel and the mass surface is rather smooth. In future, precision mass measurements of ^{68}Co, ^{68}Fe, and ^{71}Co would be highly desirable to further extent our knowledge of the evolution of isomeric states in this fascinating region exhibiting shape coexistence, and to provide accurate Q-values for the weak r-process.

This work has been supported by the Academy of Finland under the Finnish Centre of Excellence Program (Nuclear and Accelerator Based Physics Research at JYFL 2012-2017) and by the European Unions Horizon 2020 research and innovation programme grant agreement No 654002 (ENSAR2). A.K. acknowledges the support from the Academy of Finland under grant No. 275389 and D.N. and L.C. under grants No. 284516 and 312544. T.E. acknowledges the support from the Academy of Finland under grant No. 295207 and A.R. under grant No. 306980. A.K. and L.C. acknowledge the funding from the European Unions Horizon 2020 research and innovation program under grant agreement No. 771036 (ERC CoG MAIDEN). We thank for the bilateral mobility grant from the Institut Français in Finland, the Embassy of France in Finland, the French Ministry of Higher Education and Research and the Finnish Society of Science and Letters. We are grateful for the mobility support from PICS MITICANS (Manipulation of Ions in Traps and Ion sourCes for Atomic and Nuclear Spectroscopy). S.G. thanks for the mobility grant from the EDPSIME.

* laetitia.l.canete@student.jyu.fi
† simon.giraud@ganil.fr

[1] D. Lunney, J. M. Pearson, and C. Thibault, Rev. Mod. Phys. **75**, 1021 (2003).
[2] J. Hakala, S. Rahaman, V.-V. Elomaa, T. Eronen, U. Hager, A. Jokinen, A. Kankainen, I. D. Moore, H. Penttilä, S. Rinta-Antila, J. Rissanen, A. Saastamoinen, T. Sonoda, C. Weber, and J. Äystö, Phys. Rev. Lett. **101**, 052502 (2008).
[3] J. Hakala, J. Dobaczewski, D. Gorelov, T. Eronen, A. Jokinen, A. Kankainen, V. S. Kolhinen, M. Kortelainen, I. D. Moore, H. Penttilä, S. Rinta-Antila, J. Rissanen, A. Saastamoinen, V. Sonnenschein, and J. Äystö, Phys. Rev. Lett. **109**, 032501 (2012).
[4] M. Dworschak, G. Audi, K. Blaum, P. Delahaye, S. George, U. Hager, F. Herfurth, A. Herlert, A. Kellerbauer, H.-J. Kluge, D. Lunney, L. Schweikhard, and C. Yazidjian, Phys. Rev. Lett. **100**, 072501 (2008).
[5] D. Atanasov, P. Ascher, K. Blaum, R. B. Cakirli, T. E. Cocolios, S. George, S. Goriely, F. Herfurth, H.-T. Janka, O. Just, M. Kowalska, S. Kreim, D. Kisler, Y. A. Litvinov, D. Lunney, V. Manea, D. Neidherr, M. Rosenbusch, L. Schweikhard, A. Welker, F. Wienholtz, R. N. Wolf, and K. Zuber, Phys. Rev. Lett. **115**, 232501 (2015).
[6] E. M. Burbidge, G. R. Burbidge, W. A. Fowler, and F. Hoyle, Rev. Mod. Phys. **29**, 547 (1957).
[7] M. Arnould, S. Goriely, and K. Takahashi, Phys. Rep. **450**, 97 (2007).
[8] C. J. Horowitz, A. Arcones, B. Côté, I. Dillmann, W. Nazarewicz, I. U. Roederer, H. Schatz, A. Aprahamian, D. Atanasov, A. Bauswein, J. Bliss, M. Brodeur, J. A. Clark, A. Frebel, F. Foucart, C. J. Hansen, O. Just, A. Kankainen, G. C. McLaughlin, J. M. Kelly, S. N. Liddick, D. M. Lee, J. Lippuner, D. Martin, J. Mendoza-Temis, B. D. Metzger, M. R. Mumpower, G. Perdikakis, J. Pereira, B. W. O'Shea, R. Reifarth, A. M. Rogers, D. M. Siegel, A. Spyrou, R. Surman, X. Tang, T. Uesaka, and M. Wang, arXiv e-prints , arXiv:1805.04637 (2018), arXiv:1805.04637 [astro-ph.SR].
[9] M. R. Mumpower, R. Surman, D.-L. Fang, M. Beard, P. Möller, T. Kawano, and A. Aprahamian, Phys. Rev. C **92**, 035807 (2015).
[10] M. Mumpower, R. Surman, G. McLaughlin, and A. Aprahamian, Progr.Part. Nucl. Phys. **86**, 86 (2016).
[11] B. Côté, C. L. Fryer, K. Belczynski, O. Korobkin, M. Chruliska, N. Vassh, M. R. Mumpower, J. Lippuner, T. M. Sprouse, R. Surman, and R. Wollaeger, Astrophys. J. **855**, 99 (2018).
[12] B. P. Abbott, R. Abbott, T. D. Abbott, F. Acernese, K. Ackley, C. Adams, T. Adams, P. Addesso, R. X. Adhikari, V. B. Adya, *et al.*, Astrophys. J. Lett. **848**, L12 (2017).
[13] R. N. Boyd, M. A. Famiano, B. S. Meyer, Y. Motizuki, T. Kajino, and I. U. Roederer, Astrophys. J. Lett. **744**, L14 (2012).
[14] W. Aoki, T. Suda, R. N. Boyd, T. Kajino, and M. A. Famiano, Astrophys. J. Lett. **766**, L13 (2013).
[15] G. Cescutti, C. Chiappini, R. Hirschi, G. Meynet, and U. Frischknecht, Astron. Astrophys. **553**, A51 (2013).
[16] S. Wanajo, Astrophys. J. Lett. **770**, L22 (2013).
[17] Y.-Z. Qian, Journal of Physics G: Nuclear and Particle Physics **41**, 044002 (2014).
[18] N. R. Tanvir, A. J. Levan, C. Gonzlez-Fernndez, O. Korobkin, I. Mandel, S. Rosswog, J. Hjorth, P. DAvanzo, A. S. Fruchter, C. L. Fryer, T. Kangas, B. Milvang-Jensen, S. Rosetti, D. Steeghs, R. T. Wollaeger, Z. Cano, C. M. Copperwheat, S. Covino, V. DElia, A. de Ugarte Postigo, P. A. Evans, W. P. Even, S. Fairhurst, R. F. Jaimes, C. J. Fontes, Y. I. Fujii, J. P. U. Fynbo, B. P. Gompertz, J. Greiner, G. Hodosan, M. J. Irwin, P. Jakobsson, U. G. Jrgensen, D. A. Kann, J. D. Lyman, D. Malesani, R. G. McMahon, A. Melandri, P. T. OBrien, J. P. Osborne, E. Palazzi, D. A. Perley, E. Pian, S. Piranomonte, M. Rabus, E. Rol, A. Rowlinson, S. Schulze, P. Sutton, C. C. Thne, K. Ulaczyk, D. Watson, K. Wiersema, and R. A. M. J. Wijers, Astrophys. J. Lett. **848**, L27 (2017).
[19] R. Surman, M. Mumpower, R. Sinclair, K. L. Jones, W. R. Hix, and G. C. McLaughlin, AIP Advances **4**, 041008 (2014).
[20] P. Walker and G. Dracoulis, Nature **399**, 35 (1999).
[21] P. M. Walker and J. J. Carroll, Physics Today **58**, 39 (2005).
[22] R. Broda, B. Fornal, W. Królas, T. Pawłat, D. Bazzacco, S. Lunardi, C. Rossi-Alvarez, R. Menegazzo, G. de Angelis, P. Bednarczyk, J. Rico, D. De Acuña, P. J. Daly, R. H. Mayer, M. Sferrazza, H. Grawe, K. H. Maier, and

R. Schubart, Phys. Rev. Lett. **74**, 868 (1995).
[23] O. Sorlin, S. Leenhardt, C. Donzaud, J. Duprat, F. Azaiez, F. Nowacki, H. Grawe, Z. Dombrádi, F. Amorini, A. Astier, D. Baiborodin, M. Belleguic, C. Borcea, C. Bourgeois, D. M. Cullen, Z. Dlouhy, E. Dragulescu, M. Górska, S. Grévy, D. Guillemaud-Mueller, G. Hagemann, B. Herskind, J. Kiener, R. Lemmon, M. Lewitowicz, S. M. Lukyanov, P. Mayet, F. de Oliveira Santos, D. Pantalica, Y.-E. Penionzhkevich, F. Pougheon, A. Poves, N. Redon, M. G. Saint-Laurent, J. A. Scarpaci, G. Sletten, M. Stanoiu, O. Tarasov, and C. Theisen, Phys. Rev. Lett. **88**, 092501 (2002).
[24] N. Bree, I. Stefanescu, P. A. Butler, J. Cederkäll, T. Davinson, P. Delahaye, J. Eberth, D. Fedorov, V. N. Fedosseev, L. M. Fraile, S. Franchoo, G. Georgiev, K. Gladnishki, M. Huyse, O. Ivanov, J. Iwanicki, J. Jolie, U. Köster, T. Kröll, R. Krücken, B. A. Marsh, O. Niedermaier, P. Reiter, H. Scheit, D. Schwalm, T. Sieber, J. V. de Walle, P. V. Duppen, N. Warr, D. Weisshaar, F. Wenander, and S. Zemlyanoy, Phys. Rev. C **78**, 047301 (2008).
[25] K. Langanke, J. Terasaki, F. Nowacki, D. J. Dean, and W. Nazarewicz, Phys. Rev. C **67**, 044314 (2003).
[26] H. Grawe and M. Lewitowicz, Nucl. Phys. A **693**, 116 (2001), Radioactive Nuclear Beams.
[27] C. Guénaut, G. Audi, D. Beck, K. Blaum, G. Bollen, P. Delahaye, F. Herfurth, A. Kellerbauer, H.-J. Kluge, J. Libert, D. Lunney, S. Schwarz, L. Schweikhard, and C. Yazidjian, Phys. Rev. C **75**, 044303 (2007).
[28] S. Rahaman, J. Hakala, V. V. Elomaa, T. Eronen, U. Hager, A. Jokinen, A. Kankainen, I. D. Moore, H. Penttilä, S. Rinta-Antila, J. Rissanen, A. Saastamoinen, C. Weber, and J. Äystö, Eur. Phys. J. A **34**, 5 (2007).
[29] R. Ferrer, M. Block, C. Bachelet, B. R. Barquest, G. Bollen, C. M. Campbell, M. Facina, C. M. Folden, C. Guénaut, A. A. Kwiatkowski, D. L. Lincoln, D. J. Morrissey, G. K. Pang, A. M. Prinke, R. Ringle, J. Savory, P. Schury, and S. Schwarz, Phys. Rev. C **81**, 044318 (2010).
[30] C. Izzo, G. Bollen, M. Brodeur, M. Eibach, K. Gulyuz, J. D. Holt, J. M. Kelly, M. Redshaw, R. Ringle, R. Sandler, S. Schwarz, S. R. Stroberg, C. S. Sumithrarachchi, A. A. Valverde, and A. C. C. Villari, Phys. Rev. C **97**, 014309 (2018).
[31] M. Block, C. Bachelet, G. Bollen, M. Facina, C. M. Folden, C. Guénaut, A. A. Kwiatkowski, D. J. Morrissey, G. K. Pang, A. Prinke, R. Ringle, J. Savory, P. Schury, and S. Schwarz, Phys. Rev. Lett. **100**, 132501 (2008).
[32] A. Gade and S. N. Liddick, J. Phys. G: Nucl. Part. Phys. **43**, 024001 (2016).
[33] M. Bernas, P. Dessagne, M. Langevin, J. Payet, F. Pougheon, and P. Roussel, Phys. Lett. B **113**, 279 (1982).
[34] F. Recchia, C. J. Chiara, R. V. F. Janssens, D. Weisshaar, A. Gade, W. B. Walters, M. Albers, M. Alcorta, V. M. Bader, T. Baugher, D. Bazin, J. S. Berryman, P. F. Bertone, B. A. Brown, C. M. Campbell, M. P. Carpenter, J. Chen, H. L. Crawford, H. M. David, D. T. Doherty, C. R. Hoffman, F. G. Kondev, A. Korichi, C. Langer, N. Larson, T. Lauritsen, S. N. Liddick, E. Lunderberg, A. O. Macchiavelli, S. Noji, C. Prokop, A. M. Rogers, D. Seweryniak, S. R. Stroberg, S. Suchyta, S. Williams, K. Wimmer, and S. Zhu, Phys. Rev. C **88**, 041302 (2013).
[35] S. Suchyta, S. N. Liddick, Y. Tsunoda, T. Otsuka, M. B. Bennett, A. Chemey, M. Honma, N. Larson, C. J. Prokop, S. J. Quinn, N. Shimizu, A. Simon, A. Spyrou, V. Tripathi, Y. Utsuno, and J. M. VonMoss, Phys. Rev. C **89**, 021301 (2014).
[36] F. Flavigny, D. Pauwels, D. Radulov, I. J. Darby, H. De Witte, J. Diriken, D. V. Fedorov, V. N. Fedosseev, L. M. Fraile, M. Huyse, V. S. Ivanov, U. Köster, B. A. Marsh, T. Otsuka, L. Popescu, R. Raabe, M. D. Seliverstov, N. Shimizu, A. M. Sjödin, Y. Tsunoda, P. Van den Bergh, P. Van Duppen, J. Van de Walle, M. Venhart, W. B. Walters, and K. Wimmer, Phys. Rev. C **91**, 034310 (2015).
[37] B. Crider, C. Prokop, S. Liddick, M. Al-Shudifat, A. Ayangeakaa, M. Carpenter, J. Carroll, J. Chen, C. Chiara, H. David, A. Dombos, S. Go, R. Grzywacz, J. Harker, R. Janssens, N. Larson, T. Lauritsen, R. Lewis, S. Quinn, F. Recchia, A. Spyrou, S. Suchyta, W. Walters, and S. Zhu, Phys. Lett. B **763**, 108 (2016).
[38] C. J. Prokop, B. P. Crider, S. N. Liddick, A. D. Ayangeakaa, M. P. Carpenter, J. J. Carroll, J. Chen, C. J. Chiara, H. M. David, A. C. Dombos, S. Go, J. Harker, R. V. F. Janssens, N. Larson, T. Lauritsen, R. Lewis, S. J. Quinn, F. Recchia, D. Seweryniak, A. Spyrou, S. Suchyta, W. B. Walters, and S. Zhu, Phys. Rev. C **92**, 061302 (2015).
[39] C. J. Chiara, D. Weisshaar, R. V. F. Janssens, Y. Tsunoda, T. Otsuka, J. L. Harker, W. B. Walters, F. Recchia, M. Albers, M. Alcorta, V. M. Bader, T. Baugher, D. Bazin, J. S. Berryman, P. F. Bertone, C. M. Campbell, M. P. Carpenter, J. Chen, H. L. Crawford, H. M. David, D. T. Doherty, A. Gade, C. R. Hoffman, M. Honma, F. G. Kondev, A. Korichi, C. Langer, N. Larson, T. Lauritsen, S. N. Liddick, E. Lunderberg, A. O. Macchiavelli, S. Noji, C. Prokop, A. M. Rogers, D. Seweryniak, N. Shimizu, S. R. Stroberg, S. Suchyta, Y. Utsuno, S. J. Williams, K. Wimmer, and S. Zhu, Phys. Rev. C **91**, 044309 (2015).
[40] Y. Tsunoda, T. Otsuka, N. Shimizu, M. Honma, and Y. Utsuno, Phys. Rev. C **89**, 031301 (2014).
[41] A. Poves, J. Phys. G: Nucl. Part. Phys. **43**, 024010 (2016).
[42] T. Otsuka, T. Suzuki, R. Fujimoto, H. Grawe, and Y. Akaishi, Phys. Rev. Lett. **95**, 232502 (2005).
[43] T. Otsuka, T. Suzuki, M. Honma, Y. Utsuno, N. Tsunoda, K. Tsukiyama, and M. Hjorth-Jensen, Phys. Rev. Lett. **104**, 012501 (2010).
[44] D. Pauwels, O. Ivanov, N. Bree, J. Büscher, T. E. Cocolios, J. Gentens, M. Huyse, A. Korgul, Y. Kudryavtsev, R. Raabe, M. Sawicka, I. Stefanescu, J. Van de Walle, P. Van den Bergh, P. Van Duppen, and W. B. Walters, Phys. Rev. C **78**, 041307 (2008).
[45] D. Pauwels, O. Ivanov, N. Bree, J. Büscher, T. E. Cocolios, M. Huyse, Y. Kudryavtsev, R. Raabe, M. Sawicka, J. V. de Walle, P. V. Duppen, A. Korgul, I. Stefanescu, A. A. Hecht, N. Hoteling, A. Wöhr, W. B. Walters, R. Broda, B. Fornal, W. Krolas, T. Pawlat, J. Wrzesinski, M. P. Carpenter, R. V. F. Janssens, T. Lauritsen, D. Seweryniak, S. Zhu, J. R. Stone, and X. Wang, Phys. Rev. C **79**, 044309 (2009).
[46] F. Recchia, S. M. Lenzi, S. Lunardi, E. Farnea, A. Gadea, N. Mărginean, D. R. Napoli, F. Nowacki, A. Poves, J. J. Valiente-Dobón, M. Axiotis, S. Aydin, D. Bazzacco,

G. Benzoni, P. G. Bizzeti, A. M. Bizzeti-Sona, A. Bracco, D. Bucurescu, E. Caurier, L. Corradi, G. de Angelis, F. Della Vedova, E. Fioretto, A. Gottardo, M. Ionescu-Bujor, A. Iordachescu, S. Leoni, R. Mărginean, P. Mason, R. Menegazzo, D. Mengoni, B. Million, G. Montagnoli, R. Orlandi, G. Pollarolo, E. Sahin, F. Scarlassara, R. P. Singh, A. M. Stefanini, S. Szilner, C. A. Ur, and O. Wieland, Phys. Rev. C **85**, 064305 (2012).

[47] S. M. Lenzi, F. Nowacki, A. Poves, and K. Sieja, Phys. Rev. C **82**, 054301 (2010).

[48] S. N. Liddick, W. B. Walters, C. J. Chiara, R. V. F. Janssens, B. Abromeit, A. Ayres, A. Bey, C. R. Bingham, M. P. Carpenter, L. Cartegni, J. Chen, H. L. Crawford, I. G. Darby, R. Grzywacz, J. Harker, C. R. Hoffman, S. Ilyushkin, F. G. Kondev, N. Larson, M. Madurga, D. Miller, S. Padgett, S. V. Paulauskas, M. M. Rajabali, K. Rykaczewski, D. Seweryniak, S. Suchyta, and S. Zhu, Phys. Rev. C **92**, 024319 (2015).

[49] M. Bernas, P. Armbruster, S. Czajkowski, H. Faust, J. P. Bocquet, and R. Brissot, Phys. Rev. Lett. **67**, 3661 (1991).

[50] W. F. Mueller, B. Bruyneel, S. Franchoo, H. Grawe, M. Huyse, U. Köster, K.-L. Kratz, K. Kruglov, Y. Kudryavtsev, B. Pfeiffer, R. Raabe, I. Reusen, P. Thirolf, P. Van Duppen, J. Van Roosbroeck, L. Vermeeren, W. B. Walters, and L. Weissman, Phys. Rev. Lett. **83**, 3613 (1999).

[51] O. Sorlin *et al.*, Nuclear Physics A **660**, 3 (1999).

[52] J. M. Daugas, I. Matea, J.-P. Delaroche, M. Pfützner, M. Sawicka, F. Becker, G. Bélier, C. R. Bingham, R. Borcea, E. Bouchez, A. Buta, E. Dragulescu, G. Georgiev, J. Giovinazzo, M. Girod, H. Grawe, R. Grzywacz, F. Hammache, F. Ibrahim, M. Lewitowicz, J. Libert, P. Mayet, V. Méot, F. Negoita, F. de Oliveira Santos, O. Perru, O. Roig, K. Rykaczewski, M. G. Saint-Laurent, J. E. Sauvestre, O. Sorlin, M. Stanoiu, I. Stefan, C. Stodel, C. Theisen, D. Verney, and J. Żylicz, Phys. Rev. C **83**, 054312 (2011).

[53] G. Audi, F. Kondev, M. Wang, W. Huang, and S. Naimi, Chin. Phys. C **41**, 030001 (2017).

[54] S. N. Liddick, A. Spyrou, B. P. Crider, F. Naqvi, A. C. Larsen, M. Guttormsen, M. Mumpower, R. Surman, G. Perdikakis, D. L. Bleuel, A. Couture, L. Crespo Campo, A. C. Dombos, R. Lewis, S. Mosby, S. Nikas, C. J. Prokop, T. Renstrom, B. Rubio, S. Siem, and S. J. Quinn, Phys. Rev. Lett. **116**, 242502 (2016).

[55] A. Spyrou, S. N. Liddick, F. Naqvi, B. P. Crider, A. C. Dombos, D. L. Bleuel, B. A. Brown, A. Couture, L. Crespo Campo, M. Guttormsen, A. C. Larsen, R. Lewis, P. Möller, S. Mosby, M. R. Mumpower, G. Perdikakis, C. J. Prokop, T. Renstrøm, S. Siem, S. J. Quinn, and S. Valenta, Phys. Rev. Lett. **117**, 142701 (2016).

[56] A. C. Larsen, J. E. Midtbø, M. Guttormsen, T. Renstrøm, S. N. Liddick, A. Spyrou, S. Karampagia, B. A. Brown, O. Achakovskiy, S. Kamerdzhiev, D. L. Bleuel, A. Couture, L. C. Campo, B. P. Crider, A. C. Dombos, R. Lewis, S. Mosby, F. Naqvi, G. Perdikakis, C. J. Prokop, S. J. Quinn, and S. Siem, Phys. Rev. C **97**, 054329 (2018).

[57] W. F. Mueller, B. Bruyneel, S. Franchoo, M. Huyse, J. Kurpeta, K. Kruglov, Y. Kudryavtsev, N. V. S. V. Prasad, R. Raabe, I. Reusen, P. Van Duppen, J. Van Roosbroeck, L. Vermeeren, L. Weissman, Z. Janas, M. Karny, T. Kszczot, A. Płochocki, K.-L. Kratz, B. Pfeiffer, H. Grawe, U. Köster, P. Thirolf, and W. B. Walters, Phys. Rev. C **61**, 054308 (2000).

[58] A. Morales, G. Benzoni, H. Watanabe, Y. Tsunoda, T. Otsuka, S. Nishimura, F. Browne, R. Daido, P. Doornenbal, Y. Fang, G. Lorusso, Z. Patel, S. Rice, L. Sinclair, P.-A. Sderstrm, T. Sumikama, J. Wu, Z. Xu, A. Yagi, R. Yokoyama, H. Baba, R. Avigo, F. B. Garrote, N. Blasi, A. Bracco, F. Camera, S. Ceruti, F. Crespi, G. de Angelis, M.-C. Delattre, Z. Dombradi, A. Gottardo, T. Isobe, I. Kojouharov, N. Kurz, I. Kuti, K. Matsui, B. Melon, D. Mengoni, T. Miyazaki, V. Modamio-Hoybjor, S. Momiyama, D. Napoli, M. Niikura, R. Orlandi, H. Sakurai, E. Sahin, D. Sohler, H. Schaffner, R. Taniuchi, J. Taprogge, Z. Vajta, J. Valiente-Dobn, O. Wieland, and M. Yalcinkaya, Phys. Lett. B **765**, 328 (2017).

[59] N. Shimizu, T. Abe, Y. Tsunoda, Y. Utsuno, T. Yoshida, T. Mizusaki, M. Honma, and T. Otsuka, Progr. Theor. Exp. Phys. **2012**, 01A205 (2012).

[60] R. Grzywacz, R. Béraud, C. Borcea, A. Emsallem, M. Glogowski, H. Grawe, D. Guillemaud-Mueller, M. Hjorth-Jensen, M. Houry, M. Lewitowicz, A. C. Mueller, A. Nowak, A. Płochocki, M. Pfützner, K. Rykaczewski, M. G. Saint-Laurent, J. E. Sauvestre, M. Schaefer, O. Sorlin, J. Szerypo, W. Trinder, S. Viteritti, and J. Winfield, Phys. Rev. Lett. **81**, 766 (1998).

[61] M. Sawicka, J. Daugas, H. Grawe, S. Cwiok, D. Balabanski, R. Béraud, C. Bingham, C. Borcea, M. La Commara, G. de France, G. Georgiev, M. Górska, R. Grzywacz, M. Hass, M. Hellström, Z. Janas, M. Lewitowicz, H. Mach, I. Matea, G. Neyens, C. O' Leary, F. de Oliveira Santos, R. Page, M. Pfützner, Z. Podolyák, K. Rykaczewski, M. Stanoiu, and J. Żylicz, Eur. Phys. J. A **16**, 51 (2003).

[62] M. König, G. Bollen, H. J. Kluge, T. Otto, and J. Szerypo, Int. J. Mass Spectrom. Ion Proc. **142**, 95 (1995).

[63] Nucl. Instrum. Meth. Phys. Res. Sect. B **317**, 208 (2013), XVIth International Conference on ElectroMagnetic Isotope Separators and Techniques Related to their Applications, December 27, 2012 at Matsue, Japan.

[64] P. Karvonen, H. Penttilä, J. Äystö, J. Billowes, P. Campbell, V.-V. Elomaa, U. Hager, J. Hakala, A. Jokinen, T. Kessler, A. Kankainen, I. Moore, K. Peräjärvi, S. Rahaman, S. Rinta-Antila, J. Rissanen, J. Ronkainen, A. Saastamoinen, T. Sonoda, B. Tordoff, and C. Weber, Nucl. Instrum. Meth. Phys. Res. Sect. B **266**, 4454 (2008), Proceedings of the XVth International Conference on Electromagnetic Isotope Separators and Techniques Related to their Applications.

[65] A. Nieminen, J. Huikari, A. Jokinen, J. Äystö, P. Campbell, and E. Cochrane, Nucl. Instrum. Meth. Phys. Res. Sect. A **469**, 244 (2001).

[66] T. Eronen, V. S. Kolhinen, V. V. Elomaa, D. Gorelov, U. Hager, J. Hakala, A. Jokinen, A. Kankainen, P. Karvonen, S. Kopecky, I. D. Moore, H. Penttilä, S. Rahaman, S. Rinta-Antila, J. Rissanen, A. Saastamoinen, J. Szerypo, C. Weber, and J. Äystö, The European Physical Journal A **48**, 46 (2012).

[67] G. Savard, S. Becker, G. Bollen, H.-J. Kluge, R. Moore, T. Otto, L. Schweikhard, H. Stolzenberg, and U. Wiess, Phys. Lett. A **158**, 247 (1991).

[68] G. Gräff, H. Kalinowsky, and J. Traut, Z. Phys. A **297**, 35 (1980).

[69] M. Kretzschmar, Int. J. Mass Spectrom. **264**, 122 (2007).

[70] S. George, K. Blaum, F. Herfurth, A. Herlert, M. Kretzschmar, S. Nagy, S. Schwarz, L. Schweikhard, and C. Yazidjian, Int. J. Mass Spectrom. **264**, 110 (2007).

[71] S. George, S. Baruah, B. Blank, K. Blaum, M. Breitenfeldt, U. Hager, F. Herfurth, A. Herlert, A. Kellerbauer, H.-J. Kluge, M. Kretzschmar, D. Lunney, R. Savreux, S. Schwarz, L. Schweikhard, and C. Yazidjian, Phys. Rev. Lett. **98**, 162501 (2007).

[72] L. Canete, A. Kankainen, T. Eronen, D. Gorelov, J. Hakala, A. Jokinen, V. S. Kolhinen, J. Koponen, I. D. Moore, J. Reinikainen, and S. Rinta-Antila, Eur. Phys. J. A **52**, 124 (2016).

[73] L. Canete, Ph.D. thesis, University of Jyväskylä (2019).

[74] M. Wang, G. Audi, F. Kondev, W. Huang, S. Naimi, and X. Xu, Chin. Phys. C **41**, 030003 (2017).

[75] H. L. Seifert, J. M. Wouters, D. J. Vieira, H. Wollnik, X. G. Zhou, X. L. Tu, Z. Y. Zhou, and G. W. Butler, Z. Phys. A **349**, 25 (1994).

[76] Y. Bai, D. J. Vieira, H. L. Seifert, and J. M. Wouters, in *American Institute of Physics Conference Series*, American Institute of Physics Conference Series, Vol. 455, edited by B. M. Sherill, D. J. Morrissey, and C. N. Davids (1998) pp. 90–93.

[77] A. Estradé, M. Matoš, H. Schatz, A. M. Amthor, D. Bazin, M. Beard, A. Becerril, E. F. Brown, R. Cyburt, T. Elliot, A. Gade, D. Galaviz, S. George, S. S. Gupta, W. R. Hix, R. Lau, G. Lorusso, P. Möller, J. Pereira, M. Portillo, A. M. Rogers, D. Shapira, E. Smith, A. Stolz, M. Wallace, and M. Wiescher, Phys. Rev. Lett. **107**, 172503 (2011).

[78] M. Matoš, A. Estradé, H. Schatz, D. Bazin, M. Famiano, A. Gade, S. George, W. Lynch, Z. Meisel, M. Portillo, A. Rogers, D. Shapira, A. Stolz, M. Wallace, and J. Yurkon, Nucl. Instrum. Meth. Phys. Res. Sect. A **696**, 171 (2012).

[79] Z. Meisel, *Extension of the nuclear mass surface for neutron-rich isotopes of argon through iron*, Ph.D. thesis, Michigan State University (2015).

[80] M. Matos, *Isochronous Mass Measurements of Short-Lived Neutron Rich Nuclides at the FRS-ESR Facilities*, Ph.D. thesis, Justus-Liebig-Universität Giessen (2004).

[81] X. Xing, W. Meng, Z. Yu-Hu, X. Hu-Shan, S. Peng, T. Xiao-Lin, Y. A. Litvinov, Z. Xiao-Hong, S. Bao-Hua, Y. You-Jin, X. Jia-Wen, Y. Jian-Cheng, K. Blaum, C. Rui-Jiu, C. Xiang-Cheng, F. Chao-Yi, G. Zhuang, H. Zheng-Guo, H. Wen-Jia, L. Da-Wei, L. Yi-Hua, M. Xin-Wen, M. Rui-Shi, T. Uesaka, X. Guo-Qing, X. Yuan-Ming, T. Yamaguchi, Y. Yamaguchi, Z. Qi, Y. Xin-Liang, Z. Hong-Wei, Z. Tie-Cheng, Z. Wei, and Z. Wen-Long, Chin. Phys. C **39**, 104001 (2015).

[82] F. Nowacki, A. Poves, E. Caurier, and B. Bounthong, Phys. Rev. Lett. **117**, 272501 (2016).

[83] S. Franchoo, M. Huyse, K. Kruglov, Y. Kudryavtsev, W. F. Mueller, R. Raabe, I. Reusen, P. Van Duppen, J. Van Roosbroeck, L. Vermeeren, A. Wöhr, H. Grawe, K.-L. Kratz, B. Pfeiffer, and W. B. Walters, Phys. Rev. C **64**, 054308 (2001).

[84] S. Eliseev, K. Blaum, M. Block, C. Droese, M. Goncharov, E. Minaya Ramirez, D. A. Nesterenko, Y. N. Novikov, and L. Schweikhard, Phys. Rev. Lett. **110**, 082501 (2013).

[85] D. A. Nesterenko, T. Eronen, A. Kankainen, L. Canete, A. Jokinen, I. D. Moore, H. Penttilä, S. Rinta-Antila, A. de Roubin, and M. Vilen, Eur. Phys. J. A **54**, 154 (2018).

[86] R. Knöbel, *Neuartige isochrone Massenmessung kurzlebiger neutronenreicher, gespeicherter Kerne am FRS-ESR*, Ph.D. thesis, Justus-Liebig-Universität Giessen (2008).

[87] J. Ljungvall, A. Görgen, A. Obertelli, W. Korten, E. Clément, G. de France, A. Bürger, J.-P. Delaroche, A. Dewald, A. Gadea, L. Gaudefroy, M. Girod, M. Hackstein, J. Libert, D. Mengoni, F. Nowacki, T. Pissulla, A. Poves, F. Recchia, M. Rejmund, W. Rother, E. Sahin, C. Schmitt, A. Shrivastava, K. Sieja, J. J. Valiente-Dobón, K. O. Zell, and M. Zielińska, Phys. Rev. C **81**, 061301 (2010).

[88] A. Gade, R. V. F. Janssens, T. Baugher, D. Bazin, B. A. Brown, M. P. Carpenter, C. J. Chiara, A. N. Deacon, S. J. Freeman, G. F. Grinyer, C. R. Hoffman, B. P. Kay, F. G. Kondev, T. Lauritsen, S. McDaniel, K. Meierbachtol, A. Ratkiewicz, S. R. Stroberg, K. A. Walsh, D. Weisshaar, R. Winkler, and S. Zhu, Phys. Rev. C **81**, 051304 (2010).

[89] T. Braunroth, A. Dewald, H. Iwasaki, S. M. Lenzi, M. Albers, V. M. Bader, T. Baugher, T. Baumann, D. Bazin, J. S. Berryman, C. Fransen, A. Gade, T. Ginter, A. Gottardo, M. Hackstein, J. Jolie, A. Lemasson, J. Litzinger, S. Lunardi, T. Marchi, V. Modamio, C. Morse, D. R. Napoli, A. Nichols, F. Recchia, S. R. Stroberg, R. Wadsworth, D. Weisshaar, K. Whitmore, and K. Wimmer, Phys. Rev. C **92**, 034306 (2015).

[90] H. L. Crawford, R. M. Clark, P. Fallon, A. O. Macchiavelli, T. Baugher, D. Bazin, C. W. Beausang, J. S. Berryman, D. L. Bleuel, C. M. Campbell, M. Cromaz, G. de Angelis, A. Gade, R. O. Hughes, I. Y. Lee, S. M. Lenzi, F. Nowacki, S. Paschalis, M. Petri, A. Poves, A. Ratkiewicz, T. J. Ross, E. Sahin, D. Weisshaar, K. Wimmer, and R. Winkler, Phys. Rev. Lett. **110**, 242701 (2013).

[91] R. H. Cyburt, A. M. Amthor, R. Ferguson, Z. Meisel, K. Smith, S. Warren, A. Heger, R. D. Hoffman, T. Rauscher, A. Sakharuk, H. Schatz, F. K. Thielemann, and M. Wiescher, Astrophys. J. Suppl. Ser. **189**, 240 (2010).

[92] T. Rauscher and F.-K. Thielemann, At. Data Nucl. Data Tables **75**, 1 (2000).

[93] T. Rauscher and F.-K. Thielemann, At. Data Nucl. Data Tables **79**, 47 (2001).

[94] G. Audi and A. Wapstra, Nucl. Phys. A **595**, 409 (1995).

[95] P. Moller, J. Nix, W. Myers, and W. Swiatecki, At. Data and Nucl. Data Tables **59**, 185 (1995).

IV

HIGH-PRECISION PROTON-CAPTURE Q VALUES FOR ^{25}Al(p,γ)^{26}Si AND ^{30}P(p,γ)^{31}Si

by

L. Canete, A. Kankainen, T. Eronen, D. Gorelov,J. Hakala, A. Jokinen,
V. Kolhinen, J. Koponen, I.D. Moore, J. Reinikainen, S. Rinta-Antila

JPS Conf. Proc., 020503 (2017). Proceedings of the 14th International Symposium on Nuclei in the Cosmos (NIC2016)

http://urn.fi/URN:NBN:fi:jyu-201801081094

V

HIGH-PRECISION MASS MEASUREMENTS FOR THE rp-PROCESS AT JYFLTRAP

by

L. Canete, T. Eronen, A. Jokinen, A. Kankainen, I.D. Moore, D.A. Nesterenko, and Sami Rinta-Antila

Conferences 165, 01008 (2017). Proceedings of the Nuclear Physics in Astrophysics VIII (NPA8)

http://urn.fi/URN:NBN:fi:jyu-201801091123